Western Graduate&PostdoctoralStudies

Western University
Scholarship@Western

Electronic Thesis and Dissertation Repository

8-8-2023 2:00 PM

Investigating Novel Luminescent Materials Towards Applications in Light Emitting Electrochemical Cells

Kenneth Chu, *Western University*

Supervisor: Ding, Zhifeng, *The University of Western Ontario*

A thesis submitted in partial fulfillment of the requirements for the Doctor of Philosophy degree in Chemistry

© Kenneth Chu 2023

Follow this and additional works at: https://ir.lib.uwo.ca/etd

Part of the Analytical Chemistry Commons

Recommended Citation

Chu, Kenneth, "Investigating Novel Luminescent Materials Towards Applications in Light Emitting Electrochemical Cells" (2023). *Electronic Thesis and Dissertation Repository*. 9593.
https://ir.lib.uwo.ca/etd/9593

This Dissertation/Thesis is brought to you for free and open access by Scholarship@Western. It has been accepted for inclusion in Electronic Thesis and Dissertation Repository by an authorized administrator of Scholarship@Western. For more information, please contact wlswadmin@uwo.ca.

Abstract

The search for new and better luminescent materials is becoming increasingly important, as there are significant cost-savings in using luminophores that are brighter and more efficient. Carbon quantum dots (CQDs) and other luminescent materials such as Pt-Ag nanoclusters and TADF compounds are an extremely appealing alternative to existing light-emitting materials, as they are low-cost, easy to synthesize, and non-toxic.

This thesis explores the properties and performance of different luminescent materials to be used in light-emitting electrochemical cells (LECs). In this work, we focused on LECs as their low cost and ease of fabrication aligns well with the ethos of CQDs and carbon-based nanomaterials. Firstly, we carried out some foundational work: developing a method to accurately determine the absolute quantum efficiency of the materials we tested. This method was tested using a variety of photodetectors to increase the analytical applicability, including photomultiplier tubes and spectrograph/CCD camera setups, and addresses many of the problems with reporting relative ECL efficiency. We also looked at several different novel materials – Pt-Ag bimetallic nanoclusters, and organic compounds that exhibit thermally activated delayed fluorescence (TADF) to enhance quantum efficiency – to evaluate their feasibility for use in LECs. In addition, we developed a set of computer simulations using COMSOL Multiphysics to model these light-emitting reactions. Using these models, we are able to learn important parameters, such as the bimolecular annihilation rate constant in electrochemiluminescence reactions, gain more knowledge about how these materials can emit light, and further optimize their luminous performance and efficiency.

In the final chapter of this thesis, we demonstrate our CQD-based LEC devices. These devices are the first example of CQDs being used in this fashion, and they exhibited bright white emission under electrical excitation. These CQDs, and, optimistically, derivatives of the material that are inspired by this work, are expected to be a substantial advancement in the research of next-generation, high performance light-emitting devices.

Keywords

Electrochemiluminescence (ECL) · Electrochemistry · Graphene Quantum Dots (CQD or GQD) · Thermally Activated Delayed Fluorescence (TADF) · Absolute Quantum Efficiency · Light Emitting Electrochemical Cell (LEC) · Photoelectrochemistry

Summary for Lay Audience

The search for new and better luminescent materials is becoming increasingly important at this time, as low-cost and more efficient light sources can greatly benefit society.

This thesis explores the performance of different materials to be used in light-emitting electrochemical cells (LECs). Along the way, we carried out some foundational work: developing a method to accurately determine the quantum efficiency (how well a material can transform input electricity into visible light) of the materials we tested. We also looked at several different novel materials – nanoclusters of noble metals, and organic compounds – to evaluate their feasibility for use in LECs. In addition, we developed a set of computer simulations to model these light-emitting reactions. Using these models, we are able to learn important parameters about how these materials can emit light, and further optimize their performance.

In the final section of this thesis, we demonstrate our CQD-based LEC devices. These devices are the first example of CQDs being used in this fashion, and they exhibited bright white emission under electrical excitation. These CQDs, and, optimistically, derivatives of the material that are inspired by this work, are expected to be a substantial advancement in the research of next-generation, high performance light-emitting devices.

Co-Authorship Statement

This thesis contains material from seven published papers presented in Chapters 2, 3, 4, 5, 6, 8, and 9. Also included in this thesis are two manuscripts in preparation (Chapters 1 and Chapter 7).

Chapter 1 is authored by Kenneth Chu, Zhifeng Ding, and Eli Zysman-Colman, and is published in *Chemistry – European Journal* (**2023**) DOI: 10.1002/chem.202301504. KC wrote the manuscript. ZD and EZC edited and finalized the manuscript.

Chapter 2 is authored by Kenneth Chu and Zhifeng Ding. KC and ZD planned and organized the manuscript. KC wrote the manuscript, and ZD edited and finalized the manuscript.

Chapter 3 is published in *The Journal of Physical Chemistry C* (**2021**) 125, 22274-22282 co-authored by Kenneth Chu, Jonathan Adsetts, Jing Ma, Congyang Zhang, Mahdi Hesari, Liuqing Yang, and Zhifeng Ding. KC and JM carried out the electrochemistry, electrochemiluminescence, and quantum efficiency calculations for the $Ru(bpy)_3^{2+}$ ECL system. JA assisted with the calibration procedure and instrumentation. KC was responsible for writing the manuscript, which was edited by CZ, MH, and LY. ZD finalized the manuscript.

Chapter 4 contains work published in *The Journal of Physical Chemistry C* (**2022**) 47, 20155-20162 co-authored by Jonathan Adsetts, Kenneth Chu (equally contributed first authors), Mahdi Hesari, Zackry Whitworth, Xiaoli Qin, Ziying Zhan, and Zhifeng Ding. MH performed the synthesis of the Au nanoclusters. JA carried out the electrochemistry and electrochemiluminescence experiments. KC was responsible for the calculations and code to determine the ECL quantum efficiency of the Au nanoclusters. JA and KC wrote the manuscript, which was edited by ZW, XQ, and ZZ, and finalized by ZD.

Chapter 5 is published in *The Journal of the American Chemical Society* (**2022**) 144, 20421-20433 co-authored by Xiao Wei, Kenneth Chu (equally contributed first authors),

Jonathan Adsetts, Hao Li, Xi Kang, Zhifeng Ding, and Manzhou Zhu. XW carried out the synthesis and characterization. KC performed the electrochemiluminescence and ECL efficiency experiments. XW and KC wrote the manuscript. JA, HL, XK, ZD, and MZ edited the manuscript. ZD and MZ finalized the manuscript.

Chapter 6 is published in *Langmuir* (**2023**) 39, 2829-2837 co-authored by Kenneth Chu, Jonathan Adsetts (equally contributed first authors), Zackry Whitworth, Shiv Kumar, Eli Zysman-Colman, and Zhifeng Ding. The compound was provided by SK. Experiments were performed by KC, JA, and ZW. KC wrote the manuscript. JA, EZC, and ZD edited the manuscript. EZC and ZD finalized the manuscript.

Chapter 7 is authored by Kenneth Chu, Ziying Zhan, Jonathan Adsetts, Congyang (Jason) Zhang, and Zhifeng Ding. KC performed the experimental and COMSOL simulation work. ZZ provided the ultramicroelectrodes for this work. KC wrote the manuscript. ZZ, JA, CZ, and ZD edited the manuscript. ZD finalized the manuscript.

Chapter 8 is published in *Chemistry – European Journal* (**2020**) 26, 15892-15900 co-authored by Kenneth Chu, Jonathan Adsetts, Shiujian He, Ziying Zhan, Jonathan Wong, David Love, and Zhifeng Ding. KC carried out the synthesis, characterization, and electrochemiluminescence experiments, and wrote the manuscript. JA, SH, ZZ, JW, and DL edited the manuscript. ZD finalized the manuscript.

Chapter 9 is published in *ACS Applied Electronic Materials* (**2020**) 2, 3825-3830 co-authored by Kenneth Chu, Jonathan Adsetts, Conrad Moore, and Zhifeng Ding. KC performed the experimentation and wrote the manuscript. JA and CM edited the manuscript. ZD finalized the manuscript.

Acknowledgments

This research and thesis could not have been possible without the support and guidance of many people.

First and foremost, my PhD supervisor Dr. Zhifeng Ding was instrumental in the completion of my thesis. Without his valuable guidance and advice, this thesis would not be the work that it is. His willingness to help and support me throughout my graduate program, as well as being an endless source of knowledge and enthusiasm, are unmatched. I feel incredibly fortunate to have been one of Dr. Ding's students.

I would also like to thank all the members of Dr. Ding's research group, past and present, for their help. Dr. Shuijian "Joey" He, thank you for being my first mentor in grad school and being so patient and professional always; Dr. Mahdi Hesari, thank you for all the great discussions and advice on things chemistry and not chemistry; Dr. Ruizhong "Joanne" Zhang, thank you for being friendly and my mentor in the lab. To Jon Adsetts, Brandon, Jon Wong, Vishy, Jason, Fraser, Matt, Michelle, Dan, Amy, Ziying, Sara, Dr. Xiaoli Qin, thank you all for the great times we spent together. Lucas, Jing, and Zack, thank you for having me as your 4491 mentor and being such good students.

I would like to thank my committee members and graduate school advisors. Dr. Ken Yeung and Dr. Yang Song, thank you for reading my thesis and being my committee members. To Dr. Clara Wren, Dr. James Wisner, Dr. Stella Constas, and Dr. Silvia Mittler, thank you all for helping me throughout my graduate school journey. To Dr. Andy Sun, thank you so much for teaching me all about material characterizations in your class, and thank you for being an amazing academic reference for so many applications. As well to Dr. Russ Algar, thank you for being my external examiner and helping me to improve my thesis. To Dr. Martin Stillman, thank you for allowing me to be a part of two CanBIC conferences, it was an unforgettable experience.

I have also been extremely fortunate to have the opportunity to work and collaborate with many researchers from other universities and institutions. Thank you to Dr. Eli Zysman-

Colman, Dr. Manzhou Zhu, and Dr. Xi Kang for their help and support. Thank you as well to Dr. Mark Biesinger at Surface Science Western for his aid and expertise in all things related to surface analysis and characterization. I would like to mention the invaluable contribution from the Electronic Shop at the Western Chemistry Department. Thank you to John Vanstone, Alex Crawford, Melanie Glover, and Barakat Misk for their time and help.

Thank you Mom and Dad for their love and support all these years. Everything you have done has made me into the person I am today. Thank you Freddy for the snacks that I can always count on when I visit home. Thank you to Grandma and Grandpa for their love. Because of all of you guys I have a family. Thanks to Kirsty for being at my side always: you are my best friend and every day with you is a true blessing.

Table of Contents

Abstract ii

Keywords iii

Summary for Lay Audience iv

Co-Authorship Statement v

Acknowledgments vii

Table of Contents ix

List of Tables xvi

List of Figures xviii

List of Appendices xxxviii

List of Abbreviations and Symbols xxxix

Chapter 1 1

1 Materials for Electrochemiluminescence: TADF, Hydrogen-bonding, and Aggregation- and Crystallization-Induced Emission Luminophores 1

1.1 Introduction 1

1.2 Thermally Activated Delayed Fluorescence (TADF) 3

1.2.1 Donor-Acceptor TADF Compounds 5

1.2.2 Multi-resonance (MR)-TADF Compounds 11

1.3 Hydrogen bonding system ECL 13

1.4 Enhanced ECL from AIE and CIE 16

1.4.1 Aggregation-induced electrochemiluminescence (AI-ECL) 17

1.4.2 Crystallization-induced electrochemiluminescence (CI-ECL) 19

1.5 Conclusions and outlook 21

1.6 References 22

1.7 Scope of Thesis 26

Chapter 2 28

2 Preparation, properties, and applications of highly luminescent carbon quantum dots from biomaterials: a review 28

2.1 Introduction 28

2.2 Synthesis of CQDs 30

2.2.1 Top-down strategies 31

2.2.2 Bottom-up strategies 32

2.2.3 Purification and functionalization of CQDs 33

2.3 Properties and applications of CQDs 34

2.3.1 Structure and properties of CQDs 34

2.3.2 Luminescence mechanisms 35

2.3.3 Core bandgap transitions of conjugated π-domains 35

2.3.4 Surface state defects 36

2.3.5 Core vs. surface emission states 37

2.3.6 Enhanced luminescence from aggregation-induced emission (AIE) 38

2.4 Light-emitting applications for CQDs 38

2.4.1 Electrochemiluminescence 38

2.4.2 Light-emitting electrochemical cells 39

2.4.3 Chemiluminescence 41

2.5 Conclusions and outlook 42

2.6 References 43

Chapter 3 49

3 Physical Strategy to Determine Absolute Electrochemiluminescence Quantum Efficiencies of Coreactant Systems Using a Photon-Counting Photomultiplier Device 49

3.1 Introduction 49

3.2 Methods 52
3.2.1 Materials and reagents 52
3.2.2 Instrumentation for electrochemistry and electrochemiluminescence 52
3.2.3 ECL spectroscopy 53
3.2.4 Instrument considerations 53
3.2.5 The ECL-QE formula 57
3.2.6 Sample calculation for the absolute quantum efficiency 58
3.2.7 Calibration of the PCH 59
3.2.8 The average photodetector response to ECL emission: The C-value 62
3.2.9 Photodetector surface area correction 66
3.2.10 Electrode reflectivity correction 67
3.2.11 Solution self-absorption correction 68
3.2.12 Corrected total photons 68
3.2.13 Correction for the Faradaic current 69
3.3 Results and discussion 70
3.3.1 $Ru(bpy)_3^{2+}$ ECL via the annihilation pathway 70
3.3.2 The $Ru(bpy)_3^{2+}$/TPrA ECL coreactant system 72
3.4 Conclusions 76
3.5 References 77
Chapter 4 80
4 The Absolute Electrochemiluminescence Efficiency of Au Nanoclusters by Means of a Spectroscopy Charge-coupled Device Camera 80
4.1 Introduction 81
4.2 Experimental 83
4.2.1 Materials and reagents 83
4.2.2 Electrochemistry and ECL 83

4.2.3 Absolute ECL Quantum efficiencies 84

4.3 Results and Discussion 84

4.3.1 Instrument setup and measurements 84

4.3.2 Correction factors in determining the AQE 86

4.3.3 Φ_{AQE} of the 0.1 mM Au_{25}^0/6.25 mM TPrA coreactant system 95

4.3.4 Φ_{AQE} verification with 1 mM $Ru(bpy)_3^{2+}$ in pulsing mode 96

4.3.5 Φ_{AQE} of 0.1 mM $Ru(bpy)_3^{2+}$ with various TPrA concentrations and discussion on Φ_{AQE} of other Au clusters 97

4.4 Conclusions 99

4.5 References 101

Chapter 5 104

5 Nanocluster Transformation Induced by SbF_6^- Anions Toward Boosting Photochemical Activities 104

5.1 Introduction 105

5.2 Experimental 106

5.2.1 Chemicals 106

5.2.2 Synthesis of $[Pt_1Ag_{28}(S\text{-}Adm)_{18}(PPh_3)_4]Cl_2$ (Pt1Ag28-Cl) 107

5.2.3 Transformation from Pt_1Ag_{28}-Cl to $[Pt_1Ag_{28}(S\text{-}Adm)_{18}(PPh_3)_4](SbF_6)_2$ (Pt_1Ag_{28}-SbF_6) 107

5.2.4 Transformation from Pt_1Ag_{28}-Cl to $[Pt_1Ag_{30}Cl_1(S\text{-}Adm)_{18}(PPh_3)_3](SbF_6)_3$ (Pt_1Ag_{30}-SbF_6) 107

5.2.5 Transformation to Pt_1Ag_{28}-Cl to polydispersed Pt-Ag compounds 108

5.2.6 Crystallization of Pt_1Ag_{28}-SbF_6 and Pt_1Ag_{30}-SbF_6 108

5.2.7 X-ray crystallography 108

5.2.8 Preparation of nanocluster crystalline films 108

5.2.9 Electrochemistry and spectroscopy 109

5.2.10 Characterization 110

5.2.11 Determination of the absolute ECL efficiency 111

5.3 Results and Discussion 112

5.3.1 Synthesis and structure evolution 112

5.3.2 Photochemical studies 131

5.3.3 Electrochemistry and electrochemiluminescence 138

5.3.4 Absolute ECL Quantum Efficiency 155

5.4 Conclusions 159

5.5 Supporting Information 161

5.6 References 163

Chapter 6 169

6 Elucidation of an Aggregate Excited State in the Electrochemiluminescence and Chemiluminescence of a Thermally Activated Delayed Fluorescence (TADF) Emitter 169

6.1 Introduction 169

6.2 Experimental 171

6.2.1 Materials and reagents 171

6.2.2 Electrochemistry and electrochemiluminescence 172

6.2.3 Determination of the absolute ECL quantum efficiency 174

6.2.4 Chemiluminescence 174

6.3 Results and Discussion 175

6.3.1 Electrochemiluminescence via the annihilation pathway 175

6.3.2 Electrochemiluminescence with benzoyl peroxide as coreactant 184

6.3.3 Determination of the absolute ECL quantum efficiency 192

6.3.4 Chemiluminescence of TPA-ace-TRZ and its quantum efficiency 193

6.4 Conclusions 199

6.5 References 200

Chapter 7 205

7 Determining the Bimolecular Rate Constants for Annihilation Reactions of Electrogenerated $Ru(bpy)_3^{2+}$ Radical Ions by Means of Electrochemiluminescence at an Ultramicroelectrode 205

7.1 Introduction 205

7.2 Experimental 207

7.2.1 Materials and reagents 207

7.2.2 Electrochemistry and electrochemiluminescence 207

7.2.3 Building the COMSOL simulation model: geometry and meshing 209

7.2.4 Simulated Diffusion and Reaction kinetics 211

7.2.5 Parametric simulation of the bimolecular ECL annihilation rate constant (k_{ann}) 215

7.3 Results and Discussion 219

7.3.1 Electrochemistry of $Ru(bpy)_3^{2+}$ 219

7.4 Conclusions 223

7.5 References 225

Chapter 8 227

8 Electrogenerated chemiluminescence and Electroluminescence of N-Doped Graphene Quantum Dots Fabricated from an Electrochemical Exfoliation Process in Nitrogen-Containing Electrolytes 227

8.1 Introduction 227

8.2 Experimental 229

8.2.1 Chemicals and reagents 229

8.2.2 Top-down electrochemical exfoliation 229

8.2.3 Absorption and photoluminescence spectroscopy 230

8.2.4 X-ray photoelectron spectroscopy (XPS) 230

8.2.5 Electrochemistry and electrochemiluminescence 231

8.2.6 LEC fabrication and testing 232

8.3 Results and discussion 232

8.3.1 Characterization of top-down graphene quantum dots 232

8.3.2 Electrochemistry and electrochemiluminescence of top-down graphene quantum dots 237

8.3.3 GQD-based light-emitting electrochemical cells 242

8.4 Conclusions 245

8.5 References 246

Chapter 9 249

9 Spooling Electroluminescence Spectroscopy of $Ru(bpy)_3^{2+}$ Light-Emitting Electrochemical Cells with an Atomic Layer Deposited Zinc Oxide Electron-Transporting/Hole-Blocking Interlayer 249

9.1 Introduction 249

9.2 Experimental 251

9.2.1 Materials and reagents 251

9.2.2 LEC fabrication and testing 251

9.3 Results and Discussion 257

9.4 Conclusions 268

9.5 References 269

Chapter 10 271

10 Conclusions and Future Work 271

10.1 Conclusions 271

10.2 Future Work 273

Appendices 275

Curriculum Vitae 287

List of Tables

Table 2.1. Summary of bottom-up synthesis strategies for CQDs. 32

Table 3.1. Calculated quantum efficiencies of the $Ru(bpy)_3^{2+}$ annihilation and $Ru(bpy)_3^{2+}$/TPrA ECL systems. $Ru(bpy)_3^{2+}$ concentration was 1 mM for all experiments. Every experiment was repeated at least three times. Errors provided represent one standard deviation calculated across individual measurements. 76

Table 4.1. The ECL QE values determined from the test in **Figure 4.2** and two other replicate tests. 95

Table 4.2. ECL QEs of 0.1 mM $Ru(bpy)_3(PF_6)_2$ in 0.1 M $TBAPF_6$ 1:1 benzene:acetonitrile solution with various TPrA concentrations under constant potential of 1.5 V. 99

Table 5.1. Atom ratio of Pt and Ag in Pt_1Ag_{28} and Pt_1Ag_{30} nanoclusters. Atom ratios of Pt and Ag in $[Pt_1Ag_{28}(S\text{-}Adm)_{18}(PPh_3)_4]Cl_2$, $[Pt_1Ag_{28}(S\text{-}Adm)_{18}(PPh_3)_4](SbF_6)_2$, and $[Pt_1Ag_{30}Cl_1(S\text{-}Adm)_{18}(PPh_3)_3](SbF_6)_3$ nanoclusters were calculated from inductively coupled plasma (ICP) and X-ray photoelectric spectroscopy (XPS). 126

Table 5.2. Absolute and relative ECL quantum efficiencies for Pt-Ag nanoclusters. ... 156

Table 5.3. Relative ECL efficiencies of Pt_1Ag_{30}-SbF_6 and Pt_1Ag_{28}-SbF_6 vs. $Ru(bpy)_3^{2+}$ with 1 mM TPrA as coreactant. Efficiencies were calculated using ECL accumulation spectrum peak heights and integrated peak areas obtained from the spectrograph/CCD setup. Charge was calculated by integrating the current vs. time plot in a cyclic voltammogram experiment. Concentration of $Ru(bpy)_3^{2+}$ = 0.20 µM, Pt_1Ag_{30}-SbF_6 = 0.32 µM, Pt_1Ag_{28}-SbF_6 = 0.28 µM. 157

Table 5.4. Photon flux for some common light sources. Measured using an Ocean Optics USB2000+ miniature fiber optic (200-micron diameter) spectrometer controlled with SpectraSuite software. 157

Table 5.5. Absolute ECL quantum efficiencies of Pt-Ag nanoclusters at high concentration. TPrA concentration was 1 mM. 158

Table 5.6. Crystal data and structure refinement for the $[Pt_1Ag_{28}(S\text{-}Adm)_{18}(PPh_3)_4](SbF_6)_2$ nanocluster. 161

Table 5.7. Crystal data and structure refinement for the $[Pt_1Ag_{30}Cl_1(S\text{-}Adm)_{18}(PPh_3)_3](SbF_6)_3$ nanocluster. 162

Table 6.1. Summary of photoluminescence (PL), electrochemiluminescence (ECL), and chemiluminescence (CL) emission in anhydrous dichloromethane. Numbers in parentheses in red color represent ECL efficiencies calculated relative to the $Ru(bpy)_3^{2+}$/BPO system. 183

Table 6.2. Summary of ECL onset, peak maxima, and end during ECL pulsing experiments. 183

Table 6.3. Absolute and relative ECL quantum efficiencies for TPA-ace-TRZ in the presence of 10 mM benzoyl peroxide as coreactant. The concentration was 1.5 mM for both luminophores and calculated during a cyclic voltammogram experiment (scan rate was 0.1 V/s). 193

Table 7.1. COMSOL model definitions. 211

Table 7.2. COMSOL reactions and their rate constants. 213

Table 7.3. COMSOL integration parameters. 213

Table 8.1. Photoluminescence quantum yields (PLQY) for GQDs prepared at various current densities. 236

List of Figures

Figure 1.1. (A) Molecular structures of 2CzPN, 4CzPN, 4CzIPN, and 4CzTPN. (B) UV-Vis absorption (dotted) and PL spectra (solid lines) of 25 μM TADF emitter in DCM (top) and MeCN (bottom). (C) Normalized ECL spectra of TADF emitters in DCM (top) and MeCN (bottom). Adapted with permission from Ref. **[24]**. Copyright 2014, Wiley-VCH. 6

Figure 1.2. (A–C) CVs (red) along with ECL–voltage curves (blue) during potential pulsing at a pulsing frequency of 10 Hz for PPOCzPN, PPSCzPN and DiPPOCzPN, respectively, all with 10 mM BPO was added as a co-reactant. (D–F) Spooling ECL spectroscopy of the corresponding systems described in Figures A to C. Insets of Figures D–F represent respective stacked spooling ECL spectra. Adapted with permission from Ref. **[25]**. Copyright 2022. The Royal Society of Chemistry. 7

Figure 1.3. (A) Structure of TPA-ace-TRZ. (B) Spooling ECL spectra of TPA-ace-TRZ with 10 mM BPO as the co-reactant. (C) Top: ECL accumulation spectrum of TPA-ace-TRZ with 10 mM BPO as the co-reactant. Bottom: Current-time and ECL-time profiles of TPA-ace-TRZ with the BPO co-reactant system. (D) Top-left: Colour photographs of TPA-ace-TRZ CL reaction vial before/after adding H_2O_2. Top-right: CIE colour coordinate diagram of TPA-ace-TRZ CL. Bottom: CL accumulation spectrum of TPA-ace-TRZ system. Adapted with permission from Ref. [26]. Copyright 2023, American Chemical Society. 8

Figure 1.4. Chemical structures of (A) PCzAPT10 TADF polymer, (B) 4CzIPN, and (C) BPAPTC molecules. (D) Cyclic voltammograms of PCzAPT10-modified GCE with TPrA. (E) ECL-voltage curve of PCzAPT10. Inset shows PL in neat film vs. MeCN, and ECL spectrum of the PCzAPT10/TPrA co-reactant system. Cyclic voltammograms (F) and ECL-voltage curves (G) of 4CzIPN in dichloromethane with 0.1 M $TBAPF_6$ and 40 mM TPrA. Adapted with permission from Ref. [27] and [28]. Copyright 2021, Wiley-VCH. 10

Figure 1.5. (A) Structure and calculated difference density plots of Mes_3DiKTa. (B) Time-resolved ECL experiments with 0.2 mM Mes_3DiKTa in acetonitrile via the annihilation pathway. (C) Spooling ECL spectra of 0.2 mM Mes_3DiKTa in the presence of 20 mM TPrA as a co-reactant, with a scan rate of 0.02 V/s and exposure time of 2 s. Adapted with permission from Refs. [35] and [36]. Copyright 2020, Wiley-VCH. Copyright 2023, IOP Publishing. 12

Figure 1.6. (A) Chemical structures of Ir(III) complex [1] and pyrimido-[4,5]-cisoquinolin-3-amine [3], which combine through H-bonding to form complex [1•3]. (C) Spooling ECL spectra of complex [1•3] with 5 mM BPO as co-reactant. ECL spectrum at (D) −1.34 V and (E) −1.50 V. Adapted with permission from Ref. [39]. Copyright 2022, Elsevier B.V. 14

Figure 1.7. (A) Intermolecular interactions of phenyDAT in Tr-HOFs with the labeled distance extracted from its crystal packing data. (B) View of the Hirshfeld surface mapped over the normalized distance of the N–H bond for phenyDAT in Tr-HOFs. (C) 3D packing framework of Tr-HOFs. Reproduced with permission from Ref. [41]. Copyright 2021, American Chemical Society. 16

Figure 1.8. ECL intensity variation as the H_2O fraction of a DMSO-H_2O solvent mixture is increased. Reproduced with permission from Ref. [50]. Copyright 2018, American Chemical Society. 18

Figure 1.9. (A) Molecular structure of carboranyl carbazole AI-ECL luminophore. (B) ECL intensity of 1.0 mM T-3 in increasing H_2O fractions. (C) PL spectrum (black) of T-3 in 95% H_2O and ECL spectrum (red) of T-3 modified GCE in 95% H_2O. Reproduced with permission from Ref. [30]. Copyright 2019, Wiley-VCH. 18

Figure 1.10. (A) PL spectra of crystalline DBC film (blue) and in acetonitrile (black). (B) Images of recrystallized DBC, DBC after mechanical grinding, and DBC after exposure to acetone vapours (left to right). (C) XRD spectra of recrystallized DBC (blue) and upon grinding (black). DBC unit cell in inset. Spooling ECL spectra of (D) solid state

ECL/BPO co-reactant system and (E) homogeneous DBC/BPO system. Reproduced with permission from Ref. [57]. Copyright 2020, Wiley-VCH. 20

Figure 2.1. Carbon quantum dots (CQDs) and their light-emitting applications..... 30

Figure 2.2. Top-down vs. bottom-up synthesis strategies for preparing CQDs..... 31

Figure 2.3. (A) TEM images of CQDs. (B) Fluorescent microscopy images of CQDs. (C) High resolution-TEM images of CQDs. Optical images of different size CQDs under (D) daylight and (E) ultraviolet light. (F) Photoluminescence spectra of different size CQDs. The relationship between CQD size and (G) the bandgap energy, and (H) the HOMO-LUMO energy gap.[49] 36

Figure 2.4. Core vs. surface emissive pathways in CQDs. 37

Figure 2.5. Summary of electroluminescent (EL) emissions from various LEC luminophores. Bottom-up CQDs from hydrothermal synthesis, Livilux PDY-132 (SuperYellow), top-down GQDs from electrochemical exfoliation[7], Ru(bpy)3(PF6)2-based LEC, tPDI2N-hex (PDI, perylene diimide). 40

Figure 3.1. A schematic overview of the photon counting head (PCH) instrumentation setup. All instrument connections have been colour-coded, where possible, to better illustrate the pathways of data and communication signals. A vertical cross-section is shown for the ECL cell, the plastic holder, and the PCH to show how the components fit together. Inset circle (outlined and magnified in dotted red) illustrates the path of the ECL emission from the platinum electrode towards the photodetector surface. The counts represented as potential pulses from the PCH is passed through an attenuator, before being sent to the SR430, where it is sorted into individual bins. An external voltage trigger is generated by the Autolab potentiostat to synchronize the start of each record. Two separate computer workstations were used to control the potentiostat and SR430 photon counter through NOVA and LabVIEW software, respectively. 54

Figure 3.2. Photograph of the ECL cell in its black plastic light-proof holder, and the photon counting head. 56

Figure 3.3. Photograph of the ECL glass cell and its assembly, showing the orientation of the working, counter, and reference electrodes. 57

Figure 3.4. Counts per second (corrected for bin widths) of a red LED measured using the Hamamatsu H6240-02 photon counting head at different operating voltages (1.58 V – 1.65 V). 60

Figure 3.5. Optical power (in Watts) of a red LED measured using a Thorlabs calibrated silicon photodiode at different operating voltages (1.58 V – 1.65 V). 60

Figure 3.6. Calibration plot of the response of the PCH photodetector measured against a calibrated silicon photodiode. Measurements for both devices have been converted into units of photon flux (*photons/sec*). 61

Figure 3.7. Background corrected, intensity-normalized $Ru(bpy)_3^{2+}$ ECL emission spectrum (red) and the calibrated responsivity curve of the photon counting head in counts per photon (blue) as a function of the wavelength. 62

Figure 3.8. Quantum efficiency of the Hamamatsu H6240-02 photon counting head (measured in cps/pW) vs. the incoming emission wavelength. 63

Figure 3.9. Quantum efficiency of the Hamamatsu H6240-02 photon counting head (measured in counts/incident photon) vs. the incoming emission wavelength. 64

Figure 3.10. Calibrated quantum efficiency of the Hamamatsu H6240-02 photon counting head (measured in counts/incident photon) vs. the incoming emission wavelength. Obtained by applying the calibration factor to **Figure 3.9**. 65

Figure 3.11. Background-corrected and normalized intensity ECL emission spectra of $Ru(bpy)_3^{2+}$ annihilation and TPrA coreactant systems. 65

Figure 3.12. A comparison of angles (circles) vs. solid angles (spheres). A circle contains 2π radians, while a sphere contains 4π steradians. The solid angle (in steradians) of a unit sphere is analogous to the planar angle (in radians) of a unit circle. Radians = ratio of the

length of the arc vs. radius of the circle. Steradians = ratio of the spherical surface area vs. the square of the radius of the sphere.[34] 67

Figure 3.13. Cyclic voltammogram (red) and ECL-voltage curve (blue) of 1 mM $Ru(bpy)_3(PF_6)_2$ in acetonitrile with 0.1 M $TBAPF_6$ as the supporting electrolyte. Dotted lines highlight the potentials for the first reduction and oxidation. Scan rate for the cyclic voltammogram was 100 mV/sec. Bin width = 10.48 msec, number of bins = 14 336, trigger level = 0.3 V, records per scan = 1. 71

Figure 3.14. Potential stepping of $Ru(bpy)_3^{2+}$ between 1.35 V and −1.36 V at 10 Hz (100 msec pulse width). Current shown in red, and ECL photon counts shown in blue, ECL measured by the H6240-02 photon counting head. Bin width = 40.96 msec, number of bins = 13 312, trigger level = −1.10 V, records per scan = 1. 72

Figure 3.15. Cyclic voltammogram (red) and ECL-voltage curve (blue) of 1 mM $Ru(bpy)_3^{2+}$ in acetonitrile with 10 mM TPrA. Scan rate for the cyclic voltammogram was 100 mV/sec. Bin width = 2.62 msec, number of bins = 11 264, trigger level = 0.30 V, records per scan = 1. 73

Figure 3.16. Potential step experiment of 1 mM $Ru(bpy)_3^{2+}$ with 10 mM TPrA, between 0 V and 1.50 V at 10 Hz (100 msec pulse width). Current is shown in red, and ECL intensity (as photon counts) is shown in blue. Bin width = 81.92 μsec, number of bins = 13 312, trigger level = −1.40 V, records per scan = 1. 74

Figure 4.1. Instrumental setup for measuring Φ_{AQE} with a CCD camera coupled to a spectrometer. 84

Figure 4.2. Data for evaluating quantum efficiency for a 0.1 mM Au_{25}^0 1:1 benzene:acetonitrile solution with 6.25 mM TPrA. (A) The current-time curve collected with a potentiostat is shown along with the two successive oxidation reactions during the constant potential procedure at 0.89 V. (B) The corresponding accumulation ECL spectrum with the Au_{25}^0/TPrA ECL mechanism in the inset. 85

Figure 4.3. A UV-Vis (red) and corrected ECL (blue) spectrum of Au_{25}^{0} at the same concentration. The dashed line is a calculated example of a gaussian peak that could fit the blue line. 87

Figure 4.4. Pyrex window transmission percentage.[34] 87

Figure 4.5. (A) The calibration curve for the red LED measured on both the Thorlabs calibrated photodiode and the CCD camera coupled to a spectrometer. Each point corresponds to 3 averaged 60 s scans each at a single potential applied to the LED, ranging from 750 mV to 800 mV. (B) The manufacturer provided QE of a DU401a-BR-DD Andor CCD camera cooled to −70 °C seen as the red trace. The calibrated QE curve which considers light losses in the spectrometer and the CCD camera ($Q(\lambda)$) is seen as the blue trace. (C) The blue curve from Figure 4.5B multiplied by the gain factor. 89

Figure 4.6. The stability (top) and the center wavelength (bottom) of the LED calibration source over a 5 minute scan. 90

Figure 4.7. Data transformations for the data in **Figure 4.2**. (A) The total electron flux applied to the ECL cell. (B) The red trace shows the generated charge carriers in electrons on each pixel of the CCD camera by multiplying the counts generated by the gain factor. The blue trace shows the total photons flux emitted onto each pixel of the CCD camera in the entire 2 s accumulation. 92

Figure 4.8. Spooling ECL spectroscopy of $Ru(bpy)_3(PF_6)_2$. A solution of 1 mM $Ru(bpy)_3(PF_6)_2$ and 0.1 M $TBAPF_6$ in acetonitrile was pulsed between −1.6 and 1.0 V vs. Pt wire to produce this spooling spectrum which was collected by a spectrometer coupled to a CCD camera. Each spectrum is a 1 s accumulation and 50 accumulations were taken in total. Calculations converting CCD counts to photon flux were carried out by using Equation 4.6. 96

Figure 4.9. A 1 mM $Ru(bpy)_3(PF_6)_2$ and a 0.1 M $TBAPF_6$ solution in acetonitrile pulsed at 10 Hz between −1.6 and 1.0 V vs. Pt wire. The total summed photon flux is calculated from the equations described earlier and are plotted on the left y-axis. The electron flux is plotted on the right y axis. 97

Figure 5.1. (A) Total structure of $[Pt_1Ag_{28}(S\text{-}Adm)_{18}(PPh_3)_4]Cl_2$. No Cl counterion was observed in the crystal lattice because of the high disorder of these Cl atoms, which has been demonstrated in previous works (Chem. Sci., 2017, 8, 2581; Chem. Sci., 2020, 11, 1691). Color legends: dark green, Pt; blue, Ag; red, S; magenta, P; gray, Cl; pale gray, C; white, H. (B) The presence of counterion Cl^- in $[Pt_1Ag_{28}(S\text{-}Adm)_{18}(PPh_3)_4]Cl_2$ has also been verified by the energy-dispersive X-ray spectroscopy measurement..... 112

Figure 5.2. Total structure of $[Pt_1Ag_{28}(S\text{-}Adm)_{18}(PPh_3)_4](SbF_6)_2$. In this figure, one of three SbF_6^- counterion are in 100% occupancy, and the other two are in 50% occupancy. In this context, the number of SbF_6^- counterions are two, fitting with the $[Pt_1Ag_{28}(S\text{-}Adm)_{18}(PPh_3)_4](SbF_6)_2$ formula in ESI-MS. Color legends: dark green, Pt; blue, Ag; red, S; magenta, P; pale gray, C; white, H; orange, Sb; pink, F. 114

Figure 5.3. Structure comparison between Pt_1Ag_{28}-Cl and Pt_1Ag_{28}-SbF_6 nanoclusters. (A) Total structure of Pt_1Ag_{28}-Cl. (B) Total structure of Pt_1Ag_{28}-SbF_6. (C) Distort FCC Pt_1Ag_{12} kernel and asymmetric $Ag_4(S\text{-}Adm)_6(PPh_3)_1$ surface structure of Pt_1Ag_{28}-Cl. (D) FCC Pt_1Ag_{12} kernel and symmetric $Ag_4(S\text{-}Adm)_6(PPh_3)_1$ surface structure of Pt_1Ag_{28}-SbF_6. Color legends: dark green sphere, Pt; dark blue sphere, kernel Ag; blue sphere, surface Ag; red sphere, S; magenta sphere, P; gray sphere, Cl; orange sphere, Sb; pink sphere, F. For clarity, all C and H atoms are omitted. 115

Figure 5.4. Structure anatomy of the Pt_1Ag_{30}-SbF_6 nanocluster. (A) The icosahedral Pt_1Ag_{12} kernel. (B) The $Ag_2(S\text{-}Adm)_3(PPh_3)_1$ surface unit. (C) The $Pt_1Ag_{18}(S\text{-}Adm)_9(PPh_3)_3$ structure. (D) The $Ag_4(S\text{-}Adm)_4$ surface unit. (E) The $Pt_1Ag_{27}Cl_1(S\text{-}Adm)_{18}(PPh_3)_3$ structure. (F) The Ag linker. (G,H) The $Pt_1Ag_{30}Cl_1(S\text{-}Adm)_{18}(PPh_3)_3$ structure from different views. (I) Total structure of Pt_1Ag_{30}-SbF_6. (J) The C_3 symmetry axis of the Pt_1Ag_{30}-SbF_6 nanocluster. Color legends: dark green sphere, Pt; dark blue sphere, kernel Ag; blue/green/orange sphere, surface Ag; red sphere, S; magenta sphere, P; gray sphere, Cl; pale gray sphere, C. For clarity, all H atoms are omitted..... 117

Figure 5.5. Total structure of $[Pt_1Ag_{30}Cl_1(S\text{-}Adm)_{18}(PPh_3)_3](SbF_6)_3$. The number of SbF_6^- counterions is three, suggested by the ESI-MS result. However, only two SbF_6^- counterions are observed in the crystal lattice. The loss of the third SbF_6^- counterion may

result from its high disorder, or the steric hindrance that the third one is hard to be included in the crystal lattice. Color legends: dark green, Pt; blue, Ag; gray, Cl; red, S; magenta, P; pale gray, C; white, H; orange, Sb; pink, F..... 118

Figure 5.6. Optical absorption of the $[Pt_1Ag_{30}Cl_1(S\text{-}Adm)_{18}(PPh_3)_3](SbF_6)_3$. Black line: the freshly prepared nanocluster. Red line: the nanocluster was stirred for 7 days in the air. 119

Figure 5.7. ESI-MS results of (A) polydispersed Pt-Ag compounds, (B) Pt_1Ag_{28}-Cl, (C) Pt_1Ag_{28}-SbF_6, and (D) Pt_1Ag_{30}-SbF_6. No signal of Pt_1Ag_{28}-Cl, Pt_1Ag_{28}-SbF_6, or Pt_1Ag_{30}-SbF_6 is observed in the ESI-MS result of polydispersed Pt-Ag compounds. 120

Figure 5.8. UV-vis spectrum of the poly-dispersed Pt-Ag compounds. 120

Figure 5.9. (A) Crystal structure of $[Pt_1Ag_{28}(S\text{-}Adm)_{18}(PPh_3)_4]Cl_2$. (B) XPS spectrum of the $[Pt_1Ag_{28}(S\text{-}Adm)_{18}(PPh_3)_4]Cl_2$ nanoclusters. (C) XPS of Ag 3d of the $[Pt_1Ag_{28}(S\text{-}Adm)_{18}(PPh_3)_4]Cl_2$ nanocluster. (D) XPS of Pt 4f of the $[Pt_1Ag_{28}(S\text{-}Adm)_{18}(PPh_3)_4]Cl_2$ nanocluster. 121

Figure 5.10. (A) Crystal structure of $[Pt_1Ag_{28}(S\text{-}Adm)_{18}(PPh_3)_4]Cl_2$. (B-G) Elemental mapping images of the $[Pt_1Ag_{28}(S\text{-}Adm)_{18}(PPh_3)_4]Cl_2$ nanocluster crystal. 122

Figure 5.11. (A) Crystal structure of $[Pt_1Ag_{28}(S\text{-}Adm)_{18}(PPh_3)_4](SbF_6)_2$. (B) XPS spectrum of the $[Pt_1Ag_{28}(S\text{-}Adm)_{18}(PPh_3)_4](SbF_6)_2$ nanoclusters. (C) XPS of Ag 3d of the $[Pt_1Ag_{28}(S\text{-}Adm)_{18}(PPh_3)_4](SbF_6)_2$ nanocluster. (D) XPS of Pt 4f of the $[Pt_1Ag_{28}(S\text{-}Adm)_{18}(PPh_3)_4](SbF_6)_2$ nanocluster. 123

Figure 5.12. (A) Crystal structure of $[Pt_1Ag_{28}(S\text{-}Adm)_{18}(PPh_3)_4](SbF_6)_2$. (B-G) Elemental mapping images of the $[Pt_1Ag_{28}(S\text{-}Adm)_{18}(PPh_3)_4](SbF_6)_2$ nanocluster crystal..... 124

Figure 5.13. (A) Crystal structure of $[Pt_1Ag_{30}Cl_1(S\text{-}Adm)_{18}(PPh_3)_3](SbF_6)_3$. (B) XPS spectrum of the $[Pt_1Ag_{30}Cl_1(S\text{-}Adm)_{18}(PPh_3)_3](SbF_6)_3$ nanoclusters. (C) XPS of Ag 3d of the $[Pt_1Ag_{30}Cl_1(S\text{-}Adm)_{18}(PPh_3)_3](SbF_6)_3$ nanocluster. (D) XPS of Pt 4f of the $[Pt_1Ag_{30}Cl_1(S\text{-}Adm)_{18}(PPh_3)_3](SbF_6)_3$ nanocluster..... 125

Figure 5.14. EDS result of $[Pt_1Ag_{30}Cl_1(S\text{-}Adm)_{18}(PPh_3)_3](SbF_6)_3$. 126

Figure 5.15. The addition of SbF_6^- induced stepwise transformation from Pt_1Ag_{28}-Cl to Pt_1Ag_{28}-SbF_6, Pt_1Ag_{30}-SbF_6, and poly-dispersed Pt-Ag compounds. Color legends: dark green sphere, Pt; dark blue sphere, kernel Ag; blue sphere, surface Ag; gray sphere, Cl; red sphere, S; magenta sphere, P; orange sphere, Sb; pink sphere, F. For clarity, all C and H atoms are omitted. 127

Figure 5.16. Crystalline packing modes of (A) Pt_1Ag_{28}-Cl, (B) Pt_1Ag_{28}-SbF_6, and (C) Pt_1Ag_{30}-SbF_6, and the comparison of crystal lattice parameters. 128

Figure 5.17. Packing of $[Pt_1Ag_{28}(S\text{-}Adm)_{18}(PPh_3)_4]Cl_2$ in the crystal lattice from different views. The counterions are omitted for clarity. 129

Figure 5.18. Packing modes of $[Pt_1Ag_{28}(S\text{-}Adm)_{18}(PPh_3)_4](SbF_6)_2$ in the crystal lattice from different views. The counterions are omitted for clarity. 130

Figure 5.19. Packing of $[Pt_1Ag_{30}Cl_1(S\text{-}Adm)_{18}(PPh_3)_3](SbF_6)_3$ in the crystal lattice from different views. The counterions are omitted for clarity. 131

Figure 5.20. Optical properties of Pt_1Ag_{28}-Cl, Pt_1Ag_{28}-SbF_6, and Pt_1Ag_{30}-SbF_6 nanoclusters. (A) Comparison of optical absorptions and emissions (nanoclusters were dissolved in CH_2Cl_2) of Pt_1Ag_{28}-Cl (black lines), Pt_1Ag_{28}-SbF_6 (red lines), and Pt_1Ag_{30}-SbF_6 (blue lines) nanoclusters. Insets: photos of luminescence of Pt_1Ag_{28}-Cl, Pt_1Ag_{28}-SbF_6, and Pt_1Ag_{30}-SbF_6 nanoclusters in CH_2Cl_2. (B) Comparison of optical absorptions and emissions (nanoclusters were in a crystallized film) of Pt_1Ag_{28}-Cl (black lines), Pt_1Ag_{28}-SbF_6 (red lines), and Pt_1Ag_{30}-SbF_6 (blue lines) nanoclusters. Insets: photos of luminescence of Pt_1Ag_{28}-Cl, Pt_1Ag_{28}-SbF_6, and Pt_1Ag_{30}-SbF_6 nanocluster crystallized films. 132

Figure 5.21. Concentration-dependent photoluminescence intensity of the $[Pt_1Ag_{28}(S\text{-}Adm)_{18}(PPh_3)_4](SbF_6)_2$ nanocluster (dissolved in CH_2Cl_2). (A) The concentration of the nanocluster was enhanced from 1.64×10^{-6} to 10.0×10^{-6} mol/L. The photoluminescence intensity was enhanced significantly with the increase of the concentration. (B) The

concentration of the nanocluster was enhanced from 10.0×10^{-6} to 109.88×10^{-6} mol/L. As the concentration increased, the photoluminescence of the nanocluster solution was quenched. 133

Figure 5.22. Concentration-dependent photoluminescence intensity of the $[Pt_1Ag_{30}Cl_1(S\text{-}Adm)_{18}(PPh_3)_3](SbF_6)_3$ nanocluster (dissolved in CH_2Cl_2). (A) The concentration of the nanocluster was enhanced from 2.5×10^{-6} to 20.0×10^{-6} mol/L. The photoluminescence intensity was enhanced significantly with the increase of the concentration. (B) The concentration of the nanocluster was enhanced from 1.96×10^{-5} to 4.90×10^{-5} mol/L. As the concentration increased, the photoluminescence of the nanocluster solution was quenched. 134

Figure 5.23. Fluorescence lifetimes of different nanoclusters. (A) The microsecond photoluminescence decay traces of $[Pt_1Ag_{28}(S\text{-}Adm)_{18}(PPh_3)_4]Cl_2$ (dissolved in CH_2Cl_2) under ambient, N_2-purged, or O_2-saturated conditions. (B) The microsecond photoluminescence decay traces of $[Pt_1Ag_{28}(S\text{-}Adm)_{18}(PPh_3)_4](SbF_6)_2$ (dissolved in CH_2Cl_2) under ambient, N_2-purged, or O_2-saturated conditions. (C) The microsecond photoluminescence decay traces of $[Pt_1Ag_{30}Cl_1(S\text{-}Adm)_{18}(PPh_3)_3](SbF_6)_3$ (dissolved in CH_2Cl_2) under ambient, N_2-purged, or O_2-saturated conditions..... 135

Figure 5.24. (A) Comparison of the emission spectra of CH_2Cl_2 solutions of $[Pt_1Ag_{28}(S\text{-}Adm)_{18}(PPh_3)_4]Cl_2$ under ambient, N_2-purged, or O_2-saturated conditions. (B) Comparison of the emission spectra of CH_2Cl_2 solutions of $[Pt_1Ag_{28}(S\text{-}Adm)_{18}(PPh_3)_4](SbF_6)_2$ under ambient, N_2-purged, or O_2-saturated conditions. (C) Comparison of the emission spectra of CH_2Cl_2 solutions of $[Pt_1Ag_{30}Cl_1(S\text{-}Adm)_{18}(PPh_3)_3](SbF_6)_3$ under ambient, N_2-purged, or O_2-saturated conditions. 136

Figure 5.25. (A) Near-infrared photoluminescence of ambient, N_2-purged, and O_2-saturated CH_2Cl_2 solutions of $[Pt_1Ag_{28}(S\text{-}Adm)_{18}(PPh_3)_4]Cl_2$. (B) Near-infrared photoluminescence of ambient, N_2-purged, and O_2-saturated CH_2Cl_2 solutions of $[Pt_1Ag_{28}(S\text{-}Adm)_{18}(PPh_3)_4](SbF_6)_2$. (C) Near-infrared photoluminescence of ambient, N_2-purged, and O_2-saturated CH_2Cl_2 solutions of $[Pt_1Ag_{30}Cl_1(S\text{-}Adm)_{18}(PPh_3)_3](SbF_6)_3$. . 136

Figure 5.26. ESI-MS results of (A) $[Pt_1Ag_{28}(S\text{-}Adm)_{18}(PPh_3)_4]Cl_2$, (B) $[Pt_1Ag_{28}(S\text{-}Adm)_{18}(PPh_3)_4](SbF_6)_2$, and (C) $[Pt_1Ag_{30}Cl_1(S\text{-}Adm)_{18}(PPh_3)_3](SbF_6)_3$ nanoclusters after the photoluminescence test. The unchanged mass results (compared to the results in Figure S4) demonstrated the high photostability of these three nanoclusters. 137

Figure 5.27. Differential pulse voltammogram of (A) 1.5 µM Pt_1Ag_{30}-SbF_6 and (B) 1.3 µM Pt_1Ag_{28}-SbF_6 in dichloromethane containing 0.1 M $TBAPF_6$ as supporting electrolyte. Initial scan direction is indicated with arrows. Pulse peak. amplitude was 50 mV, pulse with was 0.05 s, and pulse period was 0.20 s. 139

Figure 5.28. ECL voltage curve of 1.5 µM Pt_1Ag_{30}-SbF_6 in dichloromethane with 0.1 M $TBAPF_6$ using a 2-mm platinum disc electrode in the annihilation pathway. Scan rate = 0.1 V/sec. 139

Figure 5.29. ECL voltage curve of 1.3 µM Pt_1Ag_{28}-SbF_6 in the annihilation pathway. 140

Figure 5.30. Spooling ECL spectra of 0.32 µM Pt_1Ag_{30}-SbF_6 with 1 mM TPrA during a potentiodynamic scan between −0.20 V and 1.30 V vs. SCE. Scan rate used was 0.1 V/s, and each spectrum was acquired at a 0.5 s time interval. Inset plot is an ECL accumulation spectrum of the same system collected over 30s. 142

Figure 5.31. ECL-voltage curve of 1.5 µM Pt_1Ag_{30}-SbF_6 in dichloromethane with 1 mM TPrA. 142

Figure 5.32. (A) Primary ECL mechanism for $Pt_1Ag_{30}SbF_6$ in the presence of TPrA. ECL enhancement mechanisms involving (B) the recycling of Pt_1Ag_{30}-SbF_6^0 from Pt_1Ag_{30}-SbF_6^{1+} in a positive feedback loop catalyzed at the electrode surface, and (C) ECL cascade enhancement driven by an excess of $TPrA^{\bullet}$. 143

Figure 5.33. Stacked spooling ECL spectra of Pt_1Ag_{30}-SbF_6 with 1 mM TPrA. 0.5 sec per spectrum, scan rate = 0.1 V/sec. 145

Figure 5.34. (A) Spooling photoluminescence spectra of 0.32 µM Pt_1Ag_{30}-SbF_6 collected at (B) 0.00 V, (C) 0.53 V, (D) 0.79 V, and (E) 1.10 V, obtained by excitation at 532 nm with a solid-state laser. 146

Figure 5.35. ECL voltage curve of 1.5 μM Pt_1Ag_{28}-SbF_6 in dichloromethane with 1 mM TPrA..... 147

Figure 5.36. Spooling ECL spectra of 0.28 μM Pt_1Ag_{28}-SbF_6 with 1 mM TPrA during a potentiodynamic scan between −0.20 V and 1.55 V vs. SCE. Scan rate used was 0.1 V/s, and each spectrum was acquired at a 0.5 s time interval. Inset plot is an ECL accumulation spectrum of the same system collected in one cycle of potentiodynamic scan between −0.20 V and 1.55 V within 35s. 148

Figure 5.37. ECL mechanisms for Pt_1Ag_{28}-SbF_6 in the presence of TPrA. (a) Primary reaction mechanism. (b) ECL enhancement from catalytic feedback loop. (c) ECL cascade enhancement from an excess of TPrA. 149

Figure 5.38. (A) Spooling photoluminescence spectra of 0.28 μM Pt_1Ag_{28}-SbF_6 collected at (B) 0.00 V, (C) 0.56 V, (D) 0.68 V, and (E) 0.89 V, obtained by photoexcitation by a 532 nm solid-state laser. 150

Figure 5.39. Stacked spooling ECL spectra of Pt_1Ag_{30}-SbF_6 with 1 mM TPrA. 0.5 sec per spectrum, scan rate = 0.1 V/sec. 151

Figure 5.40. Accumulation ECL spectrum of Pt_1Ag_{28}-Cl..... 151

Figure 5.41. Accumulation ECL spectrum of Pt_1Ag_{28}-Cl..... 152

Figure 5.42. Calculations of kernel surface areas of different nanoclusters. (A) The sum of the Pt_1Ag_{12} kernel surface area of $[Pt_1Ag_{28}(S\text{-}Adm)_{18}(PPh_3)_4](SbF_6)_2$ is 74.40 $Å^2$. (B) The sum of the Pt_1Ag_{12} kernel surface area of $[Pt_1Ag_{30}Cl_1(S\text{-}Adm)_{18}(PPh_3)_3](SbF_6)_3$ is 72.36 $Å^2$. 154

Figure 5.43. Calculation of the effective area of each nanocluster. The effective areas (i.e., the sum of the reactive facets) of (A) Pt_1Ag_{28}-SbF_6 and (B) Pt_1Ag_{30}-SbF_6 nanoclusters are determined as 13.62 and 25.33 $Å^2$, respectively. Color legends: dark green sphere, Pt; dark blue sphere, kernel Ag; blue sphere, surface Ag; red sphere, S; magenta sphere, P; gray sphere, Cl. For clarity, all C and H atoms are omitted. The green arrows point out corridors toward facets, which TPrA radicals reach..... 155

Figure 5.44. Potential stepping of Pt_1Ag_{30}-SbF_6 (10 Hz) in the annihilation pathway.. 159

Figure 5.45. Potential stepping of Pt_1Ag_{28}-SbF_6 (10 Hz) in the annihilation pathway.. 159

Figure 6.1. Structures of (A) TPA-ace-TRZ (B) TPA-ace, (C) TPA-ace-CN, and (D) 2TPA-ace. 171

Figure 6.2. (A) Illustrative calibration procedure of the spectrometer and integrating sphere detection system. The LS-1-CAL-INT standard lamp was radiometrically calibrated by Ocean Insight Inc. to provide a known quantity of light. The lamp is automatically tracked by the OceanView software to provide the absolute irradiance power spectrum (power in unit of $\mu W/nm$ vs. wavelength in nm). (B) Measuring the absolute chemiluminescence (CL) quantum efficiency. The CL reagents are added to the reaction vial, and the resulting emission is collected in absolute photon numbers by the calibrated spectrometer system. (C) Transformation from absolute power (μW/nm) to absolute number of photons (1/nm) at each individual wavelength, using Equations 2-3. The number of total photons can then be obtained by summing up the photons at each wavelength in the visible range between 400 and 700 nm. Dotted lines in the figure correspond to connections via an optical fiber. 173

Figure 6.3. (A) Differential pulse voltammogram of 1.42 mM TPA-ace-TRZ in dichloromethane. Initial scan direction is indicated with arrows. (B) CV (red) and corresponding ECL voltage curve (blue) of 1.42 mM TPA-ace-TRZ in dichloromethane with 0.1 M $TBAPF_6$ as supporting electrolyte. Scan rate was 0.1 V/s. (C) Potential-time (black), current-time (red), and ECL-time (blue) profiles of TPA-ace-TRZ during potential stepping experiments at a pulsing frequency of 10 Hz. 176

Figure 6.4. Accumulation spectrum of TPA-ace-TRZ ECL in the annihilation pathway. 178

Figure 6.5. CV and ECL voltage curve of TPA-ace in dichloromethane with 0.1 M $TBAPF_6$ as the supporting electrolyte..... 178

Figure 6.6. Differential pulse voltammograms of TPA-ace..... 179

Figure 6.7. ECL-time curves during potential stepping experiments (10 Hz pulse frequency) of TPA-ace ECL in the annihilation pathway. 179

Figure 6.8. Accumulation ECL spectrum of TPA-ace in the annihilation pathway. 179

Figure 6.9. CV and ECL voltage curve of TPA-ace-CN in dichloromethane with 0.1 M $TBAPF_6$ as the supporting electrolyte..... 180

Figure 6.10. Differential pulse voltammograms of TPA-ace-CN..... 180

Figure 6.11. ECL-time curves for TPA-ace-CN ECL in the annihilation pathway..... 180

Figure 6.12. ECL accumulation spectrum for TPA-ace-CN in the annihilation pathway. 181

Figure 6.13. CV and corresponding ECL voltage curve of 2TPA-ace with 0.1 M $TBAPF_6$ as supporting electrolyte. 181

Figure 6.14. Differential pulse voltammograms of 2TPA-ace..... 181

Figure 6.15. ECL-time curves during potential stepping experiment (10 Hz) for 2TPA-ace in the annihilation pathway..... 182

Figure 6.16. Accumulation ECL spectrum for 2TPA-ace in the annihilation pathway during potential pulsing experiments..... 182

Figure 6.17. (A) Cyclic voltammogram (red) and ECL voltage curve (blue) of 1.42 mM TPA-ace-TRZ in dichloromethane and 0.1 M $TBAPF_6$ with 10 mM benzoyl peroxide as coreactant. Scan rate = 0.1 V/s. (B) ECL accumulation spectrum of TPA-ace-TRZ with 10 mM benzoyl peroxide (BPO). (C) Current-time (red) and ECL-time (blue) profile of TPA-ace-TRZ during potential pulsing (pulsing frequency was 10 Hz)..... 185

Figure 6.18. CV and ECL voltage curve of TPA-ace with 10 mM BPO as coreactant. 186

Figure 6.19. Accumulation ECL spectrum of TPA-ace with 10 mM BPO. 186

Figure 6.20. Spooling ECL spectrum of TPA-ace with 10 mM BPO as coreactant. Scan rate = 0.1 V/s, 1 spectrum/s. 187

Figure 6.21. CV and ECL voltage curve for TPA-ace-CN with 5 mM BPO as coreactant. 187

Figure 6.22. ECL accumulation spectrum for TPA-ace-CN with 5 mM BPO as coreactant. 188

Figure 6.23. ECL spooling spectrum of TPA-ace-CN with 5 mM BPO as coreactant. Scan rate was 0.1 V/s, 1 spectrum/s. 188

Figure 6.24. CV and ECL voltage curve for 2TPA-ace in the presence of 5 mM BPO as coreactant. 189

Figure 6.25. ECL accumulation spectrum of 2TPA-ace with 5 mM BPO. 189

Figure 6.26. Spooling ECL spectra of 2TPA-ace with 5 mM BPO. Scan rate = 0.1 V/s, 1 spectrum/s. 190

Figure 6.27. Spooling ECL spectra of TPA-ace-TRZ in the presence of 10 mM BPO as coreactant during a potentiodynamic experiment. The scan rate was 0.1 V/s and the exposure time of each spectrum was 1 s. 191

Figure 6.28. Overlaid ECL spooling spectra of TPA-ace-TRZ with 10 mM BPO as coreactant. 191

Figure 6.29. ECL reaction scheme for luminophore in the presence of BPO as coreactant. A = TPA-ace-TRZ, BPO = benzoyl peroxide. 192

Figure 6.30. Colour photograph of TPA-ace-TRZ CL reaction vial (A) before adding H_2O_2 and (B) after addition of H_2O_2. (C) CIE colour coordinate diagram of the TPA-ace-TRZ CL reaction (0.3 mg/mL TPA-ace-TRZ, 10 mg/mL CPPO, 3 mL 30% H_2O_2). (D) Accumulation CL spectrum of 0.3 mg/mL TPA-ace-TRZ in dichloromethane;

accumulation time was 10 s. The inset shows the calculated colour of the CL emission represented by coordinates x = 0.50 and y = 0.48. 194

Figure 6.31. Photoluminescence excitation and emission spectra for TPA-ace-TRZ in dichloromethane..... 196

Figure 6.32. Spooling CL spectra of TPA-ace-TRZ with CPPO and H_2O_2 collected using a calibrated Ocean Insights optical spectrometer. Each spectrum is a 5 s exposure. 197

Figure 6.33. Total photons per spectrum calculated from the spooling CL experiment of TPA-ace-TRZ with CPPO and H_2O_2. 198

Figure 6.34. Linear extrapolation of the total CL photons to baseline. Linear fit performed using curve fitting function. 198

Figure 7.1. Instrument setup for generating high-frequency potential steps and measuring electrochemiluminescence. 209

Figure 7.2. (A) Two-dimensional geometry of COMSOL simulation model with labelled boundaries. The electrode surface boundary was set to 12.5 µm, matching the radius of the experimental UME. (B) Triangular meshing pattern (advancing front algorithm) used in simulation model consisting of *2977* total elements. Geometry boundaries are labelled (as in the main text) for clarity..... 210

Figure 7.3. ECL reactions. (A) Reduction of $Ru(bpy)_3^{2+}$ to form $Ru(bpy)_3^{+}$. (B) Oxidation of $Ru(bpy)_3^{2+}$ to form $Ru(bpy)_3^{+}$. (C) Annihilation reaction between $Ru(bpy)_3^{2+}$ and $Ru(bpy)_3^{+}$ to form the excited state $*Ru(bpy)_3^{2+}$. (D) Relaxation of $*Ru(bpy)_3^{2+}$ excited state to release an ECL photon. 212

Figure 7.4. Comparison between reference 1-D simulation ECL (Shen *et al*. 2010)[15] and the 2-D simulations presented in this work..... 214

Figure 7.5. (A) Simulated ECL transients for different values of k_{ann} (the annihilation rate constant), where the diffusion coefficient was 5.8×10^{-10} m^2/s and the concentration

was 0.5 mol/m^3. Pulsing frequency was 10 Hz. (B) Current-time profile (10 Hz) for simulated ECL experiment. 216

Figure 7.6. Simulated ECL transients for different values of k_{ann} (the annihilation rate constant), where the diffusion coefficient was 5.8×10^{-10} m^2/s and the concentration was 0.5 mol/m^3. Pulsing frequency was 1 Hz. 217

Figure 7.7. Simulated ECL transients for different values of k_{ann} (the annihilation rate constant), where the diffusion coefficient was 5.8×10^{-10} m^2/s and the concentration was 0.5 mol/m^3. Pulsing frequency was 100 Hz. 218

Figure 7.8. Simulated ECL transients for different values of k_{ann} (the annihilation rate constant), where the diffusion coefficient was 5.8×10^{-10} m^2/s and the concentration was 0.5 mol/m^3. Pulsing frequency was 1000 Hz. 219

Figure 7.9. (A) Cyclic voltammogram of 0.5 mM $Ru(bpy)_3(PF_6)_2$ in acetonitrile with 0.1 M $TBAPF_6$ as supporting electrolyte at a platinum ultramicroelectrode with a diameter of 25 µm at a scan rate of 0.02 V/s. Indicated potentials represent reducing and oxidizing potentials for $Ru(bpy)_3^{2+}$ to generate the anodic and cathodic radical species. (B) Potential stepping vs. time program (solid) and corresponding simulated ECL profile (dotted). 220

Figure 7.10. Comparison of experimental (coloured traces) and simulated (dotted traces) ECL transients of 0.5 mM $Ru(bpy)_3^{2+}$ via the annihilation pathway. (A) 10 Hz, cathodic ECL peak, (B) 10 Hz, anodic ECL peak, (C) 100 Hz, cathodic ECL peak, (D) 100 Hz, anodic ECL peak. For 10 Hz experiments, the bin width was 40.96 µs and the bins per record was 10240. For 100 Hz experiments, the bin width was 5.120 µs and the bins per record was 9216. For all experiments, a total of 1000 records were collected. 221

Figure 7.11. Comparison of experimental and simulated ECL transients. (E) 1000 Hz, cathodic ECL peak, (F) 1000 Hz, anodic ECL peak, (G) 10 kHz, cathodic, and (H) 10 kHz, anodic. For 1000 Hz experiments, the bin width = 640 ns, bins per record = 7168. For 10 kHz experiments, bin width = 40 ns, bins per record = 6144. For all experiments, a total of 1000 records were collected. 223

Figure 8.1. (A) Low-magnification TEM image of electrochemically prepared GQDs. Inset is an expanded high-resolution TEM image, showing the lattice structure. (B) Particle size distribution histogram with the data fitted using a Gaussian distribution function. Particle size was determined by FIJI image processing software, by comparison of the attached scale bar with at least 50 individual dots. 233

Figure 8.2. (A) XPS survey scan and high-resolution XPS spectra of (B) C1s, (C) O1s, and (D) N1s for GQD-40. 235

Figure 8.3. (A) UV-visible absorption (blue trace) and photoluminescence excitation and emission spectra (red trace) of top-down GQDs. Left and right insets show GQDs dispersed in water viewed under daylight and UV light, respectively. (B) Photoluminescence spectra of GQDs at different excitation wavelengths. 236

Figure 8.4. Correlation of photoluminescence intensity to absorbance of GQD samples and a 0.1 mM quinine sulfate solution. 237

Figure 8.5. (A) Differential pulse voltammograms (DPVs) of GQDs in acetonitrile (red trace). Blank experiment is shown in the dotted black trace. The arrows indicate the initial scan direction. (B) Cyclic voltammogram (CV) and the corresponding ECL voltage curve for GQDs in the annihilation pathway. 238

Figure 8.6. (A) Cyclic voltammograms and ECL voltage curves of 1 mg/mL GQDs in acetonitrile with 0.1 M TBAP in the presence of 5 mM BPO. (B) Accumulation ECL spectrum of the GQD-BPO coreactant system. 239

Figure 8.7. The proposed GQD-BPO ECL coreactant mechanism. 240

Figure 8.8. ECL spooling spectra of GQDs with 5 mM BPO. Scan rate was 0.1 V/sec. Red traces show spectra before emission maximum. Blue traces are spectra after emission maximum. Inset shows overlapped spectra. 241

Figure 8.9. (A) Cyclic voltammograms and voltammetric ECL curves of 1 mg/mL GQDs in acetonitrile with 5 mM TPrA. (B) Accumulation ECL spectrum of the GQD-TPrA coreactant system. 242

Figure 8.10. (A) A linear voltage sweep of the GQD-based LECs. Inset is a schematic of the LEC device showing the individual layers (not to scale). (B) 1 mA constant current experiment. (C) 120 second accumulation spectrum. Original spectrum is shown as a dotted black line, which was curve fitted using a Gaussian distribution function. The inset shows a colour photograph of the LEC during operation. (D) CIE (*Commision Internationale de l'eclairage)* 1931 coordinate colour diagram of GQD-LEC emission. 244

Figure 9.1. Cathode Radiant Sensitivity versus wavelength (left) and Quantum Efficiency versus wavelength (right) of the used photomultiplier tube, R928 (Hamamatsu, Japan). Digital curves revealed in PDF format online at https://www.hamamatsu.com/resources/pdf/etd/R928_R928P_R955_R955P_TPMS1091E.pdf were requested from Hamamatsu, Japan. 253

Figure 9.2. Intensity normalized background-corrected emission spectrum of RuBPY LECs. 255

Figure 9.3. Intensity normalized background-corrected emission spectrum of red reference LED. 255

Figure 9.4. The photopic luminosity function, which describes the average spectral sensitivity of the human eye. This spectrum was multiplied by a correction factor of 683.002 lm/W before being used in any calculations. 256

Figure 9.5. Expanded device structure of RuBPY-LEC with a 10 nm ZnO ETL/HBL. 257

Figure 9.6. EL intensity vs. applied potential plots for RuBPY-LECs with a 10 nm ZnO-ETL/HBL (red trace) and without the ZnO layer (blue trace). The scan rate used was at 0.05 V/s. Insets (A) and (B), respectively, show colour photographs of the two RuBPY LECs during operation. 258

Figure 9.7. Current and EL intensity vs. applied potential for RuBPY-LECs in the presence of the 10 nm ZnO layer. 259

Figure 9.8. Current and EL intensity vs. applied potential for reference RuBPY-LECs with no ZnO layer. 260

Figure 9.9. Relative PMT efficiency histogram of ZnO-RuBPY-LECs vs. reference RuBPY-LECs in the initial test of linear voltage sweep experiments as in **Figure 9.7** and **Figure 9.8.** 260

Figure 9.10. Energy level diagram of RuBPY-LECs showing the constituting layers in the LEC architecture. The values for energy levels of Al, ZnO, PEDOT:PSS, and ITO were taken from literature.[20-23] HOMO and LUMO energy levels for RuBPY were estimated from the oxidation and reduction potentials , of $Ru(bpy)_3^{2+}$, respectively..... 261

Figure 9.11. Repeated voltage cycling of the RuBPY-LECs with and without a ZnO layer. The numbers above the bars indicate the number of times each device was tested. Error bars heights represent one standard deviation measured across at least eight different devices. 262

Figure 9.12. Relative electroluminescent efficiency histogram of ZnO-RuBPY-LECs vs. RuBPY-LECs from test 5 as in **Figure 9.11**..... 263

Figure 9.13. Luminous efficiency (lm/W) of ZnO-RuBPY-LECs vs. current density.. 263

Figure 9.14. Luminous efficiency (lm/W) of reference RuBPY-LECs vs. current density. 264

Figure 9.15. Spooling EL spectra of RuBPY-LECs with the added ZnO-ETL/HBL (A) and without the ZnO-ETL/HBL (B) during a forward potential scan. Insets for each figure correspond to selected spectrum collected at three specific voltages. 265

Figure 9.16. Accumulation spectra and their CIE chromaticity diagrams (insets) for a ZnO-RuBPY-LEC (A) and RuBPY-LEC (B)..... 267

List of Appendices

Appendix A: Reproduction Permission for paper "Nanocluster Transformation Induced by SbF_6^- Anions toward Boosting Photochemical Activities." 275

Appendix B: Reproduction Permission for paper "Physical Strategy to Determine Absolute Electrochemiluminescence Quantum Efficiencies of Coreactant Systems Using a Photon-Counting Photomultiplier Device." 276

Appendix C: Reproduction permission for paper "Absolute Electrochemiluminescence Quantum Efficiency of Au Nanoclusters by Means of a Spectroscopy Charge-Coupled Device Camera." 277

Appendix D: Reproduction permission for paper "Electrogenerated Chemiluminescence and Electroluminescence of N-Doped Graphene Quantum Dots Fabricated from an Electrochemical Exfoliation Process in Nitrogen-Containing Electrolytes." 278

Appendix E: Reproduction permission for paper "Spooling Electroluminescence Spectroscopy of $Ru(bpy)_3^{2+}$ Light-Emitting Electrochemical Cells with an Atomic Layer Deposited Zinc Oxide Electron-Transporting/Hole-Blocking Interlayer." 286

List of Abbreviations and Symbols

Abbreviation	Definition
ACQ	Aggregation caused quenching
ADC	Analog-to-digital convertor
AIE	Aggregation induced emission
AIECL	Aggregation induced electrochemiluminescence
ALD	Atomic layer deposition
AlInGaP	Aluminum gallium indium phosphide
AQE	Absolute quantum efficiency
BE	Binding energy
BPO	Benzoyl peroxide
CCD	Charge-coupled device
CE	Counter electrode
CIBS	Crystallization induced blue shift
CIE	Crystallization induced emission
CL	Chemiluminescence
CPPO	Bis(2,4,5-trichloro-6-(pentyloxycarbonyl)phenyl)oxalate
CQD	Carbon quantum dot
CT	Charge transfer
CV	Cyclic voltammetry
DCM	Dichloromethane
DFT	Density functional theory
DMSO	Dimethyl sulfoxide
DPV	Differential pulse voltammetry
ECD	Electrochemical doping
ECL	Electrochemiluminescence or electrogenerated chemiluminescence
ECL-QE	Electrochemiluminescence quantum efficiency
EDS	Energy dispersive x-ray spectroscopy
EL	Electroluminescence

EQE	External quantum efficiency
ESI-MS	Electrospray ionization mass spectrometry
ETL	Electron transport layer
Fc	Ferrocene
GCE	Glassy carbon electrode
HBL	Hole blocking layer
HOF	Hydrogen bonding organic framework
HOMO	Highest occupied molecular orbital
HPS	Hexaphenylsilole
ICP-AES	Inductively coupled plasma atomic emission spectroscopy
Im	Iminium ion
InGaAs	Indium gallium arsenide
IREC	Intra-reticular electron coupling
ISC	Intersystem crossing
iTMC	Ionic transition metal complex
ITO	Indium-tin-oxide
LEC or LEEC	Light-emitting electrochemical cell
LED	Light-emitting diode
LED	Light-emitting diode
LiTf	Lithium trifluoromethanesulfonate
LUMO	Lowest unoccupied molecular orbital
MR-TADF	Multiresonance thermally activated delayed fluorescence
NFCCF	Non-Faradaic current correction factor
OD	Optical density
OLECL	Organic long persistent electrochemiluminescence
OLED	Organic light-emitting diode
OLEL	Organic long persistent electroluminescence
OLPL	Organic long persistent photoluminescence
PCH	Photon counting head
PEDOT:PSS	Poly(3,4-ethylenedioxythiophene) polystyrene sulfonate
PEG	Polyethylene glycol

PEO	Polyethylene oxide
PL	Photoluminescence
PLQY	Photoluminescent quantum yield
PMT	Photomultiplier tube
PTFE	Polytetrafluoroethylene
PVD	Physical vapour deposition
RE	Reference electrode
RIR	Restriction of intramolecular rotation
RISC	Reverse intersystem crossing
RRDE	Rotating ring disc electrode
$Ru(bpy)_3^{2+}$	Tris(2,2'-bipyridine)ruthenium(II)
SCE	Saturated calomel electrode
TADF	Thermally activated delayed fluorescence
$TBAPF_6$	Tetrabutylammonium hexafluorophosphate
TEM	Transmission electron microscopy
TMPE	Trimethylolpropane ethoxylate
TPrA	*n*-tripropylamine
TSCT	Through-space charge transfer
TTL	Transistor-transistor logic
WE	Working electrode
XPS	X-ray photoelectron spectroscopy
XRD	X-ray diffraction spectroscopy
ZnO	Zinc oxide

"… in whom are hidden all the treasures of wisdom and knowledge."

Chapter 1

In this opening chapter, we discuss different strategies to enhance the electrochemiluminescence properties of luminophores. These approaches include thermally activated delayed fluorescence, hydrogen-bonding, aggregation- and crystallization-induced emission. For each strategy, we also provide applications and outlook for the future of the field of enhanced ECL research.

1 Materials for Electrochemiluminescence: TADF, Hydrogen-bonding, and Aggregation- and Crystallization-Induced Emission Luminophores†

Electrochemiluminescence (ECL) is a rapidly growing discipline with many analytical applications from immunoassays to single molecule detection. At the forefront of ECL research is materials chemistry which looks at engineering new materials and compounds exhibiting enhanced ECL efficiencies compared to conventional fluorescent materials. In this minireview, we summarize recent molecular design strategies that lead to high efficiency ECL. In particular, we feature recent advances in the use of thermally activated delayed fluorescence (TADF) emitters to produce enhanced electrochemiluminescence. We also document how hydrogen-bonding, aggregation, and crystallization can each be recruited in the design of materials showing enhanced electrochemiluminescence.

1.1 Introduction

Electrochemiluminescence (ECL) is the process where electrogenerated radical species undergo electron transfer in the vicinity of a biased electrode to produce excitons (excited states); relaxation of these excited states produces ECL emission.[1, 2] ECL has been exploited in biosensing[3-5], single molecule detection[6-8], light-emitting electrochemical cells (LECs) [9, 10], and imaging[11-13] due to its high sensitivity, selectivity, and excellent signal-to-noise ratio. ECL can proceed via two mechanistic pathways. The annihilation

---

† This work has been published. Chu, K.; Ding, Z.; Zysman-Colman, E. *Chem. Eur. J.* (**2023)** e202301504.

pathway involves the generation of radical cations (holes) and radical anions (electrons) produced at the electrode from alternating oxidizing and reducing potentials, respectively. The electron transfer between these two electrogenerated radicals produces an exciton, which then can radiatively decay to produce the light. In the co-reactant route, the co-reactant, upon oxidation or reduction, can form a highly reactive intermediate that can interact with ECL luminophore polaron to produce the exciton. *n*-Tripropylamine (TPrA) is an example of an 'oxidative-reductive' co-reactant, because upon oxidation, $TPrA^{\bullet+}$ deprotonates to form the TPrA radical ($TPrA^{\bullet}$), which is a strong reductant. On the other hand, benzoyl peroxide (BPO) is known as a 'reductive-oxidative' co-reactant, since upon reduction and subsequent cleavage, the so formed benzoate radical ($PhCO_2^{\bullet}$) is strongly oxidizing. The use of co-reactants leads to enhanced ECL due to both the high oxidizing or reducing power of the reactive intermediates as well as their relatively high concentration compared to luminophore.[14, 15] Organic long-persistent emission is characterized in compounds that remain luminescent for several seconds, even after the excitation source is removed. This phenomenon has been reported as organic long-persistent photoluminescence (OLPL) and electroluminescence (OLEL), particularly in TADF compounds that have large ΔE_{ST}.[16, 17] More recently, this effect has also been observed in electrochemiluminescence (OLECL).[18]

The efficiency of an ECL reaction is defined as the ratio of the total number of photons produced by radiative relaxation of the electrically generated excitons to the total number of Faradaic electrons injected into the system.[1] Until recently, the ECL efficiency of a system was reported relative to that of a well-known ECL luminophore, $[Ru(bpy)_3]^{2+}$ in the annihilation pathway or that of a $[Ru(bpy)_3]^{2+}$/co-reactant system. Methodologies to reproducibly and quantitatively determine the absolute ECL quantum efficiency have recently been made possible by us, utilizing on-demand calibrated detection systems such as photomultiplier tubes (PMTs)[19], photon-counting heads (PCHs) along with a spectrometer[20], or a calibrated spectrograph/CCD camera array.[21] The accurate determination of the quantum efficiency of ECL luminophores is essential to assess the performance of the materials employed, as optimizing the photons-out/electrons-in ratio can represent significant cost savings for consumers. Enhancing the luminous efficiency

of ECL processes can also improve the detection limit for sensing and imaging applications.

In general, the ratio of singlet to triplet excitons generated by recombination of Fermionic holes and electrons is 1:3 due to spin statistics.[22] Under electrical excitation this limits the maximum efficiency of fluorophores (compounds that are fluorescent) to 25%, since spin-forbidden transitions such as reverse intersystem crossing and radiative decay from the triplet state in the form of phosphorescence are slow and the triplet excitons are therefore prone to decay via alternative non-radiative relaxation pathways. In thermally activated delayed fluorescence (TADF) materials, in contrast, there is an efficient thermal up-conversion of triplet excitons to singlets, enabling the harvesting of both singlet and triplet excitons to produce light, and which unlike phosphorescent complexes, does not require the presence of a heavy metal to achieve internal quantum efficiencies up to 100%. For this reason, TADF material design has become extremely attractive in developing high efficiency emitters for electroluminescent devices, and by extension should be very promising in ECL applications. Other mechanisms, such as aggregation-induced electrochemiluminescence (AI-ECL), crystallization-induced electrochemiluminescence (CI-ECL), and hydrogen-bonding ECL (H-bonding ECL), can also be used to enhance the ECL efficiency. In contrast to TADF – which leverages chemical properties of the emitting molecules to deliver enhanced emission – AI-ECL, CI-ECL, and H-bonding ECL utilize intermolecular interactions, that is, interactions between luminophore molecules, to result in enhanced emission.

In this minireview, we summarize the new and emerging materials design strategies in developing high performance, high efficiency ECL luminophores. We focus on thermally activated delayed fluorescence (TADF) emitters, aggregated induced electrochemiluminescence (AI-ECL), crystallization induced electrochemiluminescence (CI-ECL), and hydrogen-bonding enhanced ECL.

1.2 Thermally Activated Delayed Fluorescence (TADF)

Phosphorescent molecules harvest both singlet and triplet excitons, converting the former into the latter by efficient intersystem crossing and then emit by phosphorescence, these

processes mediated usually by the presence of a heavy atom that increases spin-orbit coupling. However, long excited state lifetimes make triplet excitons prone to decaying by non-radiative pathways including by interacting with polarons or other excitons. Furthermore, phosphorescent materials usually incorporate expensive and scarce heavy metal elements such as ruthenium, platinum, or iridium. Molecules that emit via TADF are equally capable of harvesting both singlet and triplet excitons to produce light, but do not need the heavy elements. Functionally, TADF results from triplet excitons upconverting to singlets via reverse intersystem crossing (rISC) followed by radiative relaxation from S_1 to S_0. This process results in a delayed emission identical to the prompt fluorescence that also occurs from directly generated singlet excitons that radiatively decay, except it occurs on longer time scales. The efficiency of the TADF process is, to a first approximation, governed by the degree of spin-orbit coupling (ξ_{ST}) between the singlet and triplet excited states and the energy gap between them, ΔE_{ST} (**Equation 1.1**). Also included in this equation is k_B (the Boltzmann constant) and T (the temperature). Generally, as ΔE_{ST} decreases, the efficiency of the up-conversion process increases.

The magnitude of ΔE_{ST} is, in turn, determined by the exchange integral *J*, which describes the Coulombic repulsion between two electrons (**Equation 1.2**). In other words, ΔE_{ST} will be small if the highest occupied molecular orbital (HOMO) and lowest unoccupied molecular orbital (LUMO) are spatially separated in the molecule.[23]

$$k_{RISC} \propto \xi_{ST}^2 e^{\left(\frac{-\Delta E_{ST}}{k_B T}\right)}$$

Equation 1.1

$$\Delta E_{ST} = 2J = 2\int\int \phi_H(r_1)\phi_L(r_2)\frac{1}{|r_2 - r_1|}\phi_H(r_2)\phi_L(r_1)dr_1 dr_2$$

Equation 1.2

The dominant strategy to spatially separate the HOMO and LUMO in an organic molecule is for it to adopt a highly twisted donor-acceptor geometry. In this context, the

lowest lying excited state is one of charge-transfer (CT) character from the donor, where the HOMO is localized, to the acceptor, where the LUMO is localized. By selecting suitable D and A subunits, the HOMO/LUMO energy levels (and therefore the energy of the CT excited state) can be rationally tuned, providing compounds that emit from the ultraviolet to the near-infrared range. D-A architectures are not the only ones that can produce molecules/systems with small ΔE_{ST}. Through-space charge transfer (TSCT) emitters, multi-resonant TADF (MR-TADF) emitters and exciplexes are all categories of materials that have been explored as emitters in electroluminescent devices.

1.2.1 Donor-Acceptor TADF Compounds

In 2014, Ishimatsu, Adachi, Imato and co-workers were the first to demonstrate ECL from donor-acceptor TADF emitters (2CzPN, 4CzPN, 4CzIPN, and 4CzTPN) in the annihilation pathway (**Figure 1.1A**).[24] These TADF molecules, incorporating carbazolyl and dicyanobenzene groups as donors and acceptors, respectively, demonstrated quasi-reversible reduction and irreversible multi-electron oxidation. The authors speculated that oxidation of these compounds could initiate polymerization (the polymer film on the electrode surface inhibits electrochemical activity) from the known unstable carbazole-centred radical cation. A small red-shift (approximately 10-20 nm) was observed when the solvent polarity was increased from DCM to MeCN (**Figure 1.1B** and **Figure 1.1C**), due the positive solvatochromism typically observed for compounds with CT emission. Furthermore, the authors observed a small red-shift between the ECL and PL emission, which was likely due to contributions from oligomers formed during the oxidation process in the ECL. They showed that **4CzIPN** could achieve a relative ECL efficiency of 50%, which both exceeded the 25% limit associated with fluorescent ECLphores imposed by spin statistics and approached the maximum efficiency dictated by the intrinsic photoluminescence quantum yield, Φ_{PL}, of the materials. Emission maxima, λ_{PL}, of 544 and 565 nm were reported in DCM and acetonitrile, respectively while the λ_{ECL} in these respective solvents were 555 and 565 nm. Since the PL and ECL spectra in MeCN matched for **4CzIPN**, the authors concluded that under ECL this compound showed TADF.

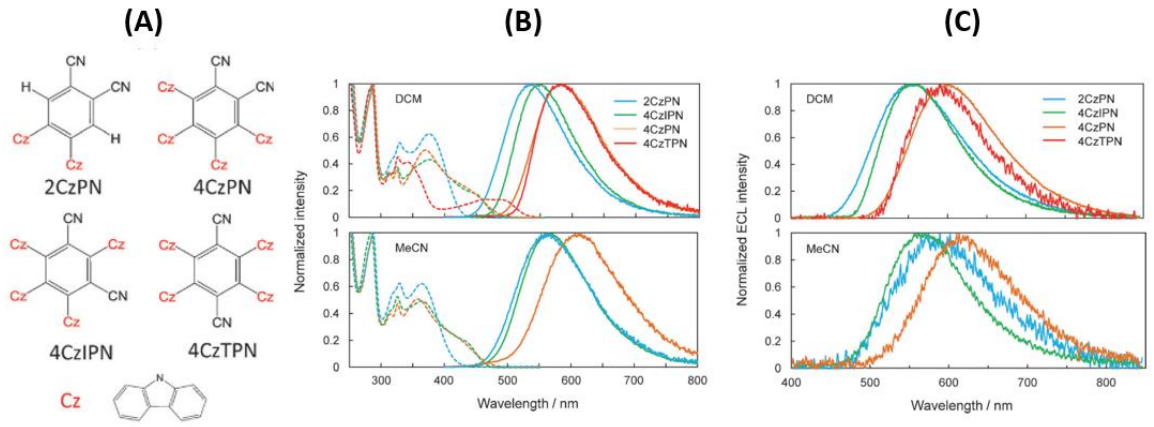

Figure 1.1. (A) Molecular structures of 2CzPN, 4CzPN, 4CzIPN, and 4CzTPN. (B) UV-Vis absorption (dotted) and PL spectra (solid lines) of 25 μM TADF emitter in DCM (top) and MeCN (bottom). (C) Normalized ECL spectra of TADF emitters in DCM (top) and MeCN (bottom). Adapted with permission from Ref. [24]. Copyright 2014, Wiley-VCH.

Our groups studied three D-A-TADF compounds **PPOCzPN**, **PPSCzPN**, and **DiPPOCzPN** (the molecular structures are displayed in the insets of **Figure 1.2A**, **Figure 1.2B**, and **Figure 1.2C**) for ECL, where the phosphine-chalcogenide modified carbazolyl donor groups stabilized the HOMO level to promote a blue-shifted emission (**Figure 1.2**).[25] Compounds **PPOCzPN**, **PPSCzPN**, and **DiPPOCzPN** emit at 498, 501, and 465 nm, respectively, in DCM. **DiPPOCzPN** showed the highest photoluminescence quantum yield, Φ_{PL}, of 61% of the three compounds. These three compounds demonstrated strong blue-green ECL emission in the presence of 10 mM BPO as the co-reactant (**PPOCzPN** λ_{ECL}=520 nm, **PPSCzPN** λ_{ECL}=500 nm, **DiPPOCzPN** λ_{ECL}=545 nm). In particular, **PPOCzPN** showed a 17% ECL efficiency relative to that of the reference $[Ru(bpy)_3]^{2+}$. Interestingly, we observed a delay in the ECL onset times, which we attributed to a phenomenon called organic long persistent ECL (OLECL), caused by a dissociation/association equilibrium between emissive excimer species and dissociated constituents. The magnitude of the ECL delay was also determined to be correlated with the ΔE_{ST}. For **PPOCzPN**, the ECL and PL emission matched, which indicates the same excited state was present in all pathways and suggests TADF behavior. In contrast, **PPSCzPN** and **DiPPOCzPN** displayed red-shifted ECL emission compared to their PL.

This indicates likely exciplex involvement under the ECL conditions and may help to explain the decreased ECL efficiency when compared to **PPOCzPN**.

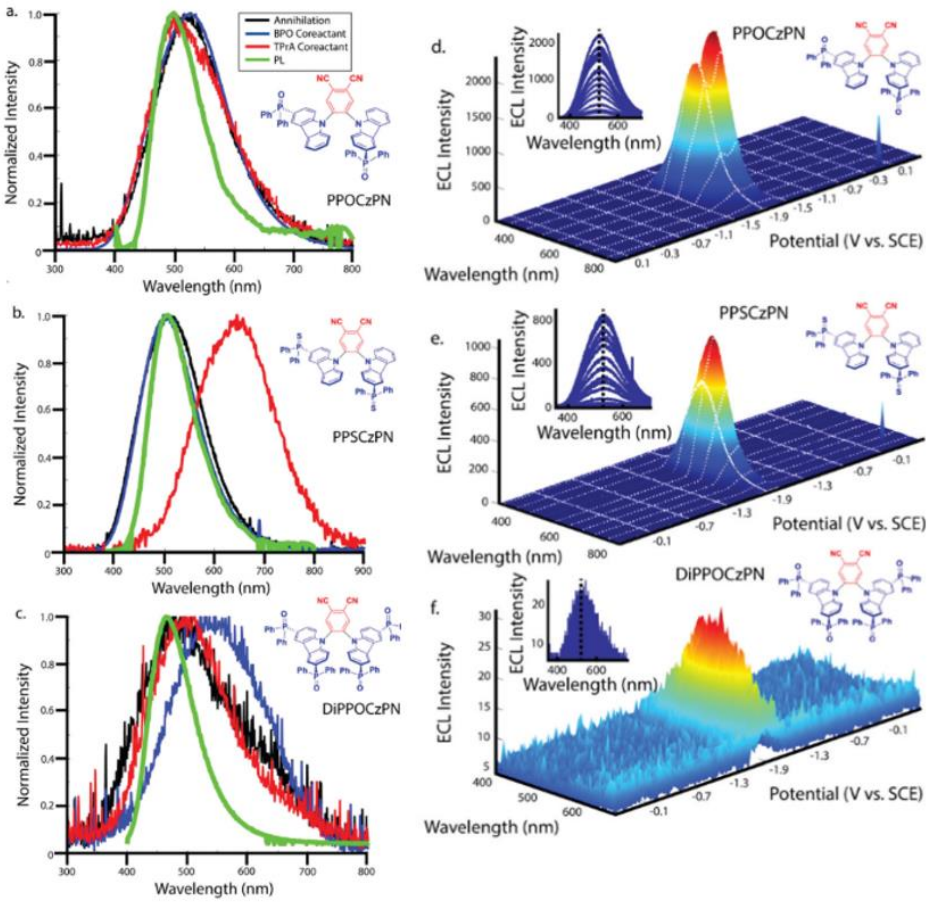

Figure 1.2. (A–C) CVs (red) along with ECL–voltage curves (blue) during potential pulsing at a pulsing frequency of 10 Hz for PPOCzPN, PPSCzPN and DiPPOCzPN, respectively, all with 10 mM BPO was added as a co-reactant. (D–F) Spooling ECL spectroscopy of the corresponding systems described in Figures A to C. Insets of Figures D–F represent respective stacked spooling ECL spectra. Adapted with permission from Ref. [25]. Copyright 2022. The Royal Society of Chemistry.

We also investigated the ECL behavior of the TSCT TADF molecule **TPA-ace-TRZ** (**Figure 1.3A**).[26] This emitter produced ECL emission via both the annihilation and co-reactant pathways that was significantly red-shifted compared to the PL emission (**Figure 1.3B**). A significant delay in the ECL onset was seen (**Figure 1.3C**), which as observed

with the inefficient D-A TADF emitters in **Figure 1.2**, hints at the formation of an exciplex. Exciplex formation is promoted by intermolecular excited CT states and typically also emit via TADF.[23] Using a standardized CCD camera/spectrograph instrument setup, the absolute ECL quantum efficiency of **TPA-ace-TRZ** was determined to be 0.028%, which was 9-fold stronger than that of the $[Ru(bpy)_3]^{2+}$ reference. Additionally, we explored the performance of **TPA-ace-TRZ** under a chemiluminescence pathway. **TPA-ace-TRZ** produced bright yellow emission from the oxidation of the phenyl oxalate ester in the presence of hydrogen peroxide (**Figure 1.3D**). Notably, the emission wavelengths observed in PL, ECL, and CL spectra were all very close to each other, which strongly suggests the same exciplex excited state is present in all three pathways. Therefore, the interaction between **TPA-ace-TRZ** and high-energy intermediates formed from the CL reagents was proposed to form exciplexes, which is very uncommon in CL pathways.

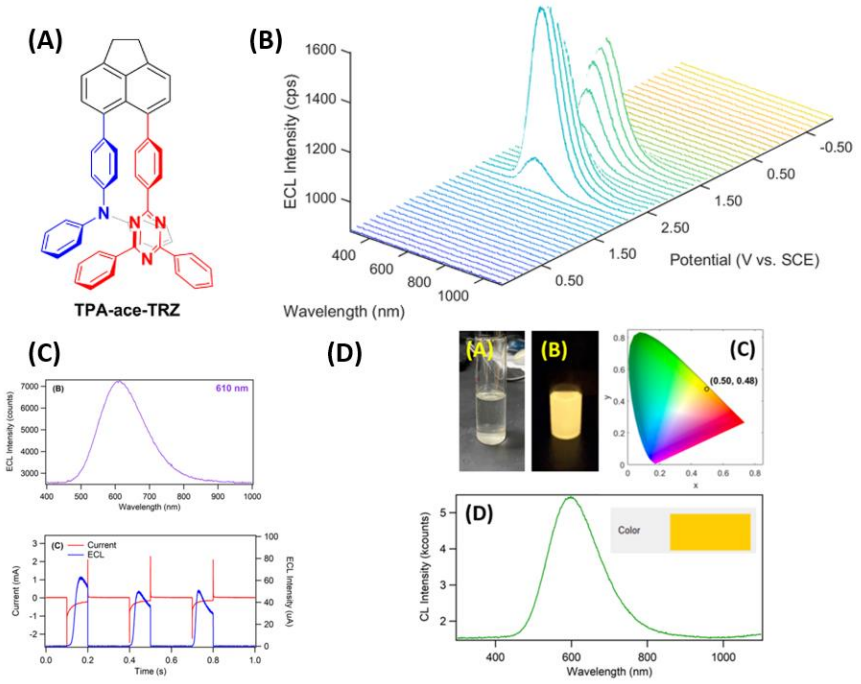

Figure 1.3. (A) Structure of TPA-ace-TRZ. (B) Spooling ECL spectra of TPA-ace-TRZ with 10 mM BPO as the co-reactant. (C) Top: ECL accumulation spectrum of TPA-ace-TRZ with 10 mM BPO as the co-reactant. Bottom: Current-time and ECL-time profiles of TPA-ace-TRZ with the BPO co-reactant system. (D) Top-left: Colour photographs of

TPA-ace-TRZ CL reaction vial before/after adding H_2O_2. Top-right: CIE colour coordinate diagram of TPA-ace-TRZ CL. Bottom: CL accumulation spectrum of TPA-ace-TRZ system. Adapted with permission from Ref. [26]. Copyright 2023, American Chemical Society.

Niu and co-workers reported ECL from a D-A TADF polymer **PCzAPT10** (**Figure 1.4**).[27] **PCzAPT10** displayed a broad PL at λ_{PL} of 508 nm in chlorobenzene, attributed to the emission of the TADF co-monomer chromophore. Using a glassy carbon **PCzAPT10**-modified electrode, they observed ECL under the TPrA co-reactant mechanism using MeCN as the solvent, where the ECL signal was red-shifted to 587 nm. The authors contended that the ECL electron-transfer processes could occur close to the **PCzAPT10**/MeCN solid/liquid interface, and therefore the so formed CT excitons located on the TADF co-monomer would be stabilized in the polar solvent. Due to the TADF nature of **PCzAPT10**, the ECL efficiency was enhanced fourfold compared to that of a fluorescent polymer standard F8BT, and two times to that of the $[Ru(bpy)_3]^{2+}$/TPrA system. The same group also studied the ECL behavior of **4CzIPN** and the TSCT emitter **BPAPTC** in dichloromethane.[28] In this work, the authors were able to demonstrate ECL emission under both annihilation and co-reactant pathways, with a maximum ECL efficiency of approximately two times relative to $[Ru(bpy)_3]^{2+}$. When compared to the results provided by Ishimatsu, Adachi, Imato and co-workers who investigated the ECL of **4CzIPN** in the annihilation pathway (λ_{ECL}=555 nm)**,** a red-shifted emission at 600 nm was observed for the **4CzIPN**-BPO co-reactant system. This red-shift in the ECL emission could be due to the increased reactivity of BPO to promote oligomerization and/or aggregated excited states. Due to the low oxidation potential of **BPAPTC**, an ECL onset potential as low as +0.46 V vs. Ag/AgCl was achieved. It was also confirmed that the PL and ECL spectra were very close for these two TADF luminophores under co-reactant pathways, providing strong evidence for TADF emission under ECL conditions.

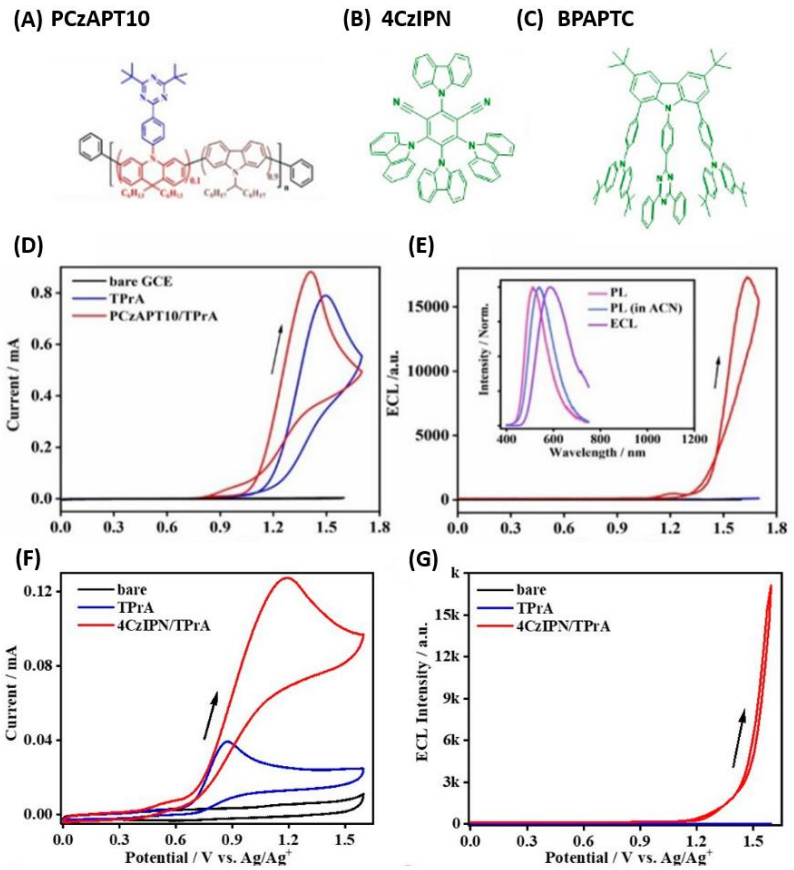

Figure 1.4. Chemical structures of (A) PCzAPT10 TADF polymer, (B) 4CzIPN, and (C) BPAPTC molecules. (D) Cyclic voltammograms of PCzAPT10-modified GCE with TPrA. (E) ECL-voltage curve of PCzAPT10. Inset shows PL in neat film vs. MeCN, and ECL spectrum of the PCzAPT10/TPrA co-reactant system. Cyclic voltammograms (F) and ECL-voltage curves (G) of 4CzIPN in dichloromethane with 0.1 M $TBAPF_6$ and 40 mM TPrA. Adapted with permission from Ref. [27] and [28]. Copyright 2021, Wiley-VCH.

TADF compounds have also been used in conjunction with other materials to produce enhanced ECL. Niu and co-workers encapsulated **4CzIPN** within an amphiphilic ethylene glycol based polymer (DSPE-PEG2000) to improve the water solubility for aqueous ECL applications.[29] The nanoencapsulated product displayed excellent stability and electrochemical reversibility, and demonstrated strong ECL emission in both annihilation and TPrA co-reactant pathways. Interestingly, the authors noted a small red-shift in the ECL emission compared to the PL, which they have attributed to involvement of molecular surface states, doubtless the effect of the nanoencapsulation strategy.

4CzIPN, in this nanoencapsulated design, showed virtually the same PL characteristics as reported by the Ishimatsu, Adachi, Imato and co-workers (λ_{PL}=555 nm), although the ECL emission was slightly red-shifted to 572 nm. The authors attributed this to the involvement surface states under electrochemical excitation.[30] The same group used a similar method to encapsulate instead conjugated TADF polymer dots (TADF-Pdots).[31] This report showed that the TADF-Pdots were capable of exhibiting the same ECL and PL emissions at 510 nm, and had a relative ECL efficiency in the TPrA co-reactant pathway of 11.73% vs. the $Ru(bpy)_3^{2+}$/TPrA reference system.

The Ju group improved significantly the Φ_{ECL} by creating Pdots using poly(TMTPA-DBC) as the TADF precursor.[32] The resulting TADF-Pdots showed very similar PL and ECL emission at 517 nm and 520 nm, respectively, indicating that the same excited state could be formed in the two pathways. As well, the Φ_{ECL} was enhanced up to 49.9% in the TPrA co-reactant system.

1.2.2 Multi-resonance (MR)-TADF Compounds

As intimated earlier, another molecular design, first introduced by Hatakeyama *et al.* in 2016, is the MR-TADF emitter.[33] These compounds typically possess electron donor atoms and electron acceptor atoms that are arranged within a polycyclic aromatic hydrocarbon skeleton such that the HOMO and the LUMO are localized on alternating atoms, producing short-range CT (SRCT) excited states. This structure provides simultaneously a sufficiently small ΔE_{ST} to promote TADF while suppressing molecular vibration, leading to narrowband emission and high Φ_{PL}.[34]

Our research groups reported the MR-TADF emitter **Mes_3DiKTa** (**Figure 1.5A**), which has a ΔE_{ST} of 0.26 eV and high Φ_{PL} of 80% at 3.5 wt% doped films in 1,3-bis(N-carbazolyl)benzene (mCP), and studied its ECL behaviour in acetonitrile.[35, 36] Strong ECL was detected for this compound in the presence of TPrA as a co-reactant, with a relative efficiency of 79% recorded at a TPrA concentration of 20 mM versus $[Ru(bpy)_3]^{2+}$. Both delayed onset (about 5 ms after the application of potential) and slow decay (~10 ms after the applied potential returns to 0 V) of the ECL reaction were observed in the potential pulsing experiment where the ECL emission could be monitored

with respect to the potential steps. (**Figure 1.5B**). This may be due to OLECL, a process that involves the charge separation and slow recombination in exciplexes that may be particularly relevant to systems with a moderate ΔE_{ST}. However, competing processes for delayed emission including TTA and TADF could not be completely ruled out in this instance. The presence of OLECL was also proposed to enhance the overall ECL emission; accordingly, the absolute ECL efficiencies of **Mes$_3$DiKTa** were determined to be 0.0013% in the annihilation route and 1.1% in the TPrA co-reactant system. Using spooling ECL spectroscopy (**Figure 1.5C**), we identified that a combination of monomer and aggregate excited states contributed to the ECL emission.

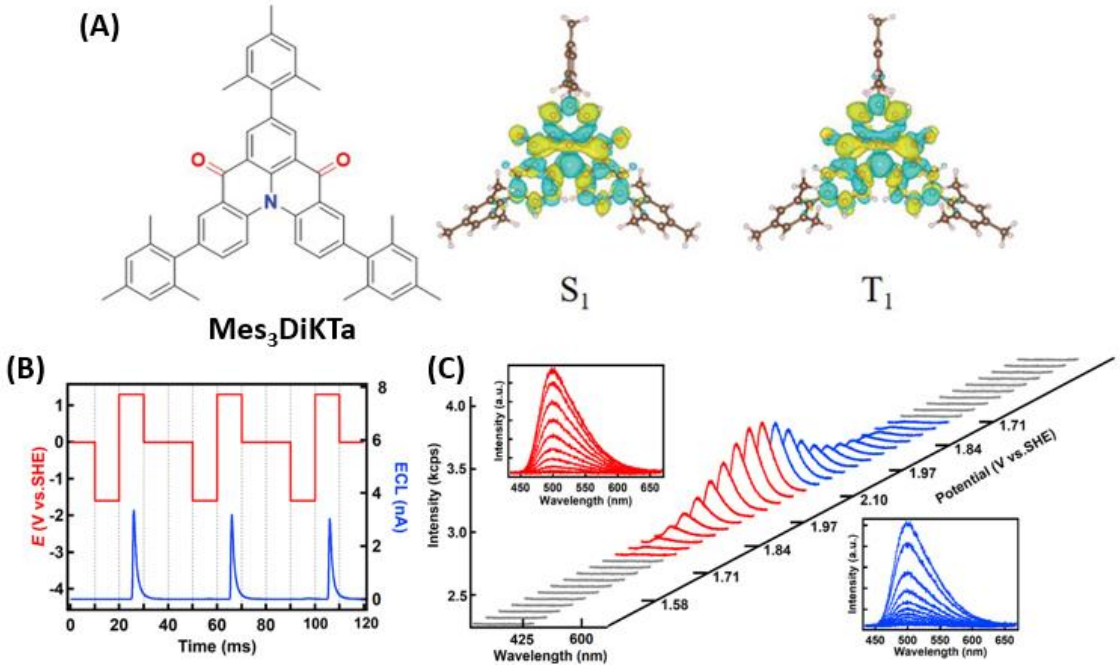

Figure 1.5. (A) Structure and calculated difference density plots of Mes$_3$DiKTa. (B) Time-resolved ECL experiments with 0.2 mM Mes$_3$DiKTa in acetonitrile via the annihilation pathway. (C) Spooling ECL spectra of 0.2 mM Mes$_3$DiKTa in the presence of 20 mM TPrA as a co-reactant, with a scan rate of 0.02 V/s and exposure time of 2 s. Adapted with permission from Refs. [35] and [36]. Copyright 2020, Wiley-VCH. Copyright 2023, IOP Publishing.

Of the three systems reported for OLECL, there appears to be a direct correlation between the magnitude of ΔE_{ST} and the delayed onset time in the ECL: the compound

with the smallest ΔE_{ST} (TPA-ace-TRZ, ΔE_{ST} = 0.06 eV) also displayed the longest delay onset (25 ms) and persistent emission (57 ms), while Mes_3DiKTa (ΔE_{ST} = 0.26 eV) and PPOCzPN (ΔE_{ST} = 0.21 eV) had shorter delay onsets, 5 ms and 7 ms, respectively. While additional verification is required, these results suggest that a small ΔE_{ST} may promote delayed emission following the OLECL pathway. Furthermore, this indicates that the engagement of OLECL and exciplex formation may be a competing mechanism to TADF.

1.3 Hydrogen bonding system ECL

Hydrogen bonding between ECL luminophores is another strategy to produce enhanced electrochemiluminescence. This bonding interaction to create self-assemblies could effectively restrict intramolecular rotation to enhance ECL in an alternative pathway towards aggregation-induced emission. For example, hydrogen bond organic frameworks (HOFs) can be self-assembled from organic ligands using hydrogen bonding interactions. HOFs can facilitate the aggregation of molecular luminophores that result in AIE, which is then exploited to produce enhanced ECL.[37, 38] Among other strategies to enhance ECL, favorable hydrogen bonding (H-bonding) interactions between the emitter and secondary compounds could both promote ECL activity via pre-organization and stabilize the ECL. Our groups studied that H-bonding interaction between an Ir(III) complex (**1**) and pyrimido-[4,5-c]isoquinolin-3-amine (**3**), and its effects on the ECL (**Figure 1.6**).[39] In electrochemical measurements, the H-bonding complex of **[1•3]** showed additional reduction signals that were not present in either precursor. The **[1•3]** adduct also showed enhanced multi-peak ECL emission with BPO as a co-reactant, with emission peaks originating from a combination of exciplexes between **1**, **3**, and BPO radicals. The addition of DMF to suppress H-bonding also significantly changed the electrochemical and ECL properties, revealing a highly dynamic ECL environment.

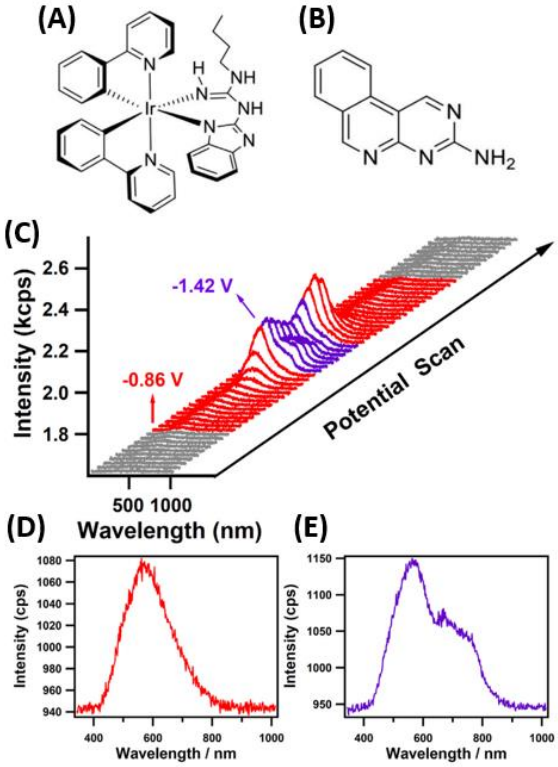

Figure 1.6. (A) Chemical structures of Ir(III) complex [1] and pyrimido-[4,5]-cisoquinolin-3-amine [3], which combine through H-bonding to form complex [1•3]. (C) Spooling ECL spectra of complex [1•3] with 5 mM BPO as co-reactant. ECL spectrum at (D) −1.34 V and (E) −1.50 V. Adapted with permission from Ref. [39]. Copyright 2022, Elsevier B.V.

H-bonding can also play a more structural role in enhancing ECL. You *et al.* showed that a $[Ru(dcbpy)_3]^{2+}$/carbon quantum dot (CQD) matrix could act as an effective sensing platform, where the H-bonding facilitated electron transfer due to the decreased intermolecular distance between emitter and co-reactant.[40] The authors speculated that H-bonds could form between oxygen-rich functional groups, and this effect was confirmed by an enhancement in the electrochemical oxidation current of the $[Ru(dcbpy)_3^{2+}]$/CQD composite vs. the unmodified electrode. This H-bonded composite showed an ECL emission at 660 nm, which closely matched its PL emission. Using this platform, they were able to successfully realize the detection of 17-β estradiol (B2) at micromolar concentrations.

Feng *et al.* demonstrated that a self-assembled triazinyl-based hydrogen bond organic framework (**Tr-HOF**) constructed from 2,4-diaminotriazinyl (phenyDAT) could achieve an enhanced ECL compared to that using the individual phenyDAT monomers.[41] The three-dimensional structure of the **Tr-HOF** is stabilized by N···H hydrogen bonds, suppressing the quenching effects of ligand π-π stacking while simultaneously providing large active surface area for efficient electron transfer (**Figure 1.7**). This unique system attained 21% ECL efficiency relative to $[Ru(bpy)_3]^{2+}$, which was a substantial improvement from monomeric phenyDAT. **Tr-HOF** demonstrated an ECL emission at 643 nm that is red-shifted by 10 nm from its PL emission, which the authors asserted was due to emission from different excited states in the two processes. In a similar vein, Lei *et al.* assembled two kinds of HOFs, **HOF-101** and **HOF-100** using 1,3,6,8-tetra(4-carboxylphenyl)pyrene and 1,3,6,8-tetracarboxy pyrene, respectively.[42] **HOF-101** demonstrated an effect termed intra-reticular electron coupling (IREC), which improves long-range charge transfer.[43] **HOF-101** displayed very similar PL and ECL emission in aqueous solution at 502 and 503 nm, respectively. IREC was thought to contribute to an enhancement in the ECL efficiency up to 64.7% vs. $[Ru(bpy)_3]^{2+}$ when using TPrA as a co-reactant. Importantly, the authors also noted that the stacking morphology driven by intermolecular and intramolecular H-bonds could have a significant impact on the charge transfer (and therefore ECL) capabilities.

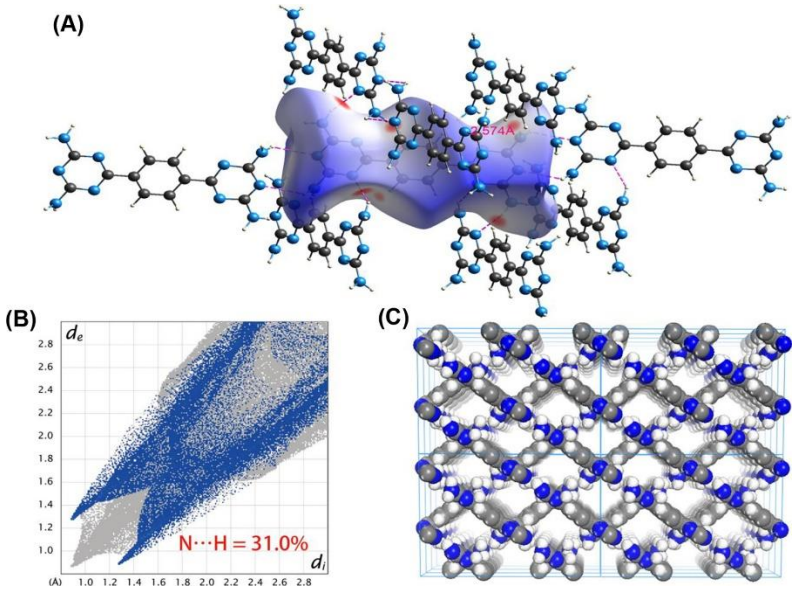

Figure 1.7. (A) Intermolecular interactions of phenyDAT in Tr-HOFs with the labeled distance extracted from its crystal packing data. (B) View of the Hirshfeld surface mapped over the normalized distance of the N–H bond for phenyDAT in Tr-HOFs. (C) 3D packing framework of Tr-HOFs. Reproduced with permission from Ref. [41]. Copyright 2021, American Chemical Society.

1.4 Enhanced ECL from AIE and CIE

In 2011, Tang *et al.* introduced the concept of aggregation induced emission (AIE), where they observed the unprecedented enhancement of emission upon molecular aggregation in siloles. The intramolecular rotation of phenyl 'rotors' in hexaphenylsilole (HPS) serves to quench the excited state via non-radiative decay. Suppression of this effect via restriction of intramolecular rotation (RIR) therefore enhances the emission of the aggregated state.[44, 45] The combination of AIE and ECL, termed aggregated induced electrochemiluminescence (AIECL), focuses on the smart design of ECL luminophores that can simultaneously exploit the AIE mechanism.[46] The first example of AI-ECL was introduced by Cola *et al.*, who explored the formation of supramolecular structures of Pt(II) complexes.[47] Since this work, there have been numerous advancements in this field of research. Crystallization-induced emission (CIE) is based upon the same principle as AIE – the restriction of intramolecular rotation to block the non-radiative emission pathways – by means of lattice formation.[48] CIE luminophores demonstrate enhanced

emission from crystallization, but not amorphization.[49] In CIE, the molecular structure, conformation, and morphological packing all play an important role in enhancing the emission. Solvent fuming, which is a technique to induce crystallization in chromophores, can be used as a reversible method to attain crystallization-induced electrochemiluminescence (CI-ECL). Significant enhancement to the ECL efficiency is possible with CIE luminophores.

1.4.1 Aggregation-induced electrochemiluminescence (AI-ECL)

Ye *et al.* designed a cyclometalated iridium(III) complex for AIECL.[50] AIE behavior was confirmed with increasing H_2O content during the ECL acquisition, as demonstrated in **Figure 1.8**. This iridium(III) complex showed strong PL emission at 643 nm, which closely matched its ECL emission at 640 nm in dimethylsulfoxide (DMSO)/water using TPrA as the co-reactant. The authors were able to demonstrate a 39-fold enhancement in the ECL efficiency compared to the monomolecular state, and 4-fold enhancement vs. the $[Ru(bpy)_3]^{2+}$ reference. In a related work, Wei *et al.* encapsulated *fac*-$Ir(ppy)_3$ in apoferritin (apoFt), creating a $Ir(ppy)_3$@apoFt bioconjugate. Through pH-controlled reversible dissociation of apoFt subunits[51, 52] and analysis using optical emission spectroscopy, the authors were able to confine, on average, 44.3 molecules of *fac*-$Ir(ppy)_3$ into the cavity of the protein core, effectively restricting intramolecular movement to produce AIECL.[53] Using TPrA as a co-reactant, the authors demonstrated enhanced PL (565 nm), ECL (531 nm), and electrochemical activity of the aggregates compared to the monomers. The ECL emission was blue-shifted compared to the PL, possibly due to the RIR effect afforded by AIE, wherein the blocking of non-radiative energy loss promotes a higher energy emission wavelength. This effect may be related to the crystallization-induced blue-shift (CIBS) observed by Tang and co-workers.[49, 54] They were also able to use $Ir(ppy)_3$@apoFt to construct an immunosensor for CYFRA-21 (a cancer cell biomarker) detection, attaining a wide linear response range and a low detection limit.

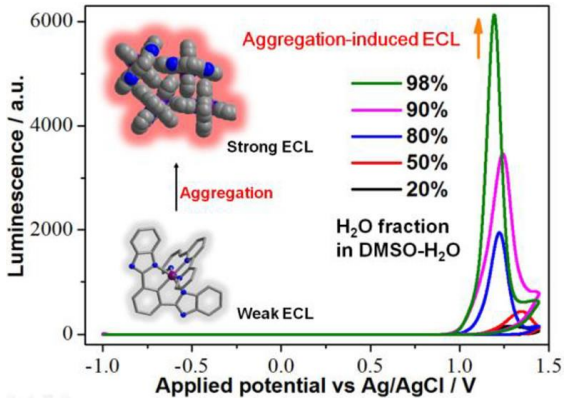

Figure 1.8. ECL intensity variation as the H_2O fraction of a DMSO-H_2O solvent mixture is increased. Reproduced with permission from Ref. [50]. Copyright 2018, American Chemical Society.

Xu *et al.* studied the AIECL properties of carboranyl carbazoles (**Figure 1.9A**).[30] These metal-free "organic dots" were weakly emissive until the water fraction reached over 85%, at which point their emission intensity dramatically increased (**Figure 1.9B**). Their model compound **T-3** exhibited slightly red-shifted ECL emission (582 nm) compared with their PL emission (547 nm), which the authors have attributed to surface-state transitions, which are commonly accessed in ECL pathways. The morphology and the size of the carboranyl carbazole aggregates were also found to have a significant influence on the AIE and ECL character of this luminophore. **T-3** displayed a 20-fold enhancement in the ELC performance when compared to the reference compound without AIE behaviour.

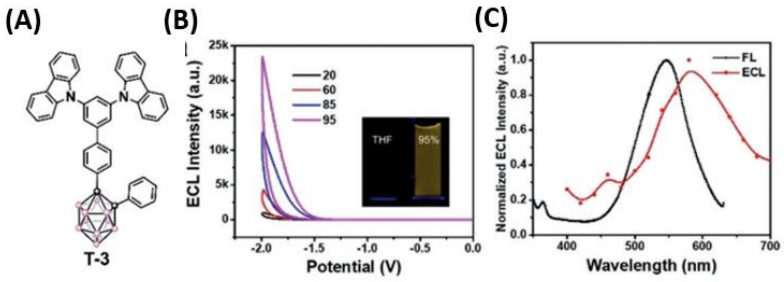

Figure 1.9. (A) Molecular structure of carboranyl carbazole AI-ECL luminophore. (B) ECL intensity of 1.0 mM T-3 in increasing H_2O fractions. (C) PL spectrum (black) of T-3

in 95% H_2O and ECL spectrum (red) of T-3 modified GCE in 95% H_2O. Reproduced with permission from Ref. [30]. Copyright 2019, Wiley-VCH.

An example of aggregation induced delayed fluorescence electrochemiluminescence (AIDF-ECL) was reported by the Niu group; this system can be considered a combination of the enhancement effects from aggregation induced emission and thermally activated delayed fluorescence. They tested **mCP-BP-PXZ**, which was an AIDF luminophore, and compared it to **TPE-TAPBI**, a reference AIECL luminophore. **mCP-BP-PXZ** displayed 5.4-fold stronger ECL when tested in thin-film modified GCE in the presence of TPrA as co-reactant versus the **TPE-TAPBI** reference, which the authors explain by means of effective utilization of triplet excitons generated by electrochemical excitation. Also, the ECL spectrum (596 nm) was red-shifted 53 nm vs. the PL spectrum (543 nm); this may be due to the involvement of surface state transitions which are commonly observed in semiconductor type ECL emitters.

1.4.2 Crystallization-induced electrochemiluminescence (CI-ECL)

This effect in ECL was first documented by the Wang, Ding and co-workers who studied a di-boron complex (DBC).[55] Using PL and X-ray diffraction techniques, they were able to unambiguously observe crystallization induced blue-shifted (CIBS) emission as well as enhanced PL emission in the crystalline state (**Figure 1.10**). A strong increase in the ECL activity was also recorded, particularly in the BPO co-reactant pathway, when using glassy carbon electrodes modified with DBC (5-fold enhancement in the crystalline film versus the solution phase). Finally, through the use of spooling ECL spectroscopy,[56] it was discovered that ECL reactions can occur at different locations following annihilation and co-reactant pathways, where in the DBC/BPO system the ECL reactions are confined predominantly at the solid-solution interface.

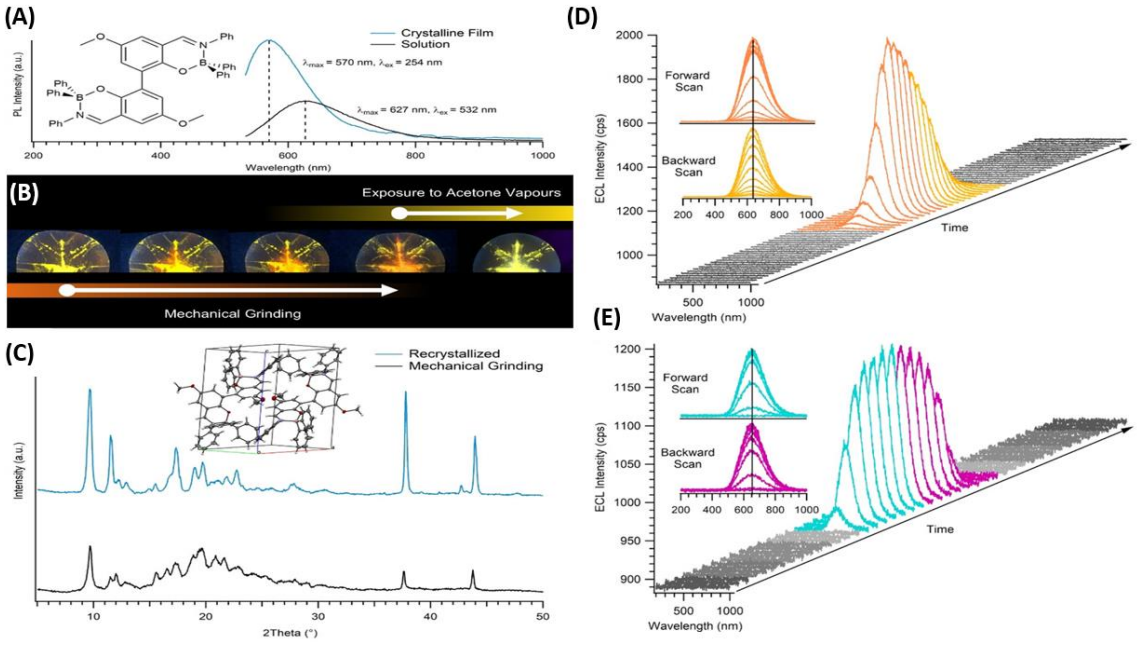

Figure 1.10. (A) PL spectra of crystalline DBC film (blue) and in acetonitrile (black). (B) Images of recrystallized DBC, DBC after mechanical grinding, and DBC after exposure to acetone vapours (left to right). (C) XRD spectra of recrystallized DBC (blue) and upon grinding (black). DBC unit cell in inset. Spooling ECL spectra of (D) solid state ECL/BPO co-reactant system and (E) homogeneous DBC/BPO system. Reproduced with permission from Ref. [57]. Copyright 2020, Wiley-VCH.

More recently, Zhu and co-workers created a $[Ru(bpy)_3]^{2+}$ derivative **Ru-TPE**, incorporating the AIE-active tetraphenylethene (TPE) group.[58] The resulting compound exhibited strong CIECL driven by the TPE group that overcame the inherent ACQ nature of $[Ru(bpy)_3]^{2+}$. The authors observed an increased crystallinity of the **Ru-TPE** crystals compared to plain crystals of $[Ru(bpy)_3]^{2+}$, confirmed by pXRD measurements. By using an ITO/Ru-TPE modified electrode, where the ECL emission originated from a solid-state film, an impressive ECL efficiency of 236% vs. the $[Ru(bpy)_3^{2+}]$/TPrA reference system (in the solution state) was recorded. **Ru-TPE** showed an ECL at 631 nm, red-shifted by 30 nm from its PL emission (601 nm), which suggests that the emissive excited state of **Ru-TPE** may originate from surface-state transitions.

1.5 Conclusions and outlook

Enhanced electrochemiluminescence continues to be one of the perpetual targets for researchers as evidenced by the rapid growth in ECL applications and technologies. The landscape of ECLphores and strategies to promote ECL have rapidly expanded in recent years. In this minireview we summarize, for the first time, the advances in materials that have resulted in greatly enhanced electrochemiluminescence efficiencies. In particular, TADF materials have ushered in a new era of high-performance ECL luminophores. Several challenges in ECL research in those involving TADF luminophores, include improving the ECL efficiency up to the level of photoluminescent pathways utilizing similar compounds. It is possible that the more complex mechanisms of ECL, particularly the co-reactant pathways, suffer from increased likelihood of non-radiative decay, reducing the overall luminous efficiency. In a related avenue, there is an urgent need to elucidate the mechanistic pathways of TADF ECL molecules, as they will be fundamental in understanding and improving their efficiencies. Finally, using a standardized method to report the absolute ECL efficiency will be an enormous improvement when assessing the performance of new ECL luminophores. It is evident that there is still much chemical space and opportunity to explore to produce materials with enhanced ECL and also that the future is bright for the design of smart ECL materials.

1.6 References

[1] Richter, M. M. *Chem. Rev.* **2004,** *104*, 3003-36.

[2] Hesari, M.; Ding, Z. *J. Electrochem. Soc.* **2016,** *163*, H3116-H3131.

[3] Miao, W.; Bard, A. J. *Anal. Chem.* **2004,** *76*, 7109-7113.

[4] Egashira, N.; Morita, S.-i.; Hifumi, E.; Mitoma, Y.; Uda, T. *Anal. Chem.* **2008,** *80*, 4020-4025.

[5] Tian, D.; Duan, C.; Wang, W.; Li, N.; Zhang, H.; Cui, H.; Lu, Y. *Talanta* **2009,** *78*, 399-404.

[6] Bard, A. J.; Fan, F.-R. F. *Acc. Chem. Res.* **1996,** *29*, 572-578.

[7] Dong, J.; Lu, Y.; Xu, Y.; Chen, F.; Yang, J.; Chen, Y.; Feng, J. *Nature* **2021,** *596*, 244-249.

[8] Lu, Y.; Huang, X.; Wang, S.; Li, B.; Liu, B. *ACS Nano* **2023,** *17*, 3809-3817.

[9] Chu, K.; Adsetts, J. R.; Moore, C.; Ding, Z. *ACS Appl. Electron. Mater.* **2020,** *2*, 3825-3830.

[10] Adsetts, J. R.; Zhang, R.; Yang, L.; Chu, K.; Wong, J. M.; Love, D. A.; Ding, Z. *Front. Chem.* **2020,** *8*, 580022.

[11] Valenti, G.; Scarabino, S.; Goudeau, B.; Lesch, A.; Jović, M.; Villani, E.; Sentic, M.; Rapino, S.; Arbault, S.; Paolucci, F.; Sojic, N. *J. Am. Chem. Soc.* **2017,** *139*, 16830-16837.

[12] Zhang, H.; Liu, Y.; Yao, M.; Han, W.; Zhang, S. *Anal. Chem.* **2023,** *95*, 570-574.

[13] Huang, X.; Li, B.; Lu, Y.; Liu, Y.; Wang, S.; Sojic, N.; Jiang, D.; Liu, B. *Angew. Chem. Int. Ed.* **2023,** *62*, e202215078.

[14] Miao, W. *Chem. Rev.* **2008,** *108*, 2506-53.

[15] Li, L.; Chen, Y.; Zhu, J.-J. *Anal. Chem.* **2017,** *89*, 358-371.

[16] Li, W.; Li, Z.; Si, C.; Wong, M. Y.; Jinnai, K.; Gupta, A. K.; Kabe, R.; Adachi, C.; Huang, W.; Zysman-Colman, E.; Samuel, I. D. W. *Adv. Mater.* **2020,** *32*, 2003911.

[17] Jinnai, K.; Nishimura, N.; Adachi, C.; Kabe, R. *Nanoscale* **2021,** *13*, 8412-8417.

[18] Kumar, S.; Tourneur, P.; Adsetts, J. R.; Wong, M. Y.; Rajamalli, P.; Chen, D.; Lazzaroni, R.; Viville, P.; Cordes, D. B.; Slawin, A.; Olivier, Y.; Cornil, J.; Ding, Z.; Zysman-Colman, E. *J. Mater. Chem. C* **2022,** *10*, 4646-4667.

[19] Adsetts, J. R.; Chu, K.; Hesari, M.; Ma, J.; Ding, Z. *Anal. Chem.* **2021,** *93*, 11626-11633.

[20] Chu, K.; Adsetts, J. R.; Ma, J.; Zhang, C.; Hesari, M.; Yang, L.; Ding, Z. *J. Phys. Chem. C* **2021,** *125*, 22274-22282.

[21] Adsetts, J. R.; Chu, K.; Hesari, M.; Whitworth, Z.; Qin, X.; Zhan, Z.; Ding, Z. *J. Phys. Chem. C* **2022,** *126*, 20155-20162.

[22] Wong, M. Y.; Zysman-Colman, E. *Adv. Mater.* **2017,** *29*, 1605444.

[23] Nakanotani, H.; Tsuchiya, Y.; Adachi, C. *Chem. Lett.* **2021,** *50*, 938-948.

[24] Ishimatsu, R.; Matsunami, S.; Kasahara, T.; Mizuno, J.; Edura, T.; Adachi, C.; Nakano, K.; Imato, T. *Angew. Chem. Int. Ed.* **2014,** *53*, 6993-6996.

[25] Kumar, S.; Tourneur, P.; Adsetts, J. R.; Wong, M. Y.; Rajamalli, P.; Chen, D.; Lazzaroni, R.; Viville, P.; Cordes, D. B.; Slawin, A. M. Z.; Olivier, Y.; Cornil, J.; Ding, Z.; Zysman-Colman, E. *J. Mater. Chem. C* **2022,** *10*, 4646-4667.

[26] Chu, K.; Adsetts, J. R.; Whitworth, Z.; Kumar, S.; Zysman-Colman, E.; Ding, Z. *Langmuir* **2023,** *39*, 2829-2837.

[27] Huang, P.; Zhang, B.; Hu, Q.; Zhao, B.; Zhu, Y.; Zhang, Y.; Kong, Y.; Zeng, Z.; Bao, Y.; Wang, W.; Cheng, Y.; Niu, L. *ChemPhysChem* **2021,** *22*, 726-732.

[28] Huang, P.; Zou, X.; Xu, Z.; Lan, Y.; Chen, L.; Zhang, B.; Niu, L. *Molecules*, **2022**, *27*, 7457.

[29] Zeng, Z.; Huang, P.; Kong, Y.; Tong, L.; Zhang, B.; Luo, Y.; Chen, L.; Zhang, Y.; Han, D.; Niu, L. *Chem. Commun.* **2021,** *57*, 5262-5265.

[30] Wei, X.; Zhu, M.-J.; Cheng, Z.; Lee, M.; Yan, H.; Lu, C.; Xu, J.-J. *Angew. Chem. Int. Ed.* **2019,** *58*, 3162-3166.

[31] Luo, Y.; Zhao, B.; Zhang, B.; Lan, Y.; Chen, L.; Zhang, Y.; Bao, Y.; Niu, L. *Analyst* **2022,** *147*, 2442-2451.

[32] Wang, C.; Wu, J.; Huang, H.; Xu, Q.; Ju, H. *Anal. Chem.* **2022,** *94*, 15695-15702.

[33] Hatakeyama, T.; Shiren, K.; Nakajima, K.; Nomura, S.; Nakatsuka, S.; Kinoshita, K.; Ni, J.; Ono, Y.; Ikuta, T. *Adv. Mater.* **2016,** *28*, 2777-2781.

[34] Madayanad Suresh, S.; Hall, D.; Beljonne, D.; Olivier, Y.; Zysman-Colman, E. *Adv. Funct. Mater.* **2020,** *30*, 1908677.

[35] Hall, D.; Suresh, S. M.; dos Santos, P. L.; Duda, E.; Bagnich, S.; Pershin, A.; Rajamalli, P.; Cordes, D. B.; Slawin, A. M. Z.; Beljonne, D.; Köhler, A.; Samuel, I. D. W.; Olivier, Y.; Zysman-Colman, E. *Adv. Opt. Mater.* **2020,** *8*, 1901627.

[36] Yang, L.; Dong, L.; Hall, D.; Hesari, M.; Olivier, Y.; Zysman-Colman, E.; Ding, Z. *SmartMat* **2023,** *4*, e1149.

[37] Zhou, H.; Ye, Q.; Wu, X.; Song, J.; Cho, C. M.; Zong, Y.; Tang, B. Z.; Hor, T. S. A.; Yeow, E. K. L.; Xu, J. *J. Mater. Chem. C* **2015,** *3*, 11874-11880.

[38] Simard, M.; Su, D.; Wuest, J. D. *J. Am. Chem. Soc.* **1991,** *113*, 4696-4698.

[39] Yang, L.; Zhang, R.; Balónová, B.; True, A. E.; Chu, K.; Adsetts, J. R.; Zhang, C.; Qin, X.; Zysman-Colman, E.; Blight, B. A.; Ding, Z. *J. Electroanal. Chem.* **2022,** *920*, 116594.

[40] Liu, X.; Li, L.; Luo, L.; Bi, X.; Yan, H.; Li, X.; You, T. *J. Colloid Interface Sci.* **2021,** *586*, 103-109.

[41] Zhang, N.; Wang, X.-T.; Xiong, Z.; Huang, L.-Y.; Jin, Y.; Wang, A.-J.; Yuan, P.-X.; He, Y.-B.; Feng, J.-J. *Anal. Chem.* **2021,** *93*, 17110-17118.

[42] Hou, H.; Wang, Y.; Wang, Y.; Luo, R.; Zhu, D.; Zhou, J.; Wu, X.; Ju, H.; Lei, J. *J. Mater. Chem. C* **2022,** *10*, 14488-14495.

[43] Xie, L. S.; Skorupskii, G.; Dincă, M. *Chem. Rev.* **2020,** *120*, 8536-8580.

[44] Hong, Y.; Lam, J. W. Y.; Tang, B. Z. *Chem. Commun.* **2009**, 4332-4353.

[45] Hong, Y.; Lam, J. W.; Tang, B. Z. *Chem. Soc. Rev.* **2011,** *40*, 5361-88.

[46] Wei, X.; Zhu, M. J.; Yan, H.; Lu, C.; Xu, J. J. *Chem. Eur. J.* **2019,** *25*, 12671-12683.

[47] Carrara, S.; Aliprandi, A.; Hogan, C. F.; De Cola, L. *J. Am. Chem. Soc.* **2017,** *139*, 14605-14610.

[48] Qian, L.; Tong, B.; Shen, J.; Shi, J.; Zhi, J.; Dong, Y.; Yang, F.; Dong, Y.; Lam, J. W. Y.; Liu, Y.; Tang, B. Z. *J. Phys. Chem. B* **2009,** *113*, 9098-9103.

[49] Dong, Y.; Lam, J. W. Y.; Qin, A.; Li, Z.; Sun, J.; Sung, H. H. Y.; Williams, I. D.; Tang, B. Z. *Chem. Commun.* **2007**, 40-42.

[50] Gao, T.-B.; Zhang, J.-J.; Yan, R.-Q.; Cao, D.-K.; Jiang, D.; Ye, D. *Inorg. Chem.* **2018,** *57*, 4310-4316.

[51] Jutz, G.; van Rijn, P.; Santos Miranda, B.; Böker, A. *Chem. Rev.* **2015,** *115*, 1653-1701.

[52] Yang, L.; Fan, D.; Zhang, Y.; Ding, C.; Wu, D.; Wei, Q.; Ju, H. *Anal. Chem.* **2019,** *91*, 7145-7152.

[53] Yang, L.; Sun, X.; Wei, D.; Ju, H.; Du, Y.; Ma, H.; Wei, Q. *Anal. Chem.* **2021,** *93*, 1553-1560.

[54] Gong, Y.; Zhao, L.; Peng, Q.; Fan, D.; Yuan, W. Z.; Zhang, Y.; Tang, B. Z. *Chem. Sci.* **2015,** *6*, 4438-4444.

[55] Wong, J. M.; Zhang, R.; Xie, P.; Yang, L.; Zhang, M.; Zhou, R.; Wang, R.; Shen, Y.; Yang, B.; Wang, H.-B.; Ding, Z. *Angew. Chem. Int. Ed.* **2020,** *59*, 17461-17466.

[56] Hesari, M.; Ding, Z. *Nat. Protoc.* **2021,** *16*, 2109-2130.

[57] Wong, J. M.; Zhang, R.; Xie, P.; Yang, L.; Zhang, M.; Zhou, R.; Wang, R.; Shen, Y.; Yang, B.; Wang, H. *Angew. Chem., Int. Ed.* **2020,** *59*, 17461.

[58] Han, T.; Cao, Y.; Wang, J.; Jiao, J.; Song, Y.; Wang, L.; Ma, C.; Chen, H. Y.; Zhu, J. J. *Adv. Funct. Mater.* **2023,** *33*, 2212394.

1.7 Scope of Thesis

This thesis work explores the frontiers of electrochemiluminescence, chemiluminescence, and electroluminescence luminophores for light-emitting applications. The electrochemical and spectroscopic characterization of various luminophores are performed, and optimizations toward maximizing their luminous efficiency are carried out. The goal of this thesis is to successfully design and fabricate a light-emitting electrochemical cell using carbon quantum dots (CQDs).

Chapter 1 describes TADF complexes, hydrogen-bonding compounds, and aggregation- and crystallization-induced emission compounds. This chapter also provides an overview of the various light-emitting pathways discussed in this work, namely electrochemiluminescence, chemiluminescence, and electroluminescence.

Chapter 2 serves as an introduction to summarize the synthesis, unique properties, and applications of carbon quantum dots.

In Chapter 3, the development of a methodology to properly evaluate the absolute electrochemiluminescence efficiency was performed. At first inception, the instrumentation involved a photomultiplier tube operating in photon-counting head mode. Later, this was further developed to use a spectrograph/CCD camera to increase the analytical applicability (Chapter 4)

In Chapters 5 and 6, we study the ECL mechanisms of novel materials. Chapter 5 discusses the photochemistry, electrochemistry, and electrochemiluminescence properties of bimetallic Pt-Ag nanoclusters. Chapter 6 studies the electrochemiluminescence and chemiluminescence of a TADF emitter TPA-ace-TRZ. In Chapter 7, we use COMSOL simulations to model the $Ru(bpy)_3^{2+}$ ECL annihilation system to estimate the bimolecular annihilation rate constant.

In Chapter 8, we explore the use of carbon quantum dots in light-emitting electrochemical cells (LECs). The PL, ECL, and electrochemical properties of CQDs are

also discussed. In Chapter 9, the use of a zinc oxide interlayer in LECs is investigated to further improve the performance, efficiency, and stability of these light-emitting devices.

Finally. Chapter 10 provides conclusions and perspectives for possible future directions.

Chapter 2

In Chapter 2, we introduce carbon quantum dots (CQDs), their properties, and their applications for optoelectronic and light emitting devices. We also discuss top-down and bottom-up synthesis strategies, different emissive pathways and mechanisms for CQDs, as well as an outlook and future perspective for this promising nanomaterial.

2 Preparation, properties, and applications of highly luminescent carbon quantum dots from biomaterials: a review†

In recent years, carbon quantum dots (CQDs) have shown great potential for biomedical and analytical applications due to their easily tunable luminescence, low cost, and good biocompatibility. CQDs can be synthesized using a multitude of precursors and procedures, but their synthesis using highly abundant and very low cost biomaterials represents a promising and prospective area of research. In this review, we summarize the latest research on the synthesis, properties, and applications of "green" CQDs from biomaterials. We also discuss some current challenges to the successful adoption of CQDs to light-emitting applications.

2.1 Introduction

Carbon quantum dots (CQDs) are classified as a type of zero-dimension carbon-based nanomaterials, typically less than 10 nm in diameter and having a defined crystal lattice parameter of 0.34 nm matching that of the 002 interlayer spacing of graphite.[1] CQDs display highly desirable optical characteristics, such as tunable photoluminescence (PL) due to their pronounced quantum confinement effect (QCE)[2], good photostability[3], and high biocompatibility.[4] In addition, the presence of surface functional groups can impart excellent hydrophilicity and opportunities for surface functionalization. Compared to semiconductor quantum dots which might contain heavy metals with toxic effects even at low levels and could be challenging to dispose properly – CQDs can be considered

† This work is in preparation to be submitted.

relatively non-toxic. Finally, owing to their low cost and ease of synthesis, CQDs have rapidly gained much research attention in the last few years as a promising material for many optoelectronic applications.

CQDs were first isolated in 2004 during the purification of single-walled carbon nanotubes produced from arc discharge soot.[5] Since then, a great variety of synthesis procedures to produce CQDs have become available, which may be further subdivided into top-down or bottom-up categories depending on the starting material and how it is further processed. In general, the chemical components of the precursors used in the synthesis will end up in the final product. This means that careful selection of the starting material is a crucial step in CQD fabrication. As an aside, this process also allows opportunities to introduce new heteroatoms into the CQD structure to improve or impart new properties, a process known as doping. Synthesis using biomaterials (here loosely defined as any material derived from a biological source, and may include amino acids, sugars, foods, and other compounds involved in human metabolism) could represent a relatively unexplored area of significant cost-savings; many of these precursors are considered waste or by-products of other processes, and their recycling into CQDs that can still be useful for other applications could be greatly beneficial to reduce chemical and food waste.

In this review, we will assess latest developments on the synthesis strategies, photophysical and chemical properties, and applications of CQDs produced from biomaterials. We place particular emphasis on properties pertinent to electrochemiluminescence and chemiluminescence emission pathways, and their associated light-emitting applications. We also discuss some challenges and barriers

towards the continual evolution of CQDs, and what should be done to realize the full potential of this nanomaterial for future applications.

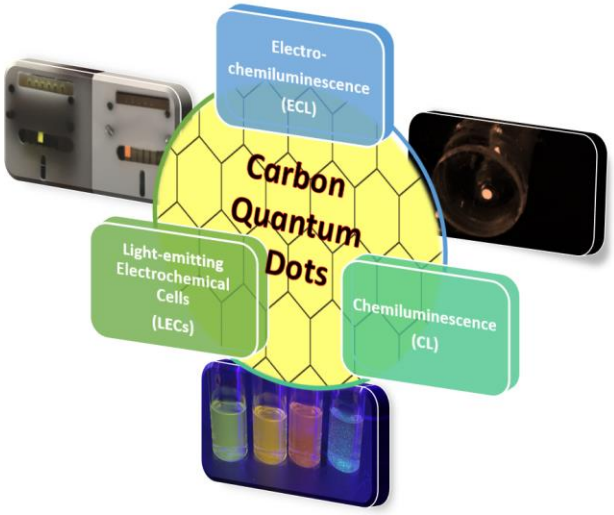

Figure 2.1. Carbon quantum dots (CQDs) and their light-emitting applications.

2.2 Synthesis of CQDs

CQD synthesis may be classified into two categories: *top-down* and *bottom-up*. Top-down strategies involve the breaking down of large carbon-containing structures, while bottom-up approaches build up CQDs using small molecular precursors. Cost is one of the major advantages of CQDs over semiconductor quantum dots; many research groups are quickly adopting cost-effective procedures to remain competitive. *Doping* of CQDs (the introduction of new heteroatoms into the CQD structure) is an alternative strategy to enhance the emission quantum yield or change the emission wavelength. Doping is typically accomplished at the synthesis stage by integrating heteroatom-containing precursors.

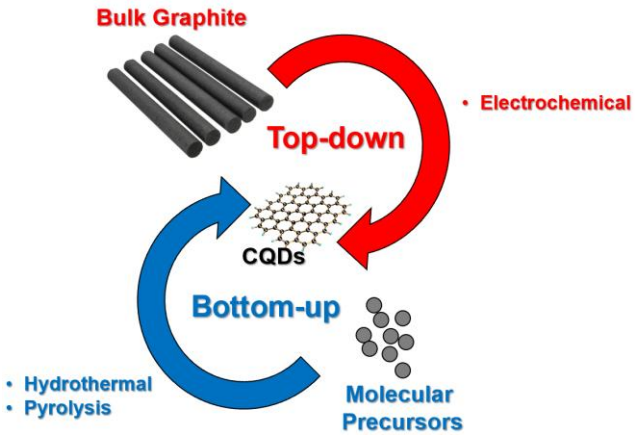

Figure 2.2. Top-down vs. bottom-up synthesis strategies for preparing CQDs.

2.2.1 Top-down strategies

Top-down synthesis strategies involve breaking down bulk carbon materials by physical or chemical procedures. In general, top-down strategies are characterized by high synthetic yield while using very low-cost bulk materials (usually graphite or other bulk carbonaceous material); this process is summarized in **Figure 2.2**. The Ding research group pioneered the electrochemical preparation of luminescent nanocrystals – later discovered to be CQDs – from multi-walled carbon nanotubes (MWCNTs) by repeated potential cycling between -2.0 and 2.0 V in a degassed solution of acetonitrile.[6] This procedure was later developed further when nitrogen-doped CQDs could be synthesized by the electrochemical intercalation/exfoliation method of graphite rods.[7] In this work, the top-down synthesis of CQDs was performed with a galvanostatic method, allowing precise control of the final product size with high efficiency.[8] The current density was optimized to 40 mA/cm, with the CQDs showed bright blue PL at 450 nm and a PLQY of 4-5%. These CQDs were also used for the first time to construct light-emitting electrochemical cells, with the devices exhibiting a broad emission at 610 nm. CQDs can also be prepared through other liquid-phase exfoliation methods such as ultrasonication[9] or chemical exfoliation using strong acid.[10] Other techniques that have been studied for breaking down bulk graphite into smaller pieces include direct laser ablation[11, 12] and magnetron sputtering.[13]

2.2.2 Bottom-up strategies

In contrast, bottom-up synthesis strategies involve reacting smaller molecular precursors with pressure and heat (**Figure 2.2**); it is proposed that the stepwise dehydration, polymerization, carbonization, and finally passivation of the reagents is responsible for the formation of the CQD structure.[14] Using this approach, researchers can more precisely control the size and morphology of the CQD product. In addition, bottom-up techniques are highly scalable. Bottom-up procedures include hydrothermal, solvothermal, microwave-assisted synthesis, and pyrolysis; these various techniques are summarized in **Table 2.1**.

For example, the Ding research group used the hydrothermal method at 200°C with cysteine and tryptophan to synthesize nitrogen and sulfur doped CQDs (NS-CQDs), achieving a high PLQY of 73%. In addition, the ECL efficiency of these CQDs when utilized in a modified GCE was determined to be 24% in the $K_2S_2O_8$ system relative to $Ru(bpy)_3^{2+}$.[15] Under the pyrolysis procedure, the same research group was able to synthesize N,S-codoped CQDs using citric acid and L-cysteine. These CQDs showed a maximum of 32% ECL quantum efficiency vs. $Ru(bpy)_3^{2+}$ in the $K_2S_2O_8$ coreactant system.[16] Using the same precursors but under the microwave-assisted hydrothermal method (700 W power) Yu *et al.* produced amino carbon dots (ACDs) that demonstrated bright blue emission at 447 nm with a high PLQY of 53.4%.[17] Thermal calcination involves the high temperature treatment of carbonaceous material. Bhasin *et al*. used this method to process agarose waste, composed of mainly polysaccharides, at 450°C for 4 hours to yield CQDs (λ_{em}=450 nm) with a high PLQY of 62%.[18]

Table 2.1. Summary of bottom-up synthesis strategies for CQDs.

Technique	Precursors	Temp.	PLQY (%)	Ref.
Hydrothermal	Citric acid, urea	160°C	88%	[19]
	Green pomelo peel	180°C	17%	[20]
	Chitin	150°C	9%	[21]
	Citric acid, ethylenediamine	250°C	73%	[22]
	Lactic acid, ethylenediamine	150°C	46%	[23]
	Folic acid, glycerol	160°C	25%	[24]
	L-glutamic acid	230°C	41%	[25]
	Citrus peel	180°C	2%	[26]

Pyrolysis	Phosphonic acid, sodium citrate	200°C	18%	[27]
	Cysteine, tryptophan	200°C	73%	[15]
	Banyan fig tree latex (*Ficus benghalensis*)	185°C	41%	[28]
	Glucose, L-tryptophan, glycine	200°C	24%	[29]
	Citric acid, urea, L-cysteine	180°C	22%	[30]
	Acriflavin	180°C	31%	[31]
	Lignin	180°C	11%	[32]
	2% milk	200°C	8%	[33]
	Dried lemon peel	200°C	11%	[34]
	Orange peel, gingko leaves, magnolia flower	200°C	8%	[35]
	Citric acid, urea	160°C	34%	[36]
	1,5-diaminonaphthalene, cysteine	150°C	13%	[37]
	Collagen	350°C	7%	[38]
	Histidine	300°C	14%	[39]
	Citric acid, L-cysteine	240°C	84-fold vs. $Ru(bpy)_3^{2+}$	[16]
Microwave synthesis	Malic acid, urea		10%	[40]
	Citric acid, L-cysteine		53%	[17]
	Maleic acid, arginine		12%	[41]
	Glycine, histidine, leucine		17%	[42]
	Chitosan		12%	[43]
Thermal calcination	Taurine	350°C	7%	[44]
	Coconut husk	300°C	40%	[45]
	Agar waste	450°C	62%	[18]
	Atlantic salmon (*Salmo salar L.*)	200°C	12%	[46]

2.2.3 Purification and functionalization of CQDs

Purification of CQDs is an important step, as it allows the removal of by-products and unreacted precursor material. This procedure has increased significance for synthesis techniques utilizing bioresources and biomaterials, as these ingredients will often contain non-carbonaceous matter. Dialysis is the process whereby solvated molecules can be separated through a semipermeable membrane by the basis of their molecular size. By selecting an appropriate molecular weight cut-off (MWCO), smaller unreacted particles can be purified out.[47] Due to the ease of the dialysis procedure, it is implemented in nearly every CQD synthesis procedure, allowing researchers to quickly and easily purify their CQD products prior to characterization. Chromatography (thin layer, silica packed

column, liquid chromatography) is a more advanced method of CQD purification, albeit more labour- and cost-intensive. For example, Yuan et al. utilized silica column chromatography to precisely isolate different CQDs from a solvothermal process.[48] The separated CQDs had very high purity and performance, demonstrating a colour-purity (FWHM=30-39 nm) for light-emitting applications. Other groups have also used column chromatography to separate and purify CQDs, resulting in products with narrow size distributions and high QYs.[49-52]

2.3 Properties and applications of CQDs

2.3.1 Structure and properties of CQDs

CQDs often adopt a quasi-spherical structure with diameters between 10 – 20 nm.[53] CQDs usually possess amorphous carbon cores; on the other hand, graphene quantum dots (GQDs) have a graphitic structure (primarily sp^2 carbons) composed of up to 10 layers of graphene.[54] Due to the quantum confinement effect (QCE), the electronic and optical properties of CQDs can be finely tuned based on their sizes.[55, 56] Typically, the in-plane lattice spacing between individual graphene sheets is from 0.18 – 0.24 nm.[57] High resolution transmission electron microscopy (HR-TEM) is a widely used technique in confirming the morphology of CQDs (**Figure 2.3C**). Other techniques, such as infrared spectroscopy or x-ray photoelectron spectroscopy (XPS) may be useful in determining the nature and atomic ratios of CQDs.

In addition, the presence of oxygen-containing surface functional groups impart superb water solubility to CQDs, improving their suitability for many applications. These functional groups also allow the possibility of *surface passivation* (the treatment of CQDs using polymers and other organic molecules to stabilize and enhance fluorescence emission) and further *surface functionalization* (the introduction of new functional groups to modify the CQD properties).[58, 59] Surface functionalization of CQDs is an effective strategy to tune the properties to target specific applications. Many different approaches exist, such as covalent bonding[60], coordination[61], and π-π interactions.[62] These surface modifications can introduce different functional groups, and lead to wide variations in the fluorescence properties. Sometimes, surface passivation and functionalization can be

accomplished in the same step, greatly simplifying the post-treatment step; for example, Huang et al. employed diamine-terminated poly(ethylene glycol) to simultaneously improve the hydrophilicity and the quantum yield of their C-dots.[63]

The doping of the CQD structure with new heteroatoms can also significantly enhance the fluorescence properties.[64] Typically, atoms such as nitrogen, phosphorous, boron, and sulphur have the greatest compatibility with the carbon core of CQDs, and many researchers have had success incorporating them into the synthesis recipes. Doped CQDs exhibit significantly altered electronic properties, and their novel chemical structures can even access new excited energy potentials, leading to improved luminescence yields.[64]

2.3.2 Luminescence mechanisms

While the optical properties of many CQDs have been extensively studied, the actual mechanisms of their luminescence is still a highly debated topic. Because their synthesis is largely an imprecise science, often samples of CQDs display great heterogeneity even from a single synthetic batch. Nevertheless, two predominant models have been proposed: the former suggests luminescence originates from bandgap transitions in conjugated π-domains, while the latter is associated with surface-related defect states.

2.3.3 Core bandgap transitions of conjugated π-domains

The first source of luminescence in CQDs arises from bandgap transitions between conjugated π domains in the carbon core. A well-known feature of CQDs is their quantum confinement effect (QCE), which occurs when the quantum dot diameter is smaller than their *exciton Bohr radius*.[65] The π and π* electronic levels of aromatic sp^2 domains in the carbon core can therefore be strongly confined, and radiative recombination of electron-hole pairs (excitons) in these clusters can lead to luminescence.[66, 67] Kang et al. used theoretical calculations to correlate the relationship between the HOMO-LUMO gap and the size of the carbon fragments, proving that the luminescence of the CQDs originated from the quantum-sized graphite structure (**Figure 2.3**).[49] These luminescent characteristics are particularly evident in CQDs with high core crystallinity and relatively pristine surfaces.

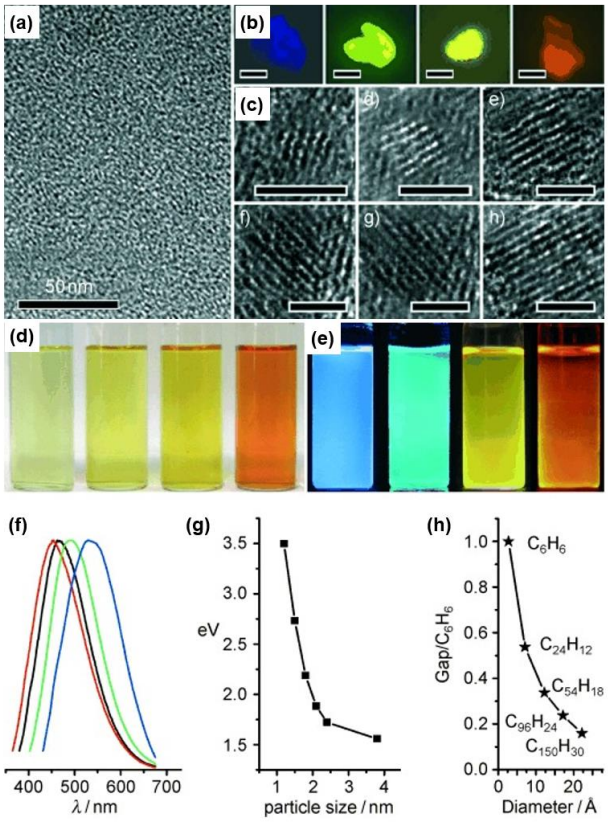

Figure 2.3. (A) TEM images of CQDs. (B) Fluorescent microscopy images of CQDs. (C) High resolution-TEM images of CQDs. Optical images of different size CQDs under (D) daylight and (E) ultraviolet light. (F) Photoluminescence spectra of different size CQDs. The relationship between CQD size and (G) the bandgap energy, and (H) the HOMO-LUMO energy gap.[49]

2.3.4 Surface state defects

The second source of luminescence comes from the surface states, specifically surface sites with imperfect sp^2 domains, which create *surface energy traps*.[1] These are thought to capture, and re-emit the excitons originating from the absorption of photons by the π-conjugated electrons in the sp^2 region (i.e. the CQD core). CQDs typically demonstrate high optical absorption in the UV-region, with a broad peak at 230 nm is attributed to the π- π* transition of C=C bonds, while the peak at 300 nm is attributed to the n- π* transition of C=O containing groups.[68, 69] Surface defect states generally come from functional groups present on the surface of CQDs either directly from the synthesis

process or from targeted functionalization. These sites can have varied excitation and emission properties, and can be responsible for the multi-coloured luminescence often observed in CQDs. A phenomenon known as *excitation dependent emission* occurs where the emission is tunable when excited at different wavelengths. This observation may be due to the numerous surface states present on the CQDs, as different areas are sensitive to different excitation wavelengths, leading to distinctive broad emission peaks. Surface passivation is a proven technique wherein the surface functional groups are protected and stabilized – usually by amino-terminated reagents such as polyethylene glycol – thereby enhancing their fluorescent properties.[70, 71] Passivation is therefore a method to improve the emission originating from surface states of CQDs.

2.3.5 Core vs. surface emission states

One important distinction to be made is *core emission* versus *surface emission* in CQDs (**Figure 2.4**). Depending on the excitation source used, which can vary considerably among different light-emitting applications, emission from CQDs can originate from different states. Commonly, it is accepted that photoluminescence, which uses an optical excitation source, is emitted from the core states of CQDs (therefore the first luminescence mechanism is responsible). Furthermore, it has been proposed that electrochemiluminescence and chemiluminescence utilize surface emission states, which emphasizes the importance of these surface functional groups in these particular applications.

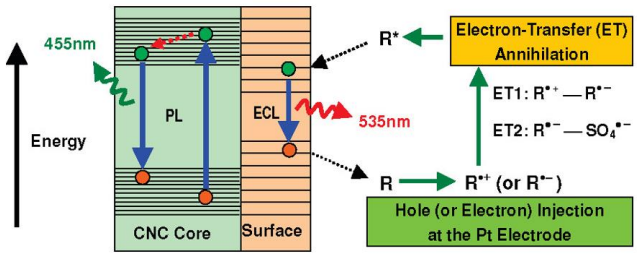

Figure 2.4. Core vs. surface emissive pathways in CQDs.

2.3.6 Enhanced luminescence from aggregation-induced emission (AIE)

A phenomenon known as aggregation caused quenching (ACQ) occurs when the luminescence of a system is drastically reduced with increasing aggregation of the luminophores. In contrast, aggregation induced emission (AIE) – the enhancement of luminescence when an aggregate is formed – occurs when the restriction of intramolecular rotation blocks non-radiative pathways.[72, 73] The solvent fraction experiment of hexaphenylsilole (HPS) demonstrates this effect well.[74] AIE can allow the smart design of 'AIEgens' – luminophores that have been specially designed to exploit the AIE process. Understanding luminescence pathways in the presence of aggregation is especially important when studying CQDs, as many of their applications involve solid-state layers and films, where the ACQ affect is most pronounced. Ding et al. showed in their study using nitrogen- and sulfur-doped carbon quantum dots that different areas of the CQD structure could contribute to different emission pathways.[75] For instance, they observed three distinct emission peaks at 425 nm, 575 nm, and 820 nm, which were attributed to intrinsic (core) emission, aggregation-induced emission, and sulfur surface-based emission, respectively; these assignments were confirmed by analyzing the emission of nitrogen-doped and undoped CQD samples.

2.4 Light-emitting applications for CQDs

2.4.1 Electrochemiluminescence

Electrochemiluminescence (ECL) is a process whereby electrogenerated species at an electrode surface interact to produce excited states that can relax to emit light.[76] As an analytical technique, ECL has many advantages including excellent signal-to-noise, and high selectivity and sensitivity.[77] In the annihilation pathway, the electron transfer reaction between the radical anion and cation produced at cathodic and anodic potentials, respectively, generates the excited state. In the coreactant pathway, the electron transfer between the radical luminophore and radical coreactant species generates the excited state. Due to the high redox power of coreactant molecules, ECL can be dramatically enhanced using coreactant routes.[78]

The electrochemistry, photochemistry, and ECL of various CQDs has been extensively studied by the Ding research group. The ECL of N-doped (Adsetts, et al.[36]) and N,S co-doped CQDs (Zhang, et al.[16]) prepared by hydrothermal synthesis was studied, where bright ECL could be observed in the presence of potassium persulfate as a coreactant. Chu et al. prepared N-doped CQDs from a top-down electrochemical intercalation procedure, where strong ECL could be detected when using benzoyl peroxide as a coreactant.[7] More recently, the ECL of NIR-emitting N- and S-doped GQDs from a solvothermal recipe was studied by Yang, et al.[37], demonstrating strong emission from the persulfate coreactant pathway; in particular, this report emphasized the importance of surface excited states in ECL light emission, hinting at strong applications in film- and solid-state ECL. These landmark studies highlight the viability of CQDs in ECL applications, especially in coreactant pathways.

2.4.2 Light-emitting electrochemical cells

Light-emitting electrochemical cells (LECs) are a class of electroluminescent devices characterized by electrochemical reactions involving mobile ions and luminophore molecules.[79] LECs have been developed in tandem with organic light-emitting diodes (OLEDs), and have many industrial advantages including low cost and complexity. In the electrochemical doping (ECD) model, the injection of electrons and holes at the negative electrode (cathode) and the positive electrode (anode), respectively, causes the redistribution of mobile ions to correct the charge imbalance.[80, 81] Successful formation of a p-i-n junction allows the transfer of higher electric current, and the radiative recombination of electrons and holes in the junction region results in electroluminescence (EL).[82]

The first example of a CQD-based LEC device was demonstrated by Chu et al, where top-down CQDs produced from electrochemical exfoliation was used in the light-emitting layer of LECs.[7] The device displayed broad white emission at 660 nm, with a relative efficiency of 0.14%. Adsetts et al. used N-doped CQDs in an electrochemical ‘half cell’, wherein a filmed electrode of CQD/persulfate and CQD/TPrA acted as the cathode and anode, respectively, in a separated version of an LEC.[36] The half cells exhibited strong electroluminescence, showing the enhancement effect of higher density

filmed substrates. Liu et al. also demonstrated a host-guest carbon nanodot (CND)-LEC device.[83] CNDs were fabricated from a solvothermal process, thereby allowing the dispersion of the CNDs in hydrophilic solvents. These CNDs were prone to aggregation-caused quenching, but by incorporation into a 2,7-bis(diphenylphosphoryl)-9,9'-spirobifluorene (SPPO13) host compound, the ACQ could be alleviated resulting in peak luminance of 118 cd/m^2 at a current efficiency of 0.41 cd/A.

Other classes of luminophores have also been successfully incorporated into LECs, including tPDI$_2$N-hex (PDI, perylene diimide)[84], an 'atomic precision graphene model', Ru(bpy)$_3$(PF$_6$)$_2$[85], and PDY-132 SuperYellow polymer. In short, using these various luminophores, full coverage of the visible spectrum (400 – 700 nm) is possible, demonstrating the luminescent applications of LECs (**Figure 2.5**).

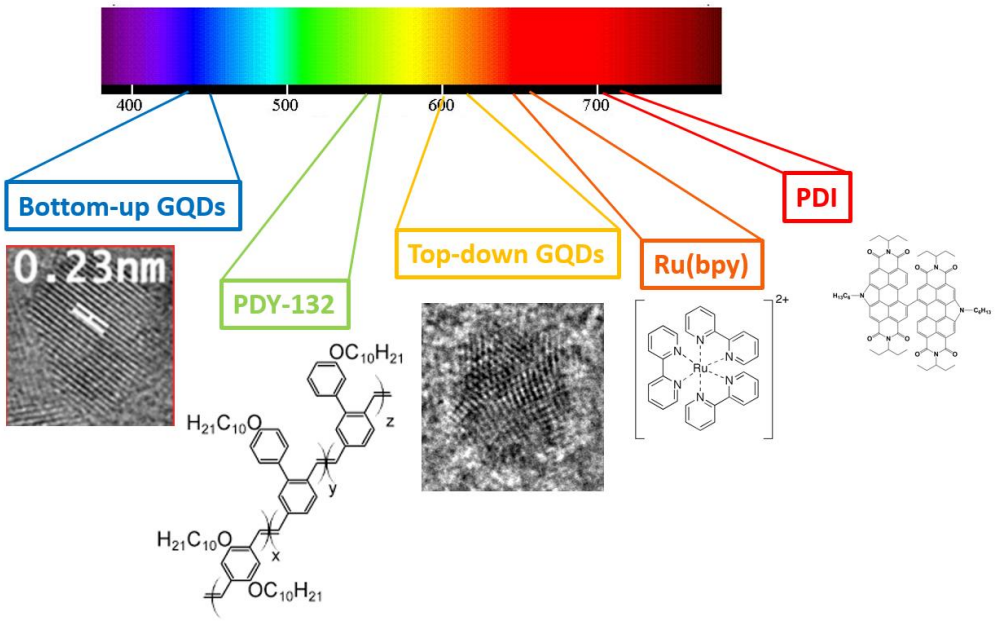

Figure 2.5. Summary of electroluminescent (EL) emissions from various LEC luminophores. Bottom-up CQDs from hydrothermal synthesis, Livilux PDY-132 (SuperYellow), top-down GQDs from electrochemical exfoliation[7], Ru(bpy)3(PF6)2-based LEC, tPDI2N-hex (PDI, perylene diimide).

2.4.3 Chemiluminescence

Chemiluminescence (CL) is the process where the energy to form luminophore excited states comes from chemical reactions. For example, the well-known reaction between the peroxyoxalate bis(2-carbopentyloxy-3,5,6-trichlorophenyl) (CPPO) and hydrogen peroxide (H_2O_2) generates a high-energy intermediate 1,2-dioxetanedione, which decomposes into CO_2, releasing energy. This energy can then be absorbed by an appropriate luminophore to produce CL.[86, 87] There are many different luminophores that have been used for CL applications, including luminol[88], rubrene[89], and 9,10-diphenylanthracene (DPA).[90] However, CQDs present an intriguing alternative, as they are low-cost, easily synthesized, and highly accessible.

The Ding research group studied N, S-codoped CQDs as a chemiluminescence emitter[75], synthesized from citric acid and L-cysteine using a one-pot pyrolysis method. The CL system using CPPO and H_2O_2 in the presence of sodium salicylate as the base catalyst demonstrated bright blue emission; as well, the absolute CL efficiency of the reaction was determined to be 0.01%. The contribution of different emission pathways (intrinsic core emission, aggregation-induced emission, and surface state emission) could be determined using spooling CL spectroscopy.

There have been some studies that utilize CQDs to enhance the overall emission of a CL system. For example, Teng et al. used acidified potassium permanganate with CQDs synthesized via a bottom-up pathway, which resulted in CL emission centered at 500 nm.[91] Furthermore, they proposed that the surface functional groups of the CQDs were an important contributor to the CL emission, as the reduced variant of CQDs (r-CQDs) demonstrated even stronger emission. Another study by Lin et al. showed that the chemiluminescence of the peroxynitrous-carbonate system could be greatly enhanced by introducing CQDs.[92] Here, it was suggested that the CQDs could act as an energy acceptor in the CL mechanism, improving the native performance of existing luminophores. CQDs can also be used directly as a chemiluminescent luminophore, demonstrated by Zhao et al., who synthesized polyamine-functionalized CQDs from a pyrolysis procedure.[93] The functionalized CQD showed strong CL in alkaline solution, which was significantly enhanced in the presence of Fe(III) ions. This enhancement was

found to be linear with an increase in the ferric ion concentration, establishing the analytical capability of a CL-based probe.

2.5 Conclusions and outlook

It is clear that the future of CQDs is bright, with much research and development to bring forth advanced applications in optoelectronics and bioimaging. Since 2004, a great number of synthetic procedures to manufacture CQDs have become possible, enabling the low-cost and flexibility in applying CQDs to different applications, such as bioimaging and light-emitting electrochemical cells. However, there are still some challenges that need to be addressed for CQDs to become truly competitive in the field dominated by semiconductor quantum dots, noble metal nanoparticles, and inorganic compounds. Firstly, CQDs with high quantum yield and colour purity are urgently required. These attributes will facilitate their adoption into existing light-emitting applications, such as display technologies. To achieve this step, a greater knowledge of the luminescent mechanisms that govern the emission of light from CQDs is very important. We have already discussed the widely accepted models of core bandgap transitions, surface defects, and aggregation-induced emissions in this review. However, by fully understanding these mechanisms, high efficiency and optimization of CQD applications can be achieved. Secondly, the precise process by which CQDs are constructed from the various discussed top-down and bottom-up strategies should be further investigated in order to better control the size, morphology, and surface properties. This knowledge will enable a more meaningful comparison between CQDs fabricated using different procedures.

2.6 References

[1] Lim, S. Y.; Shen, W.; Gao, Z. *Chem. Soc. Rev.* **2014,** *44*, 362-381.

[2] Liu, Q.; Guo, B.; Rao, Z.; Zhang, B.; Gong, J. R. *Nano. Lett.* **2013,** *13*, 2436-2441.

[3] Li, H.; Kang, Z.; Liu, Y.; Lee, S.-T. *J. Mater. Chem.* **2012,** *22*, 24230-24253.

[4] Umar, E.; Ikram, M.; Haider, J.; Nabgan, W.; Haider, A.; Imran, M.; Nazir, G. *SM&T* **2023,** *35*, e00529.

[5] Xu, X.; Ray, R.; Gu, Y.; Ploehn, H. J.; Gearheart, L.; Raker, K.; Scrivens, W. A. *J. Am. Chem. Soc.* **2004,** *126*, 12736-12737.

[6] Zhou, J.; Booker, C.; Li, R.; Zhou, X.; Sham, T.-K.; Sun, X.; Ding, Z. *J. Am. Chem. Soc.* **2007,** *129*, 744-745.

[7] Chu, K.; Adsetts, J. R.; He, S.; Zhan, Z.; Yang, L.; Wong, J. M.; Love, D. A.; Ding, Z. *Chem. Eur. J.* **2020,** *26*, 15892-15900.

[8] Rocco, D.; Moldoveanu, V. G.; Feroci, M.; Bortolami, M.; Vetica, F. *ChemElectroChem* **2023,** *10*, e202201104.

[9] Luo, Z.; Qi, G.; Chen, K.; Zou, M.; Yuwen, L.; Zhang, X.; Huang, W.; Wang, L. *Adv. Funct. Mater.* **2016,** *26*, 2739-2744.

[10] Dong, Y.; Pang, H.; Ren, S.; Chen, C.; Chi, Y.; Yu, T. *Carbon* **2013,** *64*, 245-251.

[11] Gonçalves, H.; Jorge, P. A. S.; Fernandes, J. R. A.; Esteves da Silva, J. C. G. *Sens. Actuators B Chem.* **2010,** *145*, 702-707.

[12] Sun, Y.-P.; Zhou, B.; Lin, Y.; Wang, W.; Fernando, K. A. S.; Pathak, P.; Meziani, M. J.; Harruff, B. A.; Wang, X.; Wang, H.; Luo, P. G.; Yang, H.; Kose, M. E.; Chen, B.; Veca, L. M.; Xie, S.-Y. *J. Am. Chem. Soc.* **2006,** *128*, 7756-7757.

[13] Zhu, H.; Liu, A.; Xu, Y.; Shan, F.; Li, A.; Wang, J.; Yang, W.; Barrow, C.; Liu, J. *Carbon* **2015,** *88*, 225-232.

[14] Molaei, M. J. *Anal. Methods* **2020,** *12*, 1266-1287.

[15] Chen, Y.; Lin, J.; Zhang, R.; He, S.; Ding, Z.; Ding, L. *Analyst* **2021,** *146*, 5287-5293.

[16] Zhang, R.; Adsetts, J. R.; Nie, Y.; Sun, X.; Ding, Z. *Carbon* **2018,** *129*, 45-53.

[17] Feng, Z.; Yang, T.; Liang, T.; Wu, Z.; Wu, T.; Zhang, J.; Yu, L. *Mater. Des.* **2022,** *217*, 110644.

[18] Chauhan, P.; Saini, J.; Chaudhary, S.; Bhasin, K. K. *Mater. Res. Bull.* **2021,** *134*, 111113.

[19] Han, T. T.; Huang, Y.; Gao, T. Y.; Xia, C. Y.; Sun, C.; Xu, W. M.; Wang, D. Y. *Food Chem.* **2023,** *404*.

[20] Zhang, D.; Zhang, F.; Liao, Y.; Wang, F.; Liu, H. *Molecules*, **2022**, *27*, 4099.

[21] Feng, M.; Wang, Y.; He, B.; Chen, X.; Sun, J. *ACS Appl. Nano Mater.* **2022,** *5*, 7502-7511.

[22] Koç, Ö. K.; Üzer, A.; Apak, R. *ACS Appl. Nano Mater.* **2022,** *5*, 5868-5881.

[23] Chang, K.; Zhu, Q.; Qi, L.; Guo, M.; Gao, W.; Gao, Q. *Materials* **2022,** *15*.

[24] Meng, A.; Huangfu, B.; Sheng, L.; Hong, X.; Li, Z. *Microchem. J.* **2022,** *174*, 106981.

[25] Qi, C.; Wang, H.; Yang, A.; Wang, X.; Xu, J. *ACS Omega* **2021,** *6*, 32904-32916.

[26] Šafranko, S.; Stanković, A.; Hajra, S.; Kim, H.-J.; Strelec, I.; Dutour-Sikirić, M.; Weber, I.; Bosnar, M. H.; Grbčić, P.; Pavelić, S. K.; Széchenyi, A.; Mishra, Y. K.; Jerković, I.; Jokić, S. *Pharmaceuticals*, **2021**, *14*.

[27] Zhang, S.-R.; Cai, S.-K.; Wang, G.-Q.; Cui, J.-Z.; Gao, C.-Z. *J. Mol. Struct.* **2021,** *1246*, 131173.

[28] Yadav, P. K.; Upadhyay, R. K.; Kumar, D.; Bano, D.; Chandra, S.; Jit, S.; Hasan, S. H. *New J. Chem.* **2021,** *45*, 12549-12556.

[29] Yan, C.; Guo, L.; Shao, X.; Shu, Q.; Guan, P.; Wang, J.; Hu, X.; Wang, C. *Anal. Bioanal. Chem.* **2021,** *413*, 3965-3974.

[30] Das, A.; Arefina, I. A.; Danilov, D. V.; Koroleva, A. V.; Zhizhin, E. V.; Parfenov, P. S.; Kuznetsova, V. A.; Ismagilov, A. O.; Litvin, A. P.; Fedorov, A. V.; Ushakova, E. V.; Rogach, A. L. *Nanoscale* **2021,** *13*, 8058-8066.

[31] Rong, M.; Wang, D.; Li, Y.; Zhang, Y.; Huang, H.; Liu, R.; Deng, X. *J. Anal. Test.* **2021,** *5*, 51-59.

[32] Janus, L.; Piatkowski, M.; Radwan-Praglowska, J.; Sierakowska, A. *Inz. Miner.* **2020,** *2*, 57-61.

[33] He, S.; Turnbull, M. J.; Nie, Y.; Sun, X.; Ding, Z. *Surf. Sci.* **2018,** *676*, 51-55.

[34] Su, A.; Wang, D.; Shu, X.; Zhong, Q.; Chen, Y.; Liu, J.; Wang, Y. *Chem. Res. Chin. Univ.* **2018,** *34*, 164-168.

[35] Wang, C.; Shi, H.; Yang, M.; Yan, Y.; Liu, E.; Ji, Z.; Fan, J. *Mater. Res. Bull.* **2020,** *124*, 110730.

[36] Adsetts, J. R.; Zhang, R.; Yang, L.; Chu, K.; Wong, J. M.; Love, D. A.; Ding, Z. *Front. Chem.* **2020,** *8*, 580022.

[37] Yang, L.; De-Jager, C. R.; Adsetts, J. R.; Chu, K.; Liu, K.; Zhang, C.; Ding, Z. *Anal. Chem.* **2021,** *93*, 12409-12416.

[38] Qin, X.; Fu, C.; Zhang, J.; Shao, W.; Qin, X.; Gui, Y.; Wang, L.; Guo, H.; Chen, F.; Jiang, L.; Wu, G.; Bikker, F. J.; Luo, D. *Front. Chem.* **2022,** *10*.

[39] Wang, Q.; Zhang, Z.; Yang, T.; Han, Y.; Cheng, Y.; Wu, J.; Bai, J.; Ma, C.; Niu, Y.; Shuang, S. *Spectrochim. Acta A Mol. Biomol. Spectrosc.* **2022,** *269*, 120742.

[40] Cui, J.; Zhu, X.; Liu, Y.; Liang, L.; Peng, Y.; Wu, S.; Zhao, Y. *ACS Appl. Nano Mater.* **2022,** *5*, 7268-7277.

[41] Tang, H.; Tang, Y.; Zhu, H.; Xiao, M.; Guo, M. *J. Mol. Struct.* **2022,** *1251*, 132034.

[42] Chen, M.; Liu, X. *J. Fluoresc.* **2021,** *31*, 1153-1160.

[43] Janus, Ł.; Piątkowski, M.; Radwan-Pragłowska, J.; Bogdał, D.; Matysek, D. *Nanomater.* **2019,** *9*.

[44] Sharma, A.; Tejwan, N.; Thakur, S.; Sharma, V.; Singh, T. A.; Das, J. *Opt. Mater.* **2022,** *124*, 111995.

[45] Chauhan, P.; Mundekkad, D.; Mukherjee, A.; Chaudhary, S.; Umar, A.; Baskoutas, S. *Nanomater.* **2022,** *12*.

[46] Song, Y.; Wu, Y.; Wang, H.; Liu, S.; Song, L.; Li, S.; Tan, M. *Food Chem.* **2019,** *293*, 387-395.

[47] Zhou, S.; Sui, Y.; Zhu, X.; Sun, X.; Zhuo, S.; Li, H. *Chem. Asian J.* **2021,** *16*, 348-354.

[48] Yuan, F.; Yuan, T.; Sui, L.; Wang, Z.; Xi, Z.; Li, Y.; Li, X.; Fan, L.; Tan, Z. a.; Chen, A.; Jin, M.; Yang, S. *Nat. Comm.* **2018,** *9*, 2249.

[49] Li, H.; He, X.; Kang, Z.; Huang, H.; Liu, Y.; Liu, J.; Lian, S.; Tsang, C. H. A.; Yang, X.; Lee, S.-T. *Angew. Chem. Int. Ed.* **2010,** *49*, 4430-4434.

[50] Ding, Y.; Zheng, J.; Wang, J.; Yang, Y.; Liu, X. *J. Mater. Chem. C* **2019,** *7*, 1502-1509.

[51] Zhang, D.; Chao, D.; Yu, C.; Zhu, Q.; Zhou, S.; Tian, L.; Zhou, L. *J. Phys. Chem. Lett.* **2021,** *12*, 8939-8946.

[52] Li, H.; Liu, R.; Kong, W.; Liu, J.; Liu, Y.; Zhou, L.; Zhang, X.; Lee, S.-T.; Kang, Z. *Nanoscale* **2014,** *6*, 867-873.

[53] Du, Y.; Guo, S. *Nanoscale* **2016,** *8*, 2532-2543.

[54] Zhou, X.; Zhang, Y.; Wang, C.; Wu, X.; Yang, Y.; Zheng, B.; Wu, H.; Guo, S.; Zhang, J. *ACS Nano* **2012,** *6*, 6592-6599.

[55] Zhu, S.; Song, Y.; Wang, J.; Wan, H.; Zhang, Y.; Ning, Y.; Yang, B. *Nano Today* **2017,** *13*, 10-14.

[56] Liu, Z.; Zou, H.; Wang, N.; Yang, T.; Peng, Z.; Wang, J.; Li, N.; Huang, C. *Sci. China Chem.* **2018,** *61*, 490-496.

[57] Shen, J.; Zhu, Y.; Yang, X.; Li, C. *Chem. Commun.* **2012,** *48*, 3686-3699.

[58] Nicollian, E. H. *J. Vac. Sci.* **1971,** *8*, S39-S49.

[59] Anilkumar, P.; Cao, L.; Yu, J.-J.; Tackett Ii, K. N.; Wang, P.; Meziani, M. J.; Sun, Y.-P. *Small* **2013,** *9*, 545-551.

[60] Yang, Y.; Cui, J.; Zheng, M.; Hu, C.; Tan, S.; Xiao, Y.; Yang, Q.; Liu, Y. *Chem. Commun.* **2012,** *48*, 380-382.

[61] Zhao, H. X.; Liu, L. Q.; Liu, Z. D.; Wang, Y.; Zhao, X. J.; Huang, C. Z. *Chem. Commun.* **2011,** *47*, 2604-2606.

[62] Li, H.; Zhang, Y.; Wang, L.; Tian, J.; Sun, X. *Chem. Commun.* **2011,** *47*, 961-963.

[63] Huang, X.; Zhang, F.; Zhu, L.; Choi, K. Y.; Guo, N.; Guo, J.; Tackett, K.; Anilkumar, P.; Liu, G.; Quan, Q.; Choi, H. S.; Niu, G.; Sun, Y.-P.; Lee, S.; Chen, X. *ACS Nano* **2013,** *7*, 5684-5693.

[64] Kou, X.; Jiang, S.; Park, S.-J.; Meng, L.-Y. *Dalton Trans.* **2020,** *49*, 6915-6938.

[65] Chen, C.-F.; Park, C.-H.; Boudouris, B. W.; Horng, J.; Geng, B.; Girit, C.; Zettl, A.; Crommie, M. F.; Segalman, R. A.; Louie, S. G.; Wang, F. *Nature* **2011,** *471*, 617-620.

[66] Chien, C.-T.; Li, S.-S.; Lai, W.-J.; Yeh, Y.-C.; Chen, H.-A.; Chen, I. S.; Chen, L.-C.; Chen, K.-H.; Nemoto, T.; Isoda, S.; Chen, M.; Fujita, T.; Eda, G.;

Yamaguchi, H.; Chhowalla, M.; Chen, C.-W. *Angew. Chem. Int. Ed.* **2012,** *51*, 6662-6666.

[67] Zhu, S.; Song, Y.; Zhao, X.; Shao, J.; Zhang, J.; Yang, B. *Nano Res.* **2015,** *8*, 355-381.

[68] Lin, L.; Zhang, S. *Chem. Commun.* **2012,** *48*, 10177-10179.

[69] Dong, Y.; Chen, C.; Zheng, X.; Gao, L.; Cui, Z.; Yang, H.; Guo, C.; Chi, Y.; Li, C. M. *J. Mater. Chem.* **2012,** *22*, 8764-8766.

[70] Baker, S. N.; Baker, G. A. *Angew. Chem. Int. Ed.* **2010,** *49*, 6726-6744.

[71] Liu, J.; Liu, X.; Luo, H.; Gao, Y. *RSC Adv.* **2014,** *4*, 7648-7654.

[72] Hong, Y.; Lam, J. W. Y.; Tang, B. Z. *Chem. Soc. Rev.* **2011,** *40*, 5361-5388.

[73] Chen, Y.; Lam, J. W. Y.; Kwok, R. T. K.; Liu, B.; Tang, B. Z. *Mater. Horiz.* **2019,** *6*, 428-433.

[74] Zhao, Z.; Zhang, H.; Lam, J. W. Y.; Tang, B. Z. *Angew. Chem. Int. Ed.* **2020,** *59*, 9888-9907.

[75] Qin, X.; Zhan, Z.; Zhang, R.; Chu, K.; Whitworth, Z.; Ding, Z. *Nanoscale* **2023,** *15*, 3864-3871.

[76] Richter, M. M. *Chem. Rev.* **2004,** *104*, 3003-36.

[77] Miao, W. *Chem. Rev.* **2008,** *108*, 2506-53.

[78] Hesari, M.; Ding, Z. *J. Electrochem. Soc.* **2016,** *163*, H3116-H3131.

[79] Gao, J. *Curr. Opin. Electrochem.* **2018,** *7*, 87-94.

[80] Xu, J.; Sandström, A.; Lindh, E. M.; Yang, W.; Tang, S.; Edman, L. *ACS Appl. Mater. Interfaces* **2018,** *10*, 33380-33389.

[81] He, L.; Wang, X.; Duan, L. *ACS Appl. Mater. Interfaces* **2018,** *10*, 11801-11809.

[82] Miyazaki, M.; Sakanoue, T.; Takenobu, T. *JJAP* **2018,** *57*, 03EF01.

[83] Liu, Y.; Tang, S.; Wu, X.; Boulanger, N.; Gracia-Espino, E.; Wågberg, T.; Edman, L.; Wang, J. *Nano Res.* **2022,** *15*, 5610-5618.

[84] Yang, L.; Hendsbee, A. D.; Xue, Q.; He, S.; De-Jager, C. R.; Xie, G.; Welch, G. C.; Ding, Z. *ACS Appl. Mater. Interfaces* **2020,** *12*, 51736-51743.

[85] Chu, K.; Adsetts, J. R.; Moore, C.; Ding, Z. *ACS Appl. Electron. Mater.* **2020,** *2*, 3825-3830.

[86] Eghlimi, A.; Jubaer, H.; Surmiak, A.; Bach, U. *J. Chem. Educ.* **2019,** *96*, 522-527.

[87] Kuntzleman, T. S.; Rohrer, K.; Schultz, E. *J. Chem. Educ.* **2012,** *89*, 910-916.

[88] Merényi, G.; Lind, J.; Eriksen, T. E. *J. Biolumin. Chemilumin.* **1990,** *5*, 53-56.

[89] Bezman, R.; Faulkner, L. R. *J. Am. Chem. Soc.* **1972,** *94*, 6324-6330.

[90] Arnous, A.; Petrakis, C.; Makris, D. P.; Kefalas, P. *J. Pharmacol. Toxicol. Methods* **2002,** *48*, 171-177.

[91] Teng, P.; Xie, J.; Long, Y.; Huang, X.; Zhu, R.; Wang, X.; Liang, L.; Huang, Y.; Zheng, H. *J. Lumin.* **2014,** *146*, 464-469.

[92] Lin, Z.; Dou, X.; Li, H.; Ma, Y.; Lin, J.-M. *Talanta* **2015,** *132*, 457-462.

[93] Zhao, L.; Geng, F.; Di, F.; Guo, L.-H.; Wan, B.; Yang, Y.; Zhang, H.; Sun, G. *RSC Adv.* **2014,** *4*, 45768-45771.

Chapter 3

In this chapter, the methodology, instrumentation, and mathematical calculations are developed to quantify the absolute quantum efficiency (QE) of electrochemiluminescence systems. The QE is an essential measure of the performance of ECL luminophores for light-emitting applications, and this system will be used extensively in this thesis to assess different materials for suitability for use in light emitting electrochemical cells (LECs). Chapter 3 will focus on the ECL QE methodology for a photon-counting head device.

3 Physical Strategy to Determine Absolute Electrochemiluminescence Quantum Efficiencies of Coreactant Systems Using a Photon-Counting Photomultiplier Device†

3.1 Introduction

Electrochemiluminescence or electrogenerated chemiluminescence (ECL) is a process wherein electrogenerated radicals undergo high-energy electron transfer reactions to produce excited states, which emit light upon relaxation to their ground states.[1, 2] ECL emission follows one of the following two pathways. The annihilation route involves a direct electron transfer between a radical cation and anion generated by alternating oxidation and reduction at an electrode, respectively. The coreactant route introduces an additional species that, upon oxidation or reduction, can form a highly reducing or oxidizing secondary radical that interacts with a luminophore radical to produce ECL.[3, 4] Coreactant systems have been shown to significantly enhance ECL intensity, and are a common strategy to increase the overall luminescence of an otherwise poorly emissive system.[5-7] Since the introduction of ECL in the mid 1960s,[8-10] it has since been developed into a highly sensitive and selective physical/analytical technique utilizing numerous

† This work has been published. Chu, K.; Adsetts, J. R.; Ma, J.; Zhang, C.; Hesari, M.; Yang, L.; Ding, Z., Physical Strategy to Determine Absolute Electrochemiluminescence Quantum Efficiencies of Coreactant Systems Using a Photon-Counting Photomultiplier Device. *J. Phys. Chem. C* **(2021)** 125, 22274-22282.

chemical molecules and nanomaterials as well as having various applications in immunoassays, clinical bio-detection, imaging, and more recently light emitting devices.[11-22] As with all luminescent systems, the accurate quantification of the quantum efficiency (QE) is crucial for the characterization of novel and existing luminophores. The QE has been extensively used as a criterion for selecting the 'best' luminescent materials, particularly for light-emitting applications, as the capacity to efficiently produce useable light has many cost- and energy savings benefits.

The QE of a luminescent system may be generally defined as the ratio between the output energy versus the input energy. For a photoluminescent system, this is the number of photons emitted versus the number of photons used for photoexcitation (photoluminescent quantum yield, or PLQY). For ECL, this is instead the ratio of the number of ECL photons produced to electrons injected into the system (ECL-QE). In practice, ECL photons are represented by the units of photodetector response (for example, integrated *ECL photocurrent* when a photomultiplier tube is used), and the number of electrons may be derived from the integrated electrochemical current as measured by a potentiostat.

At present, ECL-QEs are determined relative to an externally calibrated standard, almost universally the $Ru(bpy)_3^{2+}$ complex, using **Equation 3.1** where *x* is the luminophore under study and *st* is the standard. Bard et al. in 1973 reported an absolute efficiency of 5-6% for $Ru(bpy)_3^{2+}$ in the annihilation pathway, a value that has largely been accepted as the gold standard.[23] An alternative strategy is to simply assign a value of 1 to $Ru(bpy)_3^{2+}$ ϕ_{ECL} in lieu of a true reference value.[24] No absolute efficiency has ever been reported for an ECL coreactant system.

$$\Phi_{ECL} = \frac{\left(\frac{\int ECL \cdot dt}{\int Current \cdot dt}\right)_x}{\left(\frac{\int ECL \cdot dt}{\int Current \cdot dt}\right)_{st}}$$

Equation 3.1

While **Equation 3.1** is acceptable for the relative assessment of ECL luminophores, it has several critical disadvantages. Firstly, there can be many complications in instances where the emissive properties or mechanisms of the studied luminophore *x* are very different from those of *st*. This problem is only exacerbated in ECL studies, where solvent and coreactant choice, luminophore and electrolyte concentrations, and varying electrode materials can all disproportionately influence the ECL performance of the system relative to the standard. A more recent challenge comes from measuring the emission of modified film electrodes and aggregation-induced ECL,[25-28] where very significant mechanistic and matrix-related differences can occur. Secondly, because **Equation 3.1** does not consider the emission wavelength, significantly underestimated or overestimated efficiencies may occur due to photodetector wavelength-dependent responsivities. In contrast, an absolute efficiency determination will report the photons-out-electrons-in ratio of an ECL system that is free from such experimental biases. Such a measurement will allow the meaningful and objective comparison of the efficiencies of a wide variety of ECL luminophores under both the annihilation and coreactant pathways, and will be a significant boon for many ECL researchers in the future.

The challenge with absolute measurements involves precisely determining the quantities of photons produced in ECL reactions. The number of electrons can be readily determined by modern electrochemical workstations with an internal coulometer capable of sampling the charge from a measured current easily down to a nA range. Measuring the number of photons produced by a system, however, requires a more careful and systematic approach. We utilize a detection system called a *photon counting head*, which is a specialized photomultiplier tube with extremely high sensitivity and fast response time that is designed to detect individual photons in low light conditions. In conjunction with a high frequency signal counter, our instrument setup allows the precise determination of the total photon number produced via the ECL process.

In this work we demonstrate our photon counting instrument setup by determining the absolute quantum efficiency of the $Ru(bpy)_3^{2+}$/tri-*n*-propylamine (TPrA) coreactant ECL system for the first time. Special physical considerations concerning the unique emission profile of ECL, electrode-to-detector distance and surface areas, and photodetector

responsivities are introduced, and physical insights into how electrochemical reactions along with these can affect the final ECL-QE are provided.

3.2 Methods

3.2.1 Materials and reagents

Tris(2,2'-bipyridine) ruthenium(II) hexafluorophosphate, $Ru(bpy)_3(PF_6)_2$ (97%, reagent grade), tetrabutylammonium hexafluorophosphate, $TBAPF_6$ (>99.0%, electrochemical grade), Ferrocene (98%) and anhydrous acetonitrile (99.8%, SureSeal) were purchased from Sigma-Aldrich Canada and used as received. Tri-*n*-propylamine, TPrA (>98%, analytical grade) was bought from Sigma-Aldrich Canada, and stored at 4°C.

3.2.2 Instrumentation for electrochemistry and electrochemiluminescence

A three-electrode system was used for all electrochemical and electrochemiluminescence measurements, where the working electrode was a 2 mm diameter platinum disc inlaid in a glass tube, and the auxiliary and quasi-reference electrodes were coiled platinum wires. A pre-treatment procedure was used to prepare the working electrode before use: a) mechanical polishing to a mirror-like finish, using alumina slurries with particles sizes of 1.0 µm, 0.3 µm, and 0.05 µm sequentially (Buehler micropolish alumina suspensions) followed by, b) an electrochemical treatment where the applied potential was repeatedly scanned between −0.4 V and 1.2 V for at least 50 cycles in a solution of 0.1 M sulfuric acid.

All analyses were conducted inside a cylindrical glass tube with a flat quartz window at the bottom to allow for the detection of ECL light. The airtight ECL cell was assembled inside a nitrogen atmosphere glovebox (Model Nexus I, Vacuum Atmospheres Company, Hawthorne, CA) to ensure the absence of oxygen and moisture. For coreactant experiments which required the addition of semi-volatile reagents, the ECL cell was purged with argon gas for at least five minutes. The potentiostat for both cyclic voltammetry and potential stepping experiments was an Autolab electrochemical workstation (Model PGSTAT302N, Metrohm BV, Switzerland) equipped with an

ADC164 analog-to-digital converter and controlled using Autolab NOVA software (version 2.1.4). All electrochemical potentials are reported relative to the ferrocene/ferrocenium (Fc/Fc^+) redox couple, where the oxidation potential was taken to be 0.342 V vs. SCE.[29]

3.2.3 ECL spectroscopy

The annihilation and coreactant ECL spectra of $Ru(bpy)_3^{2+}$ were collected using a CCD camera (DU401a-BR-DD, Andor Technologies, Belfast, UK) cooled to −65°C, coupled with a spectrograph (Acton SP2300i, Princeton Instruments Inc., Princeton, NJ).[30] Calibration of the spectroscopy wavelength was performed using a mercury-argon source (Model HG-1, Ocean Optics, Orlando, FL). All accumulation emission spectra reported in this work have been baseline-corrected by numerical subtraction of an identical duration background scan, and intensity-normalized to allow for meaningful comparison.

The PCH was set according to the following sections: Principles of photomultiplier tube operation in photon-counting mode and Photon counting head pulse pair resolution as well as Electrode-to-detector distance settings.

3.2.4 Instrument considerations

Figure 3.1 shows a schematic illustration of the instrument setup used to measure the absolute ECL efficiency. The photodetector used was a Hamamatsu H6240-02 side-on photon counting head (abbreviated hereafter as ‘PCH’) which is an all-in-one unit incorporating a photomultiplier tube (PMT) and high-speed amplifier/discriminator/high voltage power supply circuits in a compact housing. The unit requires a +5 Vdc input power, which was provided using the voltage delivery pins on a standard universal serial bus (USB type A) connection. The output signal from the photon counting head was passed through an attenuator to reduce the outgoing voltage pulse magnitude to approximately +200 mV, before being input into an SR430 multichannel scaler/averager (Stanford Research Systems) for data recording. The SR430 receives the incoming voltage pulses, and collects them into successive ‘bins’. The discriminator level, defined as the minimum pulse magnitude that will result in a recorded signal, was set to +100 mV; this value is exactly one-half of the attenuated signal to improve the signal-to-noise

ratio. A portable digital oscilloscope was used to verify the signal intensities. An external voltage trigger provided by the Autolab workstation was used to start each record, allowing the synchronous acquisition of the electrochemical current (measured by the PGSTAT302N) and the corresponding ECL signal, as photon counts (measured by the photon counting head). Metallic coated neutral density optical filters were used to avoid overexposure of the photon counting head. **Figure 3.2** and **Figure 3.3** show contain photographs of the photon counting head setup and the ECL cell, respectively.

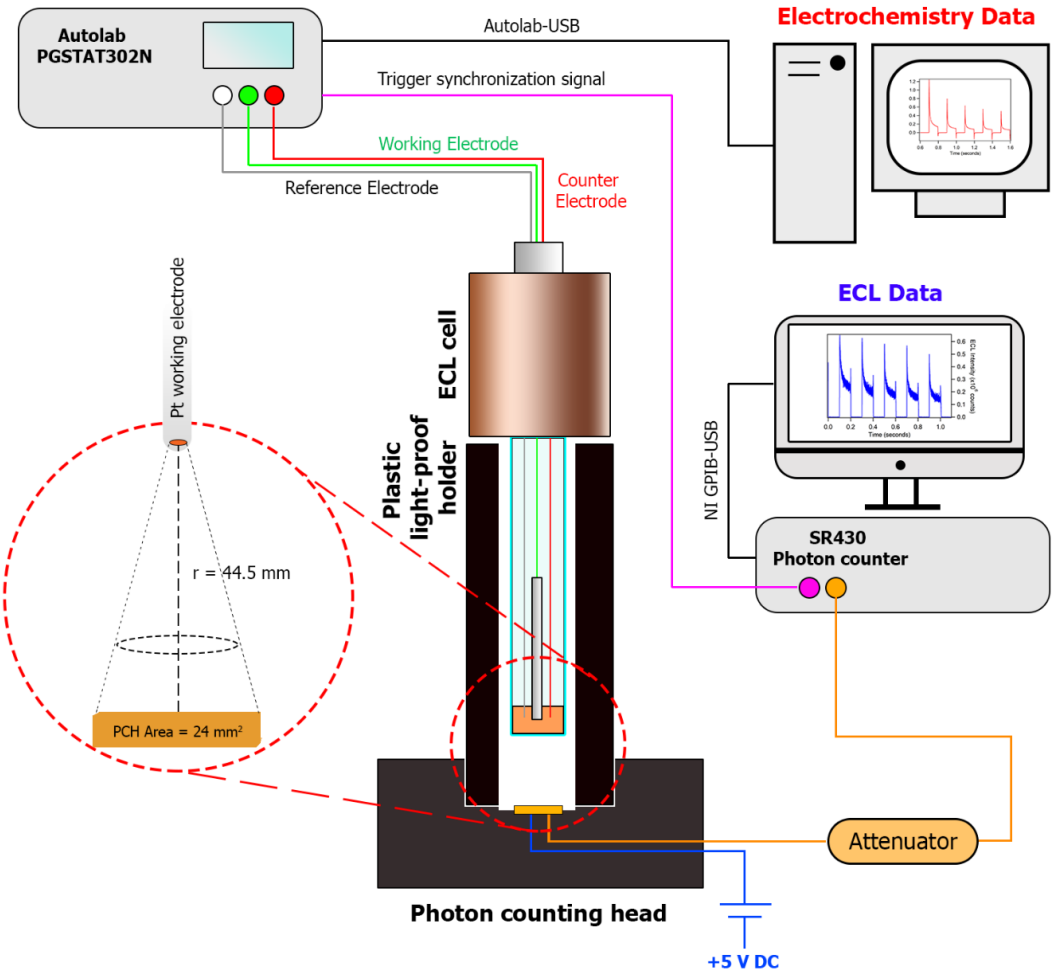

Figure 3.1. A schematic overview of the photon counting head (PCH) instrumentation setup. All instrument connections have been colour-coded, where possible, to better illustrate the pathways of data and communication signals. A vertical cross-section is shown for the ECL cell, the plastic holder, and the PCH to show how the components fit

together. Inset circle (outlined and magnified in dotted red) illustrates the path of the ECL emission from the platinum electrode towards the photodetector surface. The counts represented as potential pulses from the PCH is passed through an attenuator, before being sent to the SR430, where it is sorted into individual bins. An external voltage trigger is generated by the Autolab potentiostat to synchronize the start of each record. Two separate computer workstations were used to control the potentiostat and SR430 photon counter through NOVA and LabVIEW software, respectively.

The remaining user-controlled settings for the SR430 instrument are notified here briefly. The *bin width* specifies the time interval for each data bin, while the *bins per record* specifies the number of bins in the measurement; these two values, taken together, represent the total acquisition time of a single record (for example: a bin width of 5.000 ns multiplied by 1024 bins equals a measurement time of 5.120 μs). The *records per scan* determines the number of repeated measurements in an experiment; the records are dynamically added together, allowing the statistical accumulation of multiple ECL emission events. Finally, the *trigger level* describes an external voltage pulse that signals the beginning of each record. These settings are highly dependent on experimental parameters and are individually specified at appropriate locations in the text. A custom LabVIEW program (NI, Austin, TX) was used to provide computer control of the SR430 instrument.

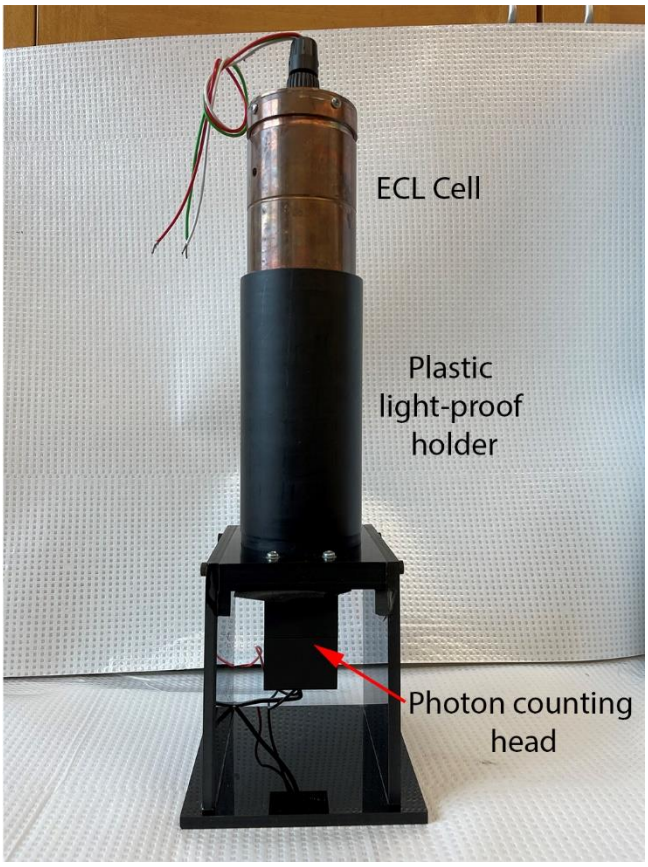

Figure 3.2. Photograph of the ECL cell in its black plastic light-proof holder, and the photon counting head.

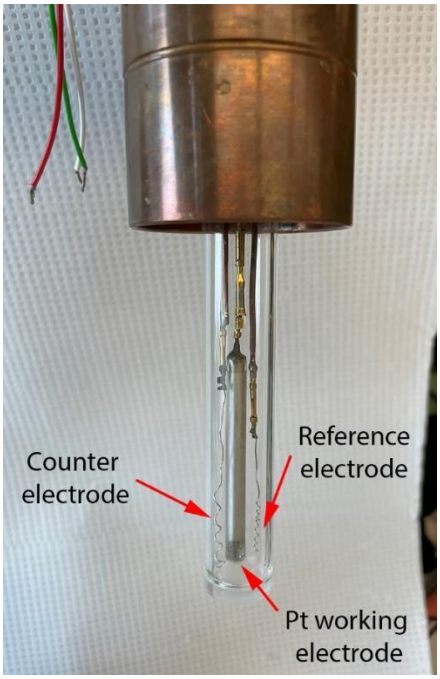

Figure 3.3. Photograph of the ECL glass cell and its assembly, showing the orientation of the working, counter, and reference electrodes.

3.2.5 The ECL-QE formula

The QE of an electrochemiluminescent system is defined as the ratio of the number of photons emitted to the number of electrons injected, expressed in **Equation 3.2** as a percentage.

$$ECL\ Quantum\ Efficiency\ (\%) = \frac{Total\ photons}{Total\ electrons} \times 100\%$$

Equation 3.2

To determine the QE, two separate quantities must be measured simultaneously in the physical chemistry process: the total number of photons emitted by the system under study, and the total number of electrons injected into the system to generate that emission. To simplify the quantification, both the numerator and the denominator of **Equation 3.2** may be reported with respect to the same time interval; therefore, the final QE result will be the ratio of absolute photons vs. absolute electrons. The following section will describe how to arrive at these two parameters, and several circumstantial

correction factors will be introduced. A full sample calculation is provided in the following section as **Equation 3.3** – **Equation 3.11**.

3.2.6 Sample calculation for the absolute quantum efficiency

Equation 3.3 to **Equation 3.11** demonstrate a full calculation of the absolute EQE for $Ru(bpy)_3^{2+}$ annihilation ECL during a potential sweep (as in Figure 4 in the main text). **Equation 3.3**: integration of the counts with respect to the bin number, multiplied by the bin width, results in total counts. **Equation 3.4**: dividing by the C value results in total photons measured by the PCH. **Equation 3.5**: calibration factor corrects to a calibrated number of photons. **Equation 3.6**: surface area correction factor. **Equation 3.7**: Electrode reflectance correction factor. **Equation 3.8**: solution self-absorbance correction factor. **Equation 3.9**: integration of the measured current with respect to time results in the total charge. **Equation 3.10**: dividing the total charge by the elementary charge constant (e = 1.602 × 10^{-19} C) yields total number of electrons. **Equation 3.11**: the ratio between the total photons vs. the total electrons results in the absolute quantum efficiency, expressed here as a percentage. Unless otherwise specified, integration limits are assumed to be from 0 = start of potentiodynamic experiment to t = end of potentiodynamic experiment, inclusive.

$$Total\ counts = \int_0^t Counts \cdot dt = 483\,000\ counts$$

Equation 3.3

$$483\,000\ counts \times \frac{1}{0.0564\ \frac{counts}{photon}} = 8.56 \times 10^6\ photons$$

Equation 3.4

$$8.56 \times 10^6\ photons \times \frac{1}{0.0769} = 1.11 \times 10^8\ photons$$

Equation 3.5

$$1.11 \times 10^{8}\ photons \times \frac{1}{9.65 \times 10^{-4}} = 1.15 \times 10^{11}\ photons$$

Equation 3.6

$$\frac{1.15 \times 10^{11}\ photons}{1.40} = 8.24 \times 10^{10}\ photons$$

Equation 3.7

$$8.24 \times 10^{10}\ photons \times 1.1952 = \mathbf{9.85 \times 10^{10}\ photons}$$

Equation 3.8

$$Total\ charge = \int_{0}^{t} Current \cdot dt = 4.38 \times 10^{-4}\ Coulombs$$

Equation 3.9

$$Total\ electrons = \frac{Total\ charge}{e} = \frac{4.38 \times 10^{-4}\ C}{1.602 \times 10^{-19}\ \frac{C}{electron}} = \mathbf{2.73 \times 10^{15}\ electrons}$$

Equation 3.10

$$EQE\ \% = \frac{Total\ photons}{Total\ electrons} \times 100 = \frac{\mathbf{9.85 \times 10^{10}\ photons}}{\mathbf{2.73 \times 10^{15}\ electrons}} \times 100 = \mathbf{0.0036\%}$$

Equation 3.11

3.2.7 Calibration of the PCH

The PCH was calibrated using a high intensity AlInGaP light-emitting diode (LED) with a center wavelength of 630 nm (Model TLHK46Q1R2, Vishay Semiconductors, Malvern, PA). In total, eight calibration points were collected by varying the forward operating voltage of the LED between 1.58 V and 1.65 V at intervals of 0.01 V (**Figure 3.4**). An optical density filter was used to reduce the radiant power of the LED down to a scale appropriate for ECL measurements, ultimately covering a range of approximately 10^5 – 10^6 counts per second (cps). These measurements were then repeated using a factory-calibrated silicon photodiode (S120VC, Thorlabs Optics, Newton, NJ) in

combination with a digital power meter (Model PM100D, Thorlabs) to calibrate the PCH reading in terms of optical power (**Figure 3.5**).

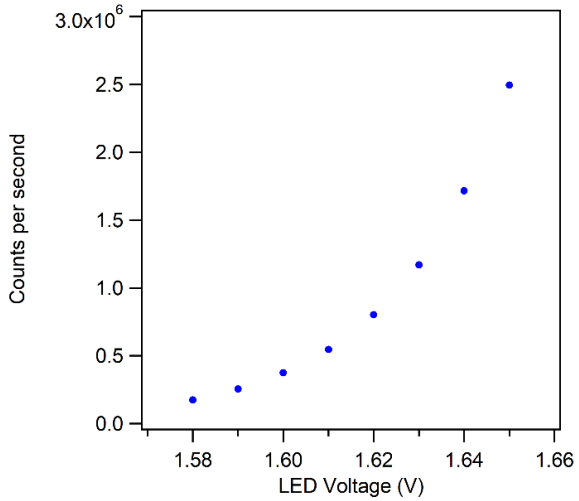

Figure 3.4. Counts per second (corrected for bin widths) of a red LED measured using the Hamamatsu H6240-02 photon counting head at different operating voltages (1.58 V – 1.65 V).

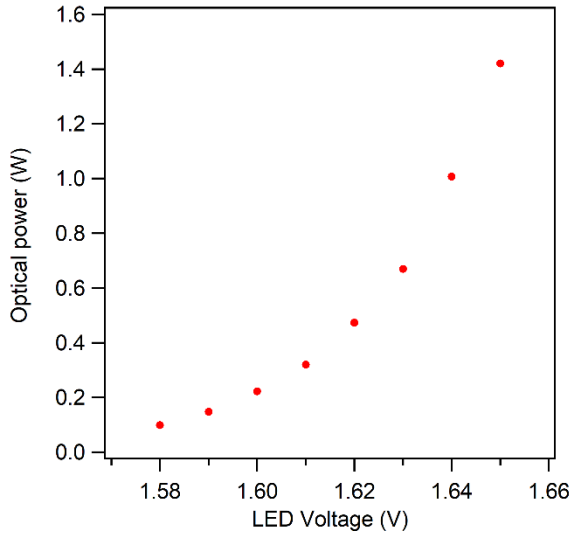

Figure 3.5. Optical power (in Watts) of a red LED measured using a Thorlabs calibrated silicon photodiode at different operating voltages (1.58 V – 1.65 V).

To simplify the units, the radiant flux (in Watts) may be transformed into the photon flux (*photons per second*) using **Equation 3.12** and **Equation 3.13**, which relates a photon's

energy with its wavelength, where h is the Planck constant (6.626×10^{-34} $J{\cdot}s$), c is the speed of light (3.00×10^{8} $msec^{-1}$) and λ is the wavelength.

$$E = \frac{hc}{\lambda} = J\ per\ photon(\lambda)$$

Equation 3.12

$$W = \frac{J}{s} \times \frac{1}{\frac{J}{photon(\lambda)}} = \frac{photons(\lambda)}{sec}$$

Equation 3.13

A linear regression was established between the counts per second measurement of the photon counting head and the photonic flux measurement of the calibrated silicon photodiode (**Figure 3.6**). The curve fitting tool in Igor Pro software (version 6.3.7) was used to generate a linear fit with a slope equal to 0.0769 and a R^2 value of 0.99.

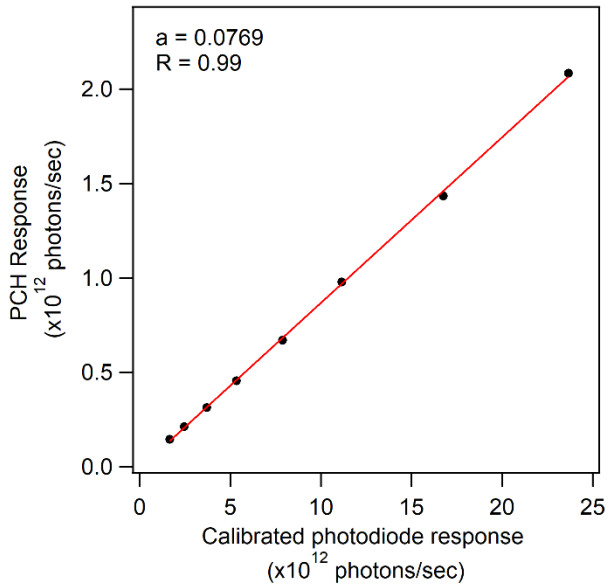

Figure 3.6. Calibration plot of the response of the PCH photodetector measured against a calibrated silicon photodiode. Measurements for both devices have been converted into units of photon flux (*photons/sec*).

3.2.8 The average photodetector response to ECL emission: The C-value

If the full width at half maximum of the emission profile of the measured light source is very small, so much so that it may be reasonably approximated as monochromatic, then a simple correspondence to a responsivity curve will be adequate for correlating the measurement from the photodetector with the radiant power of the incoming light. However, for the $Ru(bpy)_3^{2+}$ ECL emission described in this work, and likely the vast majority of ECL systems, the above 'monochromatic approximation' will not suffice. **Figure 3.7** displays the emission profile of $Ru(bpy)_3^{2+}$ ECL in red, along with the calibrated responsivity curve of the PCH photodetector in blue that was developed from the quantum efficiency curve provided by the PCH manufacturer and our calibration (**Figure 3.8** – **Figure 3.9**). A cursory examination of the overlapping sections in this figure reveals a steep variation of the PCH response in the wavelength range. It is therefore difficult to select a single wavelength that is truly representative of the PCH sensitivity to the ECL emission.

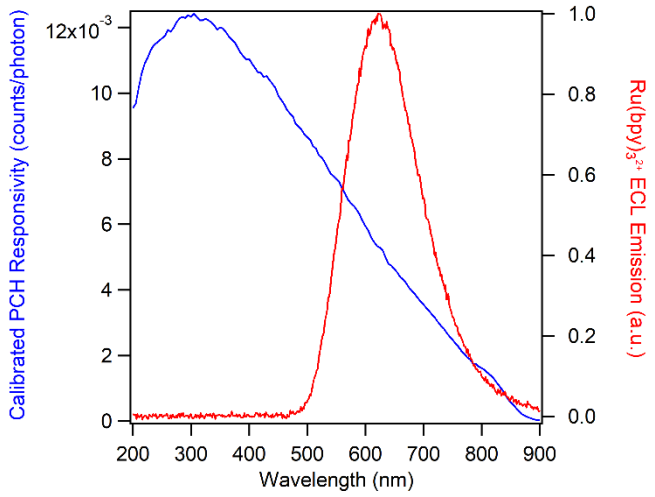

Figure 3.7. Background corrected, intensity-normalized $Ru(bpy)_3^{2+}$ ECL emission spectrum (red) and the calibrated responsivity curve of the photon counting head in counts per photon (blue) as a function of the wavelength.

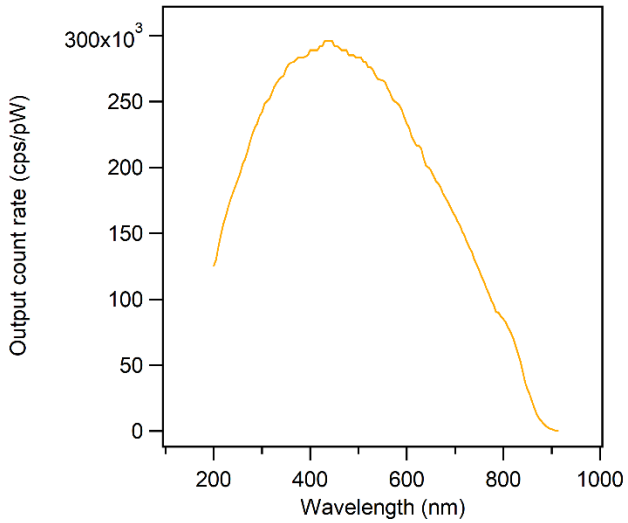

Figure 3.8. Quantum efficiency of the Hamamatsu H6240-02 photon counting head (measured in cps/pW) vs. the incoming emission wavelength.

The quantity cps/pW is equivalent to counts/incident photon, if the energy of the photons are considered. The following equations were used to relate a photon's energy with its wavelength, where h is the Planck constant ($1.986 \times 10^{-25}\ J{\cdot}m$), c is the speed of light ($3.00 \times 10^{8}\ msec^{-1}$) and λ is the wavelength in meters. In this way, subsequent calculations can be performed with more consistent units.

$$E = \frac{hc}{\lambda} = J\ per\ photon(\lambda)$$

Equation 3.14

$$W = \frac{J}{s} \times \frac{1}{\frac{J}{photon(\lambda)}} = \frac{photon(\lambda)}{s}$$

Equation 3.15

$$\frac{\frac{counts}{s}}{pW} = \frac{\frac{counts}{s}}{\frac{photons}{s}} = \frac{counts}{photon}$$

Equation 3.16

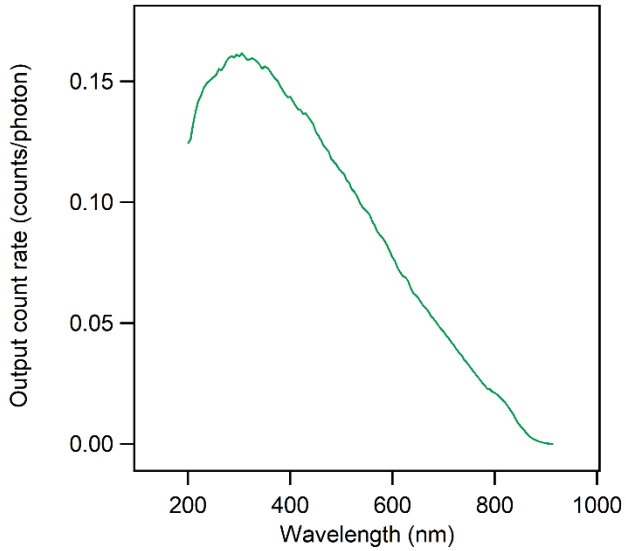

Figure 3.9. Quantum efficiency of the Hamamatsu H6240-02 photon counting head (measured in counts/incident photon) vs. the incoming emission wavelength.

To address this problem, we employ a concept formerly defined as the *C value* by Anaya et al.[31, 32] This value represents the average photodetector response to the specific emission profile of a light source under study, and is obtained using **Equation 3.17**, where $Q(\lambda)$ is the calibrated quantum efficiency at each wavelength for the H6240-02 photon counting head, and $S(\lambda)$ is the background-corrected intensity-normalized ECL emission spectrum. $Q(\lambda)$ and $S(\lambda)$ are provided in **Figure 3.10** and **Figure 3.11**, respectively.

$$C = \frac{\int Q(\lambda) \cdot S(\lambda) \cdot d\lambda}{\int S(\lambda) \cdot d\lambda}$$

Equation 3.17

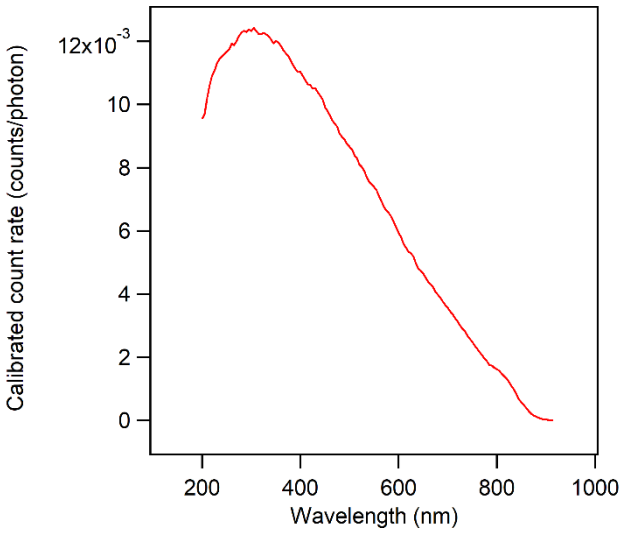

Figure 3.10. Calibrated quantum efficiency of the Hamamatsu H6240-02 photon counting head (measured in counts/incident photon) vs. the incoming emission wavelength. Obtained by applying the calibration factor to **Figure 3.9**.

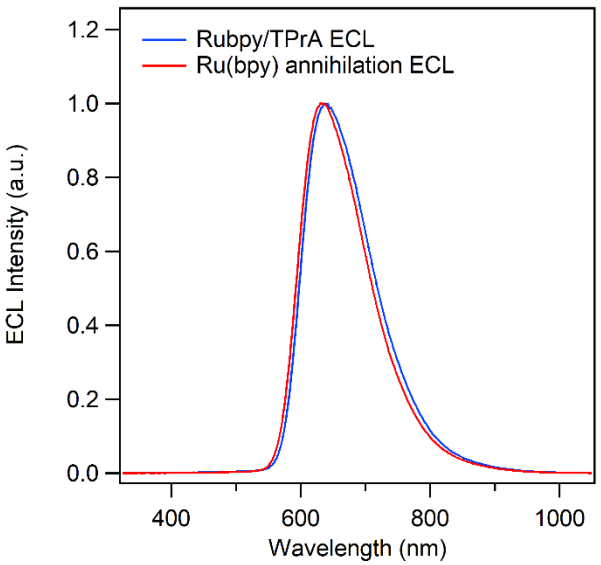

Figure 3.11. Background-corrected and normalized intensity ECL emission spectra of $Ru(bpy)_3^{2+}$ annihilation and TPrA coreactant systems.

We consider individual portions of the emission spectrum, and the corresponding detector responsivity to that portion; the size of these segments is defined by wavelength intervals equal to $d\lambda$. Summation of these portions encompassing the entirety of the emission

spectrum will yield the average photodetector response (in counts per photon) to the incoming light. The *C value* has units identical to the quantum efficiency of the photodetector. In practice, a perfect agreement of $d\lambda$ between the quantum efficiency and the emission spectrum may be difficult, as they are intrinsic properties of different instruments. We have employed mathematical interpolation to reconcile these differences to minimize the error involved in the integration process (details are provided in SI in the section *Integration and Interpolation*). We report here a C-value of 0.0564 counts per incoming $Ru(bpy)_3^{2+}$ ECL photon (obtained by applying **Equation 3.17** to the PCH responsivity curve in **Figure 3.9**). This means that approximately every 18 photons produced from ECL will result in a signal outputted from the photodetector. Adjusting the C-value by the calibration factor of 0.0769 obtained from previous sections yields the *calibrated C value* (0.0043 calibrated counts per photon, from applying **Equation 3.17** to **Figure 3.10**). The calibrated C value has the effect of combining the C-value and the calibration factor into a single entity, which significantly simplifies later calculations.

3.2.9 Photodetector surface area correction

ECL emission is assumed to follow a non-Lambertian (isotropic) profile, in that the distribution of the emitted radiation is uniform in all directions with respect to the source.[33] This means that a photodetector with a certain active surface area will capture only a small fraction of the total emitted light, and a correction factor, introduced here as the *active surface area correction*, is necessary to obtain the true value for the photons produced from the ECL process. We can imagine the emission originating from a point close to the surface of the electrode, emanating outwards in a hemispherical fashion before striking the photodetector (**Figure 3.1** inset). The fraction of the light that is intercepted by the photodetector may be described using the following relationship, where *A* is the active surface area of the photon counting head, and *r* is the distance between the surface of the electrode and the detector (**Equation 3.18**).

$$\Omega = \frac{A}{r^2} = \frac{24\ mm^2}{(44.5\ mm)^2} = 0.012\ sr$$

Equation 3.18

$$0.012\ sr\ \times \frac{1}{4\pi \times \frac{sr}{sph}} = 0.000964$$

Equation 3.19

Given a photodetector surface area of 24 mm^2 (dimensions provided by the manufacturer and verified by our own measurements) and a measured distance of 44.5 mm between the surface of the working electrode and the photon counting head, a value of 0.012 steradians was obtained. **Figure 3.12** illustrates the relationship between photodetector-electrode distance and the calculated steradian quantity. Since the full sphere contains 4π steradians, we can use **Equation 3.19** to express the solid angle in terms of the geometry of the three-dimensional sphere. The final value of 0.000964 represents the fraction of the full sphere of emission that the photodetector will capture.

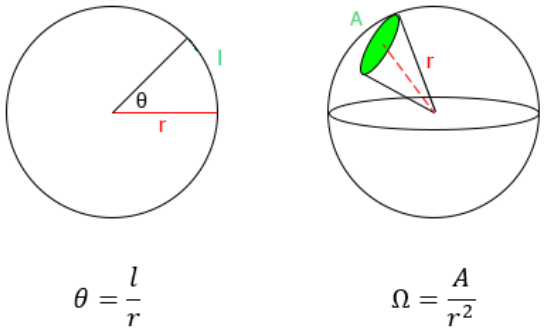

Figure 3.12. A comparison of angles (circles) vs. solid angles (spheres). A circle contains 2π radians, while a sphere contains 4π steradians. The solid angle (in steradians) of a unit sphere is analogous to the planar angle (in radians) of a unit circle. Radians = ratio of the length of the arc vs. radius of the circle. Steradians = ratio of the spherical surface area vs. the square of the radius of the sphere.[34]

3.2.10 Electrode reflectivity correction

The use of a flat disc electrode, such as the one described in this work, means that only the lower hemisphere of ECL emission will directly encounter the photodetector. However, our assumption for isotropic ECL emission means that photons are equally likely to be emitted upwards towards the electrode surface. Therefore, a consideration of

electrode reflectivity must be made. We have assumed a reflectance value of 60% for a polished platinum electrode at 620 nm,[35] which results in a correction factor of 1.40.

We first consider the two bounding scenarios of electrode reflectivity. The first occurs if the electrode surface absorbs all incident radiation; here, a correction factor of 2 is required to account for the lost photons projected towards the upper hemisphere. The second scenario occurs if the electrode surface is instead a perfect mirror, in which case no correction factor is required, because all the ECL photons will eventually end up at the photodetector. The experimental correction factor will therefore lie somewhere in between these two extremes. For the experiments described in this work, the following equation (**Equation 3.20**) provides the reflectivity correction factor (σ), where $ECL_{corrected}$ and $ECL_{observed}$ is the corrected and observed ECL intensity, respectively, and *R* is the reflectivity of the electrode (assumed to be 60%).

$$\sigma = \frac{ECL_{corrected}}{ECL_{observed}} = 2 - R = 2 - 0.6 = 1.40$$

Equation 3.20

3.2.11 Solution self-absorption correction

Partial attenuation of the ECL signal by the coloured $Ru(bpy)_3^{2+}$ solution may occur when there is significant overlap between the excitation and emission spectra of the sample. This is known as the secondary inner filter effect[36], and if left unaccounted for, may reduce the total observed photon flux. To correct for this, we first consider the absorption and emission spectrum of a $Ru(bpy)_3^{2+}$ solution at a 1 mM concentration. We approximate the ECL emission spectrum with a Gaussian distribution, and obtain the difference between the measured data and the fitted data. This ratio between the values was found to be 19% (corresponding to a correction factor of 1.19), which represents the percentage of light lost due to solution self-absorption.

3.2.12 Corrected total photons

The corrected total photons produced by the ECL process (over the duration of a potentiodynamic experiment) is the final value obtained after applying each correction

factor as described in previous sections (**Equation 3.21**). Many other properties of a luminescent system can be derived from this fundamental value, including the radiance [$W \cdot sr^{-1}$], the luminance [$cd \cdot m^2$], and the absolute quantum efficiency [%].

$$Corrected\ total\ photons = \frac{(Total\ counts) \times (Self\ absorption\ correction\ factor)}{\left(\frac{Calibrated\ counts}{photons}\right) \times (Surface\ area\ correction) \times (Reflectivity)}$$

Equation 3.21

The calibration factors described here are specific to this experimental setup. Therefore, any deviation from the procedure, such as the analysis of a different ECL luminophore, will necessitate the recalculation of several factors. In particular, the C-value and the solution self-absorption correction factor are dependent on the emissive characteristics of the luminophore, and the surface area and electrode reflectivity correction factors are dependent on the instruments and equipment used.

In the scenario where a different electrode or a modified electrode is used (GCE or ITO), the change in electrode geometry and materials will require the surface area and electrode reflectivity correction factors to be recalculated. If we switch to an aqueous system, the solution self-absorption correction factor will need to be adjusted, as the transmission of ECL light will be affected by the new solvent.

3.2.13 Correction for the Faradaic current

A consideration of the Faradaic current, i.e., the current actively involved in the oxidation of reduction of electrochemical species in solution, is required to obtain a meaningful value for ECL efficiency. The Faradaic current must be made distinct from the total (measured) electrochemical current, the latter which includes the current due to non-Faradaic processes such as double layer capacitance and ion migration. All current measurements were carried out simultaneously along with electrochemiluminescence tests using voltages slightly below the oxidation or reduction potentials of $Ru(bpy)_3^{2+}$ (for example in the instance where $Ru(bpy)_3^{2+}$ is oxidized and reduced at 1.30 V and −1.31 V vs. SCE as illustrated in **Figure 3.13**, the potentials were restricted to an intermediate range of 1.10 V to −1.10 V). This enables the approximation of the background charging current, up until potentials just

before the generation of $Ru(bpy)_3^{2+}$ radical species. Subtraction of this background charging current from the total measured electrochemical current results in an estimate of the Faradaic current. This difference was found to be 50% for annihilation cyclic voltammograms, and 9% for potential stepping at a frequency of 10 Hz. For coreactant ECL, this difference was found to be 50% for both cyclic voltammograms and potential stepping.

The total charge is the cumulative integral of the current (**Equation 3.22**). Dividing by the elementary charge constant (e = 1.602 × 10^{-19} C) yields the total number of electrons (**Equation 3.23**).

$$Total\ charge = \int_0^t Current \cdot dt$$

Equation 3.22

$$Total\ electrons = \frac{Total\ charge}{e}$$

Equation 3.23

3.3 Results and discussion

3.3.1 $Ru(bpy)_3^{2+}$ ECL via the annihilation pathway

The electrochemistry of $Ru(bpy)_3(PF_6)_2$ was first explored in anhydrous acetonitrile (**Figure 3.13**). When the applied potential was scanned in the cathodic direction, three consecutive reductions $Ru(bpy)_3^{2+}$ occurred at formal potentials of −1.31 V, −1.50 V, and −1.75 V vs. SCE; when the applied potential was scanned in the anodic direction, $Ru(bpy)_3^{2+}$ was oxidized at a formal potential of 1.30 V. An electron transfer reaction between the radical anions (produced during the cathodic scan) and the radical cations (produced during the anodic scan) generates an excited state, $Ru(bpy)_3^{2}$*, which releases light upon its relaxation to the ground state. The light generated is displayed in the blue ECL-voltage curve in **Figure 3.13**, where an emission peak of approximately 300 counts at 1.30 V coincides well with the oxidation of $Ru(bpy)_3^{2+}$. In contrast, almost no ECL signal was detected on the cathodic side of the potential scan, which suggests that the

stability of the radical cation may be limited. These findings line up well with previous reports describing $Ru(bpy)_3^{2+}$ annihilation.[23, 37] The advantage of using a PCH over a PMT is the direct reading of photon numbers while the ECL intensity expressed as photocurrent from a PMT needs an integration versus time.

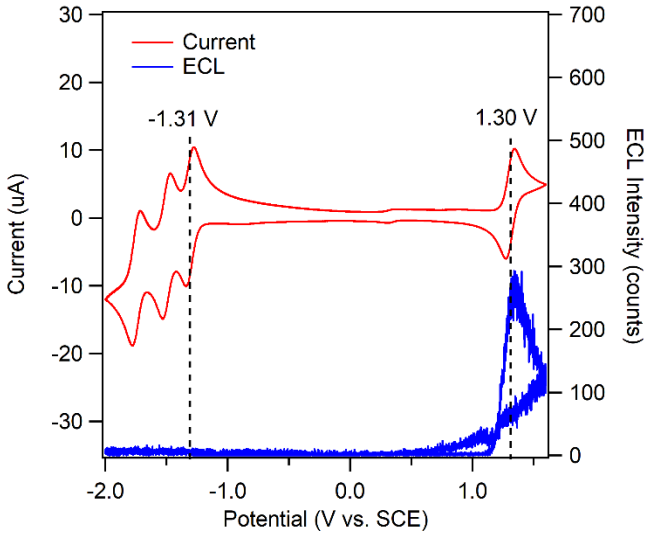

Figure 3.13. Cyclic voltammogram (red) and ECL-voltage curve (blue) of 1 mM $Ru(bpy)_3(PF_6)_2$ in acetonitrile with 0.1 M $TBAPF_6$ as the supporting electrolyte. Dotted lines highlight the potentials for the first reduction and oxidation. Scan rate for the cyclic voltammogram was 100 mV/sec. Bin width = 10.48 msec, number of bins = 14 336, trigger level = 0.3 V, records per scan = 1.

Next, potential stepping experiments were conducted, using the first oxidation and reduction potentials of $Ru(bpy)_3^{2+}$, plus an additional 50 mV of overpotential: 1.35 V and −1.36 V vs. SCE, respectively. This ensures that only the first radical cation and anions of $Ru(bpy)_3^{2+}$ will undergo annihilation, and avoids many complications that arise when analyzing the mechanisms involving doubly- and triply-reduced radical species. At a pulsing frequency of 10 Hz (corresponding to a pulse width of 100 milliseconds for each individual anodic and cathodic step) a peak of approximately 700 000 counts was observed promptly after the onset of each voltage pulse, followed by a rapid decay to the baseline (**Figure 3.14**). This large enhancement in the ECL intensity by using potential stepping has been well reported for many organometallic and nanocluster luminophores[38,

[39], and is commonly attributed to the significantly shorter time delay between the generation of the radical species required for ECL emission. As a result, more electrogenerated radicals will successfully undergo electron transfer reactions to form emissive excited states, and the overall number of ECL photons is increased.

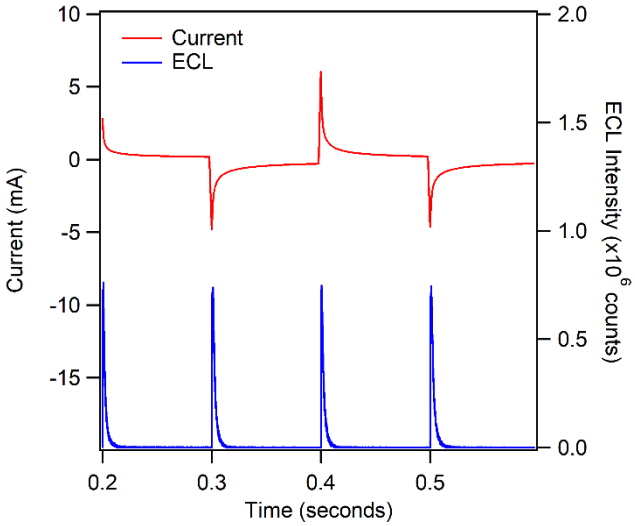

Figure 3.14. Potential stepping of $Ru(bpy)_3^{2+}$ between 1.35 V and −1.36 V at 10 Hz (100 msec pulse width). Current shown in red, and ECL photon counts shown in blue, ECL measured by the H6240-02 photon counting head. Bin width = 40.96 msec, number of bins = 13 312, trigger level = −1.10 V, records per scan = 1.

This stronger ECL signal in the potential stepping method is directly manifested as a nearly 1000-fold enhancement in the overall efficiency when compared to the potential sweep: the absolute efficiencies of these processes were determined to be 3.2 ± 0.1% and 0.0033 ± 0.0011%, respectively, through the calibration and correction steps described above. Here, one can see the significant efficiency discrepancy following varied electrochemical methods. It is very hard and inaccurate to quantify ECL QE using **Equation 3.1** relative to $Ru(bpy)_3^{2+}$ ϕ_{ECL}.

3.3.2 The $Ru(bpy)_3^{2+}$/TPrA ECL coreactant system

Next, the ECL and the associated efficiency of the $Ru(bpy)_3^{2+}$/TPrA coreactant system was explored. **Figure 3.15** shows a cyclic voltammogram of $Ru(bpy)_3^{2+}$ with the addition

of 10 mM of TPrA. During an anodic potential sweep, two consecutive peaks were observed at 0.82 V and 1.27 V corresponding to the oxidation of tripropylamine and $Ru(bpy)_3^{2+}$, respectively. A minor, but non-negligible ECL signal is present as early as 0.70 V, followed by a second prominent ECL peak at an onset voltage of 1.10 V, the latter which increased steadily to a maximum of approximately 2 million counts. The first and second ECL signals concur well with the scheme proposed by Miao et al. in 2002, where the TPrA radical ($TPrA^{\bullet}$) can participate in the oxidation of $Ru(bpy)_3^{2+}$ to form $Ru(bpy)^{+}$, thereby enabling the generation of the excited state $Ru(bpy)_3^{2*}$ at potentials lower than that required for the direct electro-oxidation of $Ru(bpy)_3^{2+}$.[40] The prominence of this first ECL peak due to the interaction between $TPrA^{\bullet}$ and $Ru(bpy)^{+}$ is enhanced at higher concentrations of TPrA which further supports the oxidative capabilities of the TPrA radical.

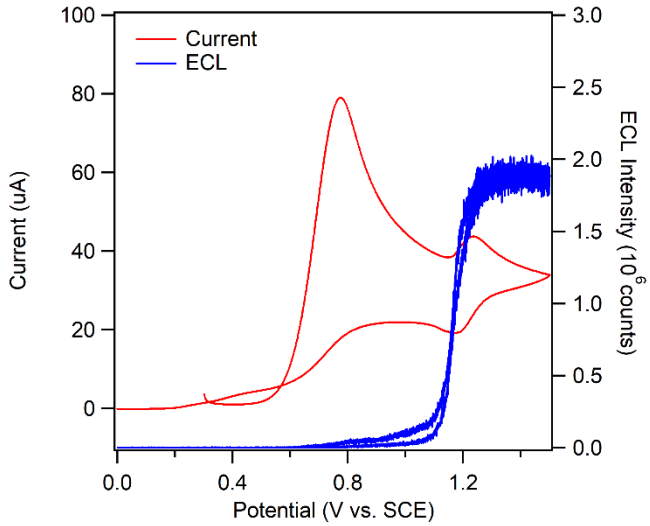

Figure 3.15. Cyclic voltammogram (red) and ECL-voltage curve (blue) of 1 mM $Ru(bpy)_3^{2+}$ in acetonitrile with 10 mM TPrA. Scan rate for the cyclic voltammogram was 100 mV/sec. Bin width = 2.62 msec, number of bins = 11 264, trigger level = 0.30 V, records per scan = 1.

The overall efficiency of this system (using potential sweeping) was calculated to be 3.1 ± 0.7% which is a considerable enhancement in comparison with that in the annihilation CV ECL (approximately 1000-fold). This can be readily explained by the closer potential

ranges over which the TPrA and $Ru(bpy)_3^{2+}$ radical species are generated: in a coreactant system, only a one-directional potential step is required, significantly reducing the time before they meet to react.

Potential pulsing experiments were then carried out with this $Ru(bpy)_3^{2+}$/TPrA system (**Figure 3.16**). Upon the application of an anodic potential step, there is a sharp increase in the ECL signal, followed by an exponential decay as the electrogenerated radicals are gradually depleted. The overall profile of the ECL peak is also much different than the one observed in annihilation, as it does not fully decay to baseline levels during the anodic steps. The persistence of the ECL signal is likely due the fact that both $TPrA^{\bullet+}$ and $Ru(bpy)_3^{\bullet+}$ radical anions are being continuously generated over the duration of the anodic pulse. This behaviour results in the most efficient ECL process discussed thus far, at 10.0 ± 1.1% efficiency. It is worth emphasizing the efficiency discrepancy with varied electrochemical methods such as CV and chronoamperometry even in a coreactant system.

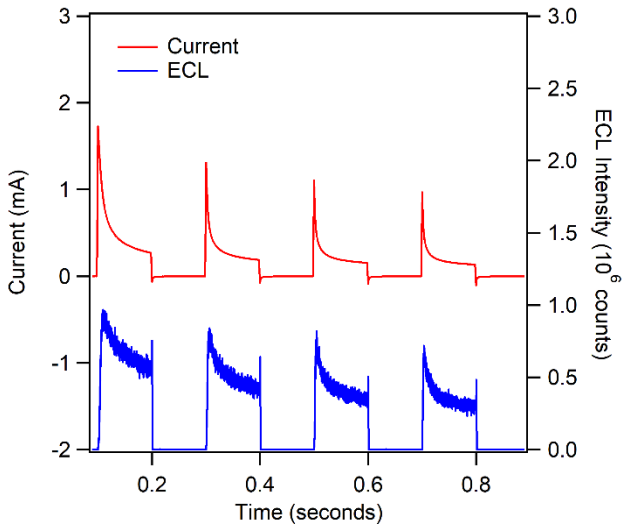

Figure 3.16. Potential step experiment of 1 mM $Ru(bpy)_3^{2+}$ with 10 mM TPrA, between 0 V and 1.50 V at 10 Hz (100 msec pulse width). Current is shown in red, and ECL intensity (as photon counts) is shown in blue. Bin width = 81.92 μsec, number of bins = 13 312, trigger level = −1.40 V, records per scan = 1.

The TPrA concentration was then increased to explore the effects of coreactant concentrations on the ECL efficiency. **Table 3.1** contains a summary of the quantum efficiencies of the annihilation and coreactant (from 5 – 50 mM of TPrA) pathways of $Ru(bpy)_3^{2+}$. The maximum ECL efficiency for this system was observed at a TPrA concentration of 10 mM, at 3.1 ± 0.7% and 10.0 ± 1.1% for the cyclic voltammetry and potential stepping methods, respectively. This range of TPrA concentrations has been reported to be optimal in the past.[41-43] At higher TPrA concentrations than 10 mM, the calculated efficiencies began to decrease. This may be due to the imbalance in the relative concentrations of the electrogenerated radicals of $Ru(bpy)_3^{2+}$ and TPrA. The results suggest that there should exist an optimal ratio between the concentrations of these two species, one that maximizes the probability of successful electron transfers between luminophore and coreactant, and therefore results in the greatest amount of ECL photons produced without needlessly oxidizing or reducing ECL reagents. When the concentration of TPrA increases above this critical value, the excessive oxidation of TPrA molecules results in a greater contribution to the electrochemical current compared to the total ECL photons produced, leading to a reduction in the ECL quantum efficiency.

Some general trends should be noted upon observation of **Table 3.1**. Firstly, potential stepping as the driving force for electro-generation of ECL radicals exhibit superior efficiency in all of our experiments, although this difference is drastically lessened when a coreactant is introduced. Secondly, the use of TPrA as a coreactant in the ECL system results in a maximum efficiency enhancement of 1000-fold and 3-fold in the potential sweeping and potential stepping methods, respectively. Thirdly, there appears to be a rather precipitous drop in the coreactant ECL efficiency at concentrations greater than 20 mM TPrA per 1 mM $Ru(bpy)_3^{2+}$, which is likely due to ECL quenching by the substantial excess of TPrA molecules. This was observed by our group on investigation of ECL-QEs relative to that of $Ru(bpy)_3^{2+}$/TPrA for the Au_{38}/TPrA coreactant system,[43] in which the fraction on the denominator in **Equation 3.2** decreases and leads to a mathematical augmentation of the relative ECL-QE that does not truly reflect the physical and chemical phenomena involved in ECL reactions and their efficiencies. Lastly, the significance of redox potential matching between the luminophore and coreactant cannot be understated: the closer the redox potentials of these two species, the greater the reaction probability

and the overall ECL efficiency. This is one of the reasons why the $Ru(bpy)_3^{2+}$/TPrA system is exemplary in this field: the two individual species have very close oxidation potentials so that the two radicals are generated simultaneously to react, leading to a high ECL efficiency.

Table 3.1. Calculated quantum efficiencies of the $Ru(bpy)_3^{2+}$ annihilation and $Ru(bpy)_3^{2+}$/TPrA ECL systems. $Ru(bpy)_3^{2+}$ concentration was 1 mM for all experiments. Every experiment was repeated at least three times. Errors provided represent one standard deviation calculated across individual measurements.

	Cyclic voltammetry (CV)*	Pulsing stepping (10 Hz)**
Annihilation	0.0033 ± 0.0011%	3.2 ± 0.1%
5 mM TPrA	1.5 ± 0.3%	7.5 ± 1.2%
10 mM TPrA	3.1 ± 0.7%	10.0 ± 1.1%
20 mM TPrA	1.8 ± 0.4%	2.0 ± 0.3%
50 mM TPrA	0.8 ± 0.1%	0.5 ± 0.2%

*The second cycle was taken. ** The average of four pulses was taken.

3.4 Conclusions

In conclusion, we have demonstrated in this work a universal and easily implemented procedure for determining the absolute QE of ECL systems, especially that of coreactant ECL systems for the first time. We showcase this method by determining the ECL QEs of $Ru(bpy)_3^{2+}$ annihilation and $Ru(bpy)_3^{2+}$/TPrA coreactant systems in various conditions such as varied electrochemical methods and TPrA concentrations. The procedures detailed here will guide researchers towards a precise, objective, and reproducible method for determining the absolute ECL QEs, which will be applicable to other light-emitting processes, and will ultimately encourage a standardized procedure to compare efficiencies between different luminophores, long-missed in the field of ECL research. With possible availability to calibrate a photon counting head by its manufacturer as the existing calibration service of a photomultiplier tube, our physical strategy to determine the absolute QE of any ECL systems will be very approachable to researchers in many scientific fields.

3.5 References

[1] Richter, M. M. *Chem. Rev.* **2004,** *104*, 3003-36.

[2] Miao, W. *Chem. Rev.* **2008,** *108*, 2506-53.

[3] Hesari, M.; Ding, Z. *J. Electrochem. Soc.* **2016,** *163*, H3116-H3131.

[4] Bard, A. J., *Electrogenerated chemiluminescence*. Marcel Dekker: New York, 2004.

[5] Yuan, Y.; Han, S.; Hu, L.; Parveen, S.; Xu, G. *Electrochim. Acta* **2012,** *82*, 484.

[6] Hesari, M.; Swanick, K. N.; Lu, J. S.; Whyte, R.; Wang, S.; Ding, Z. *J. Am. Chem. Soc.* **2015,** *137*, 11266-9.

[7] Hesari, M.; Workentin, M. S.; Ding, Z. *Chem. Sci.* **2014,** *5*, 3814-3822.

[8] Hercules, D. M. *Science* **1964,** *145*, 808.

[9] Chandross, E. A.; Sonntag, F. I. *J. Am. Chem. Soc.* **1964,** *86*, 3179.

[10] Santhanam, K. S. V.; Bard, A. J. *J. Am. Chem. Soc.* **1965,** *87*, 139.

[11] Dauphin, A. L.; Akchach, A.; Voci, S.; Kuhn, A.; Xu, G.; Bouffier, L.; Sojic, N. *J. Phys. Chem. Lett.* **2019,** *10*, 5318.

[12] Li, Z.; Wu, S.; Zhang, B.; Fu, L.; Zou, G. *J. Phys. Chem. Lett.* **2019,** *10*, 5408.

[13] Wang, Z.; Feng, Y.; Wang, N.; Cheng, Y.; Quan, Y.; Ju, H. *J. Phys. Chem. Lett.* **2018,** *9*, 5296.

[14] He, Y.; Yang, L.; Zhang, F.; Zhang, B.; Zou, G. *J. Phys. Chem. Lett.* **2018,** *9*, 6089.

[15] Qi, H.; Zhang, C. *Anal. Chem.* **2020,** *92*, 524.

[16] Lou, J.; Liu, S.; Tu, W.; Dai, Z. *Anal. Chem.* **2015,** *87*, 1145.

[17] Kurita, R.; Arai, K.; Nakamoto, K.; Kato, D.; Niwa, O. *Anal. Chem.* **2010,** *82*, 1692.

[18] Kurita, R.; Arai, K.; Nakamoto, K.; Kato, D.; Niwa, O. *Anal. Chem.* **2012,** *84*, 1799.

[19] Kong, S. H.; Lee, J. I.; Kim, S.; Kang, M. S. *ACS Photonics* **2018,** *5*, 267.

[20] Cho, K. G.; Lee, J. I.; Lee, S.; Hong, K.; Kang, M. S.; Lee, K. H. *Adv. Funct. Mater.* **2020,** *30*, 1907936.

[21] Ma, C.; Cao, Y.; Gou, X.; Zhu, J. J. *Anal. Chem.* **2020,** *92*, 431.

[22] Zhang, R.; Zhang, A.; Stillman, M. J.; Ding, Z. *J. Phys. Chem. C* **2020,** *124*, 16568.

[23] Tokel-Takvoryan, N. E.; Hemingway, R. E.; Bard, A. J. *J. Am. Chem. Soc.* **1973,** *95*, 6582.

[24] Richter, M. M.; Bard, A. J.; Kim, W.; Schmehl, R. H. *Anal. Chem.* **1998,** *70*, 310.

[25] Wong, J. M.; Zhang, R.; Xie, P.; Yang, L.; Zhang, M.; Zhou, R.; Wang, R.; Shen, Y.; Yang, B.; Wang, H. *Angew. Chem., Int. Ed.* **2020,** *59*, 17461.

[26] Adsetts, J. R.; Ding, Z. *ChemPlusChem* **2021,** *86*, 155.

[27] Adsetts, J. R.; Hoesterey, S.; Gao, C.; Love, D. A.; Ding, Z. *Langmuir* **2020,** *36*, 14432.

[28] Wong, J. M.; Xu, J.; Zhang, R.; Chu, K.; Ding, Z.; Liu, L. *J. Phys. Chem. C* **2021,** *125*, 13696.

[29] Sahami, S.; Weaver, M. J. *J. Electroanal. Chem. Interfacial Electrochem.* **1981,** *122*, 155.

[30] Hesari, M.; Ding, Z. *Nat. Protoc.* **2021,** *16*, 2109-2130.

[31] Anaya, M.; Rand, B. P.; Holmes, R. J.; Credgington, D.; Bolink, H. J.; Friend, R. H.; Wang, J.; Greenham, N. C.; Stranks, S. D. *Nat. Photon.* **2019,** *13*, 818.

[32] Bezman, R.; Faulkner, L. R. *Anal. Chem.* **1971,** *43*, 1749.

[33] Keszthelyi, C. P.; Tokel-Takvoryan, N. E.; Bard, A. J. *Anal. Chem.* **1975,** *47*, 249.

[34] Eriksson, F. *Mathematics Magazine* **1990,** *63*, 184-187.

[35] Hadley, L.; Hass, G., *American Institute of Physics Handbook*. 1972.

[36] Chen, S.; Yu, Y. L.; Wang, J. H. *Anal. Chim. Acta.* **2018,** *999*, 13-26.

[37] Wallace, W. L.; Bard, A. J. *J. Phys. Chem. A* **1979,** *83*, 1350.

[38] Swanick, K. N.; Ladouceur, S.; Zysman-Colman, E.; Ding, Z. *Chem. Commun.* **2012,** *48*, 3179-3181.

[39] Yang, L.; Zhang, B.; Fu, L.; Fu, K.; Zou, G. *Angew. Chem., Int. Ed.* **2019,** *58*, 6901.

[40] Miao, W.; Choi, J. P.; Bard, A. J. *J. Am. Chem. Soc.* **2002,** *124*, 14478.

[41] Hesari, M.; Lu, J. s.; Wang, S.; Ding, Z. *Chem. Commun.* **2015,** *51*, 1081.

[42] Hesari, M.; Barbon, S. M.; Mendes, R. B.; Staroverov, V. N.; Ding, Z.; Gilroy, J. B. *J. Phys. Chem. C* **2018,** *122*, 1258.

[43] Hesari, M.; Workentin, M. S.; Ding, Z. *ACS Nano* **2014,** *8*, 8543-8553.

Chapter 4

This chapter expands on the previous chapter to include methodology and instrumentation to measure the absolute ECL quantum efficiency with a spectroscopic approach using a charge-coupled device (digital camera). It is expected that this will enable significantly wider reach for ECL efficiency measurements presented in this work.

4 The Absolute Electrochemiluminescence Efficiency of Au Nanoclusters by Means of a Spectroscopy Charge-coupled Device Camera[†]

Currently, a luminophore's electrochemiluminescence (ECL) efficiency is evaluated by measuring the ratio of ECL intensity generated by certain number of electrons injected. Then, this ratio is compared to that of the commercial luminophore, $Ru(bpy)_3^{2+}$ under the same test conditions. However, the ECL intensity from a luminophore will be different on every instrumental setup due to wavelength-specific interaction of light with photodetectors. Also, previous absolute ECL techniques require multiple instruments, each of which has its own wavelength-specific light losses leading to complicated hardware and calculation requirements. Herein, this manuscript presents an absolute way to evaluate the ECL quantum efficiency, permitting researchers to quickly compare ECL results and elucidate ECL mechanisms. This new physical strategy is exemplified with $Au_{25}^0(SC_2H_4Ph)_{18}$ and verified with $Ru(bpy)_3^{2+}$ to represent a difficult spectroscopic challenge and to verify the precision and accuracy of the new technique in comparison to previously reported absolute measurement values. It is highly recommended for all ECL researchers to swap relative ECL efficiencies for the absolute ECL quantum efficiency. Finally, $Ru(bpy)_3^{2+}$'s ECL QE at different TPrA concentrations was evaluated to understand how the TPrA concentration affects the ECL QE of $Ru(bpy)_3^{2+}$. Along with our previous publications on Au cluster ECL, discussed are factors influencing the ECL

[†] This work has been published. Adsetts, J.[§]; Chu, K.[§]; Hesari, M.; Whitworth, Z.; Qin, X.; Zhan, Z.; Ding, Z. Absolute Electrochemiluminescence Quantum Efficiencies of Au Nanoclusters by Means of a Spectroscopy Charge-coupled Device Camera. *J. Phys. Chem. C* (**2022**) 47, 20155-20162. [§] indicates equally contributed first author.

intensity such as the diffusion of electroactive molecules, the stability of radicals, the reactivity of excited states and the analyte's reactivity. Profound variations were observed on this finding, which has large implications for past, current and future relative ECL efficiencies also discussed in length.

4.1 Introduction

In electrochemiluminescence (ECL) of a luminophore in investigations, most quantum efficiency measurements are taken relative to that of conventional standard $Ru(bpy)_3^{2+}$ by comparing their ratios of ECL emission to total charge injected in similar conditions using the following equation:[1]

$$\Phi_{ECL,x} = \Phi_{ECL,st} * \left(\frac{ECL_x}{ECL_{st}}\right) * \left(\frac{Q_{st}}{Q_x}\right)$$

Equation 4.1

where Φ_{ECL} is the ECL efficiency, *ECL* is integrated photodetector signal, *Q* is the charge in units of Coulombs, and *st* and *x* denote the standard $Ru(bpy)_3^{2+}$ and luminophore, respectively. The quantum efficiency of $Ru(bpy)_3^{2+}$(QE, $\Phi_{ECL,st}$) is commonly referenced as 5%. However, this result came from the Bard group in 1973 where they used a relatively high concentration of $Ru(bpy)_3^{2+}$ in solution with a rotating ring-disk electrode (RRDE).[2] This RRDE was rotating quickly where a ring electrode generates $Ru(bpy)_3^{3+}$ and the disk electrode generates $Ru(bpy)^{+}$,[3] which undergo an electron transfer to form an excited state emitting ECL. However, most ECL experiments are performed in static solutions and a RRDE is rarely used. Therefore, comparing ECL efficiencies to this landmark study is often inconvenient and inconsistent. Based on the vast research field on ECL fundamentals and applications,[4-18] relative Φ_{ECL} is not enough for quantitative physical measurements.

Another way to evaluate the ECL QE is through simulations.[19-24] Electrochemical oxidation rate constants of coreactants and luminophores can be found experimentally and quickly to guide simulations and to predict the ECL QE tendency.[19] These ECL QE

calculations are effective in optimizing the 3D space that ECL is emitted for enhancing sensing applications.

Literature exists for researchers to measure their own ECL QE that can refer back to the utilization of a calibrated photodiode prior to charge-coupled device (CCD) cameras.[25, 26] Very recently our group has developed methods by means of a photomultiplier in photocurrent and photon-counting modes.[27, 28] The absolute quantum efficiency (Φ_{AQE}) can be determined through the following simplified equation:[27]

$$\Phi_{AQE} = \int_{t=0}^{t=x} \frac{\sum_{pixel=1}^{pixel=w} v_{photons}(t)}{v_{electrons}(t)} dt * 100\ \%$$

Equation 4.2

where Φ_{AQE} is the percent ratio of photons emitted to electrons injected, $v_{photons}(t)$ is the total photon emission rate on a pixel in units of photons s^{-1}, $\Sigma\ v_{photons}(t)$ is the sum of all photons in a defined pixel range, w is the width of the pixel array, $v_{electrons}(t)$ is the electron input in electrons s^{-1} and x is the desired integration time to find Φ_{AQE}. However, these methods involve multiple calibrated instrument setups, greatly increasing the complexity of measurements.[27, 29] Generally in these methods, a pre-calibrated photodetector (such as a photodiode, photon counting head or photomultiplier tube), and a spectrometer are needed to properly evaluate the Φ_{AQE} of a compound. The calibrated photodetector such as a photomultiplier tube (PMT) plays a major role, for which commercial and traceable calibration services are not always available, while most calibrated photodiodes are not sensitive enough to measure certain ECL signals. Furthermore, many photodetectors may not be sensitive to certain wavelengths of light in the near-infrared region, which prevents researchers from properly analyzing their samples of interest. Having multiple instruments able to collect light over large wavelength windows can therefore be expensive and challenging.

Herein, we present an instrumentally and mathematically simpler method to determine Φ_{AQE} using only a spectrometer coupled with a spectroscopy CCD camera calibrated against a pre-calibrated photodiode. Generally, this calibration should be carried out for

the setup once a year and unless the setup is modified, the calibration should be stable. Commercial calibrations to be provided by the spectroscopy CCD camera will be great help to implement the instrumentation. This technique is exemplified with a near-infrared (NIR) emitter, $Au_{25}^{0}(SC_2H_4Ph)_{18}$ nanocluster (which will be abbreviated to Au_{25}^{0}), to demonstrate a relatively difficult spectroscopic challenge.[30]

4.2 Experimental

4.2.1 Materials and reagents

SureSeal benzene (anhydrous, 99.8%) and acetonitrile (anhydrous, 99.8%) were purchased from Sigma Aldrich Canada (Mississauga, ON), and stored in an inert atmosphere. These solvents were mixed in a 1:1 ratio to produce the final solvent mixture used in electrochemical experiments. Tetrabutylammonium perchlorate (TBAP, electrochemical grade, >99.0%) was obtained from Supelco, and used as received. Tripropylamine (TPrA, >98%) was purchased from Sigma-Aldrich Canada, and stored at 4°C. Au_{25}^{0} was synthesized and characterized following our procedure published elsewhere.[30]

4.2.2 Electrochemistry and ECL

A three-electrode system was used for all electrochemical measurements, where the working electrode was a platinum disc (2 mm diameter) inlaid in a glass tube, and the counter and reference electrodes were coiled platinum wires, **Figure 4.1**. Electrochemical measurements were conducted inside a cylindrical glass tube with a flat quartz window at the bottom to allow for the detection of ECL light. The potentiostat used was a CH Instruments Model 610a electrochemical workstation (CH Instruments Inc., Austin, TX) or a PAR 263A potentiostat/ galvanostat (EG&G Princeton Applied Research, Oak Ridge, TN) to generate the *constant potential* profile. ECL spectra were recorded using a SP2300i spectrograph (Teledyne Princeton Instruments, Trenton, NJ) with an attached CCD camera (Andor DU401-BR-DD-352, Oxford Instruments, UK) cooled to −65°C, **Figure 4.1**. Wavelength calibration was accomplished using a mercury source (HG-1, Ocean Optics, Dunedin, FL) using a center wavelength of 546 nm. Spooling ECL spectra

were acquired each at a time interval of 1 s during a cyclic voltammogram; the obtained spectra were combined in a three-dimensional plot using a custom MATLAB program.[31]

4.2.3 Absolute ECL Quantum efficiencies

AQEs were determined from ECL spectra and chronoamperograms using a MATLAB program developed in our group with equations described below.

4.3 Results and Discussion

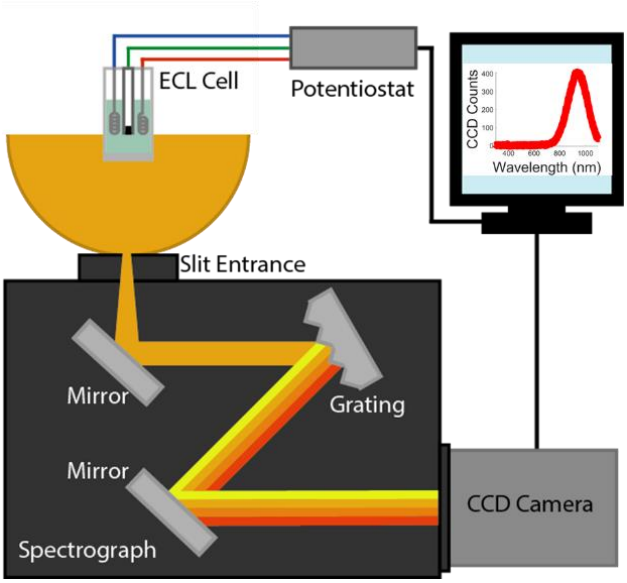

Figure 4.1. Instrumental setup for measuring Φ_{AQE} with a CCD camera coupled to a spectrometer.

4.3.1 Instrument setup and measurements

Figure 4.1 displays the entire spectroelectrochemical/photoelectrochemical setup required for measuring Φ_{AQE} with a spectrograph coupled with a CCD camera. Briefly, a potentiostat applies a working potential to an ECL cell with three electrodes immersed in a solution of 1:1 benzene:acetonitrile containing 6.25 mM tri-*n*-propylamine (TPrA), 0.1 M tetrabutyl ammonium perchlorate (TBAP) and 0.1 mM Au_{25}^{0}. A constant potential of 0.89 V vs. SCE is applied, at which TPrA is oxidized once and Au_{25}^{0} twice to ultimately produce $TPrA^{\bullet}$ and Au_{25}^{2+} respectively, seen in the schematic insets of **Figure 4.2A**, as we reported elsewhere.[30] Accordingly, the electrochemical current-time curve

(chronoamperogram) is shown in **Figure 4.2A**. The generated TPrA$^{\bullet}$ and Au_{25}^{2+} species can react to produce Au_{25}^{+}* and an iminium ion (Im^{+}) in the vicinity of the working electrode.[32] This Au_{25}^{+}* can emit light as ECL with the simplified mechanism shown in the inset of **Figure 4.2B**. For more details on Au_{25}^{0} redox chemistry and Au_{25}^{+} photoluminescence please refer the Latimer diagram we published elsewhere.[30, 33]

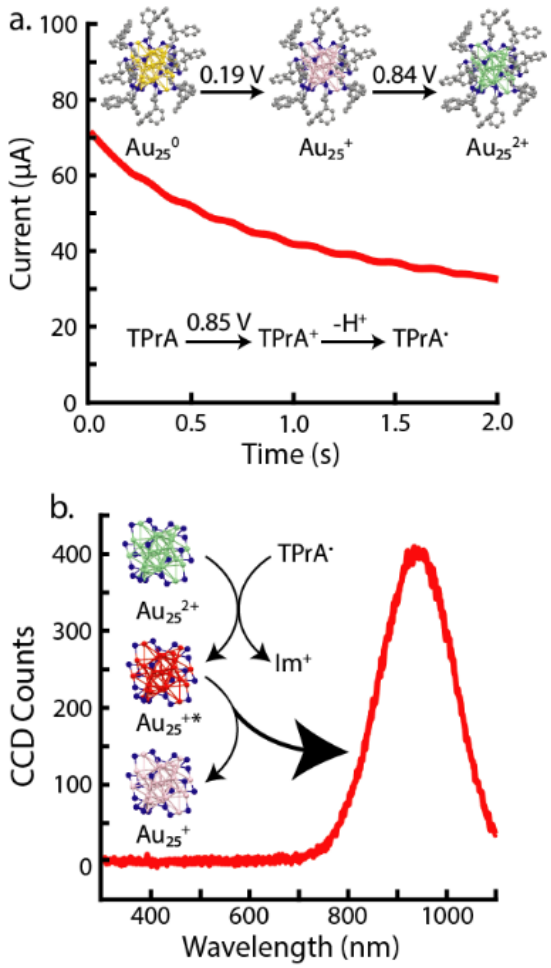

Figure 4.2. Data for evaluating quantum efficiency for a 0.1 mM Au_{25}^{0} 1:1 benzene:acetonitrile solution with 6.25 mM TPrA. (A) The current-time curve collected with a potentiostat is shown along with the two successive oxidation reactions during the constant potential procedure at 0.89 V. (B) The corresponding accumulation ECL spectrum with the Au_{25}^{0}/TPrA ECL mechanism in the inset.

For this experimental setup, the emitted ECL then enters the spectrometer through a slit at a controlled width to adjust the light intensity, **Figure 4.1**. It is assumed here that all light entering the slit will hit the first mirror and that the whole spectrometer is optically aligned. The spectrometer will then have the aluminum mirror reflecting the incident light, then a grating separating light by wavelength, finally another mirror directing the light onto a 2D CCD camera sensor array to produce a spectrum. For example, the CCD array used in this report is a 2D pixel array of 1024x127 pixels. This data is then summed by wavelength into a 1D spectrum seen as the red trace in **Figure 4.2B**. This is all the ECL data needed to calculate the Φ_{AQE} using a CCD camera.

4.3.2 Correction factors in determining the AQE

To determine the Φ_{AQE}, several corrections for the photon and electron counting have been considered for everything the photons and electrons interact with. Some of these factors are not unique to a CCD camera and have been discussed at length elsewhere.[27] The factors specific to this work will be briefly discussed below.

When an ECL photon is initially created, it will pass through the solution it is in and may be self-absorbed. By comparing a UV-visible absorption spectrum to the ECL emission spectrum at the same concentration, any self-absorption is quickly apparent by evaluating the peak overlap. The relevant absorption and emission spectra for the Au_{25}^{0} cluster are shown in **Figure 4.3**. Luckily, for this compound, negligible amounts of light are self-absorbed, meaning that this correction factor (A) is unneeded for this system.

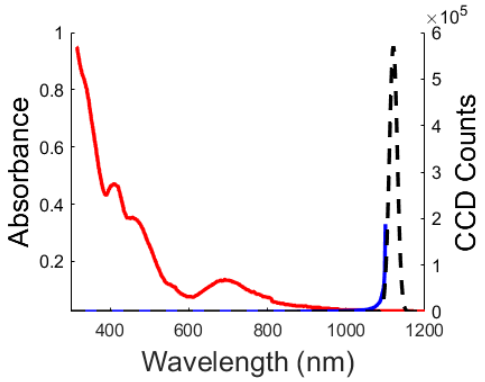

Figure 4.3. A UV-Vis (red) and corrected ECL (blue) spectrum of Au_{25}^{0} at the same concentration. The dashed line is a calculated example of a gaussian peak that could fit the blue line.

Next, the photons will pass through the Pyrex window on the bottom of our ECL cell; a transmission spectrum for this material is shown in **Figure 4.4**. The Pyrex transmits >90% of the light at 950 nm where a wavelength dependent correction for the Pyrex absorption must be applied.[34] Since the Pyrex window transmission is roughly equal over the entire spectrum range between 200 and 1100 nm, this wavelength independent correction factor of 111 % for the Pyrex window should be applied to all data.

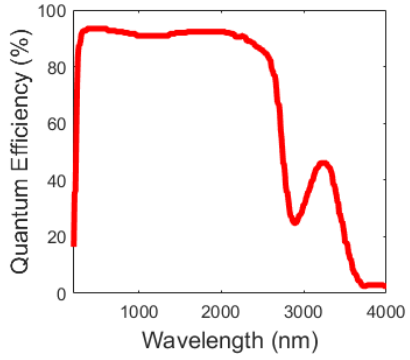

Figure 4.4. Pyrex window transmission percentage.[34]

After the Pyrex window, the photon will pass through the slit of the spectrometer (**Figure 4.1**). Since only a small percentage of the total ECL emission enters the slit, illustrated as a small part of the yellow light hemisphere in **Figure 4.1**, the total number of photons emitted during the ECL process must be corrected from the light measured on the CCD

camera with the solid angle calculation.[2, 3, 28, 35] With a 1.50 mm x 4.25 mm rectangular slit, the surface area of the light collected (A) will be 6.38 mm^2. If the distance between the electrode surface and the spectrometer slit (d) is 20 mm and the proven randomly emitted ECL is in a perfect sphere centered on the electrode,[3] the surface area of the total sphere is 5027 mm^2. However, assuming the total upper hemisphere of emitted light hits the electrode surface, a certain percentage of it will be reflected towards the spectrometer slit inflating the photon value. For a Pt electrode and a ~950 nm emitter, a platinum surface will reflect 77 % of the light which requires a reflectance correction (R_{elec}) of 0.77.[36] These discussions are summarized in the following equation:

$$\sigma_{Spherical} = \frac{A}{4 * \pi * d^2} * (1 + R_{elec})$$

Equation 4.3

where $\sigma_{Spherical}$ describes the light collected from a spherically emitting point source with units of spheres. The $\sigma_{Spherical}$ for this setup discussed so far will be 2.24×10^{-3} spheres collected which is a very small fraction.

The photon will then travel through the spectrometer which generally contains two Al mirrors and a grating as the schematic in **Figure 4.1**. Here, a wavelength specific intensity correction factor is not considered for the sack of simplicity.

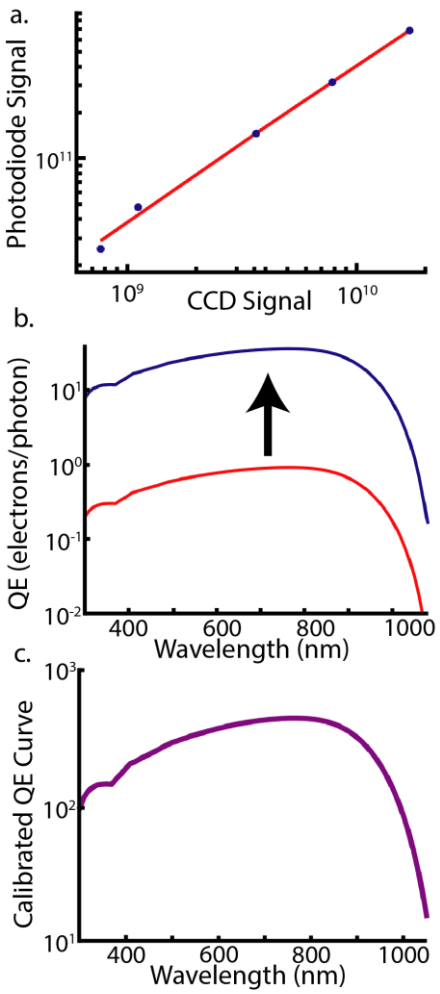

Figure 4.5. (A) The calibration curve for the red LED measured on both the Thorlabs calibrated photodiode and the CCD camera coupled to a spectrometer. Each point corresponds to 3 averaged 60 s scans each at a single potential applied to the LED, ranging from 750 mV to 800 mV. (B) The manufacturer provided QE of a DU401a-BR-DD Andor CCD camera cooled to −70 °C seen as the red trace. The calibrated QE curve which considers light losses in the spectrometer and the CCD camera ($Q(\lambda)$) is seen as the blue trace. (C) The blue curve from Figure 4.5B multiplied by the gain factor.

A CCD camera calibration of the setup's QE curve using a known, stable and wavelength-relevant light source is now required and is the key in the calibration procedure; the blue trace in **Figure 4.5B** shows the final result of this calibration while the red trace in **Figure 4.5B** is the manufacturer-reported QE of the CCD camera. This has been performed with a calibrated Thorlabs S120VC silicon photodiode connected to a

PM100D compact power and energy meter with a bright, stable LED purchased form Vishay Electronics Limited with a center wavelength of 633 nm. This LED wavelength range and stability were verified by the CCD camera in **Figure 4.6**. Briefly, this calibration was performed by measuring the LED emission for 60 s using both the CCD/spectrograph setup and calibrated photodiode. In total, five different driving voltages were used (corresponding to the points in **Figure 4.5A**) for the LED, where tests were performed in triplicate and averaged. The unitless calibration value was taken as the slope of the line of best fit for **Figure 4.5A** and was found to be 39.1. This means the LED light measurements on this spectrometer/CCD camera setup should be adjusted 39.1 times higher. Then, this calibration factor was incorporated into the QE of the CCD camera (red trace) to produce a calibrated QE for the entire setup ($Q(\lambda)$) shown as the blue trace in **Figure 4.5C**.

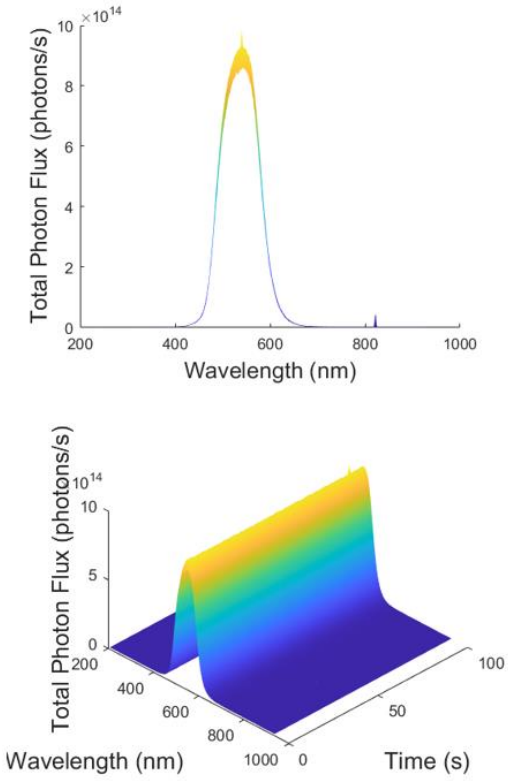

Figure 4.6. The stability (top) and the center wavelength (bottom) of the LED calibration source over a 5 minute scan.

This specific setup's $Q(\lambda)$ is incorporated into calculations as follows:

$$I_{corr} = \frac{I}{Q(\lambda)}$$

Equation 4.4

where I is the CCD camera's signal in counts and the corrected signal I_{corr} has units of counts × photons × electrons^{-1}. For example, 405 counts at 950 nm and a 41 % quantum efficiency will yield a I_{corr} value of 988 counts × photons × electrons^{-1}. In this way, every pixel in the CCD array is treated as a single photodetector. Also, collecting the intensity and corresponding wavelength is important for ECL studies where the emission peak wavelength can shift significantly from their photoluminescence (PL). For example, carbon quantum dots have many accessible surface states where the maximum wavelength of ECL emission can shift up to 150 nm from their PL peak wavelength.[35, 37, 38]

It should be noted that the CCD QE from 900-1100 nm drastically drops as seen in **Figure 4.5,** blue trace, and approaches 0 around 1100 nm. From **Equation 4.4** the CCD counts collected around 1100 nm would need to be corrected by dividing near 0 to produce very large I_{corr} as represented in **Figure 4.7B** (blue trace). We believe anything below a 3 % QE correction would introduce too much error into the absolute ECL determination. Therefore, any wavelengths above 1050 nm with this CCD array are not considered in this study.

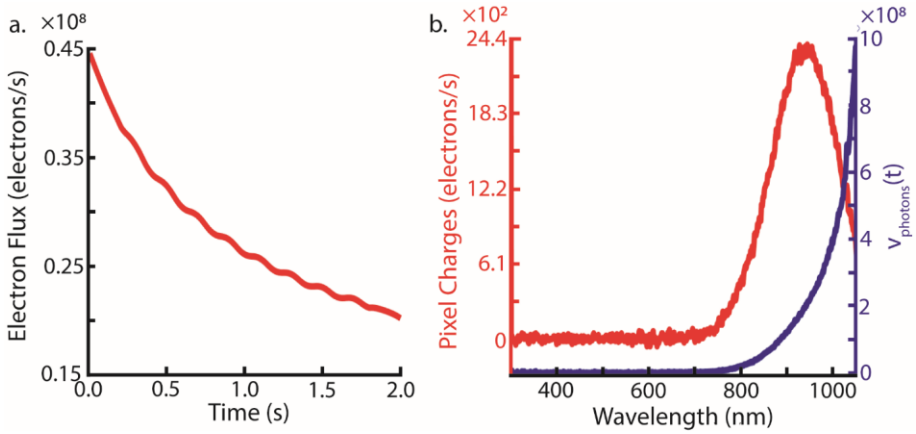

Figure 4.7. Data transformations for the data in **Figure 4.2**. (A) The total electron flux applied to the ECL cell. (B) The red trace shows the generated charge carriers in electrons on each pixel of the CCD camera by multiplying the counts generated by the gain factor. The blue trace shows the total photons flux emitted onto each pixel of the CCD camera in the entire 2 s accumulation.

Previously, setup calibrations and CCD camera QE were accounted for through a weighted photodetector sensitivity factor (*C*). This so-called *C* factor is found by multiplying the background subtracted and normalized emission spectra ($S(\lambda)$) by the CCD camera's sensitivity ($Q(\lambda)$) expressed as a ratio as follows:[3, 25, 29, 39]

$$C = \frac{\int Q(\lambda) * S(\lambda) d\lambda}{\int S(\lambda) * d\lambda}$$

Equation 4.5

However, this *C* factor requires all experimental data to be performed on both the photodetectors and a spectrometer coupled to a CCD camera. This method generally increases experimental times or leads to significantly increased experimental complexity relative to the technique presented in this manuscript.

Similar calibration methods are performed commercially. For example, Thorlabs calibrates photodiodes according to National Institute of Standards and Technology (NIST) or Physikalisch-Technische Bundesanstalt (PTB) standards where a S120VC photodiode power sensor that has a wavelength range from 200-1100 nm will have four

wavelengths calibrated.[40] The S120VC includes 200-279 nm, 280-439 nm, 440-980 nm, and 981-1100 nm calibrations. However, most importantly the calibrated wavelengths must be as close as possible to the analyte's wavelengths because of the wavelength-dependent light loss when light interacts with solid materials.

To complete this photon flux calculation, there are some additional corrections to consider. Commonly, a gain factor (*GF*) is used in CCD arrays to amplify the signal from every pixel where the *GF* typically has units of electrons × count^{-1}. For this camera, a *GF* of 12.2 electrons × count^{-1} was provided by the manufacturer.

The CCD array sums the charges produced into a 1D line seen in **Figure 4.2B** by passing the collected charges along the pixels. This pixel-to-pixel charge-transfer efficiency of this CCD camera and most CCD cameras is 99.999 % so a correction is not considered in this manuscript.[41]

These corrections so far have only affected the intensity of the emissions, and not the wavelength. This wavelength should be calibrated by an external light source that has an intense and sharp emission peak near the analyte's emission, such as a Hg lamp for visible light or a Xe lamp for NIR wavelengths.[42] A wavelength-shift is generally applied to the corrected spectrum to align the spectrometer and CCD array appropriately.

Finally, the accumulation time (*t*) that was used for the experiment must be considered which in this case is 2 s. Every correction factor to measure the true number of photons has now been discussed and the photon flux can be calculated as shown in **Figure 4.7B**.

With I_{corr} in unit of counts-photons electron^{-1}, all corrections can be applied to convert I_{corr} to $v_{photons}(t)$ with unit of photons s^{-1} sphere^{-1} pixel^{-1} in the following equation:

$$v_{photons}(t) = I_{corr} * \frac{GF * CC}{t * \sigma_{random}}$$

Equation 4.6

The resulting transformation is seen from counts in **Figure 4.2B** to photon flux in **Figure 4.7B**. For example, an I_{corr} of 988 counts-photons electrons^{-1}, a *GF* of 12.2 electrons

count^{-1}, a 39.1 calibration factor (*CC*), *t* of 2 s, and a $\sigma_{Spherical}$ of 2.24×10^{-3} spheres, a $\nu_{photons}(t)$ of 0.11×10^{9} photons s^{-1} sphere^{-1} is determined.

Interestingly, when correcting for CCD array QE, the QE curve (blue trace of **Figure 4.7B**) descends faster than the edge of the emission (red trace of **Figure 4.2B**) meaning the measured maximum wavelength will be greatly shifted. One may realize that the employed CCD camera was not sensitive to these wavelength peaks (red trace of **Figure 4.7B**), and likely did not capture the true wavelength maxima. In our lab, we attempted to measure ECL spectrum of the same Au_{25}^{0}/TPrA coreactant system on an InGaAs camera to determine the maximum wavelength emission. However, due to the low InGaAs QE, a well-defined spectrum could not be acquired.

Correcting the measured electrons is much simpler than the photons. When applying a potential, a percentage of the current is not involved in redox reactions but rather other non-redox processes is known as the non-Faradaic current. This non-Faradaic current can easily be measured by performing the same experiment but at a potential where no redox reactions occur. More details on this calculation are reported elsewhere.[27, 28] For this study, the potential was held at 0 V for 2 s and the charge was calculated. For this scan, 99 % of the current was Faradaic current which requires a non-Faradaic current correction factor (*NFCCF*) of 0.99. Combining the current with this *NFCCF* factor and the elementary charge constant (q_e) of 1.60×10^{-19} C electron^{-1} in the following equation:

$$\nu_{electrons} = \frac{i * NFCCF}{q_e}$$

Equation 4.7

the electron flux ($\nu_{electrons}$) is generated. Taking a single data point which is the highest current from **Figure 4.2A** of 70 μA and using **Equation 4.7** a $\nu_{electrons}$ of 430×10^{12} electrons per second is calculated.

The *NFCCF* remained constant for all tests as predicted. There should not be significant deviation of the non-Faradaic current between tests that use the same potentials and

concentrations. However, one test did have slightly different electrons injected. This may be due to small differences in coreactant concentration between tests.

4.3.3 Φ_{AQE} of the 0.1 mM Au_{25}^0/6.25 mM TPrA coreactant system

The final Φ_{AQE} determination proceeds as described using **Equation 4.2**. For example, summing up the red trace of **Figure 4.7B** yields 18.1×10^9 photons s^{-1} $sphere^{-1}$, then multiplying by the CCD camera accumulation time of 2 s and one whole sphere yields 36.2×10^9 photons. Integrating the electron flux by time in **Figure 4.7A** yields a total of 552×10^{12} electrons. Dividing the total photons by total electrons and multiplying by 100 yields a Φ_{AQE} of 0.0066 %. Overall, the constant voltage Φ_{QE} for the Au_{25}^0 / 6.25 mM TPrA system was found to be 0.0062 % from an average of 3 separate trials with all data summarized in **Table 4.1**.

Table 4.1. The ECL QE values determined from the test in **Figure 4.2** and two other replicate tests.

Constant Potential Voltage (V)	***NFCCF***	**Total Photons ($\times 10^{12}$)**	**Total Electrons ($\times 10^{12}$)**	***Au_{25}^0 / TPrA Φ_{QE}* (%)**
0.85	0.99	0.0362	559	0.0066
0.85	0.99	0.0370	669	0.0055
0.85	0.99	0.0368	552	0.0067

For the first time, the Φ_{AQE} is reported using only a calibrated CCD camera and spectrograph setup. In addition, for the first time, the Φ_{AQE} of a Au nanocluster / TPrA coreactant system is reported. Since the Φ_{AQE} is rather new, there are very few compounds available for Φ_{AQE} TPrA coreactant comparisons. There are currently $Ru(bpy)_3^{2+}$ / TPrA coreactant systems tested and $Ir(ppy)_3$ / benzoyl peroxide (BPO) systems tested, but these experiments employed compounds with much different concentrations, and a direct comparison is therefore difficult.[28, 43]

4.3.4 Φ_{AQE} verification with 1 mM $Ru(bpy)_3^{2+}$ in pulsing mode

To verify the accuracy and precision of this new strategy to determine Φ_{AQE} by means of a CCD the conventional standard ECL emitter, $Ru(bpy)_3^{2+}$ that has a known Φ_{AQE} value tested in the annihilation pathway was determined to produce **Figure 4.8**.[27] This test is a pulsing experiment in annihilation pathway for a 1 mM $Ru(bpy)_3(PF_6)_2$ in acetonitrile containing 0.1 $TBAPF_6$ with a pulsed potential range between −1.6 and 1.0 V at a frequency of 10 Hz. **Figure 4.9** shows the total photon flux, as well as the corresponding current. The Φ_{AQE} for this 10 Hz pulsing test was determined to be 0.64 %, which was averaged between 5 separate 50 s scans. This Φ_{AQE} value is very close to previous studies, but a PMT and a CCD camera were used to find Φ_{AQE} values of 1.0 %.[27] These similar values again attest to the accuracy of the presented CCD Φ_{AQE} technique.

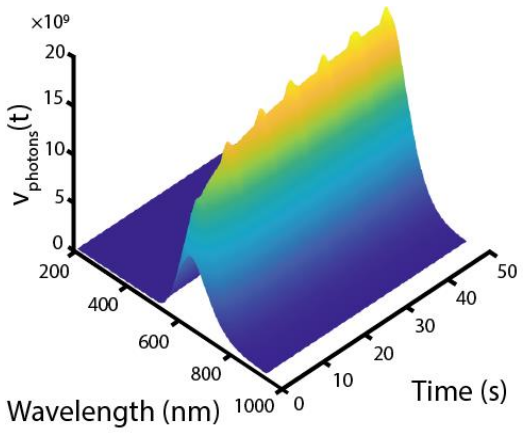

Figure 4.8. Spooling ECL spectroscopy of $Ru(bpy)_3(PF_6)_2$. A solution of 1 mM $Ru(bpy)_3(PF_6)_2$ and 0.1 M $TBAPF_6$ in acetonitrile was pulsed between −1.6 and 1.0 V vs. Pt wire to produce this spooling spectrum which was collected by a spectrometer coupled to a CCD camera. Each spectrum is a 1 s accumulation and 50 accumulations were taken in total. Calculations converting CCD counts to photon flux were carried out by using Equation 4.6.

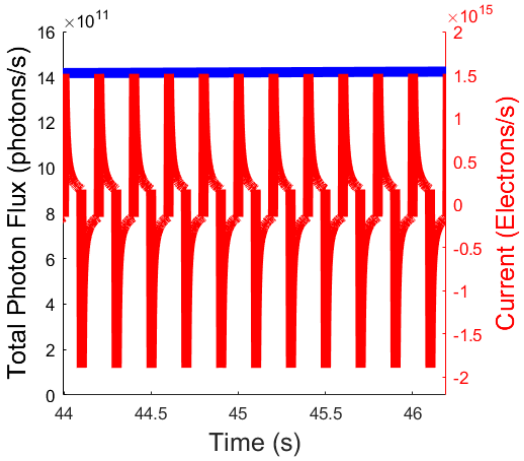

Figure 4.9. A 1 mM $Ru(bpy)_3(PF_6)_2$ and a 0.1 M $TBAPF_6$ solution in acetonitrile pulsed at 10 Hz between −1.6 and 1.0 V vs. Pt wire. The total summed photon flux is calculated from the equations described earlier and are plotted on the left y-axis. The electron flux is plotted on the right y axis.

Figure 4.8 is also significant because commonly, researchers test ECL using a photodetector such as a PMT and then perform the exact same scans over a CCD camera and spectrograph setup. Separating testing of Φ_{AQE} and wavelength creates a temporal and instrumental disconnect between intensity and emissions where emissive or spectral instabilities in some luminophores will provide inconsistent Φ_{AQE} results. Collecting both intensity and wavelength data simultaneously directly connects Φ_{AQE} values to wavelength data, eliminating this problem. Furthermore, the emissive stability luminophores can be assessed, where **Figure 4.8** displays that the $Ru(bpy)_3^{2+}$ annihilation maximum emission of about 3×10^9 gradually increases by a factor of 5 after 10 s to 15×10^9 photons s^{-1} $sphere^{-1}$ where it remains constant for 40 s. The above demonstrates a very high stability of $Ru(bpy)_3^{2+}$ ECL in the annihilation pathway upon potential pulsing.

4.3.5 Φ_{AQE} of 0.1 mM $Ru(bpy)_3^{2+}$ with various TPrA concentrations and discussion on Φ_{AQE} of other Au clusters

One final benefit of the Φ_{AQE} over the relative Φ_{ECL} technique is illustrated in

Table 4.2 in which the Φ_{AQE} of 0.1 mM $Ru(bpy)_3^{2+}$ in 1:1 acetonitrile:benzene was measured in three replicates using various TPrA coreactant concentrations in a constant potential mode at +1.50 V. Interestingly, the electrochemical current proportionally increased with augmented TPrA concentration as expected but the ECL intensity drastically decreases. This is likely because the excited state $Ru(bpy)_3^{2+}$* can react with excess TPrA, resulting in quenching of the ECL emission. While increasing the TPrA concentration from 6.25 mM to 200 mM, the Φ_{AQE} of $Ru(bpy)_3^{2+}$ decreased almost 500 times from 3.2×10^{-3} % to 6.5×10^{-6} %. $Ru(bpy)_3^{2+}$'s Φ_{AQE} value therefore drastically changing with the TPrA concentration. These dynamic Φ_{ECL} values are illustrated in our past papers. In our group's *Chem. Eur. J.* paper that analyzed Au_{18} the Φ_{ECL} increased 45 times from 5.5 % at 6.25 mM TPrA to 249 % at 200 mM TPrA.[30] Also, in our group's paper that analyzed Au_{38}, the Φ_{ECL} increased 65 times from 13 % at 6.25 mM TPrA to 836 % at 200 mM TPrA.[44] Finally, in our report on $Au_{21}(SR)_{15}$ the Φ_{ECL} increased 230 times from 1,010 % at 6.25 mM TPrA to 230,811 % at 100 mM TPrA.[45] For each of these discussed Au nanocluster Φ_{ECL} paper, our research group reported a modest Φ_{ECL} value for each cluster typically around 50 mM TPrA because of the difficulty interpreting the large Φ_{ECL} values at high TPrA concentrations. However, these Φ_{ECL} values can be better understood if the newly presented Φ_{AQE} physical strategy is used. In all cases, it appears the Au nanocluster Φ_{AQE} values remain constant whereas the $Ru(bpy)_3^{2+}$ Φ_{AQE} steadily decreases as the TPrA concentration is increased. This reactivity difference is likely due to the higher energy of the $Ru(bpy)_3^{2+}$ excited states with emissions of 660 nm instead of ~900 nm from Au nanoclusters. This higher energy excited state may be more reactive, forming non-emissive excimers or exciplexes, which will relatively decrease the Φ_{AQE} values.

Table 4.2. ECL QEs of 0.1 mM $Ru(bpy)_3(PF_6)_2$ in 0.1 M $TBAPF_6$ 1:1 benzene:acetonitrile solution with various TPrA concentrations under constant potential of 1.5 V.

TPrA Concentration (mM)	**Total Photons ($\times 10^{12}$)**	**Total Electrons ($\times 10^{12}$)**	***Ru(bpy)*$_3^{2+}$ ** TPrA Φ_{AQE} (%)**
6.25	0.0052	150	3.4×10^{-3}
12.5	0.0045	270	1.5×10^{-3}
25	0.0016	540	3.0×10^{-4}
50	0.00042	1100	4.0×10^{-5}
100	0.00016	1700	9.1×10^{-6}
200	0.00014	2200	6.4×10^{-6}

The ECL process can be complicated by factors influencing the ECL intensity such as the diffusion of electroactive molecules, the stability of radicals, the reactivity of excited states (evidenced above) and the analyte's reactivity between itself in the annihilation pathway or coreactants in the coreactant pathway. Herein, this newly presented Φ_{AQE} technique allows deconvoluting many of these variables and parameters. Furthermore, wavelength-specific light losses due to unique hardware setups of different researchers must be accounted for because these wavelength specific light losses will modify Φ_{ECL} and Φ_{AQE} when measuring luminophore's that have different maximum wavelengths than the commercial standard $Ru(bpy)_3^{2+}$.

4.4 Conclusions

Herein, a new methodology to determine ECL Φ_{AQE} of was presented which requires less instrumentation and less calculations relative to the ECL photon counting head (PCH) and PMT Φ_{AQE} techniques presented by our research group previously.[27, 28] The Φ_{AQE} of Au_{25}^0 was determined to be 0.0062 % and our past ECL studies of Au nanoclusters were reconsidered in the context of Φ_{AQE} instead of relative Φ_{ECL}. This method was verified to investigate $Ru(bpy)_3^{2+}$ in the same conditions as previous Φ_{AQE} studies to find very similar Φ_{AQE} values reported in those studies.[27] This agreement attests to the precision and accuracy of our new technique. This new ECL CCD Φ_{AQE} technique permits analysis of the wavelength of the emission during potential scans or extended pulsing. In a pulsing study, $Ru(bpy)_3^{2+}$'s max emission wavelength was found to be stable over 50 s whereas

the intensity tripled from its origin over this 50 s. Our physical strategy is by no means limited to Au clusters and $Ru(bpy)_3^{2+}$, which is anticipated to be widely utilized in ECL of vast variety of luminophores.

To consider all factors affecting the ECL efficiency properly and objectively for specific luminophores, it is simpler to consider just the Φ_{AQE} (absolute) value instead of both $Ru(bpy)_3^{2+}$ and the luminophore in Φ_{ECL} in a relative measurement. Our research group recommends using the Φ_{AQE} method to understand how all discussed ECL factors can affect the ECL performance of specific luminophores. Such an analysis will then closely resemble other well-established research disciplines such as light emitting diode (LED) research, where luminosities and luminous efficiencies for luminophores and devices are paramount.

4.5 References

[1] Booker, C.; Wang, X.; Haroun, S.; Zhou, J.; Jennings, M.; Pagenkopf, B. L.; Ding, Z. *Angew. Chem., Int. Ed.* **2008,** *47*, 7731.

[2] Tokel-Takvoryan, N. E.; Hemingway, R. E.; Bard, A. J. *J. Am. Chem. Soc.* **1973,** *95*, 6582.

[3] Keszthelyi, C. P., *Electrochemistry and Electrogenerated Chemiluminescence in Selected Solvent Systems*. 1973. [Thesis]

[4] Qi, H.; Zhang, C. *Anal. Chem.* **2020,** *92*, 524.

[5] He, Y.; Yang, L.; Zhang, F.; Zhang, B.; Zou, G. *J. Phys. Chem. Lett.* **2018,** *9*, 6089.

[6] Li, Z.; Wu, S.; Zhang, B.; Fu, L.; Zou, G. *J. Phys. Chem. Lett.* **2019,** *10*, 5408.

[7] Ma, C.; Cao, Y.; Gou, X.; Zhu, J. J. *Anal. Chem.* **2020,** *92*, 431.

[8] Wang, Z.; Feng, Y.; Wang, N.; Cheng, Y.; Quan, Y.; Ju, H. *J. Phys. Chem. Lett.* **2018,** *9*, 5296.

[9] Suraniti, E.; Kanoufi, F.; Gosse, C.; Zhao, X.; Dimova, R.; Pouligny, B.; Sojic, N. *Anal. Chem.* **2013,** *85*, 8902.

[10] Sentic, M.; Milutinovic, M.; Kanoufi, F.; Manojlovic, D.; Arbault, S.; Sojic, N. *Chem. Sci.* **2014,** *5*, 2568.

[11] Kanoufi, F.; Sojic, N. *Nature* **2021,** *596*, 194-195.

[12] Zhao, B. *J. Phys. Chem. Lett.* **2021,** *12*, 11191.

[13] Jiang, M. H.; Li, S. K.; Zhong, X.; Liang, W. B.; Chai, Y. Q.; Zhuo, Y.; Yuan, R. *Anal. Chem.* **2019,** *91*, 3710.

[14] Zhou, Y.; Chai, Y.; Yuan, R. *Anal. Chem.* **2019,** *91*, 14618.

[15] Miao, W. *Chem. Rev.* **2008,** *108*, 2506-53.

[16] Lou, J.; Liu, S.; Tu, W.; Dai, Z. *Anal. Chem.* **2015,** *87*, 1145.

[17] Liu, S.; Zhang, Q.; Zhang, L.; Gu, L.; Zou, G.; Bao, J.; Dai, Z. *J. Am. Chem. Soc.* **2016,** *138*, 1154.

[18] Wong, J. M.; Xu, J.; Zhang, R.; Chu, K.; Ding, Z.; Liu, L. *J. Phys. Chem. C* **2021,** *125*, 13696.

[19] Ding, J.; Zhou, P.; Su, B. *ChemElectroChem* **2022,** *9*, e202200236.

[20] Janakiraman, U.; Dini, D.; Preusser, A.; Holmes, A. B.; Martin, R. E.; Doblhofer, K. *Synth. Met.* **2001,** *121*, 1685.

[21] Danis, A. S.; Potts, K. P.; Perry, S. C.; Mauzeroll, J. *Anal. Chem.* **2018,** *90*, 7377.

[22] Svir, I. B.; Oleinick, A. I.; Klimenko, A. V. *J. Electroanal. Chem.* **2001,** *513*, 119.

[23] Wightman, R. M.; Forry, S. P.; Maus, R.; Badocco, D.; Pastore, P. *J. Phys. Chem. B* **2003,** *108*, 19119.

[24] Cao, Z.; Shu, Y.; Qin, H.; Su, B.; Peng, X. *ACS Cent. Sci.* **2020,** *6*, 1129.

[25] Keszthelyi, C. P.; Tokel-Takvoryan, N. E.; Bard, A. J. *Anal. Chem.* **1975,** *47*, 249.

[26] Bezman, R.; Faulkner, L. R. *Anal. Chem.* **1971,** *43*, 1749.

[27] Adsetts, J. R.; Chu, K.; Hesari, M.; Ma, J.; Ding, Z. *Anal. Chem.* **2021,** *93*, 11626-11633.

[28] Chu, K.; Adsetts, J. R.; Ma, J.; Zhang, C.; Hesari, M.; Yang, L.; Ding, Z. *J. Phys. Chem. C* **2021,** *125*, 22274-22282.

[29] Anaya, M.; Rand, B. P.; Holmes, R. J.; Credgington, D.; Bolink, H. J.; Friend, R. H.; Wang, J.; Greenham, N. C.; Stranks, S. D. *Nat. Photon.* **2019,** *13*, 818.

[30] Hesari, M.; Workentin, M. S.; Ding, Z. *Chem. Eur. J.* **2014,** *20*, 15116.

[31] Hesari, M.; Ding, Z. *Nat. Protoc.* **2021,** *16*, 2109-2130.

[32] Miao, W.; Choi, J. P.; Bard, A. J. *J. Am. Chem. Soc.* **2002,** *124*, 14478.

[33] Hesari, M.; Ding, Z. *Acc. Chem. Res.* **2017,** *50*, 218-230.

[34] präzisionsglas&optikGmBH Pyrex® 7740 Optical Transmission. https://www.pgo-online.com/intl/curves/pyrex_kurve.html (accessed June 11, 2022).

[35] Adsetts, J. R.; Ding, Z. *ChemPlusChem* **2021,** *86*, 155.

[36] Hadley, L.; Hass, G., *American Institute of Physics Handbook*. 1972.

[37] Adsetts, J. R.; Zhang, R.; Yang, L.; Chu, K.; Wong, J. M.; Love, D. A.; Ding, Z. *Front. Chem.* **2020,** *8*, 580022.

[38] Adsetts, J. R.; Hoesterey, S.; Gao, C.; Love, D. A.; Ding, Z. *Langmuir* **2020,** *36*, 14432.

[39] Parker, C. A.; Rees, W. T. *Analyst* **1960,** *85*, 587.

[40] Thorlabs Photodiode Power Sensors (C-Series). https://www.thorlabs.com/newgrouppage9.cfm?objectgroup_id=3328 (accessed June 9, 2022).

[41] Waczynski, A.; Polidan, E. J.; Marshall, P. W.; Reed, R. A.; Johnson, S. D.; Hill, R. J.; Delo, G. S.; Wassell, E. J.; Cheng, E. S. *IEEE Trans. Nucl. Sci.* **2001,** *48*, 1807.

[42] Resch-Genger, U.; DeRose, P. C. *Pure Appl. Chem.* **2010,** *82*, 2315.

[43] Yang, L.; Adsetts, J. R.; Zhang, R.; Balónová, B.; Piqueras, M. T.; Chu, K.; Zhang, C.; Zysman-Colman, E.; Blight, B. A.; Ding, Z. *J. Electroanal. Chem.* **2022,** *906*, 115891.

[44] Hesari, M.; Workentin, M. S.; Ding, Z. *ACS Nano* **2014,** *8*, 8543-8553.

[45] Hesari, M.; Ding, Z. *J. Am. Chem. Soc.* **2021,** *143*, 19474-19485.

Chapter 5

Chapter 5 begins the data chapters where we investigate novel luminophores for their light emitting properties. In this chapter, we explore a series of Pt-Ag nanoclusters, whose exceptional photoluminescent quantum yields prompted a thorough exploration into their electrochemical and electrochemiluminescence properties for potential applications in light-emitting devices.

5 Nanocluster Transformation Induced by SbF_6^- Anions Toward Boosting Photochemical Activities†

The interactions between SbF_6^- and metal nanoclusters are of significance for customizing clusters from both structure and property aspects; however, the whole-segment monitoring of this customization remains challenging. In this work, by controlling the amount of introduced SbF_6^- anions, the step-by-step nanocluster evolutions from $[Pt_1Ag_{28}(S\text{-}Adm)_{18}(PPh_3)_4]Cl_2$ (Pt_1Ag_{28}-Cl) to $[Pt_1Ag_{28}(S\text{-}Adm)_{18}(PPh_3)_4](SbF_6)_2$ (Pt_1Ag_{28}-SbF_6) and then to $[Pt_1Ag_{30}Cl_1(S\text{-}Adm)_{18}(PPh_3)_3](SbF_6)_3$ (Pt_1Ag_{30}-SbF_6) have been mapped out with x-ray crystallography, with which atomic-level SbF_6^- counterion effects in reconstructing and rearranging nanoclusters are determined. The structure-dependent optical properties, including optical absorption, photoluminescence, and electrochemiluminescence, of these nanoclusters are then explored. Notably, the Pt_1Ag_{30}-SbF_6 nanocluster was ultrabright with a high phosphorescence quantum yield of 85% in N_2-purged solutions, while Pt_1Ag_{28} nanoclusters were fluorescent with weaker emission intensities. Furthermore, Pt_1Ag_{30}-SbF_6 displayed superior electrochemiluminescence (ECL) efficiency over Pt_1Ag_{28}-SbF_6, which was rationalized by its increased effectively exposed reactive facets. Both Pt_1Ag_{30}-SbF_6 and Pt_1Ag_{28}-SbF_6 demonstrated unprecedented high absolute ECL quantum efficiencies at sub-micromolar

---

† This work has been published. Wei, X.[§]; Chu, K.[§]; Adsetts, J.; Li, H.; Kang, X.; Ding, Z.; Zhu, M. Nanocluster Transformation Induced by SbF_6^- Anions Toward Boosting Photochemical Activities. *J. Am. Chem. Soc.* (**2022**) 144, 20421-20433. [§] indicates equally contributed first author.

concentrations. This work is of great significance for revealing the SbF_6^- counterion effects on control of both structures and luminescent properties.

5.1 Introduction

The excitement generated by metal nanoclusters has been fueled by the endless possibilities they offer for fundamental research at the atomic level, and for promising applications in catalysis, sensing, nanoelectronics, energy production, and biology.[1-10] The realization of many of these promises, however, hinges on the development of effective strategies to control their geometric/electronic structures, which plays a prominent role in determining their physical/chemical properties.[11-23] This remains a priority target for nearly all existing metal nanoclusters. To date, several efficient approaches have been proposed in this respect, including the alloying to control their kernel compositions,[24-28] the ligand-exchange to tailor their surface structures,[29-32] the assembly to direct their aggregates,[33-38] and so on. Such manipulations allow the atomic-level understanding of structure-property correlations, which in turn benefit the directional preparation of cluster-based nanomaterials for their applications.[39-44]

It is plausible that the control over counterions serves as another efficient approach to manipulate the intra- or inter-cluster architectures of metal nanoclusters and to dictate their physical-chemical properties as investigated by us, Lee's and Pradeep's groups.[45-47] In general, most counterions (e.g., TOA^+, PPh_4^+, BPh_4^-, and so on) have a minor impact on intracluster architectures, but can remarkably influence their packing modes in the supracrystal lattice. The SbF_6^- counterion, by contrast, is unique in this respect: the interaction between its F terminals and surface metals in nanoclusters can induce both the reconstruction of intracluster structures and the rearrangement of cluster molecules in the supracrystal lattice.[48-50] Chen et al. reported the Ag-F interaction triggered intercluster connection in the crystal lattice,[48] and the Balch group presented several cases of the SbF_6^- counterion effect in reconstruction and rearrangement of Au(I)-based complexes.[49, 50] In many relevant cases, excess SbF_6^- counterions are required to reach the steady-state of metal clusters.[48-50] However, the whole-segment monitoring of this reconstruction of metal nanoclusters in the presence of SbF_6^- remains challenging, and the research of SbF_6^- counterion effect in regulating the physical-chemical properties of nanoclusters is

still limited up to the present, which impedes the in-depth understanding of the SbF_6^- counterion effect in the cluster science.

Herein, we present a new demonstration of the profound effect of the SbF_6^- counterion in reconstructing metal nanoclusters, leading to a boosting of their photochemical and photoelectrochemical properties. By controlling the amount of introduced SbF_6^- counterions, the step-by-step nanocluster evolution from $[Pt_1Ag_{28}(S\text{-}Adm)_{18}(PPh_3)_4]Cl_2$ (Pt_1Ag_{28}-Cl) to $[Pt_1Ag_{28}(S\text{-}Adm)_{18}(PPh_3)_4](SbF_6)_2$ (Pt_1Ag_{28}-SbF_6) and $[Pt_1Ag_{30}Cl_1(S\text{-}Adm)_{18}(PPh_3)_3](SbF_6)_3$ (Pt_1Ag_{30}-SbF_6) has been mapped out via crystallography. Structurally, the SbF_6^- counter ion effects are evaluated from two aspects: the reconstruction of nanocluster structures, which refers to the molecular chemistry, and the rearrangement of crystalline cluster molecules, which touches upon the supramolecular chemistry. The newly obtained Pt_1Ag_{30}-SbF_6 display significantly enhanced photochemical and photoelectrochemical activities relative to Pt_1Ag_{28}-Cl and Pt_1Ag_{28}-SbF_6 nanoclusters, leading to the boosted photoluminescence and electrochemiluminescence efficiencies. Such enhancements on the activities have been rationalized by analyzing the exposed reactive facets available to undergo electron transfer reactions of these metal clusters.

5.2 Experimental

5.2.1 Chemicals

All reagents were purchased from Sigma-Aldrich and used without further purification, including silver nitrate ($AgNO_3$, 99% metals basis), hexachloroplatinic (IV) acid ($H_2PtCl_6 \cdot 6H_2O$, 99.9% metals basis), adamantane-1-thiol ($C_{10}H_{15}SH$, HS-Adm, 95%), triphenylphosphine (PPh_3, 99%), sodium borohydride ($NaBH_4$, 99.9%), sodium hexafluoroantimonate ($NaSbF_6$, 99%), methylene chloride (CH_2Cl_2, HPLC, Aldrich), methanol (CH_3OH, HPLC, Aldrich), ethyl acetate ($CH_3COOC_2H_5$, HPLC, Aldrich), ether ($C_2H_5OC_2H_5$, HPLC, Aldrich), tetrabutylammonium hexafluorophosphate ($TBAPF_6$, electrochemical grade, >99.0%), ferrocene (Fc, 98%), SureSeal anhydrous dichloromethane (DCM, >99.8%). Tri-*n*-propylamine (TPrA, reagent grade, >98%) was obtained from Sigma-Aldrich Canada and was stored at 4°C.

5.2.2 Synthesis of $[Pt_1Ag_{28}(S\text{-}Adm)_{18}(PPh_3)_4]Cl_2$ (Pt1Ag28-Cl)

For the nanocluster synthesis, $AgNO_3$ (29 mg, 0.17 mmol) and $H_2PtCl_6 \cdot 6H_2O$ (5 mg, 0.01 mmol) were dissolved in $CH_3COOC_2H_5$ (35 mL) and CH_3OH (5 mL). The solution was vigorously stirred (1200 rpm) with magnetic stirring. After 15 minutes, Adm-SH (0.1 g) and PPh_3 (0.1 g) were added simultaneously and the reaction was proceeded for another 90 minutes. After that, $NaBH_4$ aqueous solution (1 mL, 20 mg mL^{-1}) was added to the above mixture. The reaction was allowed to proceed for 36 hours. After that, the aqueous layer was removed, and the mixture in the organic phase was rotavaporated under vacuum. Then approximately 30*3 mL of CH_3OH was used to wash the obtained nanocluster. The precipitate was dissolved in CH_2Cl_2, which produced the Pt_1Ag_{28}-Cl nanocluster. The yield is 45% based on the Ag element (calculated from the $AgNO_3$) for the synthesis of Pt_1Ag_{28}-Cl.

5.2.3 Transformation from Pt_1Ag_{28}-Cl to $[Pt_1Ag_{28}(S\text{-}Adm)_{18}(PPh_3)_4](SbF_6)_2$ (Pt_1Ag_{28}-SbF_6)

30 mg of Pt_1Ag_{28}-Cl was dissolved in 50 mL of CH_2Cl_2. The solution was vigorously stirred (1200 rpm) with magnetic stirring. Then, 2 mg of $NaSbF_6$ ($M_{cluster}$:M_{SbF6} = 1:2) was added and the reaction was allowed to proceed for 10 minutes. After that, the organic phase (dark red) was rotavaporated under vacuum to produce the Pt_1Ag_{28}-SbF_6 nanocluster.

5.2.4 Transformation from Pt_1Ag_{28}-Cl to $[Pt_1Ag_{30}Cl_1(S\text{-}Adm)_{18}(PPh_3)_3](SbF_6)_3$ (Pt_1Ag_{30}-SbF_6)

30 mg of Pt_1Ag_{28}-Cl was dissolved in 50 mL of CH_2Cl_2. The solution was vigorously stirred (1200 rpm) with magnetic stirring. Then, 10 mg of $NaSbF_6$ ($M_{cluster}$:M_{SbF6} = 1:10) was added and the reaction was allowed to proceed for 10 minutes. After that, the organic phase (dark red) was rotavaporated under vacuum to produce the Pt_1Ag_{30}-SbF_6 nanocluster.

5.2.5 Transformation to Pt_1Ag_{28}-Cl to polydispersed Pt-Ag compounds

30 mg of Pt_1Ag_{28}-Cl was dissolved in 50 mL of CH_2Cl_2. The solution was vigorously stirred (1200 rpm) with magnetic stirring. Then, 30 mg of $NaSbF_6$ ($M_{cluster}$:M_{SbF6} = 1:30) was added and the reaction was allowed to proceed for 10 minutes. After that, the organic phase (pale yellow) was rotavaporated under vacuum to produce polydispersed Pt-Ag compounds.

5.2.6 Crystallization of Pt_1Ag_{28}-SbF_6 and Pt_1Ag_{30}-SbF_6

Nanoclusters were crystallized in a CH_2Cl_2/ether system with a vapor diffusion method. Specifically, 20 mg of clusters was dissolved in 5 mL of CH_2Cl_2, and the obtained solution was then vapor diffused by 50 mL of ether. After 7 days, crystals of Pt_1Ag_{28}-SbF_6 and Pt_1Ag_{31}-SbF_6 were collected and subjected to X-ray diffraction to determine their structures. The CCDC numbers of Pt_1Ag_{28}-SbF_6 and Pt_1Ag_{30}-SbF_6 are 2054288 and 2054214, respectively.

5.2.7 X-ray crystallography

The data collection for single-crystal X-ray diffraction of Pt_1Ag_{28}-SbF_6 and Pt_1Ag_{30}-SbF_6 was carried out on Stoe Stadivari diffractometer under nitrogen flow, using graphite-monochromatized Cu Kα radiation (λ = 1.54186 Å). Data reductions and absorption corrections were performed using the SAINT and SADABS programs, respectively. The electron density was squeezed by Platon. The structure was solved by direct methods and refined with full-matrix least squares on F^2 using the SHELXTL software package. All non-hydrogen atoms were refined anisotropically, and all the hydrogen atoms were set in geometrically calculated positions and refined isotropically using a riding model.

5.2.8 Preparation of nanocluster crystalline films

The concentration of the CH_2Cl_2/CH_3OH (5:5 of the volume ratio) solution of these three nanoclusters was set as 30 mg/mL and then the solution was filtered with a 0.2 μm syringe filter. The solutions were stored for 12 hours before use. 50 μL of the solutions were dropped onto a quartz substrate, and spin-coated (using LAURELL WS-650MZ-

23NPPB) at 1000 rpm for 60 s. The cluster-impregnated quartz substrate was dried in the air for 12 hours before the optical property characterization.

5.2.9 Electrochemistry and spectroscopy

A three-electrode system was used for all electrochemical measurements, where the working electrode was a platinum disc (2 mm diameter) inlaid in a glass tube, and the counter and reference electrodes were coiled platinum wires. All potentials were reported relative to the Fc/Fc^+ redox couple where the formal potential was taken to be 0.342 V vs. SCE.[51] Electrochemical measurements were conducted inside a cylindrical glass tube with a flat quartz window at the bottom to allow for the detection of ECL light. The airtight ECL cell was assembled inside a nitrogen atmosphere glovebox (Model Nexus I, Vacuum Atmospheres Company, Hawthorne, CA) to ensure the absence of oxygen and moisture. For coreactant experiments which required the addition of volatile reagents, the ECL cell was purged with argon gas for at least 30 seconds. The potentiostat used was a CH Instruments Model 610a electrochemical workstation (CH Instruments Inc., Austin, TX). ECL emission was measured using a photomultiplier tube (Model R928, Hamamatsu, Japan) biased at −750 V, where the output signal as photocurrent was converted in a voltage for data acquisition using a picoammeter (Keithley 6487, Cleveland, OH). The electrochemical current and the ECL signal were recorded using a data acquisition board (DAQ Model 6036E, National Instruments, Austin, TX) and acquired using a custom LabVIEW program. ECL spectra were recorded using a spectrograph (Model SP2300i, Princeton Instruments) with an attached CCD camera (Andor DU401-BR-DD-352, Oxford Instruments, UK) cooled to −65°C. Wavelength calibration was accomplished using a mercury source (HG-1, Ocean Optics, Dunedin, FL) using a center wavelength of 546 nm. Accumulation ECL spectra were acquired by collecting all emission generated over the entire cyclic voltammogram program. Spooling ECL spectra were acquired each at a time interval of 0.5 s during a cyclic voltammogram; the obtained spectra were combined in a three-dimensional plot using a custom MATLAB program.[52] Photoluminescence (PL) spectra were collected using the same spectrograph and CCD camera set, where the nanocluster sample (solvated in DCM in a quartz cuvette) was optically excited using a 532-nm laser (Coherent Verdi V5, Santa

Clara, CA). A 532 nm long-pass filter (Semrock RazorEdge, West Henrietta, NY) was used to isolate the laser emission, and the acquisition time was 1 ms for all PL spectra. Spooling PL spectroscopy was performed by scanning the applied potential from 0.0 V to anodic region for a nanocluster solution in dichloromethane in a 0.5 mm thin layer spectroelectrochemical cell, where a Pt mesh was the working electrode, and Pt coils were the counter and reference electrodes. The 532 nm laser and spectrograph/CCD set as described above was used to photoexcite the nanoclusters and record the PL spectra, respectively, during the potentiodynamic scan. For all measurements, the spectrum recording was synchronized by means of a 5 V TTL pulse output from the potentiostat at the beginning of the potential scanning.

5.2.10 Characterization

The UV-vis absorption spectra of nanoclusters were recorded using an Agilent 8453 diode array spectrometer.

Photo-luminescence (PL) spectra were measured on an FL-4500 spectrofluorometer with the same optical density (OD) of 0.05. Absolute quantum yield (QY) was measured with dilute solutions of nanoclusters on a HORIBA FluoroMax-4P.

Electrospray ionization mass spectrometry (ESI-MS) measurements were performed by MicrOTOF-QIII high-resolution mass spectrometer. The sample was directly infused into the chamber at 5 μL/min. For preparing the ESI samples, nanoclusters were dissolved in CH_2Cl_2 (1 mg/mL) and diluted (*v*/*v* = 1:2) by CH_3OH.

Energy-dispersive X-ray spectroscopy (EDS) analyses were performed on a JEOL JEM-2100F FEG TEM operated at 200 kV. Nanocluster powder samples were used for the analysis.

X-ray photoelectron spectroscopy (XPS) measurements were performed on a Thermo ESCALAB 250 configured with a monochromated Al Kα (1486.8 eV) 150 W X-ray source, 0.5 mm circular spot size, flood gun to counter charging effects, and analysis chamber base pressure lower than 1×10^{-9} mbar.

Inductively coupled plasma-atomic emission spectrometry (ICP-AES) measurements were performed on an Atomscan advantage instrument from Thermo Jarrell Ash Corporation (USA).

5.2.11 Determination of the absolute ECL efficiency

Determination of the ECL quantum efficiency (ECL-QE) was accomplished by evaluating the ratio between the number of photons emitted by the ECL system as measured by the spectrograph/CCD array described above to the total injected charge determined by the electrochemical workstation. Recalibration of the manufacturer provided quantum efficiency curve of the Andor CCD camera was performed using a light-emitting diode with a peak wavelength of 630 nm (Model TLHK46Q1R2, Vishay Semiconductors, Malvern, PA) against a calibrated silicon photodiode (S120VC, Thorlabs, Newton, NJ) attached to an optical power meter (Model PM100D, Thorlabs), as shown in **Equation 5.1**. This calibration factor was determined to be 9.4 calibrated photons/uncalibrated photons. The "calibrated" quantum efficiency curve was then used to convert instrument counts to emitted photons, where the counts for all illuminated pixels were summated across the spectral range of interest (300 to 1150 nm); total corrected photons were obtained after applying correction factors for the distance between the electrode surface and the photodetector, self-absorption of the luminophore solution, and the reflection of light from the electrode surface (**Equation 5.2**). The total charge was obtained by integrating the measured current over the duration of an electrochemical experiment with respect to time. Conversion to electrons was achieved using the elementary charge constant (1.602×10^{-19} C); a faradaic correction factor of 99% corresponding to the proportion of the current involved in oxidation or reduction was applied (**Equation 5.3**). Finally, the ratio between the number of total photons and the total electrons is the absolute quantum efficiency (**Equation 5.4**).

$$Calibrated\ QE\ Curve = \frac{electrons}{photon} \times \frac{1}{\frac{12.2\ electrons}{count}} \times Calibration\ factor = \frac{counts}{photon}$$

Equation 5.1

$$Corrected\ photons = \frac{Counts}{Calibrated\ QE\ Curve} \times Absorbance \times \frac{1}{Distance} \times \frac{1}{Reflect}$$

Equation 5.2

$$Total\ electrons = \frac{\int Current \cdot dt}{e} \times fara\ correction$$

Equation 5.3

$$ECL_{QE}(\%) = \frac{Photons}{Electrons} \times 100$$

Equation 5.4

5.3 Results and Discussion

5.3.1 Synthesis and structure evolution

Pt_1Ag_{28}-Cl was prepared *via* an *in-situ* synthetic procedure. The counterion Cl^- in Pt_1Ag_{28}-Cl has been confirmed (**Figure 5.1**).[53, 54] We first introduced a small amount of SbF_6^- (cluster/$NaSbF_6$ = 1/2) to the solution of Pt_1Ag_{28}-Cl to produce the Pt_1Ag_{28}-SbF_6 nanocluster. The Pt_1Ag_{28}-SbF_6 was crystallized by diffusing the ether vapor to the CH_2Cl_2 solution of the nanocluster, the same as that of Pt_1Ag_{28}-Cl.

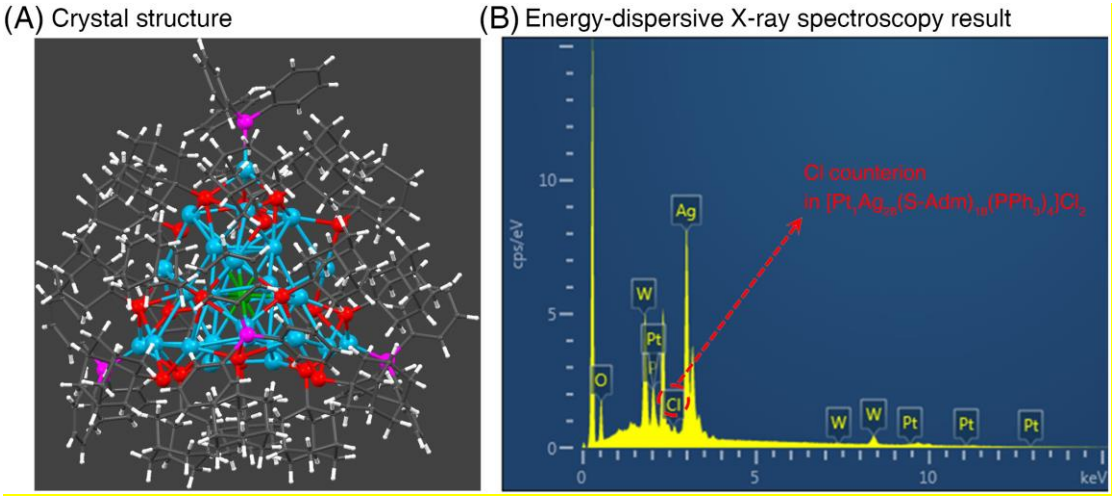

Figure 5.1. (A) Total structure of $[Pt_1Ag_{28}(S\text{-}Adm)_{18}(PPh_3)_4]Cl_2$. No Cl counterion was observed in the crystal lattice because of the high disorder of these Cl atoms, which has

been demonstrated in previous works (Chem. Sci., 2017, 8, 2581; Chem. Sci., 2020, 11, 1691). Color legends: dark green, Pt; blue, Ag; red, S; magenta, P; gray, Cl; pale gray, C; white, H. (B) The presence of counterion Cl^- in $[Pt_1Ag_{28}(S\text{-}Adm)_{18}(PPh_3)_4]Cl_2$ has also been verified by the energy-dispersive X-ray spectroscopy measurement.

The crystal structure of Pt_1Ag_{28}-SbF_6 was then determined (**Figure 5.2**), and its structural comparison to Pt_1Ag_{28}-Cl was presented in **Figure 5.3**. Both Pt_1Ag_{28} nanoclusters comprise a face-centered cubic (FCC) Pt_1Ag_{12} kernel and four $Ag_4(S\text{-}Adm)_6(PPh_3)_1$ surface units, and these four $Ag_3(S\text{-}Adm)_6(PPh_3)_1$ units make up an overall spherical $Ag_{16}(S\text{-}Adm)_{18}(PPh_3)_4$ shell *via* sharing the vertex thiol ligands. Owing to the substitution of Cl^- counterions by SbF_6^-, these two Pt_1Ag_{28} nanoclusters exhibit different configurations (**Figure 5.3A**, **Figure 5.3B**). The Pt_1Ag_{12} kernel in Pt_1Ag_{28}-Cl follows a distorted FCC configuration (**Figure 5.3C**), whereas the configuration of the Pt_1Ag_{12} kernel in Pt_1Ag_{28}-SbF_6 is a standard FCC (**Figure 5.3D**). Such a kernel transformation (i.e., from distorted FCC to standard FCC) has also been discovered in the kernel metal or vertex phosphine control of the Pt_1Ag_{28} nanocluster.[55, 56] Besides, the $Ag_4(S\text{-}Adm)_6(PPh_3)_1$ surface unit in Pt_1Ag_{28}-Cl is asymmetric, and the maximum difference of Ag-S bond length is 0.88 Å (3.21 Å – 2.33 Å; **Figure 5.3C**); by comparison, this unit in Pt_1Ag_{28}-SbF_6 is more symmetric, presenting a maximum of 0.26 Å difference of Ag-S bond length (2.82 Å – 2.56 Å; **Figure 5.3D**). In this context, although the Pt_1Ag_{12}(core)@$Ag_{16}(S\text{-}Adm)_{18}(PPh_3)_4$(shell) configuration of Pt_1Ag_{28} nanocluster remains with the counterion substitution process, the SbF_6^- counterion shows its effects in adjusting both core and shell structures to introduce a higher symmetry to the overall structure.

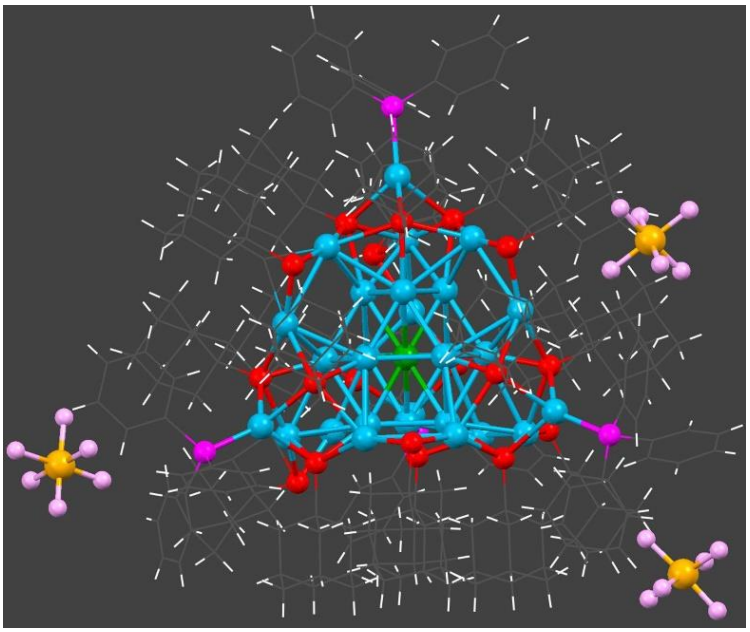

Figure 5.2. Total structure of $[Pt_1Ag_{28}(S\text{-}Adm)_{18}(PPh_3)_4](SbF_6)_2$. In this figure, one of three SbF_6^- counterion are in 100% occupancy, and the other two are in 50% occupancy. In this context, the number of SbF_6^- counterions are two, fitting with the $[Pt_1Ag_{28}(S\text{-}Adm)_{18}(PPh_3)_4](SbF_6)_2$ formula in ESI-MS. Color legends: dark green, Pt; blue, Ag; red, S; magenta, P; pale gray, C; white, H; orange, Sb; pink, F.

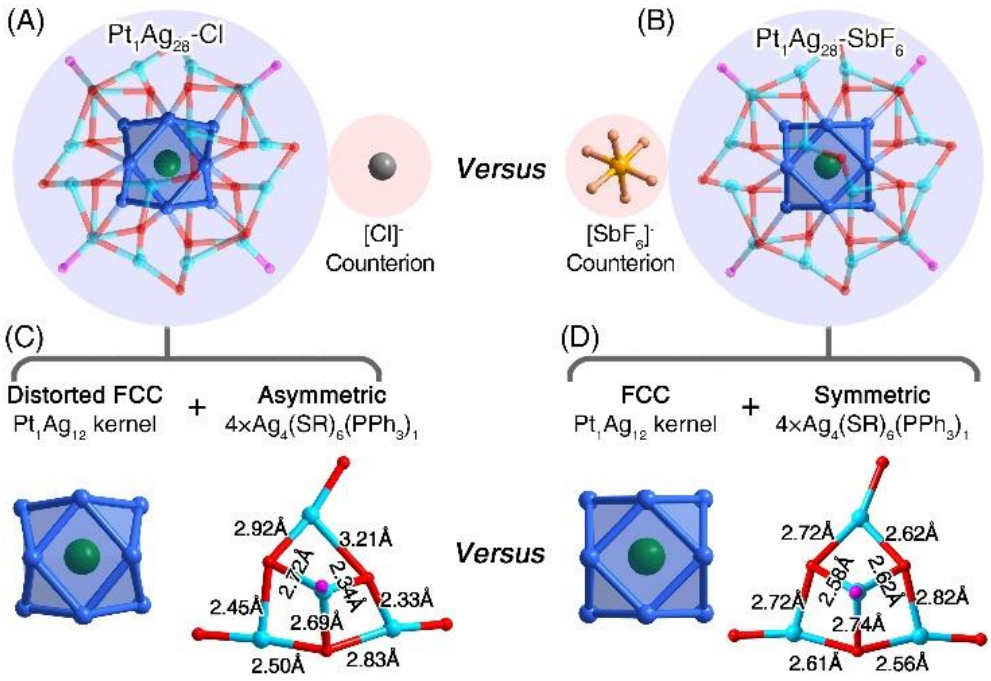

Figure 5.3. Structure comparison between Pt_1Ag_{28}-Cl and Pt_1Ag_{28}-SbF_6 nanoclusters. (A) Total structure of Pt_1Ag_{28}-Cl. (B) Total structure of Pt_1Ag_{28}-SbF_6. (C) Distort FCC Pt_1Ag_{12} kernel and asymmetric $Ag_4(S\text{-}Adm)_6(PPh_3)_1$ surface structure of Pt_1Ag_{28}-Cl. (D) FCC Pt_1Ag_{12} kernel and symmetric $Ag_4(S\text{-}Adm)_6(PPh_3)_1$ surface structure of Pt_1Ag_{28}-SbF_6. Color legends: dark green sphere, Pt; dark blue sphere, kernel Ag; blue sphere, surface Ag; red sphere, S; magenta sphere, P; gray sphere, Cl; orange sphere, Sb; pink sphere, F. For clarity, all C and H atoms are omitted.

The further addition of SbF_6^- to the CH_2Cl_2 solution of Pt_1Ag_{28}-Cl (cluster/$NaSbF_6$ = 1/10) yields a size-growth nanocluster, Pt_1Ag_{30}-SbF_6. Such a transformation suggests the progressive influence of the SbF_6^- counterion to the nanocluster structure. Specifically, the small amounts of SbF_6^- can just substitute the Cl^- counterion in Pt_1Ag_{28}-Cl and slightly adjust the structure of Pt_1Ag_{28} simultaneously. In contrast, the overall structure of Pt_1Ag_{28} is thoroughly reconstructed with the existence of a large amount of the SbF_6^-. The cluster reconstruction may result from the nonnegligible interaction between the F in SbF_6^- and the Ag atom on the surface of these Pt-Ag nanoclusters,[48] albeit no Ag-F bond has been observed in both Pt_1Ag_{28}-SbF_6 and Pt_1Ag_{30}-SbF_6. Besides, the two incorporated Ag^+ along with the transformation from Pt_1Ag_{28}-Cl to Pt_1Ag_{30}-SbF_6 should come from

the destruction of the Pt_1Ag_{28}-Cl precursors. Since the structures of Pt_1Ag_{28}-Cl and Pt_1Ag_{30}-SbF_6 are totally different in terms of their kernel and shell configurations, we speculated that such a structural transformation should be a destruction-reorganization process.

Structurally, the Pt_1Ag_{30} nanocluster contains an icosahedral Pt_1Ag_{12} kernel (**Figure 5.4A**), which is first wrapped by three $Ag_2(S\text{-}Adm)_3(PPh_3)_1$ units to make up a $Pt_1Ag_{18}(S\text{-}Adm)_9(PPh_3)_3$ structure (**Figure 5.4B**, **Figure 5.4C**). Of note, the FCC configuration of Pt_1Ag_{12} in Pt_1Ag_{28}-Cl converts into the icosahedron with the transformation from Pt_1Ag_{28}-Cl to Pt_1Ag_{30}-SbF_6, and such a conversion has also been observed in the thiol ligand and control of Pt_1Ag_{28} nanoclusters.[57, 58] The $Pt_1Ag_{18}(S\text{-}Adm)_9(PPh_3)_3$ structure is further covered by a Cl ligand and an $Ag_9(S\text{-}Adm)_9$ cap that is composed of three $Ag_4(S\text{-}Adm)_4$ ring units *via* sharing three Ag-SAdm edges (**Figure 5.4D**, **Figure 5.4E**). The introduced Cl ligand is proposed from the Cl counterion of the Pt_1Ag_{28}-Cl nanocluster. Then, the obtained $Pt_1Ag_{27}Cl_1(S\text{-}Adm)_{18}(PPh_3)_3$ structure is further stabilized by three Ag linkers, and these Ag linkers (labeled in orange) connect the surface $Ag_9(S\text{-}Adm)_9$ cap (labeled in green) and the $Ag_6(S\text{-}Adm)_9(PPh_3)_3$ bottom (labeled in blue) (**Figure 5.4F**-**Figure 5.4H**). The overall structure of Pt_1Ag_{30}-SbF_6 contains a C_3 symmetry axis, which passes through the innermost Pt core and the Cl ligand (**Figure 5.4I**, **Figure 5.4J** and **Figure 5.5**). Of note, for both Pt_1Ag_{28}-SbF_6 and Pt_1Ag_{30}-SbF_6 nanoclusters, the F terminal of SbF_6^- was not bonded to the surface Ag atoms, which is different from our previous finding that the Ag-F interaction can trigger intercluster connection in the cluster crystal lattice.[48]

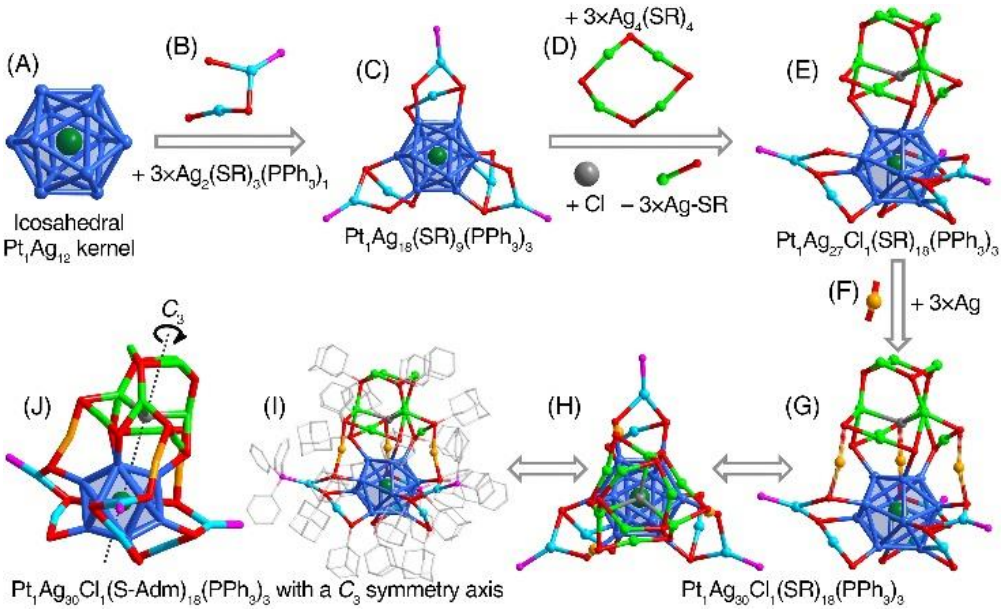

Figure 5.4. Structure anatomy of the Pt_1Ag_{30}-SbF_6 nanocluster. (A) The icosahedral Pt_1Ag_{12} kernel. (B) The $Ag_2(S\text{-}Adm)_3(PPh_3)_1$ surface unit. (C) The $Pt_1Ag_{18}(S\text{-}Adm)_9(PPh_3)_3$ structure. (D) The $Ag_4(S\text{-}Adm)_4$ surface unit. (E) The $Pt_1Ag_{27}Cl_1(S\text{-}Adm)_{18}(PPh_3)_3$ structure. (F) The Ag linker. (G,H) The $Pt_1Ag_{30}Cl_1(S\text{-}Adm)_{18}(PPh_3)_3$ structure from different views. (I) Total structure of Pt_1Ag_{30}-SbF_6. (J) The C_3 symmetry axis of the Pt_1Ag_{30}-SbF_6 nanocluster. Color legends: dark green sphere, Pt; dark blue sphere, kernel Ag; blue/green/orange sphere, surface Ag; red sphere, S; magenta sphere, P; gray sphere, Cl; pale gray sphere, C. For clarity, all H atoms are omitted.

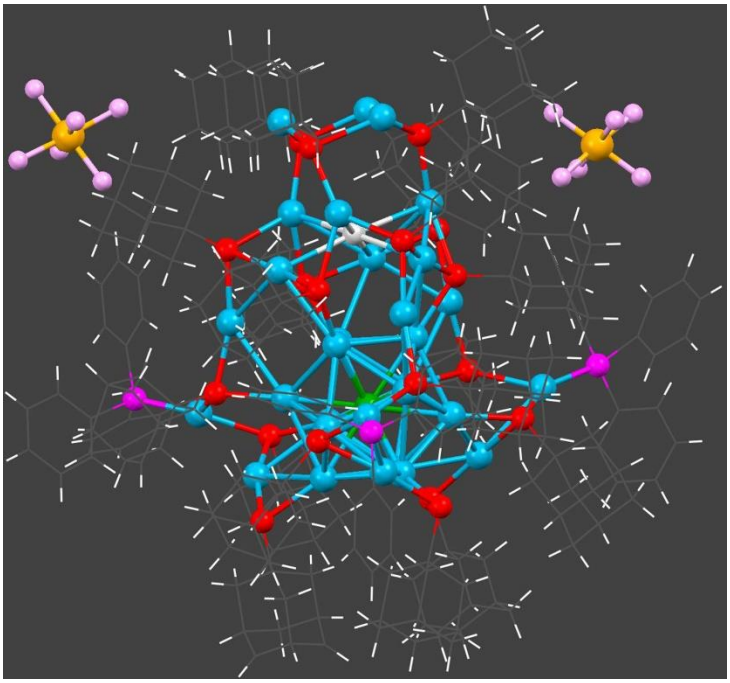

Figure 5.5. Total structure of $[Pt_1Ag_{30}Cl_1(S\text{-}Adm)_{18}(PPh_3)_3](SbF_6)_3$. The number of SbF_6^- counterions is three, suggested by the ESI-MS result. However, only two SbF_6^- counterions are observed in the crystal lattice. The loss of the third SbF_6^- counterion may result from its high disorder, or the steric hindrance that the third one is hard to be included in the crystal lattice. Color legends: dark green, Pt; blue, Ag; gray, Cl; red, S; magenta, P; pale gray, C; white, H; orange, Sb; pink, F.

The Pt_1Ag_{30}-SbF_6 was highly stable in the air and displayed unchanged optical absorptions within 7 days (**Figure 5.6**). However, this cluster would be decomposed in the presence of massive SbF_6^- counterions. Specifically, after a massive excess of SbF_6^- was introduced to the CH_2Cl_2 solution of Pt_1Ag_{28}-Cl (cluster/$NaSbF_6$ = 1/30), the solution color changed from dark red to pale yellow, and the UV-vis spectrum and ESI-MS result suggested the generation of polydispersed Pt-Ag compounds (**Figure 5.7A** and **Figure 5.8**), demonstrating the decomposition of the nanocluster. ESI-MS of Pt_1Ag_{28}-Cl, Pt_1Ag_{28}-SbF_6, and Pt_1Ag_{30}-SbF_6 nanoclusters were also recorded. Both Pt_1Ag_{28}-Cl and Pt_1Ag_{28}-SbF_6 presented the same mass signal at 3637.64 Da, suggesting the maintained composition between these two nanoclusters (**Figure 5.7B**, **Figure 5.7C**). The excellent match of the experimental and simulated isotope patterns illustrated that the measured

formula was $[Pt_1Ag_{28}(S\text{-}Adm)_{18}(PPh_3)_4]^{2+}$. For the ESI-MS of Pt_1Ag_{30}-SbF_6, a major peak centered at about m/z = 2421.32 Da was detected (**Figure 5.7D**). The magnification of this peak evidenced the +3 charge state of the nanocluster because of the 0.33 Da mass gap in the positive mode. Accordingly, the molecular weight of the nanocluster was determined as 7263.96 Da (2421.32 × 3), perfectly assigned to $[Pt_1Ag_{30}Cl_1(S\text{-}Adm)_{18}(PPh_3)_3]^{3+}$. Since the central Pt atom contributes no free valence electrons, the nominal electron counts of these three nanocluster are all 8e: 28 – 18 – 2 = 8 for Pt_1Ag_{28}-Cl, 28 – 18 – 2 = 8 for Pt_1Ag_{28}-SbF_6, and 30 – 1 – 18 – 3 = 8 for Pt_1Ag_{30}-SbF_6.[59] A combination of XPS, ICP, and EDS unambiguously identified the composition and the purity of these nanoclusters (**Figure 5.9** – **Figure 5.14** and **Table 5.1**).

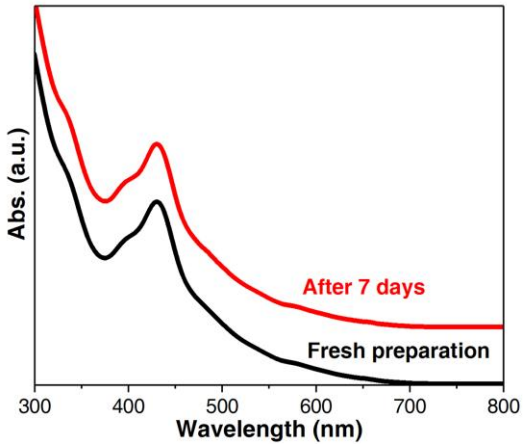

Figure 5.6. Optical absorption of the $[Pt_1Ag_{30}Cl_1(S\text{-}Adm)_{18}(PPh_3)_3](SbF_6)_3$. Black line: the freshly prepared nanocluster. Red line: the nanocluster was stirred for 7 days in the air.

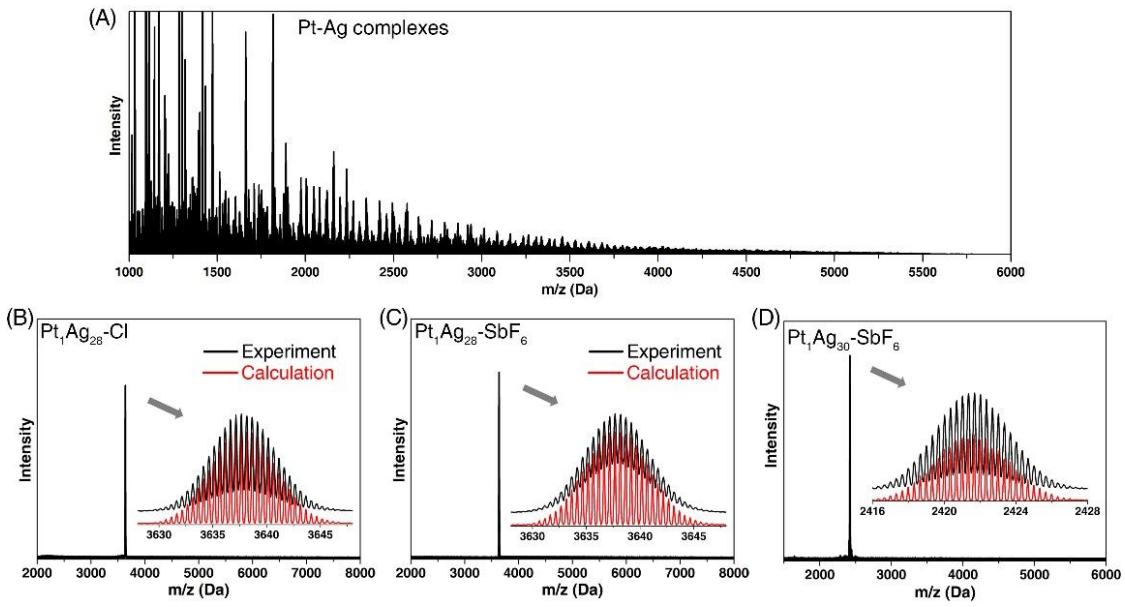

Figure 5.7. ESI-MS results of (A) polydispersed Pt-Ag compounds, (B) Pt_1Ag_{28}-Cl, (C) Pt_1Ag_{28}-SbF_6, and (D) Pt_1Ag_{30}-SbF_6. No signal of Pt_1Ag_{28}-Cl, Pt_1Ag_{28}-SbF_6, or Pt_1Ag_{30}-SbF_6 is observed in the ESI-MS result of polydispersed Pt-Ag compounds.

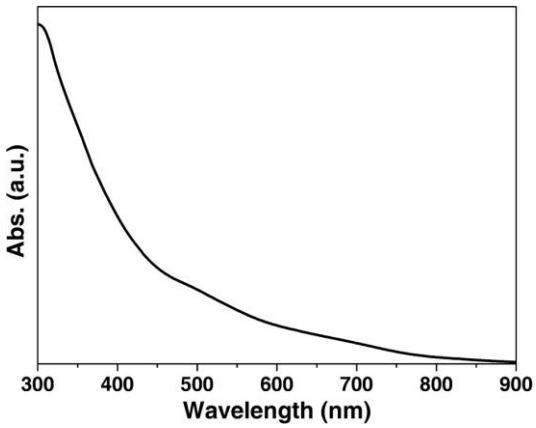

Figure 5.8. UV-vis spectrum of the poly-dispersed Pt-Ag compounds.

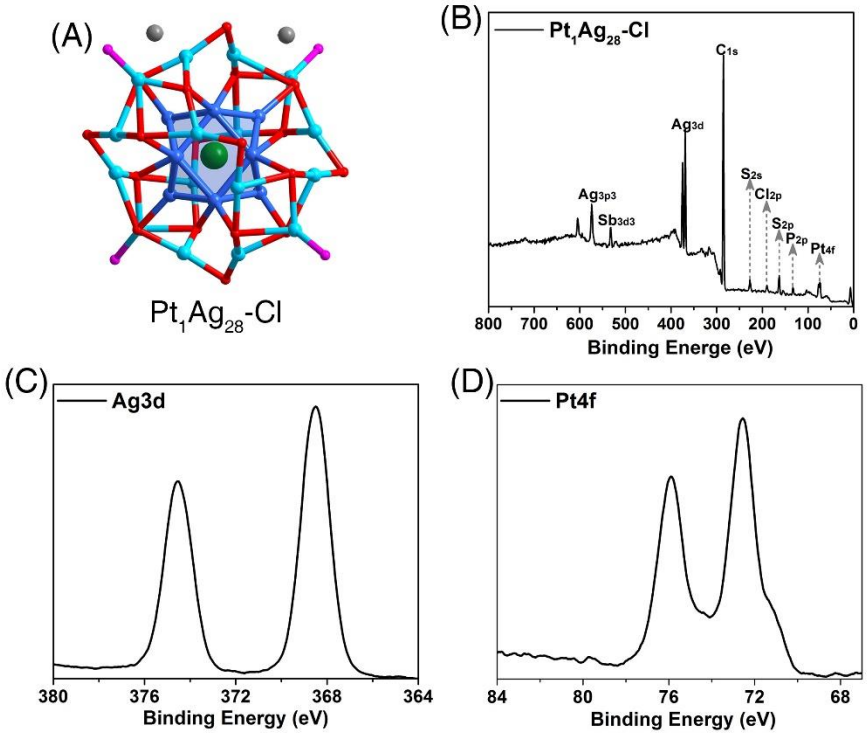

Figure 5.9. (A) Crystal structure of $[Pt_1Ag_{28}(S\text{-}Adm)_{18}(PPh_3)_4]Cl_2$. (B) XPS spectrum of the $[Pt_1Ag_{28}(S\text{-}Adm)_{18}(PPh_3)_4]Cl_2$ nanoclusters. (C) XPS of Ag 3d of the $[Pt_1Ag_{28}(S\text{-}Adm)_{18}(PPh_3)_4]Cl_2$ nanocluster. (D) XPS of Pt 4f of the $[Pt_1Ag_{28}(S\text{-}Adm)_{18}(PPh_3)_4]Cl_2$ nanocluster.

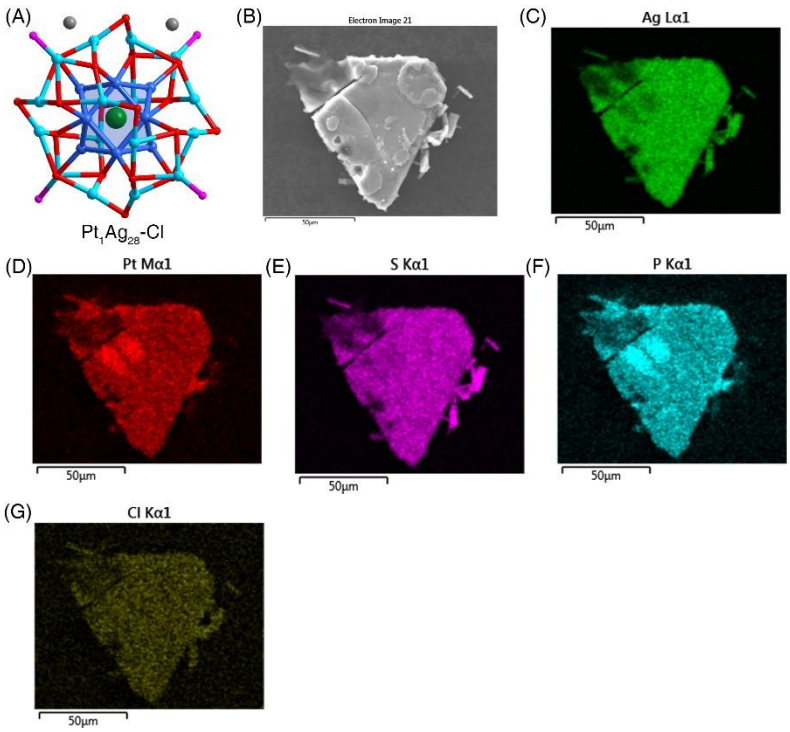

Figure 5.10. (A) Crystal structure of $[Pt_1Ag_{28}(S\text{-}Adm)_{18}(PPh_3)_4]Cl_2$. (B-G) Elemental mapping images of the $[Pt_1Ag_{28}(S\text{-}Adm)_{18}(PPh_3)_4]Cl_2$ nanocluster crystal.

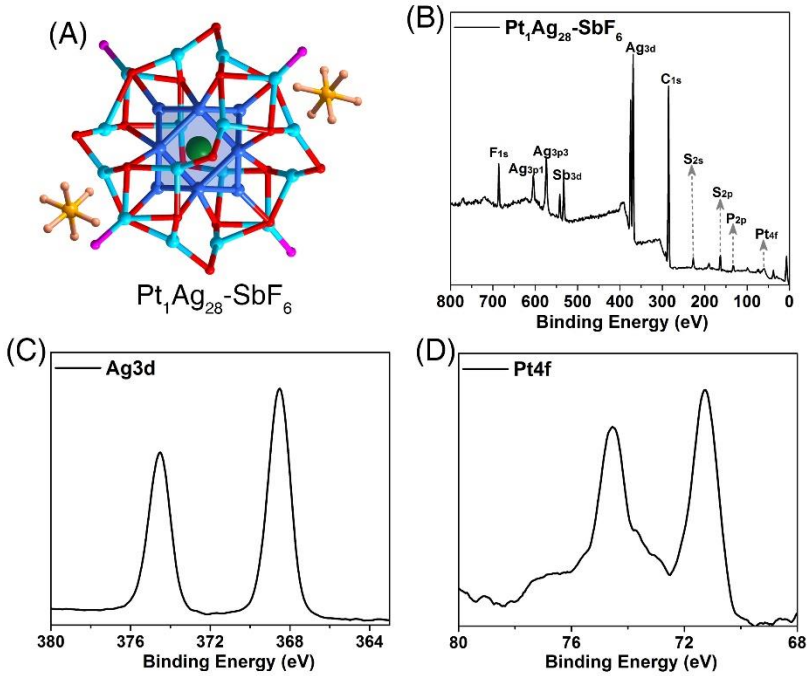

Figure 5.11. (A) Crystal structure of $[Pt_1Ag_{28}(S\text{-}Adm)_{18}(PPh_3)_4](SbF_6)_2$. (B) XPS spectrum of the $[Pt_1Ag_{28}(S\text{-}Adm)_{18}(PPh_3)_4](SbF_6)_2$ nanoclusters. (C) XPS of Ag 3d of the $[Pt_1Ag_{28}(S\text{-}Adm)_{18}(PPh_3)_4](SbF_6)_2$ nanocluster. (D) XPS of Pt 4f of the $[Pt_1Ag_{28}(S\text{-}Adm)_{18}(PPh_3)_4](SbF_6)_2$ nanocluster.

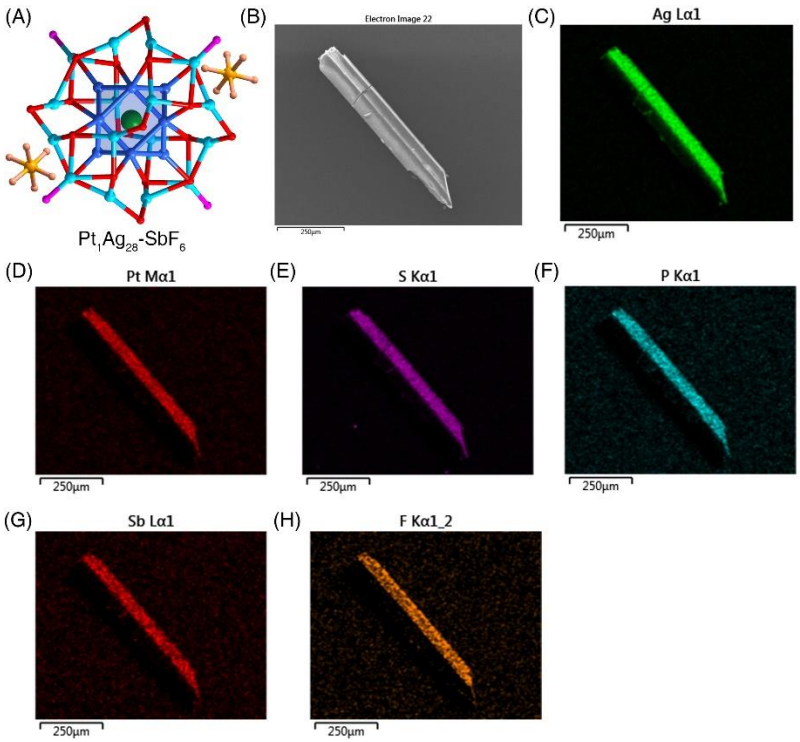

Figure 5.12. (A) Crystal structure of $[Pt_1Ag_{28}(S\text{-}Adm)_{18}(PPh_3)_4](SbF_6)_2$. (B-G) Elemental mapping images of the $[Pt_1Ag_{28}(S\text{-}Adm)_{18}(PPh_3)_4](SbF_6)_2$ nanocluster crystal.

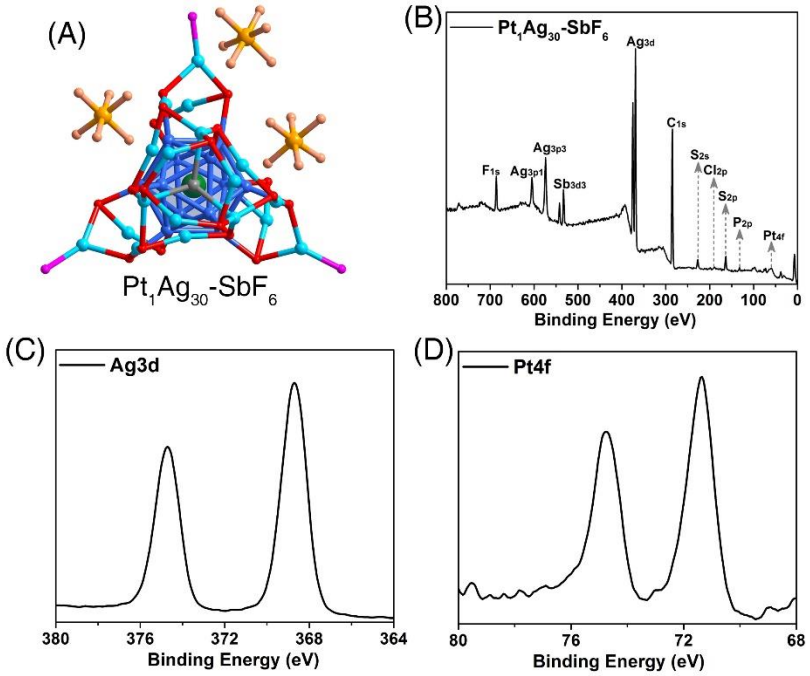

Figure 5.13. (A) Crystal structure of $[Pt_1Ag_{30}Cl_1(S\text{-}Adm)_{18}(PPh_3)_3](SbF_6)_3$. (B) XPS spectrum of the $[Pt_1Ag_{30}Cl_1(S\text{-}Adm)_{18}(PPh_3)_3](SbF_6)_3$ nanoclusters. (C) XPS of Ag 3d of the $[Pt_1Ag_{30}Cl_1(S\text{-}Adm)_{18}(PPh_3)_3](SbF_6)_3$ nanocluster. (D) XPS of Pt 4f of the $[Pt_1Ag_{30}Cl_1(S\text{-}Adm)_{18}(PPh_3)_3](SbF_6)_3$ nanocluster.

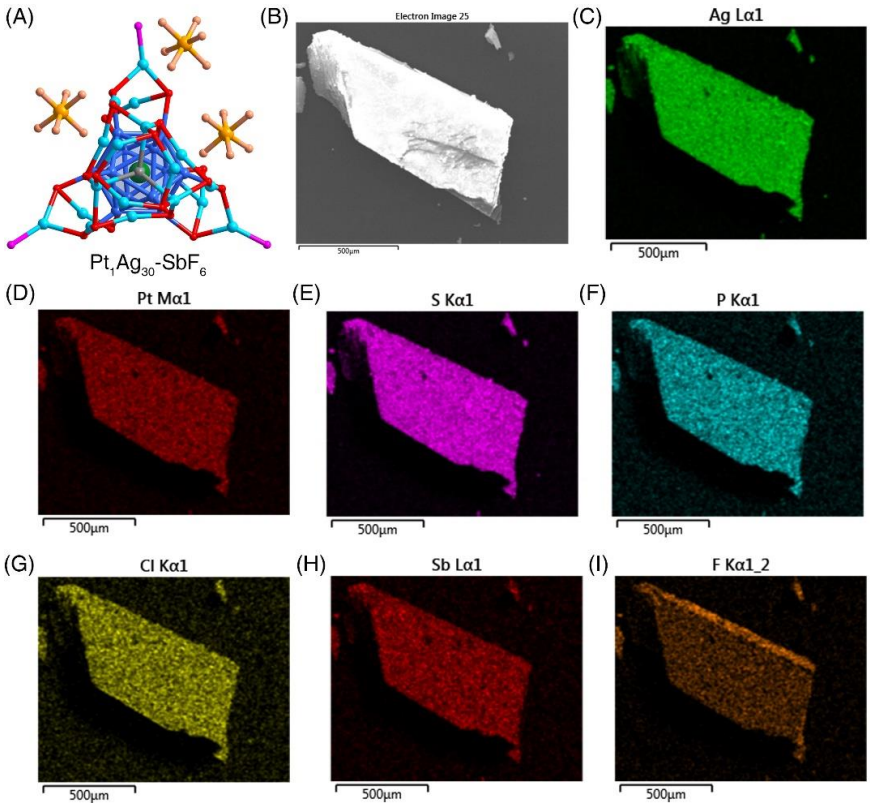

Figure 5.14. EDS result of $[Pt_1Ag_{30}Cl_1(S\text{-}Adm)_{18}(PPh_3)_3](SbF_6)_3$.

Table 5.1. Atom ratio of Pt and Ag in Pt_1Ag_{28} and Pt_1Ag_{30} nanoclusters. Atom ratios of Pt and Ag in $[Pt_1Ag_{28}(S\text{-}Adm)_{18}(PPh_3)_4]Cl_2$, $[Pt_1Ag_{28}(S\text{-}Adm)_{18}(PPh_3)_4](SbF_6)_2$, and $[Pt_1Ag_{30}Cl_1(S\text{-}Adm)_{18}(PPh_3)_3](SbF_6)_3$ nanoclusters were calculated from inductively coupled plasma (ICP) and X-ray photoelectric spectroscopy (XPS).

$[Pt_1Ag_{28}(S\text{-}Adm)_{18}(PPh_3)_4]Cl_2$	**Pt atom**	**Ag atom**
ICP Experimental Ratio	3.90%	96.10%
XPS Experimental Ratio	3.35%	96.65%
Theoretical Ratio	3.45%	96.55%
$[Pt_1Ag_{28}(S\text{-}Adm)_{18}(PPh_3)_4](SbF_6)_2$	**Pt atom**	**Ag atom**
ICP Experimental Ratio	3.34%	96.66%
XPS Experimental Ratio	3.27%	96.73%
Theoretical Ratio	3.45%	96.55%
$[Pt_1Ag_{30}Cl_1(S\text{-}Adm)_{18}(PPh_3)_3](SbF_6)_3$	**Pt atom**	**Ag atom**
ICP Experimental Ratio	3.65%	96.35%
XPS Experimental Ratio	3.38%	96.62%
Theoretical Ratio	3.23%	96.77%

Collectively, driven by the addition of SbF_6^-, the stepwise transformation from Pt_1Ag_{28}-Cl to Pt_1Ag_{28}-SbF_6, Pt_1Ag_{30}-SbF_6, and poly-dispersed Pt-Ag compounds has been accomplished (**Figure 5.15**). Several critical points are included in these cluster conversions, including (i, **Figure 5.15A** – **Figure 5.15B**) the preservation of the Pt_1Ag_{28} overall structure by simply substituting the counterion, (ii, **Figure 5.15B** – **Figure 5.15C**) the conversion from Pt_1Ag_{28} to Pt_1Ag_{30} by slightly enhancing the addition of SbF_6^-, and (iii, **Figure 5.15C** – **Figure 5.15D**) the decomposition of nanoclusters because of the massive addition of SbF_6^-. All these conversions demonstrate the SbF_6^- counterion effect in reconstructing nanoclusters at the single molecular level. Besides, with the nanocluster transformation from Pt_1Ag_{28}-Cl to Pt_1Ag_{28}-SbF_6 and Pt_1Ag_{30}-SbF_6, the cluster kernel was retained as Pt_1Ag_{12}, although the configuration of this kernel altered. In this context, the SbF_6^- counterion should have a strong effect on cluster surface structures, resulting in their significant distortion and transformation; then, such surface transformations continue to affect the Pt_1Ag_{12} kernel configuration, giving rise to its conversion from icosahedron to FCC.

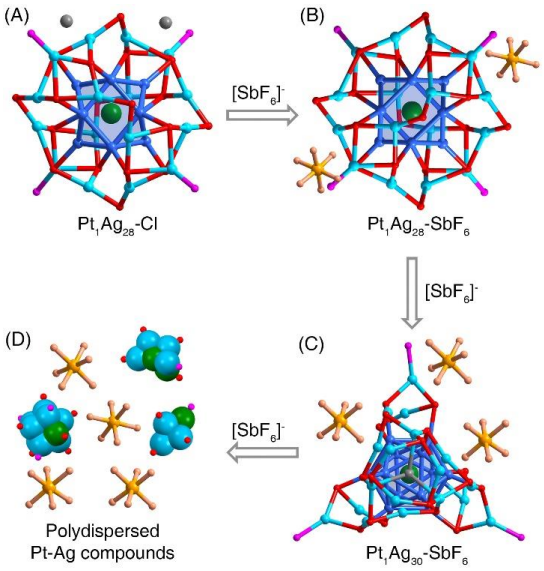

Figure 5.15. The addition of SbF_6^- induced stepwise transformation from Pt_1Ag_{28}-Cl to Pt_1Ag_{28}-SbF_6, Pt_1Ag_{30}-SbF_6, and poly-dispersed Pt-Ag compounds. Color legends: dark green sphere, Pt; dark blue sphere, kernel Ag; blue sphere, surface Ag; gray sphere, Cl;

red sphere, S; magenta sphere, P; orange sphere, Sb; pink sphere, F. For clarity, all C and H atoms are omitted.

The counterion effect has also been investigated in rearranging cluster molecules in supracrystal lattices. For the Pt_1Ag_{28} cluster framework, because of the substitution of Cl^- counterions by SbF_6^-, the space group of Pt_1Ag_{28}-Cl (i.e., *C*2/*c*) alters into *P*21/*c* of Pt_1Ag_{28}-SbF_6 (**Figure 5.16A**, **Figure 5.16B** and **Figure 5.17**, **Figure 5.18**), although both nanoclusters are crystallized into a monoclinic crystal system. The *Z* value of Pt_1Ag_{28}-Cl is 8, larger than that of Pt_1Ag_{28}-SbF_6, whereas the crystalline density of Pt_1Ag_{28}-Cl is much smaller than that of Pt_1Ag_{28}-SbF_6 (1.405 *versus* 1.712). Besides, the Pt_1Ag_{30}-SbF_6 cluster molecules are packed into a triclinic crystal lattice with a *P*-1 space group (**Figure 5.16C** and **Figure 5.19**). Although the *Z* value of Pt_1Ag_{30}-SbF_6 is the smallest among the three nanoclusters, its crystal density is the largest. These differences in packing modes (especially between Pt_1Ag_{28}-Cl and Pt_1Ag_{28}-SbF_6) reflect the SbF_6^- counterion effect in the intercluster rearrangement.

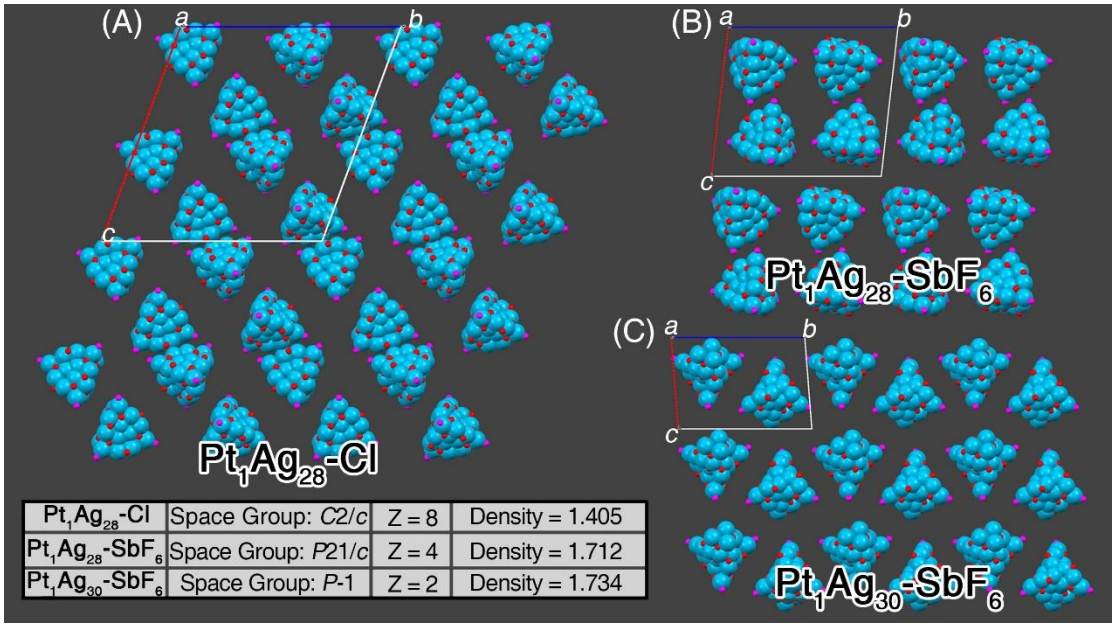

Figure 5.16. Crystalline packing modes of (A) Pt_1Ag_{28}-Cl, (B) Pt_1Ag_{28}-SbF_6, and (C) Pt_1Ag_{30}-SbF_6, and the comparison of crystal lattice parameters.

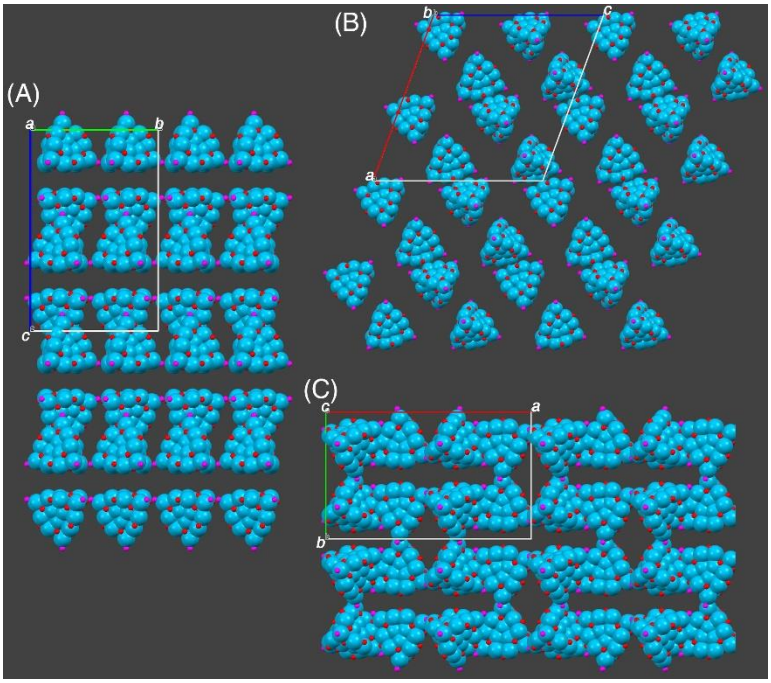

Figure 5.17. Packing of $[Pt_1Ag_{28}(S\text{-}Adm)_{18}(PPh_3)_4]Cl_2$ in the crystal lattice from different views. The counterions are omitted for clarity.

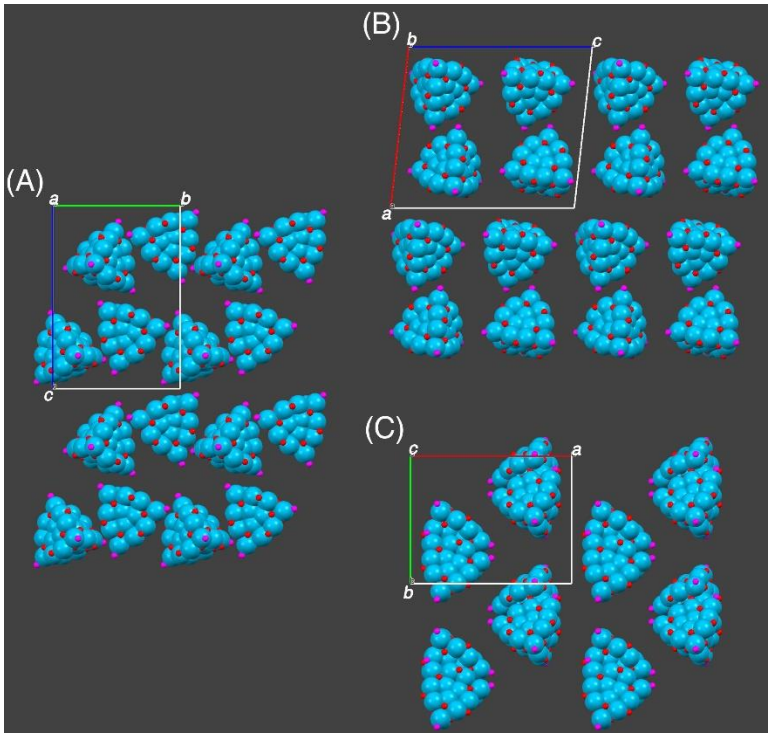

Figure 5.18. Packing modes of $[Pt_1Ag_{28}(S\text{-}Adm)_{18}(PPh_3)_4](SbF_6)_2$ in the crystal lattice from different views. The counterions are omitted for clarity.

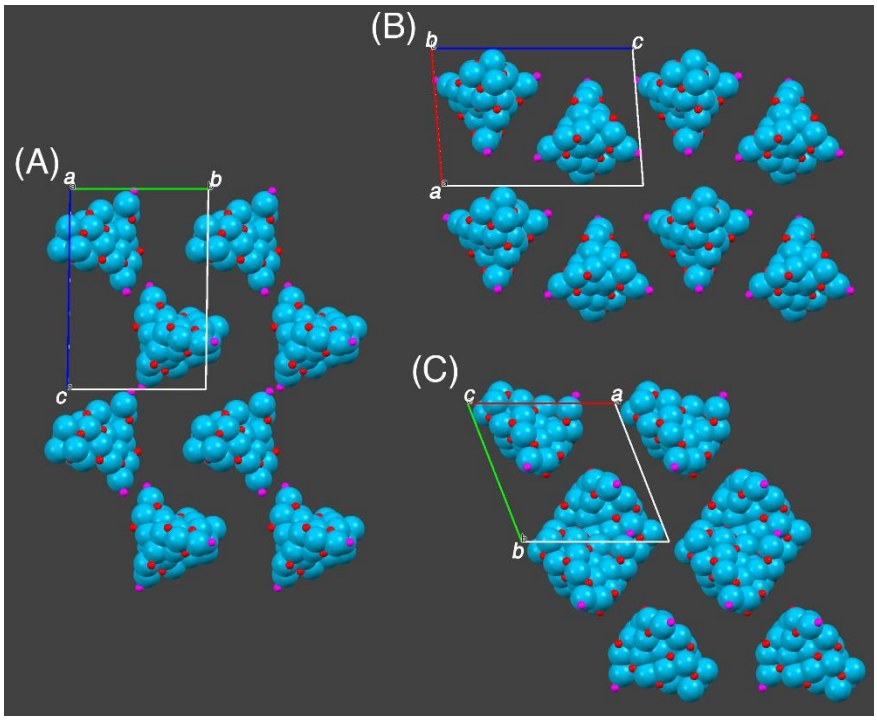

Figure 5.19. Packing of $[Pt_1Ag_{30}Cl_1(S\text{-}Adm)_{18}(PPh_3)_3](SbF_6)_3$ in the crystal lattice from different views. The counterions are omitted for clarity.

5.3.2 Photochemical studies

The structures/compositions of nanoclusters are determinants of their physical/chemical properties.[1, 12-20,60-63] Because of their different molecular structures, Pt_1Ag_{28}-Cl, Pt_1Ag_{28}-SbF_6, and Pt_1Ag_{30}-SbF_6 nanoclusters manifested distinguishable optical absorptions and emissions. The UV-vis spectra of both Pt_1Ag_{28}-Cl and Pt_1Ag_{28}-SbF_6 solutions exhibited the same signals at 445 nm. By comparison, the Pt_1Ag_{30}-SbF_6 solution showed an intense absorption at 430 nm (**Figure 5.20A**, solid lines). As for the emission of these nanocluster solutions, a 10 nm blue-shift was observed by comparing the emission wavelength of Pt_1Ag_{30}-SbF_6 (740 nm) to those of both Pt_1Ag_{28}-Cl and Pt_1Ag_{28}-SbF_6 (750 nm).[64] Besides, the photoluminescence (PL) intensity of the nanocluster was enhanced accompanied by the nanocluster transformation from Pt_1Ag_{28}-Cl to Pt_1Ag_{28}-SbF_6, and then to Pt_1Ag_{30}-SbF_6 (**Figure 5.20A**, dotted lines). Significantly, a 16-fold enhancement on emission intensity has been accomplished with the nanocluster transformation (PL spectra were measured with the same optical density of 0.05), giving rise to an ultrabright

Pt_1Ag_{30}-SbF_6 nanocluster. Although some differences existed in optical absorptions and emissions of these three Pt-Ag nanoclusters, the profiles of their optical spectra were similar (**Figure 5.20A**). In this context, there should be some similarities between the electronic structures of Pt_1Ag_{28} and Pt_1Ag_{30} cluster templates; one possible reason is that both cluster templates follow the same Pt_1Ag_{12}(kernel)@Ag-SAdm-PPh_3(surface) configuration.

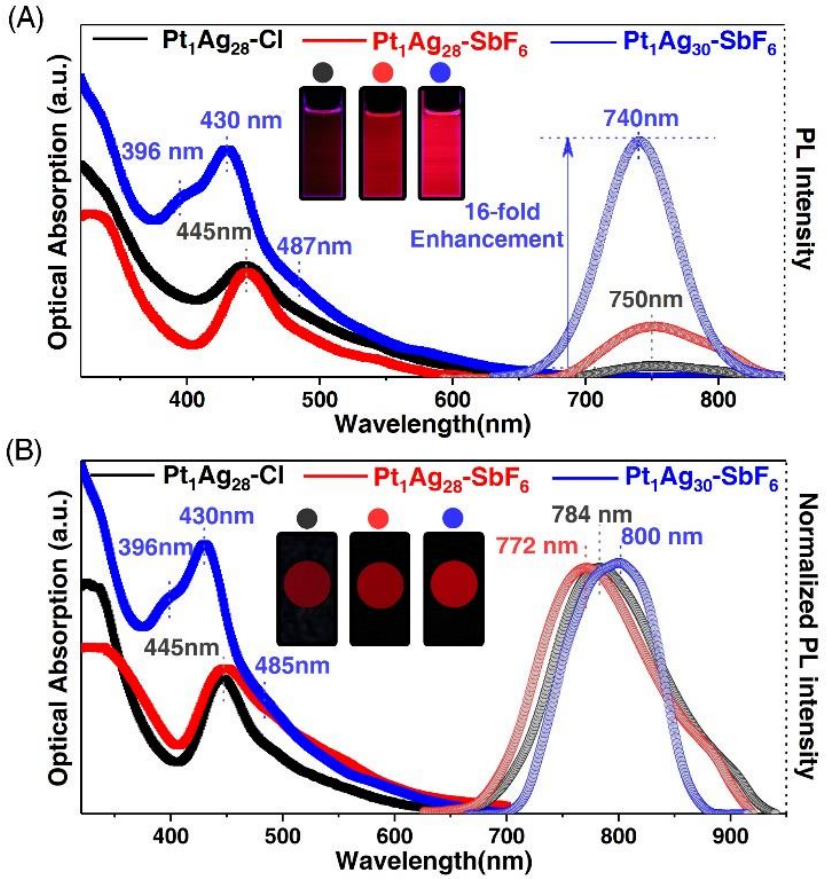

Figure 5.20. Optical properties of Pt_1Ag_{28}-Cl, Pt_1Ag_{28}-SbF_6, and Pt_1Ag_{30}-SbF_6 nanoclusters. (A) Comparison of optical absorptions and emissions (nanoclusters were dissolved in CH_2Cl_2) of Pt_1Ag_{28}-Cl (black lines), Pt_1Ag_{28}-SbF_6 (red lines), and Pt_1Ag_{30}-SbF_6 (blue lines) nanoclusters. Insets: photos of luminescence of Pt_1Ag_{28}-Cl, Pt_1Ag_{28}-SbF_6, and Pt_1Ag_{30}-SbF_6 nanoclusters in CH_2Cl_2. (B) Comparison of optical absorptions and emissions (nanoclusters were in a crystallized film) of Pt_1Ag_{28}-Cl (black lines), Pt_1Ag_{28}-SbF_6 (red lines), and Pt_1Ag_{30}-SbF_6 (blue lines) nanoclusters. Insets: photos of

luminescence of Pt_1Ag_{28}-Cl, Pt_1Ag_{28}-SbF_6, and Pt_1Ag_{30}-SbF_6 nanocluster crystallized films.

Given that the Pt_1Ag_{28}-SbF_6 and Pt_1Ag_{30}-SbF_6 nanoclusters bear the same SbF_6^- counterion, we further evaluated the concentration-dependent PL properties of these two nanoclusters. As shown in **Figure 5.21A** and **Figure 5.22A**, at low concentrations, the PL intensity increased with the nanocluster concentration, and the maximum PL intensity was detected when the concentration of Pt_1Ag_{28}-SbF_6 or Pt_1Ag_{30}-SbF_6 reached 1.0×10^{-5} or 1.2×10^{-5} mol/L, respectively. However, at high concentrations, the emission of nanoclusters quenched gradually as the concentration increased (**Figure 5.21B** and **Figure 5.22B**). The emission enhancement in the first phase was proposed to result from the increase of the fluorophore (i.e., the cluster molecules) in solution since the PL intensity was linearly correlated to the concentration. Besides, the aggregation caused-quenching (ACQ) might take place when the concentration of nanoclusters rose to a certain value, giving rise to the PL attenuation in the second phase, different from the aggregation-induced emission (AIE) that has been widely observed in metal nanoclusters.[35]

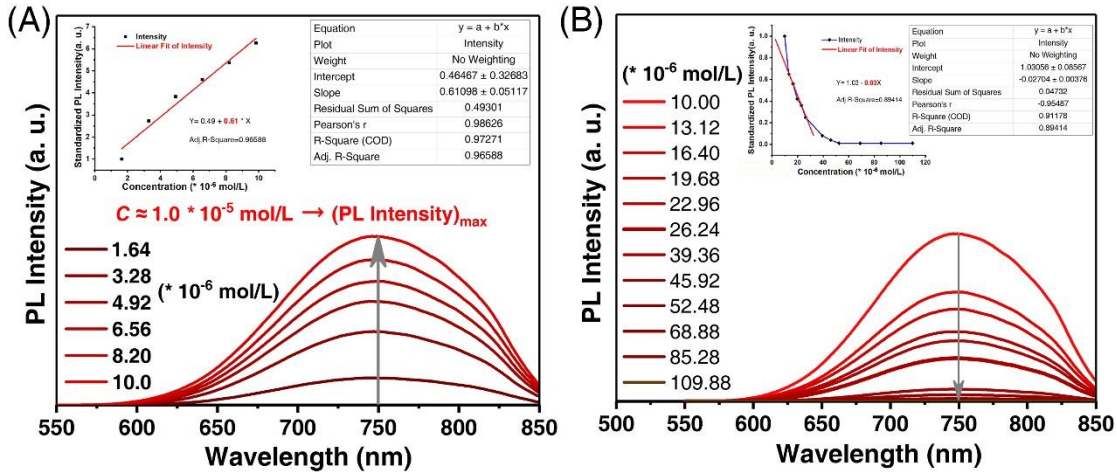

Figure 5.21. Concentration-dependent photoluminescence intensity of the $[Pt_1Ag_{28}(S\text{-}Adm)_{18}(PPh_3)_4](SbF_6)_2$ nanocluster (dissolved in CH_2Cl_2). (A) The concentration of the nanocluster was enhanced from 1.64×10^{-6} to 10.0×10^{-6} mol/L. The photoluminescence intensity was enhanced significantly with the increase of the concentration. (B) The

concentration of the nanocluster was enhanced from 10.0×10^{-6} to 109.88×10^{-6} mol/L. As the concentration increased, the photoluminescence of the nanocluster solution was quenched.

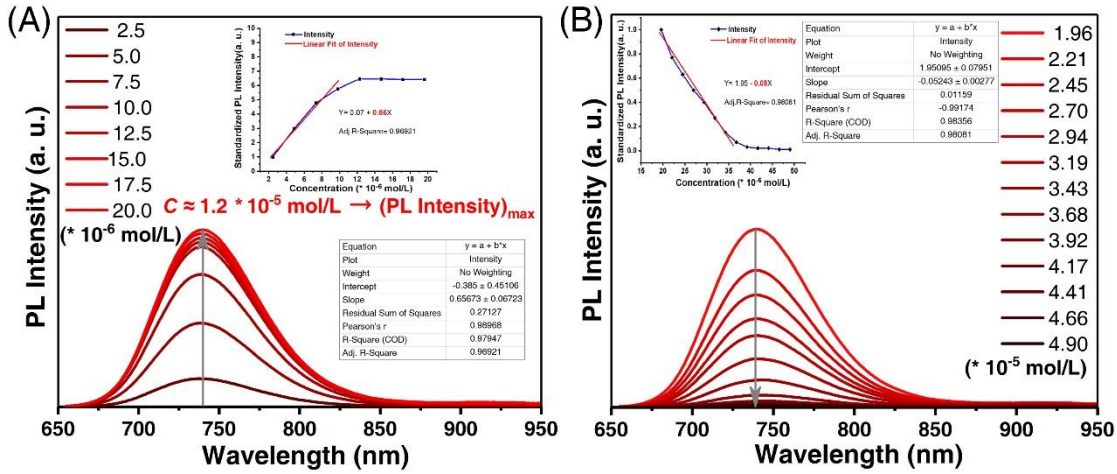

Figure 5.22. Concentration-dependent photoluminescence intensity of the $[Pt_1Ag_{30}Cl_1(S\text{-}Adm)_{18}(PPh_3)_3](SbF_6)_3$ nanocluster (dissolved in CH_2Cl_2). (A) The concentration of the nanocluster was enhanced from 2.5×10^{-6} to 20.0×10^{-6} mol/L. The photoluminescence intensity was enhanced significantly with the increase of the concentration. (B) The concentration of the nanocluster was enhanced from 1.96×10^{-5} to 4.90×10^{-5} mol/L. As the concentration increased, the photoluminescence of the nanocluster solution was quenched.

The PL lifetimes of these Pt-Ag nanoclusters were then compared. The PL lifetimes of Pt_1Ag_{28}-Cl and Pt_1Ag_{28}-SbF_6 were about 3.8 and 3.6 μs measured by time-correlated single photon counting, and were irrelevant to the atmosphere (**Figure 5.23A**, **Figure 5.23B**). In vivid contrast, the Pt_1Ag_{30}-SbF_6 solution presented atmosphere-related PL lifetimes (**Figure 5.23C**): an ambient CH_2Cl_2 solution of Pt_1Ag_{30}-SbF_6 exhibited a PL lifetime of 1.01 μs, while the PL lifetime of N_2-purged or the O_2-saturated cluster solution was extended or reduced to 2.52 or 0.51 μs, respectively. In addition, a similar trend was also observed in terms of the PL intensity of nanocluster solutions. Specifically, the PL intensities of the Pt_1Ag_{28}-Cl and Pt_1Ag_{28}-SbF_6 were identical in ambient, N_2-purged, or O_2-saturated solutions (**Figure 5.24A**, **Figure 5.24B**). The PL

quantum yields (QYs) of Pt_1Ag_{28}-Cl and Pt_1Ag_{28}-SbF_6 were determined as 5% and 39%, respectively. By comparison, the N_2-purged solution of Pt_1Ag_{30}-SbF_6 showed a higher PL QY (85%) than the ambient solution (54 %), whereas the O_2-saturated solution quenched PL to QY of 10% (**Figure 5.24C**). In this context, the PL nature of Pt_1Ag_{28} and Pt_1Ag_{30} nanoclusters might be different.[65-67] The structural reconstruction from Pt_1Ag_{28} to Pt_1Ag_{30} played a critical role in affecting the intersystem crossing from the S1 to the T1 and, subsequently, giving rise to their different PL nature.[65-67] The triplet-state emission from Pt_1Ag_{30}-SbF_6 was verified by observing $^1O_2$ production over the photoexcited Pt_1Ag_{30}-SbF_6, in which the triplet state of Pt_1Ag_{30}-SbF_6 transferred its energy to the normal triplet state $^3O_2$, giving rise to singlet state $^1O_2$.[65] The spectrum of the N_2-purged Pt_1Ag_{30}-SbF_6 solution was absent of $^1O_2$ emission, while the O_2-saturated Pt_1Ag_{30}-SbF_6 solution exhibited a distinct $^1O_2$ emission peak centered at about 1270 nm (**Figure 5.25**), demonstrating the notable generation of $^1O_2$ and the triplet-state emission of the Pt_1Ag_{30}-SbF_6 nanocluster. Of note, these nanoclusters displayed high photostability and remained unchanged before and after the PL measurements, derived from their consistent ESI-MS results (**Figure 5.26**).

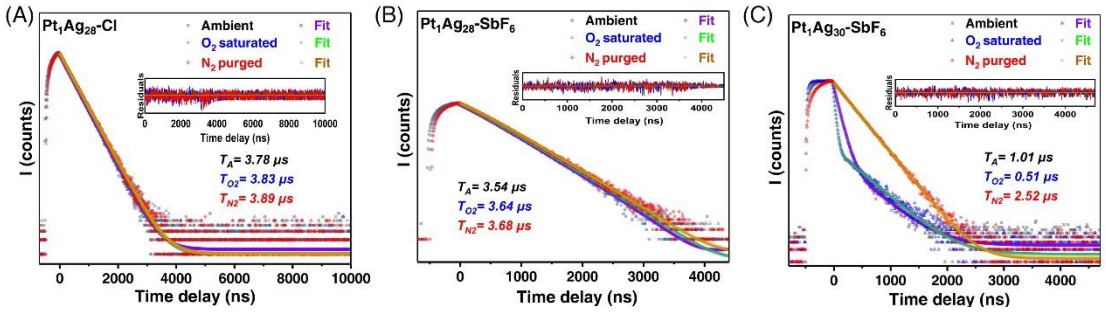

Figure 5.23. Fluorescence lifetimes of different nanoclusters. (A) The microsecond photoluminescence decay traces of $[Pt_1Ag_{28}(S\text{-}Adm)_{18}(PPh_3)_4]Cl_2$ (dissolved in CH_2Cl_2) under ambient, N_2-purged, or O_2-saturated conditions. (B) The microsecond photoluminescence decay traces of $[Pt_1Ag_{28}(S\text{-}Adm)_{18}(PPh_3)_4](SbF_6)_2$ (dissolved in CH_2Cl_2) under ambient, N_2-purged, or O_2-saturated conditions. (C) The microsecond photoluminescence decay traces of $[Pt_1Ag_{30}Cl_1(S\text{-}Adm)_{18}(PPh_3)_3](SbF_6)_3$ (dissolved in CH_2Cl_2) under ambient, N_2-purged, or O_2-saturated conditions.

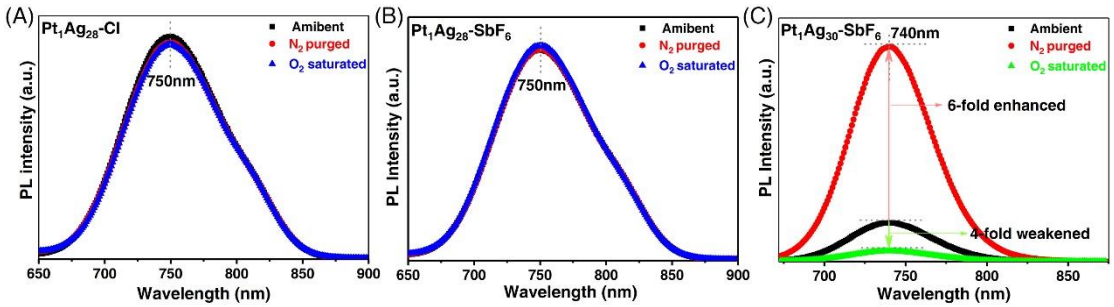

Figure 5.24. (A) Comparison of the emission spectra of CH_2Cl_2 solutions of $[Pt_1Ag_{28}(S\text{-}Adm)_{18}(PPh_3)_4]Cl_2$ under ambient, N_2-purged, or O_2-saturated conditions. (B) Comparison of the emission spectra of CH_2Cl_2 solutions of $[Pt_1Ag_{28}(S\text{-}Adm)_{18}(PPh_3)_4](SbF_6)_2$ under ambient, N_2-purged, or O_2-saturated conditions. (C) Comparison of the emission spectra of CH_2Cl_2 solutions of $[Pt_1Ag_{30}Cl_1(S\text{-}Adm)_{18}(PPh_3)_3](SbF_6)_3$ under ambient, N_2-purged, or O_2-saturated conditions.

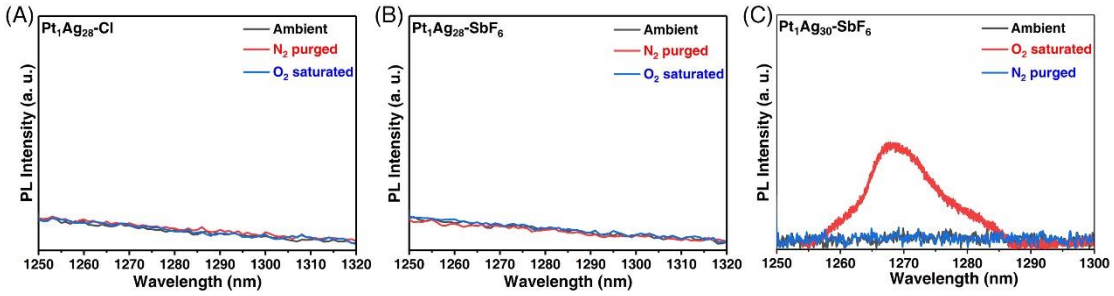

Figure 5.25. (A) Near-infrared photoluminescence of ambient, N_2-purged, and O_2-saturated CH_2Cl_2 solutions of $[Pt_1Ag_{28}(S\text{-}Adm)_{18}(PPh_3)_4]Cl_2$. (B) Near-infrared photoluminescence of ambient, N_2-purged, and O_2-saturated CH_2Cl_2 solutions of $[Pt_1Ag_{28}(S\text{-}Adm)_{18}(PPh_3)_4](SbF_6)_2$. (C) Near-infrared photoluminescence of ambient, N_2-purged, and O_2-saturated CH_2Cl_2 solutions of $[Pt_1Ag_{30}Cl_1(S\text{-}Adm)_{18}(PPh_3)_3](SbF_6)_3$.

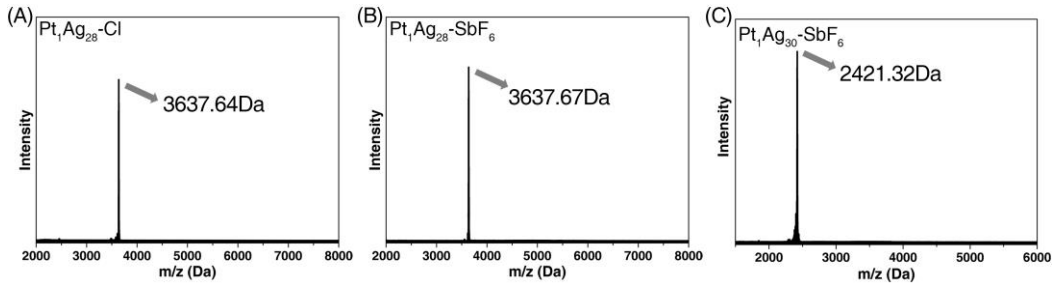

Figure 5.26. ESI-MS results of (A) $[Pt_1Ag_{28}(S\text{-}Adm)_{18}(PPh_3)_4]Cl_2$, (B) $[Pt_1Ag_{28}(S\text{-}Adm)_{18}(PPh_3)_4](SbF_6)_2$, and (C) $[Pt_1Ag_{30}Cl_1(S\text{-}Adm)_{18}(PPh_3)_3](SbF_6)_3$ nanoclusters after the photoluminescence test. The unchanged mass results (compared to the results in Figure S4) demonstrated the high photostability of these three nanoclusters.

The optical properties of nanocluster crystallized films were also investigated. The optical absorptions of these nanocluster crystallized films were almost consistent with those of nanocluster solutions (**Figure 5.20B**, solid lines). However, the emission features of these cluster crystallized films varied greatly from those of solutions (**Figure 5.20B**, dotted lines). Specifically, varying degrees of red-shifts on emissions of the nanocluster crystallized films relative to those of cluster solutions were observed. The crystallized films of Pt_1Ag_{28}-Cl and Pt_1Ag_{28}-SbF_6 emitted at 784 and 772 nm, respectively, representing 34 and 22 nm red-shifts relative to the 750 nm emission of their solutions. Besides, a 60 nm red-shift was observed by comparing the emission of the Pt_1Ag_{30}-SbF_6 crystallized film to that in the solution state. The conspicuous differences in emissions of these nanoclusters in different forms (solution and crystal film) arose from distinct combinations of the electronic coupling and the lattice-origin, non-radiative decay pathways occurring through electron-phonon interactions.[68-71] Besides, these differences could be also explained in terms of their diverse molecular and supramolecular chemistry, including (i) different surface structures between Pt_1Ag_{28} and Pt_1Ag_{30} cluster platforms and different intermolecular interactions in these cluster crystalline assemblies (i.e., cluster-Cl interactions in Pt_1Ag_{28}-Cl *versus* cluster-SbF_6 interactions in Pt_1Ag_{28}-SbF_6 and Pt_1Ag_{30}-SbF_6).

5.3.3 Electrochemistry and electrochemiluminescence

The electrochemical properties of the two novel bimetallic nanoclusters, Pt_1Ag_{30}-SbF_6 and Pt_1Ag_{28}-SbF_6, were first examined using differential pulse voltammetry. **Figure 5.27A** shows the differential pulse voltammogram (DPV) of Pt_1Ag_{30}-SbF_6. The anodic scan starting from −2.10 V reveals three successive oxidation reactions at formal potentials of 0.53 V (Ox1), 0.79 V (Ox2), and 1.10 V (Ox3) vs. SCE, while the cathodic scan shows a single reduction wave at −1.74 V (Red1). These correspond, respectively, to 3-electron removals from the HOMO orbitals of Pt_1Ag_{30}-SbF_6 and a single electron injection to the LUMO. The electrochemical HOMO-LUMO energy gap of 2.0 eV was determined using the difference between the first oxidation and the first reduction after correction for the charging energy (approximated using the potential difference between Ox1 and Ox2).[16, 72] DFT-guided calculations of other nanoclusters suggest that the frontier orbitals of the singly oxidized and reduced states may be localized primarily to the core structure, while the respective orbitals of higher oxidation states preferentially extend onto the surrounding staples.[73, 74] This defined electrochemistry does not lend itself to efficient electrochemiluminescence under the annihilation pathway, however, as no ECL was observed when the potential was scanned between sufficiently reducing and oxidizing potentials to generate the anionic and cationic radical species, respectively, of Pt_1Ag_{30}-SbF_6 (**Figure 5.28**). This is likely due to the poor electrochemical stability of these species, which can be seen in the limited reversibility of the oxidation and reduction peaks in the DPV, or due to the low reactivity of these species.

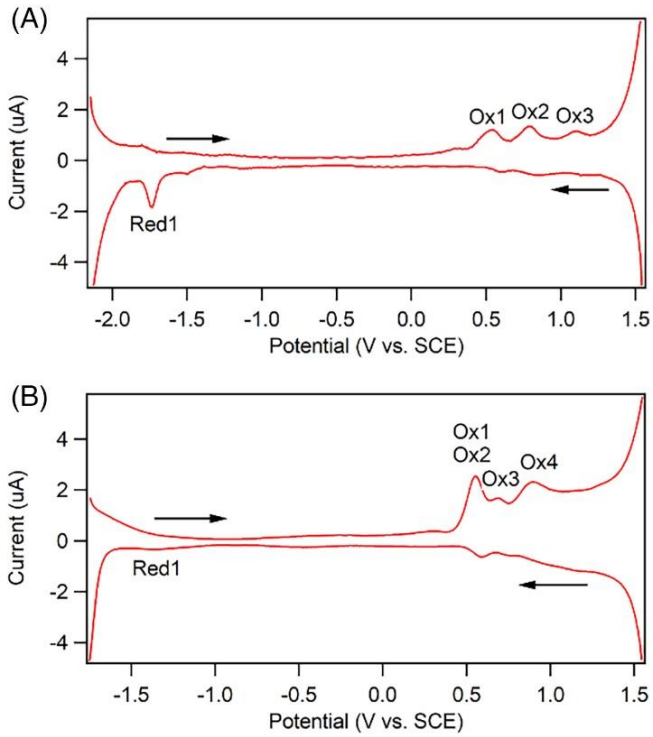

Figure 5.27. Differential pulse voltammogram of (A) 1.5 µM Pt_1Ag_{30}-SbF_6 and (B) 1.3 µM Pt_1Ag_{28}-SbF_6 in dichloromethane containing 0.1 M $TBAPF_6$ as supporting electrolyte. Initial scan direction is indicated with arrows. Pulse peak. amplitude was 50 mV, pulse with was 0.05 s, and pulse period was 0.20 s.

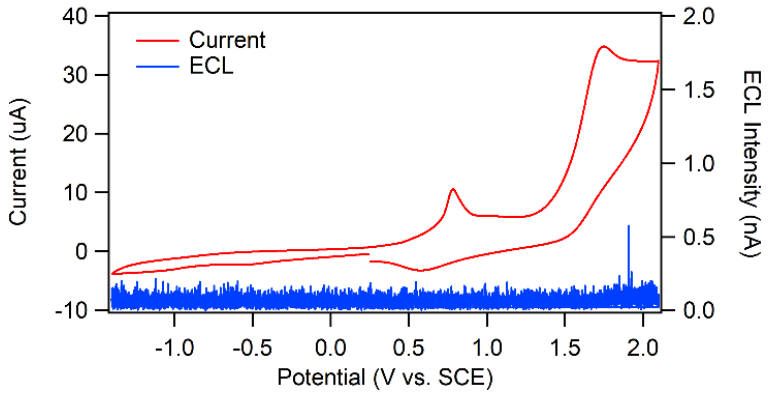

Figure 5.28. ECL voltage curve of 1.5 µM Pt_1Ag_{30}-SbF_6 in dichloromethane with 0.1 M $TBAPF_6$ using a 2-mm platinum disc electrode in the annihilation pathway. Scan rate = 0.1 V/sec.

Figure 5.27B shows the DPV of Pt_1Ag_{28}-SbF_6. The anodic scan reveals three successive oxidation peaks at formal potentials of 0.56 V, 0.68 V, and 0.89 V vs. SCE. However, due to the height of the first oxidation peak relative to its neighbors, we attribute this particular signal to a two-electron removal from Pt_1Ag_{28}-SbF_6 to produce Pt_1Ag_{28}-SbF_6^{2+}. Ox3 and Ox4 correspond to the formation of Pt_1Ag_{28}-$SbF_6^{3+\bullet}$ and Pt_1Ag_{28}-SbF_6^{4+}, respectively. On the cathodic scan, a single reduction peak can be observed at −1.34 V vs. SCE, which corresponds to the formation of Pt_1Ag_{28}-$SbF_6^{1-\bullet}$. The electrochemical HOMO-LUMO gap was calculated to be 1.8 eV, which is slightly smaller than the energy gap of Pt_1Ag_{30}-SbF_6. The electrochemistry of Pt_1Ag_{28}-SbF_6 is observably quite different compared to Pt_1Ag_{30}-SbF_6, and this can be seen in the weak ECL in the annihilation pathway (**Figure 5.29**). Approximately 0.5 nA of photocurrent can be observed when the potential is scanned anodically; since little ECL is detected on the cathodic side, it is likely that the stability of the radical cation is quite limited.

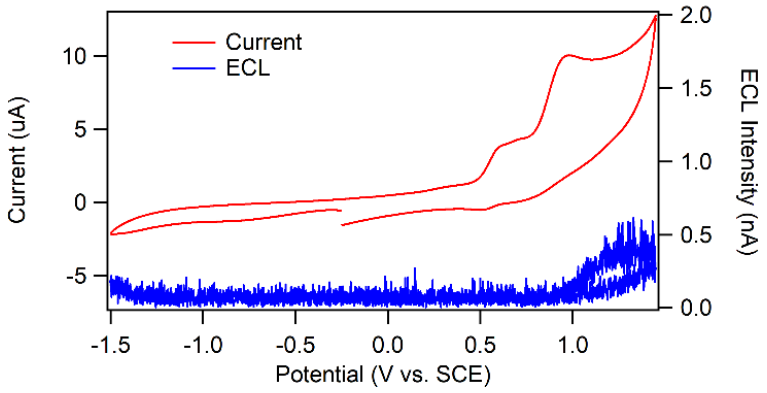

Figure 5.29. ECL voltage curve of 1.3 µM Pt_1Ag_{28}-SbF_6 in the annihilation pathway.

Studies of other metallic nanoclusters have also shown similar results under the annihilation pathway. For instance, the Au_{25} and Au_{38} nanoclusters reported by the Ding group revealed comparably weak emissions under the annihilation pathway.[75, 76] Other studies of bimetallic nanoparticles such as Au-Ag report ECL only in the presence of a coreactant.[77, 78] To the best of our knowledge, this is the first time the ECL has been reported for Pt-Ag nanoclusters of this type.

Next, the oxidative-reduction coreactant tri-*n*-propylamine (TPrA) was added to enhance the ECL. **Figure 5.30** shows the spooling ECL spectra of 0.32 µM Pt_1Ag_{30}-SbF_6 with 1 mM TPrA, where the electrode potential was scanned anodically at a rate of 0.1 V/s, and the spectrograph/CCD set recorded the ECL emission every 0.5 s. The resulting spectra have an ECL onset potential of +0.55 V at a peak wavelength of 742 nm (indicated with A). At this potential both Pt_1Ag_{30}-SbF_6 and TPrA undergo an oxidation reaction to form Pt_1Ag_{30}-SbF_6^{1+} and $TPrA^{\bullet+}$, respectively, with the highly reducing $TPrA^{\bullet}$ formed following the deprotonation of $TPrA^{\bullet+}$. **Figure 5.31** confirms that TPrA oxidation onset potential is as early as +0.30 V. The subsequent electron transfer from $TPrA^{\bullet}$ to the LUMO orbital of Pt_1Ag_{30}-SbF_6^{1+} produces the primary excited state Pt_1Ag_{30}-SbF_6^{0*}, which releases an ECL photon upon relaxation to the ground state. **Figure 5.32A** depicts this ECL pathway involving the primary interaction between Pt_1Ag_{30}-SbF_6^{1+} and $TPrA^{\bullet}$. A second ECL mechanism can be considered at this applied potential wherein the ground state generated after relaxation from excited-state Pt_1Ag_{30}-SbF_6^{0*} is immediately re-oxidized to form Pt_1Ag_{30}-SbF_6^{1+} that reacts with $TPrA^{\bullet}$ to produce Pt_1Ag_{30}-SbF_6^{0*} again, leading to a catalytic cycle (**Figure 5.32B**). This positive feedback loop similar to that in scanning electrochemical microscopy is made possible due to the proximity of these species in the vicinity of the electrode, which acts to promptly regenerate the necessary species for ECL reoccurrence. This mechanism may be an important factor in the high ECL efficiency of these nanoclusters. It is also noteworthy that the alternative TPrA mechanism proposed for the $Ru(bpy)_3^{2+}$/TPrA coreactant system by the Bard group in 2002 (where the intermediate $TPrA^{+\bullet}$ can act as an oxidizing agent to produce Pt_1Ag_{30}-SbF_6^{1+} before it is electrochemically oxidized) does not appear to play a dominant role in the generation of ECL of these Pt-Ag nanoclusters, since the ECL onset only occurs after electrochemical oxidation of both nanocluster and coreactant.[79]

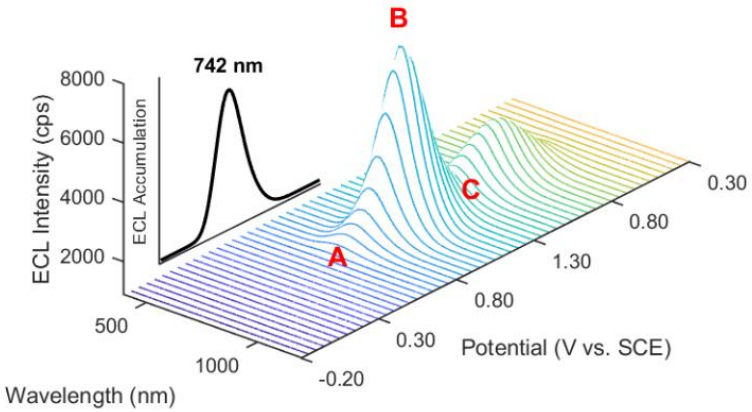

Figure 5.30. Spooling ECL spectra of 0.32 µM Pt_1Ag_{30}-SbF_6 with 1 mM TPrA during a potentiodynamic scan between −0.20 V and 1.30 V vs. SCE. Scan rate used was 0.1 V/s, and each spectrum was acquired at a 0.5 s time interval. Inset plot is an ECL accumulation spectrum of the same system collected over 30s.

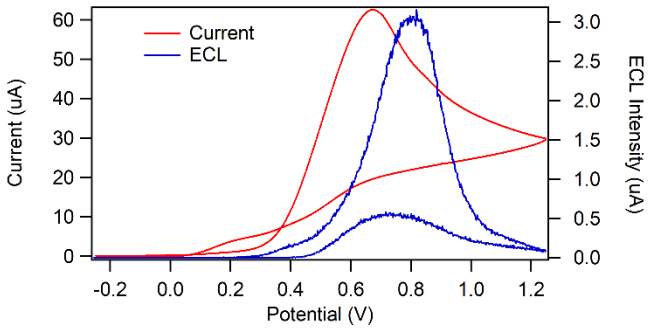

Figure 5.31. ECL-voltage curve of 1.5 µM Pt_1Ag_{30}-SbF_6 in dichloromethane with 1 mM TPrA.

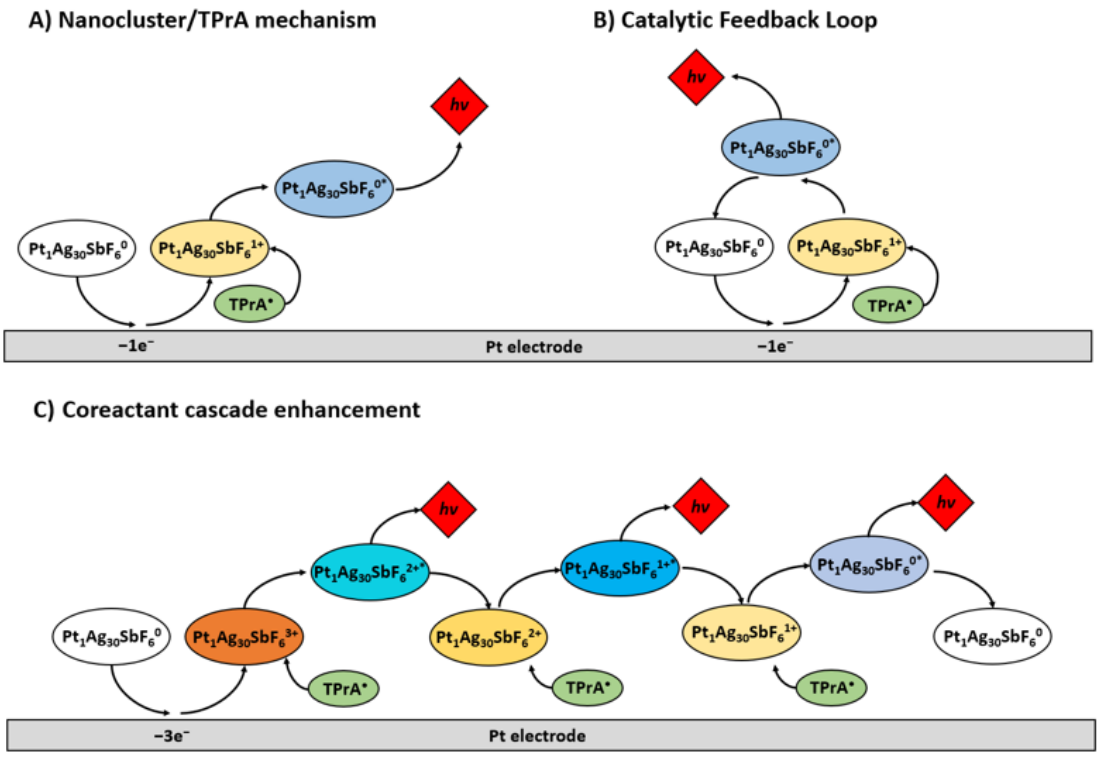

Figure 5.32. (A) Primary ECL mechanism for $Pt_1Ag_{30}SbF_6$ in the presence of TPrA. ECL enhancement mechanisms involving (B) the recycling of Pt_1Ag_{30}-SbF_6^{0} from Pt_1Ag_{30}-SbF_6^{1+} in a positive feedback loop catalyzed at the electrode surface, and (C) ECL cascade enhancement driven by an excess of TPrA•.

The ECL signal described in **Figure 5.30** increases in intensity to a maximum of 6.8 kcps at +1.10 V (indicated with **B** in **Figure 5.30**), at which Pt_1Ag_{30}-SbF_6^{2+} and Pt_1Ag_{30}-SbF_6^{3+} have both been formed (oxidized at formal potentials of 0.79 V and 1.10 V, respectively, as seen in the DPVs of **Figure 5.27A**). Electron transfers from TPrA• into the LUMO of these species form the excited states Pt_1Ag_{30}-SbF_6^{1*} and Pt_1Ag_{30}-SbF_6^{2*}, each of which is capable of producing ECL emission after relaxation to the ground state. The increased concentration of available excited species of the higher oxidation states of Pt_1Ag_{30}-SbF_6 is likely the reason for the enhanced ECL signal in this region. The presence of these excited states with higher oxidation number means higher ECL intensity. In addition, each oxidation state can react with TPrA• to yield an excited state one oxidation number lower, emitting light. The combination of the above two processes

leads to a cascade generation of ECL, as illustrated in **Figure 5.32C**. For example, the reduction of Pt_1Ag_{30}-SbF_6^{3+} by $TPrA^{\bullet}$ produces the excited state Pt_1Ag_{30}-SbF_6^{2+*}, which relaxes to Pt_1Ag_{30}-SbF_6^{2+} along with emission of an ECL photon. Pt_1Ag_{30}-SbF_6^{2+} can be further reduced by $TPrA^{\bullet}$ to generate Pt_1Ag_{30}-SbF_6^{1+*}. These ECL enhancement mechanisms are, as proposed, highly dependent on the excess of TPrA radicals (relative to the concentration of nanocluster), and their effects on the ECL intensity may be more clearly elucidated at the micromolar concentrations we have employed in this study. As the applied potential is further increased to +1.30 V (as indicated with **C** in **Figure 5.30**), we observe a decrease in the peak intensity of ECL. This suggests that the influence of the ECL mechanisms described in **Figure 5.32B** and **Figure 5.32C** may be less pronounced, possibly due to the limited diffusive ability of these nanoclusters. In addition, a second ECL intensity maximum can be seen on the reverse scan, although its intensity is lessened due to the depletion of the local concentration of reactive ECL species. Notably, the peak wavelength does not shift even as the applied potential is varied; the inset of **Figure 5.30** shows the ECL accumulation spectrum, which has a single representative peak wavelength of 742 nm. **Figure 5.33** shows the stacked spooling ECL spectra for Pt_1Ag_{30}-SbF_6 which displays clearly a single ECL emission during the potential scan.

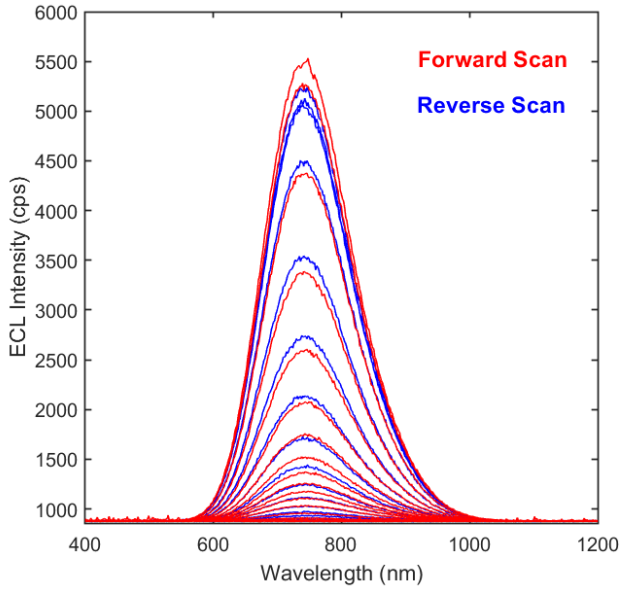

Figure 5.33. Stacked spooling ECL spectra of Pt_1Ag_{30}-SbF_6 with 1 mM TPrA. 0.5 sec per spectrum, scan rate = 0.1 V/sec.

To verify the observation that multiple excited states have the same ECL peak wavelength, we used spooling photoluminescence (PL) spectroscopy, where a potentiodynamic scan was performed for a solution of 0.32 µM Pt_1Ag_{30}-SbF_6 while PL spectra were acquired under photoexcitation at 532 nm (**Figure 5.34A**). Four PL spectra have been extracted at potentials corresponding to the formal potentials of the four oxidation states of Pt_1Ag_{30}-SbF_6: (**Figure 5.34B**) 0 at 0.00 V, (**Figure 5.34C**) 1+ at 0.53 V, (**Figure 5.34D**) 2+ at 0.79 V, and (**Figure 5.34E**) 3+ at 1.10 V. All four spectra display a peak wavelength of 742 nm, which coincides well with the accumulated ECL spectrum. This confirms that the excited states of Pt_1Ag_{30}-SbF_6 with different oxidation numbers possess the same peak wavelength at 742 nm. ECL emission from these excited states is therefore centered around 744 nm as well. This production of a multitude of ECL excited states which all emit at the same wavelength is probably why the large enhancement in the ECL appears at one peak wavelength.

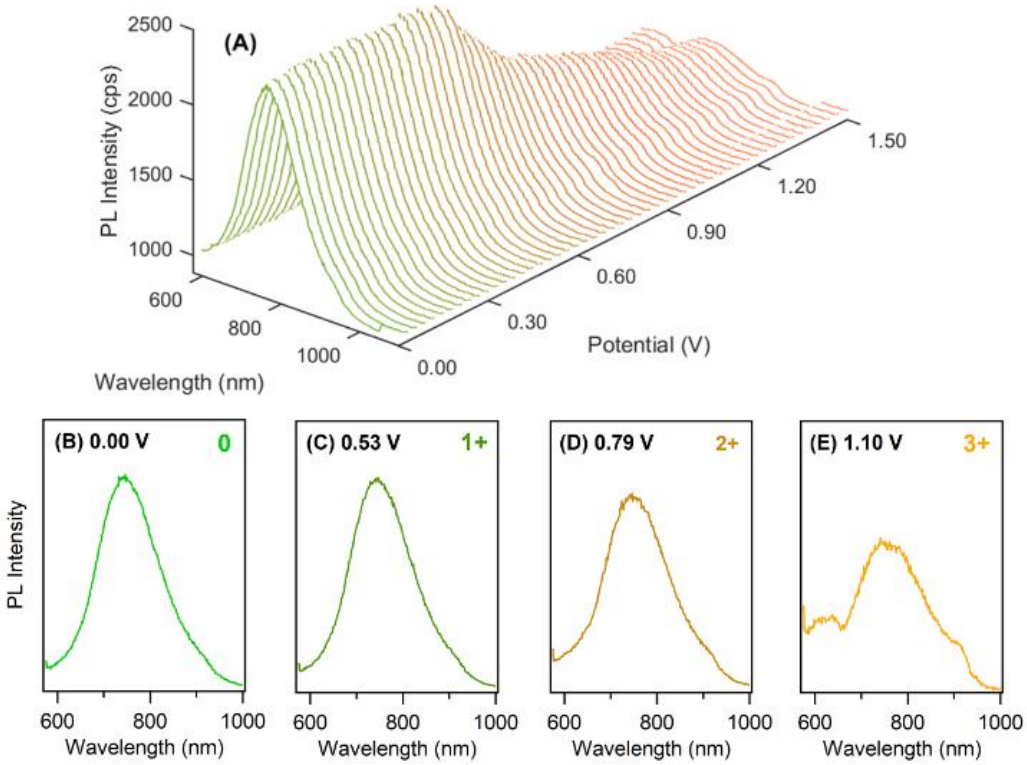

Figure 5.34. (A) Spooling photoluminescence spectra of 0.32 µM Pt_1Ag_{30}-SbF_6 collected at (B) 0.00 V, (C) 0.53 V, (D) 0.79 V, and (E) 1.10 V, obtained by excitation at 532 nm with a solid-state laser.

The Pt_1Ag_{28}-SbF_6 nanocluster behaved similarly (**Figure 5.35**). **Figure 5.36** shows the spooling ECL spectra of 0.28 µM Pt_1Ag_{28}-SbF_6 with 1 mM TPrA as the coreactant. The ECL onset potential is at +0.90 V (indicated with A); at this potential Pt_1Ag_{28}-SbF_6 has been fully oxidized to its tetracationic form. From here, an electron is transferred from $TPrA^{\bullet}$ to a LUMO of Pt_1Ag_{28}-SbF_6^{4+} producing Pt_1Ag_{28}-SbF_6^{3+*}, which releases an ECL photon upon relaxation to its ground state (**Figure 5.37A**). This ECL signal increases to a maximum of 4.5 kcps at +1.55 V (indicated with B), followed by a small decline in the peak intensity as the applied potential reaches its maximum of +1.75 V (indicated with C). The previously discussed mechanisms of feedback loops (**Figure 5.37B**) and cascade generation of excited states (**Figure 5.37C**) likely also play an important role in the generation of ECL here, with a great enhancement. Because the ECL onset potential occurs after electro-generation of Pt_1Ag_{28}-SbF_6^{1+}, Pt_1Ag_{28}-SbF_6^{2+}, and Pt_1Ag_{28}-SbF_6^{3+}, it

is unclear if these species contribute to the ECL. Again, only one ECL peak wavelength at 755 nm was observed. To confirm the unique apparent peak wavelength from all the excited states, we performed spooling PL spectroscopy to analyze and identify each of these states in question (**Figure 5.38A**), where a potentiodynamic scan was performed in the anodic region for a solution of 0.28 µM Pt_1Ag_{28}-SbF_6 while PL spectra were acquired under photoexcitation at 532 nm. It is evident that Pt_1Ag_{28}-SbF_6^0 (**Figure 5.38B**) and the electrogenerated Pt_1Ag_{28}-SbF_6^{1+}/Pt_1Ag_{28}-SbF_6^{2+} (**Figure 5.38C**), Pt_1Ag_{28}-SbF_6^{3+} (**Figure 5.38D**), Pt_1Ag_{28}-SbF_6^{4+} (**Figure 5.38E**) have the same emission peak wavelength of 755 nm. Therefore, all the excited states Pt_1Ag_{28}-SbF_6^*, Pt_1Ag_{28}-SbF_6^{1+*}/Pt_1Ag_{28}-SbF_6^{2+*}, Pt_1Ag_{28}-SbF_6^{3+*}, Pt_1Ag_{28}-SbF_6^{4+*} have the same emission peak wavelength.

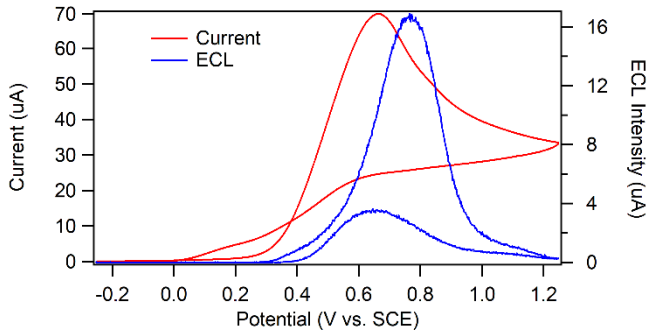

Figure 5.35. ECL voltage curve of 1.5 µM Pt_1Ag_{28}-SbF_6 in dichloromethane with 1 mM TPrA.

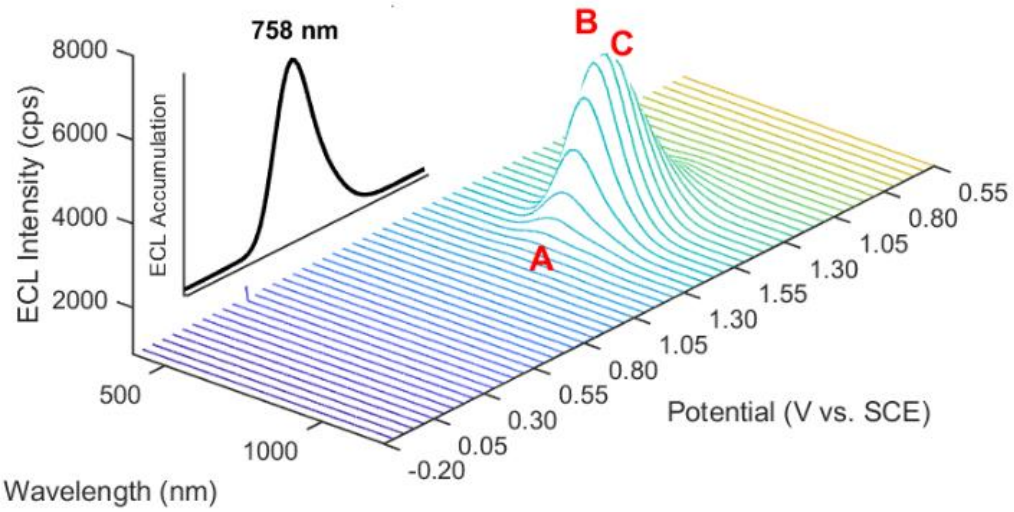

Figure 5.36. Spooling ECL spectra of 0.28 µM Pt_1Ag_{28}-SbF_6 with 1 mM TPrA during a potentiodynamic scan between −0.20 V and 1.55 V vs. SCE. Scan rate used was 0.1 V/s, and each spectrum was acquired at a 0.5 s time interval. Inset plot is an ECL accumulation spectrum of the same system collected in one cycle of potentiodynamic scan between −0.20 V and 1.55 V within 35s.

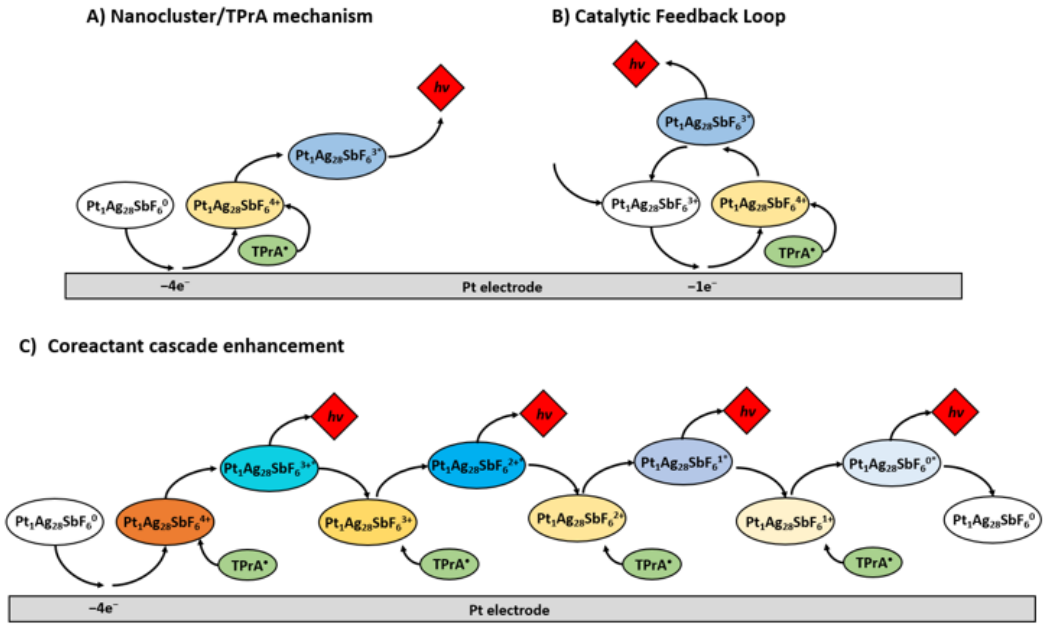

Figure 5.37. ECL mechanisms for Pt_1Ag_{28}-SbF_6 in the presence of TPrA. (a) Primary reaction mechanism. (b) ECL enhancement from catalytic feedback loop. (c) ECL cascade enhancement from an excess of TPrA.

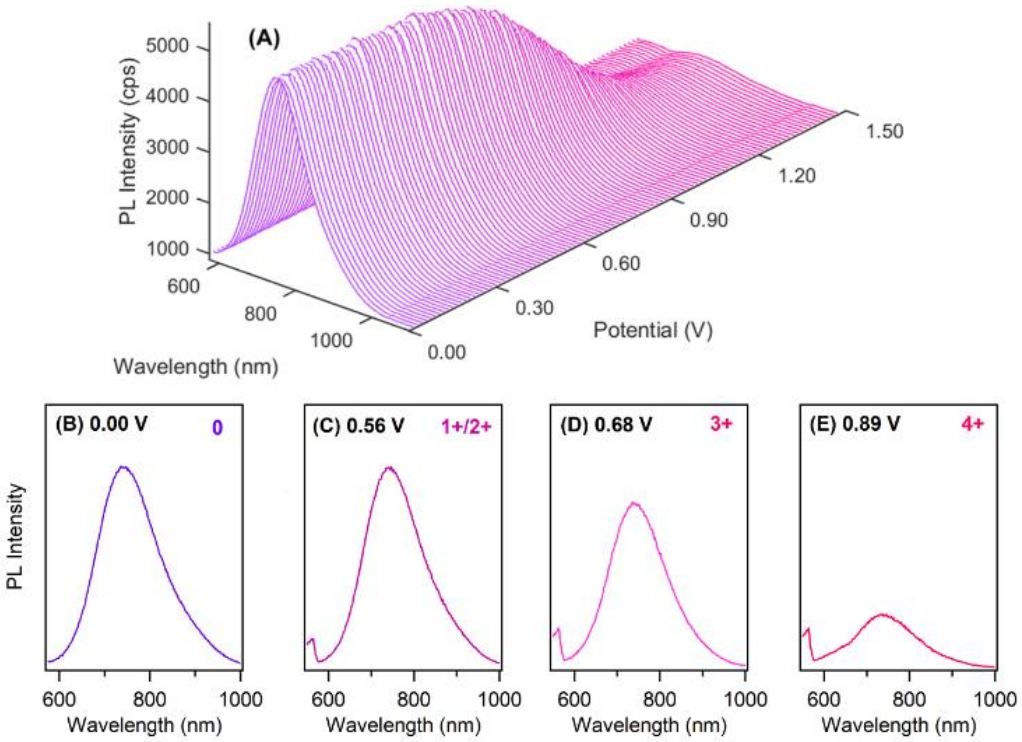

Figure 5.38. (A) Spooling photoluminescence spectra of 0.28 µM Pt_1Ag_{28}-SbF_6 collected at (B) 0.00 V, (C) 0.56 V, (D) 0.68 V, and (E) 0.89 V, obtained by photoexcitation by a 532 nm solid-state laser.

Similar to the other nanoclusters, the ECL peak wavelength does not shift even as the applied potential is increased; the spooling ECL spectra in **Figure 5.36** and their stacked format in **Figure 5.39** as well as the accumulation ECL spectrum during a potentiodynamic scan in the inset of **Figure 5.36** display a unique peak wavelength of 758 nm. Obviously, ECL from various excited states electrogenerated has the same peak maximum wavelength as well. We have also provided the ECL accumulation spectrum and ECL spooling spectra of Pt_1Ag_{28}-Cl (the beginning cluster molecule in this work) in **Figure 5.40** and **Figure 5.41,** respectively. The ECL accumulation spectrum displays a peak wavelength of 757 nm, which is very close to that of Pt_1Ag_{28}-SbF_6, and the spooling ECL spectra similarly shows a single emission peak.

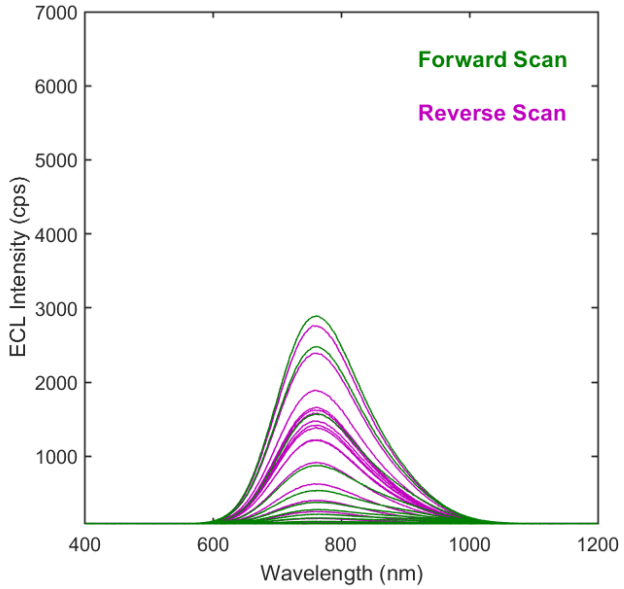

Figure 5.39. Stacked spooling ECL spectra of Pt_1Ag_{30}-SbF_6 with 1 mM TPrA. 0.5 sec per spectrum, scan rate = 0.1 V/sec.

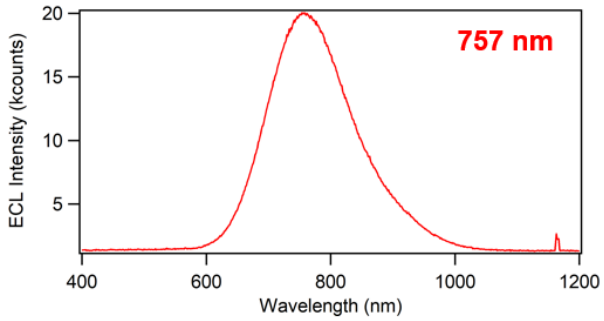

Figure 5.40. Accumulation ECL spectrum of Pt_1Ag_{28}-Cl.

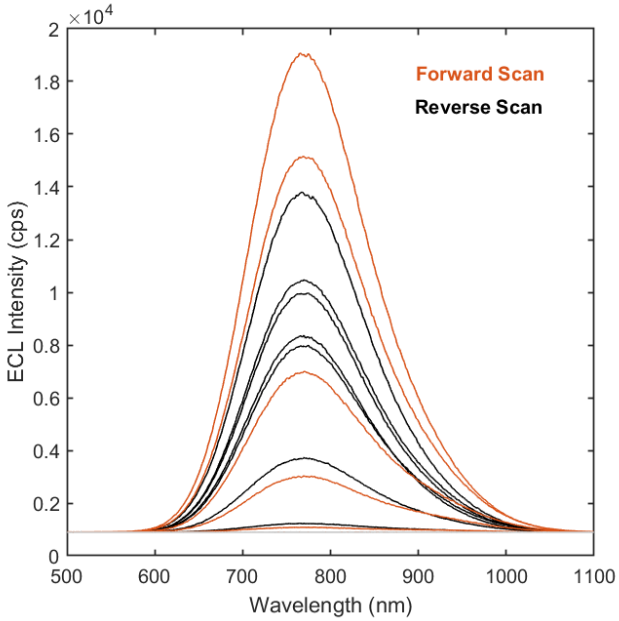

Figure 5.41. Accumulation ECL spectrum of Pt_1Ag_{28}-Cl.

Note that ECL peak wavelengths from Pt_1Ag_{30}-SbF_6 and Pt_1Ag_{28}-SbF_6 excited species are slightly longer than those of their PL. This is because their ECL wavelength ranges are far away from their absorption ones, leading to much less inner filter effect caused by self-absorption as in many conventional luminescent materials. On the other side, Pt_1Ag_{28}-SbF_6 emission peak wavelength is slightly longer than that of Pt_1Ag_{30}-SbF_6, reflecting its lower electrochemical HOMO-LUMO gap.

In addition, the apparent delay in the onset potential may be due to the decreased diffusion rate of Pt_1Ag_{28}-SbF_6, as the electrogenerated radicals may require more time to encounter $TPrA^{\bullet}$ radicals in solution. The overall reactivity of Pt_1Ag_{28}-SbF_6 might also be lower than that of Pt_1Ag_{30}-SbF_6, resulting in fewer generation of ECL excited states. This can be seen in the lower ECL peak intensity observed for Pt_1Ag_{28}-SbF_6 compared to Pt_1Ag_{30}-SbF_6 (4.5 kcps vs. 6.8 kcps, respectively).

To gain an in-depth insight into the structure-ECL correlation, the surface areas of these Pt-Ag nanoclusters were calculated, and their reactive facets were then recognized.[73] The surface areas of the exposed Pt_1Ag_{12} kernels of Pt_1Ag_{28}-SbF_6 and Pt_1Ag_{30}-SbF_6 nanoclusters were obtained using Heron's formula.[80] The total areas were first estimated

by including all the individual facets. As shown in **Figure 5.42**, the total Pt_1Ag_{12} kernel surface areas of Pt_1Ag_{28}-SbF_6 and Pt_1Ag_{30}-SbF_6 nanoclusters were 74.40 and 72.36 $Å^2$, respectively. Accordingly, the total kernel surface areas of these two nanoclusters were almost identical. We have proposed that the reactive facets of kernels played a crucial role in activating the ECL efficiency of these nanoclusters by considering the plausible interactions between these reactive facets and the electrode and $TPrA^{\bullet}$.[73] Here, the Pt_1Ag_{28}-SbF_6 nanocluster, with a symmetric configuration of the more evenly distributed staples around a FCC-configurational Pt_1Ag_{12} kernel, only provided front-access facets (green arrows in **Figure 5.43A**) to undergo electrochemical reactions in the vicinity of the electrode and chemical reaction with a $TPrA^{\bullet}$. In vivid contrast, for the more asymmetric Pt_1Ag_{30}-SbF_6 nanocluster (**Figure 5.43B**), several access points allowed for the above ECL reactions, especially for a more efficient electron exchange between the reactive Pt_1Ag_{12} kernel and $TPrA^{\bullet}$.

$$S = \frac{1}{2}(Au_{xy} + Au_{xz} + Au_{yz})$$

$$A_{facet(i)} = \sqrt{S(S - Au_{xy})(S - Au_{xz})(S - Au_{yz})}$$

$$A_t = \sum_0^i A_{facet(i)}$$

	Pt_1Ag_{28}-SbF_6	Pt_1Ag_{30}-SbF_6
S1	3.332672	3.737032
S2	3.941546	3.575628
S3	3.896728	3.636243
S4	3.456444	3.550128
S5	3.909719	3.637318
S6	3.905002	3.628433
S7	3.342404	3.566241
S8	3.948973	3.55973
S9	3.908308	3.637051
S10	3.491392	3.703824
S11	3.968009	3.637629
S12	3.926408	3.740406
S13	3.490815	3.569319
S14	3.324658	3.724843
S15	3.4843	3.570224
S16	3.314324	3.571767
S17	3.946139	3.628156
S18	3.968669	3.568286
S19	3.895547	3.548725
S20	3.945964	3.566903
Sum	74.39802	72.35789

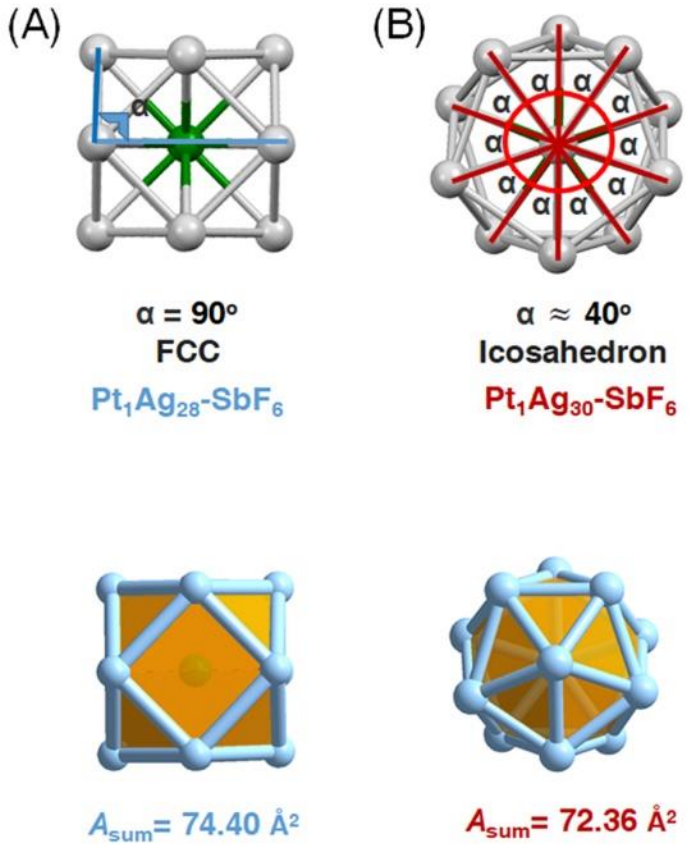

Figure 5.42. Calculations of kernel surface areas of different nanoclusters. (A) The sum of the Pt_1Ag_{12} kernel surface area of $[Pt_1Ag_{28}(S\text{-}Adm)_{18}(PPh_3)_4](SbF_6)_2$ is 74.40 $Å^2$. (B) The sum of the Pt_1Ag_{12} kernel surface area of $[Pt_1Ag_{30}Cl_1(S\text{-}Adm)_{18}(PPh_3)_3](SbF_6)_3$ is 72.36 $Å^2$.

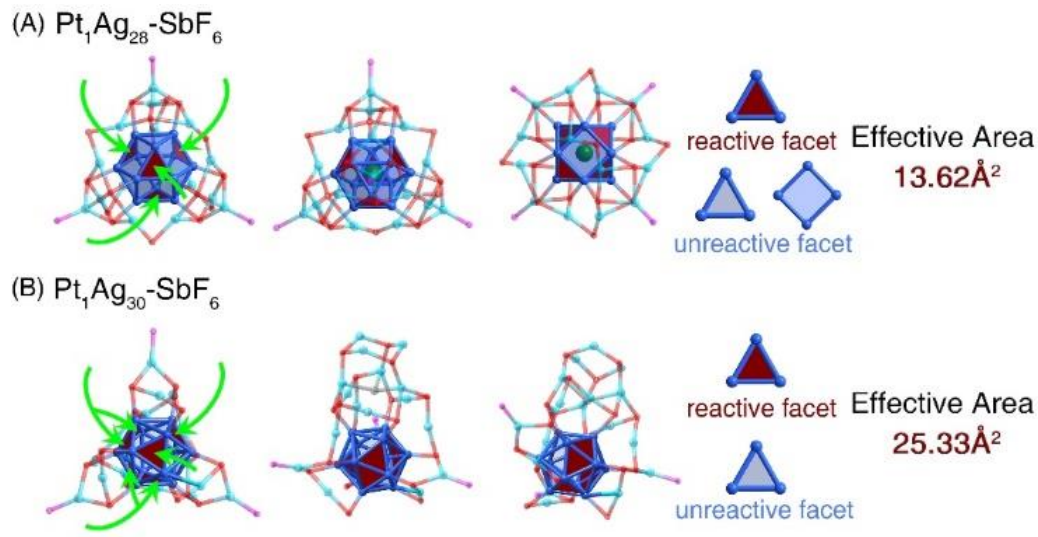

Figure 5.43. Calculation of the effective area of each nanocluster. The effective areas (i.e., the sum of the reactive facets) of (A) Pt_1Ag_{28}-SbF_6 and (B) Pt_1Ag_{30}-SbF_6 nanoclusters are determined as 13.62 and 25.33 $Å^2$, respectively. Color legends: dark green sphere, Pt; dark blue sphere, kernel Ag; blue sphere, surface Ag; red sphere, S; magenta sphere, P; gray sphere, Cl. For clarity, all C and H atoms are omitted. The green arrows point out corridors toward facets, which TPrA radicals reach.

5.3.4 Absolute ECL Quantum Efficiency

Quantitatively, the absolute ECL quantum efficiencies of these Pt-Ag nanoclusters were determined using the ECL accumulation spectra obtained from the spectrograph/CCD camera set. The absolute ECL quantum efficiencies of the two nanoclusters Pt_1Ag_{30}-SbF_6 and Pt_1Ag_{28}-SbF_6 were determined to be 0.24% and 0.11%, respectively, shown in **Table 5.2**. We note here that the increase in absolute ECL efficiency between Pt_1Ag_{30}-SbF_6 and Pt_1Ag_{28}-SbF_6 by a factor of two can be directly explained by a comparison between the total effective areas of the two nanoclusters.

Table 5.2. Absolute and relative ECL quantum efficiencies for Pt-Ag nanoclusters.

	Photons	**Electrons**	**Φ_{ECL}**	**Rel. efficiency vs. $Ru(bpy)_3^{2+}$**	**Effective Area (Å)**
$Ru(bpy)_3^{2+}$ (0.20 μM)	4.28×10^{10}	1.82×10^{15}	0.002%		
Pt_1Ag_{30}-SbF_6 (0.32 μM)	7.29×10^{12}	3.09×10^{15}	0.24%	120	25.33
Pt_1Ag_{28}-SbF_6 (0.28 μM)	4.86×10^{12}	4.61×10^{15}	0.11%	55	13.62

Figure 5.43 shows the crystal structure representations of Pt_1Ag_{30}-SbF_6 and Pt_1Ag_{30}-SbF_6 with the relevant reactive facets highlighted in brown. The assignment of the effective surface area involves a determination of which facets of the nanocluster core remain exposed and therefore accessible to external reactions;[73, 75] these areas were calculated to be 25.33 $Å^2$ (**Figure 5.43B**) and 13.62 $Å^2$ for Pt_1Ag_{30}-SbF_6 and Pt_1Ag_{28}-SbF_6 (**Figure 5.43A**), respectively. This correlation reinforces our assumption that the redox reactions necessary for the generation of ECL excited states in the TPrA coreactant system occur primarily at the core of these nanoclusters, as there is a highly linear relationship between the two parameters (**Table 5.2**). This finding well supports the use of exposed reactive facets of the nanocluster core to explain their general reactivity: this technique can have potential applications in not only PL and ECL studies, but other disciplines that explore reaction dynamics and kinetics (such as electrocatalysis or energy conversion).[81, 82]

We have also determined the ECL efficiencies of Pt_1Ag_{30}-SbF_6 and Pt_1Ag_{28}-SbF_6 to be 120-fold and 55-fold greater than the "gold standard" $Ru(bpy)_3^{2+}$/TPrA system, respectively, under similar experimental conditions (**Table 5.2**). In comparison, the traditional method of determining ECL efficiency by comparing the ratios of ECL intensity versus charge (**Equation 5.5**) against a standard system yielded values of 18.24 and 6.39 for Pt_1Ag_{30}-SbF_6 and Pt_1Ag_{28}-SbF_6, respectively, when ECL peak height was used, and 3.74 and 1.69 when ECL peak areas were used (**Table 5.3**). These relative efficiencies are significantly underestimated in this example, and truly highlight the advantages of an absolute measurement of the ECL process. Using this method, we are able to accurately quantify the number of photons that are produced from the ECL process, which takes into account the energy of each photon (the use of an optical

spectrometer as described in this work greatly streamlines this process). Combined with a measurement of the total Coulombic charge, the absolute quantum efficiency of this nanocluster/TPrA ECL system can be accurately represented. Such a determination allows meaningful comparisons to be performed between virtually any luminescent system: for example, **Table 5.4** shows an assessment of some common lighting sources.

$$\Phi_{ECL} = \frac{\left(\frac{\int ECL \times dt}{\int Current \times dt}\right)_x}{\left(\frac{\int ECL \times dt}{\int Current \times dt}\right)_{ref}}$$

Equation 5.5

Table 5.3. Relative ECL efficiencies of Pt_1Ag_{30}-SbF_6 and Pt_1Ag_{28}-SbF_6 vs. $Ru(bpy)_3^{2+}$ with 1 mM TPrA as coreactant. Efficiencies were calculated using ECL accumulation spectrum peak heights and integrated peak areas obtained from the spectrograph/CCD setup. Charge was calculated by integrating the current vs. time plot in a cyclic voltammogram experiment. Concentration of $Ru(bpy)_3^{2+}$ = 0.20 µM, Pt_1Ag_{30}-SbF_6 = 0.32 µM, Pt_1Ag_{28}-SbF_6 = 0.28 µM.

	ECL Peak Height (counts)	Integrated ECL area (counts)	Charge (C)	Φ (peak height)	Φ (integrated area)
$Ru(bpy)_3^{2+}$	2204	1.89×10^6	2338.93		
Pt_1Ag_{30}-SbF_6	56499	9.91×10^6	3286.60	18.24	3.74
Pt_1Ag_{28}-SbF_6	19119	4.34×10^6	3174.87	6.39	1.69

Table 5.4. Photon flux for some common light sources. Measured using an Ocean Optics USB2000+ miniature fiber optic (200-micron diameter) spectrometer controlled with SpectraSuite software.

	Photon flux (photons/s)	Irradiance (W/m^2)
Fluorescent bulb	2.37×10^{16}	8.82×10^1

Furthermore, an absolute ECL efficiency measurement avoids any misrepresentation that can result from an inconsistent method. In the example above, results calculated using the

ECL peak height versus the ECL peak area differ by approximately 60%. Both approaches are valid, except that they fail to account for spectral differences in peak wavelength widths. The absolute ECL determination described in this work therefore represents a much more objective strategy to quantify the performance and efficiency of novel luminophores.[83, 84]

When the concentration of the Pt-Ag nanoclusters was increased, we observed an overall improvement in the absolute ECL efficiency (**Table 5.5**). This is likely because the relative ratio between the nanoclusters and TPrA has increased, and therefore the overall reaction rate to produce ECL excited states is enhanced. It should be noted here that this ratio is still unusually low compared to ECL studies of other nanoclusters; even with the very low concentration of luminophore employed in this study, the ECL intensities were among the greatest we have observed. It is possible that these nanoclusters may undergo aggregation at increased concentrations; aggregation-induced emission (AIE), where molecules exhibit enhanced luminescence in more concentrated solutions, can then occur.[85] This phenomenon has been previously reported for gold nanoclusters[86, 87], with the justification that aggregation increases the reactivity between the nanoclusters and coreactant due to their improved proximity. In a similar manner, aggregation of these nanoclusters may also increase the contribution of catalytic feedback loops, and the cascade generation of excited states described earlier, leading to the observed enhancement in the ECL efficiency.

Table 5.5. Absolute ECL quantum efficiencies of Pt-Ag nanoclusters at high concentration. TPrA concentration was 1 mM.

	Photons	**Electrons**	**Absolute ECL Quantum Efficiency (%)**
Pt_1Ag_{30}-SbF_6 (1.5 μM)	1.99×10^{13}	3.33×10^{15}	0.6%
Pt_1Ag_{28}-SbF_6 (1.3 μM)	2.80×10^{13}	2.00×10^{15}	1.4%

Finally, the ECL electron transfer reactions in this system also appear to be highly diffusion controlled: potential stepping experiments in both annihilation and coreactant pathways showed no improvement over potential scanning (**Figure 5.44** and **Figure 5.45**), which indicates that the diffusion rate of these nanoclusters may be quite limited.

This observation can also explain the enhancement of ECL in the coreactant pathway, as the greater diffusion rate of TPrA will result in a large increase in the local concentration of ECL excited states. Such exceptional ECL efficiencies highlight the excellent physicochemical properties of these nanoclusters and will encourage unprecedented applications towards highly efficient light-emitting devices, or enable the detection of single molecules.

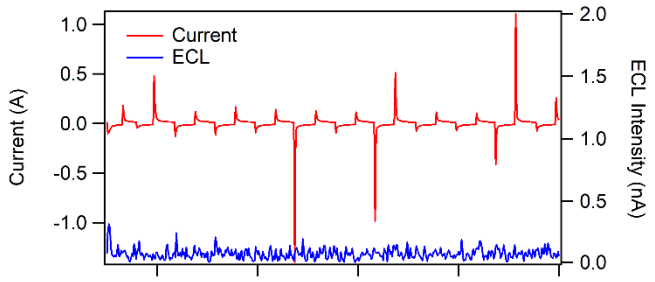

Figure 5.44. Potential stepping of Pt_1Ag_{30}-SbF_6 (10 Hz) in the annihilation pathway.

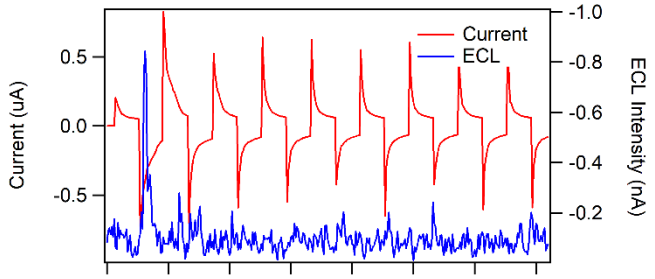

Figure 5.45. Potential stepping of Pt_1Ag_{28}-SbF_6 (10 Hz) in the annihilation pathway.

5.4 Conclusions

In summary, the SbF_6^- counterion effects have been evaluated and controlled in reconstructing metal nanoclusters and regulating their photochemical activities. Through controlling the amount of introduced SbF_6^- counterions, the stepwise evolution from Pt_1Ag_{28}-Cl to Pt_1Ag_{28}-SbF_6 and then to Pt_1Ag_{30}-SbF_6 has been mapped out. The presence of SbF_6^- not only can reconstruct the nanocluster structure, which belongs to the molecular chemistry, but also is capable of rearranging cluster molecules in the supracrystal lattice, which touches upon the supramolecular chemistry. Owing to their distinct molecular structures and crystalline packing modes, these nanoclusters

manifested distinguishable optical absorption and emission properties in solution and crystal states. Significantly, a boosted emission intensity has been accomplished with the nanocluster transformation, giving rise to an ultrabright Pt_1Ag_{30}-SbF_6 nanocluster with a PL QY as high as 78%. Furthermore, Pt_1Ag_{30}-SbF_6 displayed superior ECL quantum efficiency to that of Pt_1Ag_{28}-SbF_6, which was further supported by the increased effectively exposed reactive facets amenable to undergoing electron transfer reactions of the former nanocluster. In particular, the ultrabright Pt_1Ag_{30}-SbF_6 exhibited an unprecedented absolute ECL quantum efficiency 120-fold greater than that $Ru(bpy)_3^{2+}$ while the bright Pt_1Ag_{28}-SbF_6 demonstrate one 55-time larger than that of $Ru(bpy)_3^{2+}$, highlighting their exceptional electrogenerated emission capabilities at sub-micromolar concentrations. Overall, this work is of great significance for revealing the SbF_6^- counterion effects on nanoclusters at the atomic level from both structures and photochemical/photoelectrochemical property aspects.

5.5 Supporting Information

Table 5.6. Crystal data and structure refinement for the $[Pt_1Ag_{28}(S\text{-}Adm)_{18}(PPh_3)_4](SbF_6)_2$ nanocluster.

Name	Value
Crystal system	monoclinic
Space group	P 21/c
a/Å	32.608
b/Å	25.628
c/Å	36.988
α/°	90
β/°	96.42
γ/°	90
Volume/Å^3	30715.6
Z	4
ρ_{calc}g/cm^3	1.712
μ/mm^{-1}	17.910
F(000)	15501
Crystal size/mm^3	0.1 × 0.1 × 0.1
Radiation	CuKα (λ = 1.54186)
Index ranges	$-38 \leq h \leq 39$, $-30 \leq k \leq 30$, $-42 \leq l \leq 17$
Final R indexes [I>=2σ (I)]	$R_1 = 0.0975$, $wR_2 = 0.2671$
Final R indexes [all data]	$R_1 = 0.1207$, $wR_2 = 0.2964$

Table 5.7. Crystal data and structure refinement for the $[Pt_1Ag_{30}Cl_1(S\text{-}Adm)_{18}(PPh_3)_3](SbF_6)_3$ nanocluster.

Name	Value
Crystal system	triclinic
Space group	P -1
a/Å	22.6826(8)
b/Å	22.7851(8)
c/Å	30.8635(10)
α/°	89.078(3)
β/°	85.545(3)
γ/°	68.604(3)
Volume/Å^3	14805.6(9)
Z	2
ρ_{calc}g/cm^3	1.734
μ/mm^{-1}	19.573
F(000)	7522
Crystal size/mm^3	0.1 × 0.1 × 0.1
Radiation	CuKα (λ = 1.54186)
Index ranges	$-27 \leq h \leq 17$, $-27 \leq k \leq 17$, $-34 \leq l \leq 37$
Final R indexes [I>=2σ (I)]	$R_1 = 0.0924$, $wR_2 = 0.2499$
Final R indexes [all data]	$R_1 = 0.1010$, $wR_2 = 0.2589$

5.6 References

[1] Jin, R. C.; Zeng, C. J.; Zhou, M.; Chen, Y. X. *Chem. Rev.* **2016,** *116*, 10346-10413.

[2] Chakraborty, I.; Pradeep, T. *Chem. Rev.* **2017,** *117*, 8208-8271.

[3] Bhattarai, B.; Zaker, Y.; Atnagulov, A.; Yoon, B.; Landman, U.; Bigioni, T. P. *Acc. Chem. Res.* **2018,** *51*, 3104-3113.

[4] Takano, S.; Hasegawa, S.; Suyama, M.; Tsukuda, T. *Acc. Chem. Res.* **2018,** *51*, 3074-3083.

[5] Lei, Z.; Wan, X. K.; Yuan, S. F.; Guan, Z. J.; Wang, Q. M. *Acc. Chem. Res.* **2018,** *51*, 2465-2474.

[6] Lu, Y. Z.; Chen, W. *Chem. Soc. Rev.* **2012,** *41*, 3594-3623.

[7] Ghosh, A.; Mohammed, O. F.; Bake, O. M. *Acc. Chem. Res.* **2018,** *51*, 3094-3103.

[8] Gan, Z. B.; Xia, N.; Woo, Z. K. *Acc. Chem. Res.* **2018,** *51*, 2774-2783.

[9] Cook, A. W.; Hayton, T. W. *Acc. Chem. Res.* **2018,** *51*, 2456-2464.

[10] Sakthivel, N. A.; Dass, A. *Acc. Chem. Res.* **2018,** *51*, 1774-1783.

[11] Liu, P. X.; Qin, R. X.; Fu, G.; Zheng, N. F. *J. Am. Chem. Soc.* **2017,** *139*, 2122-2131.

[12] Yan, J. Z.; Teo, B. K.; Zheng, N. F. *Acc. Chem. Res.* **2018,** *51*, 3084-3093.

[13] Konishi, K.; Iwasaki, M.; Shichibu, Y. *Acc. Chem. Res.* **2018,** *51*, 3125-3133.

[14] Kurashige, W.; Niihori, Y.; Sharma, S.; Negishi, Y. *Coord. Chem. Rev.* **2016,** *320*, 238-250.

[15] Kang, X.; Zhu, M. Z. *Chem. Soc. Rev.* **2019,** *48*, 2422-2457.

[16] Kwak, K.; Lee, D. *Acc. Chem. Res.* **2019,** *52*, 12-22.

[17] Agrachev, M.; Ruzzi, M.; Venzo, A.; Maran, F. *Acc. Chem. Res.* **2019,** *52*, 44-52.

[18] Higaki, T.; Li, Y. W.; Zhao, S.; Li, Q.; Li, S. T.; Du, X. S.; Yang, S.; Chai, J. S.; Jin, R. C. *Angew. Chem. Int. Ed.* **2019,** *58*, 8291-8302.

[19] Aikens, C. M. *Acc. Chem. Res.* **2018,** *51*, 3065-3073.

[20] Hossain, S.; Niihori, Y.; Nair, L. V.; Kumar, B.; Kurashige, W.; Negishi, Y. *Acc. Chem. Res.* **2018,** *51*, 3114-3124.

[21] Yao, Q. F.; Wu, Z. N.; Liu, Z. H.; Lin, Y. Z.; Yuan, X.; Xie, J. P. *Chem. Sci.* **2021,** *12*, 99-127.

[22] Wang, Z.; Li, M.-D.; Shi, J.-Y.; Su, H.-F.; Liu, J.-W.; Feng, L.; Gao, Z.-Y.; Xue, Q.-W.; Tung, C.-H.; Sun, D.; Zheng, L.-S. *CCS Chem.* **2021,** *4*, 1788-1795.

[23] Zhang, S.-S.; Liu, R.-C.; Zhang, X.-C.; Feng, L.; Xue, Q.-W.; Gao, Z.-Y.; Tung, C.-H.; Sun, D. *Sci. China Chem.* **2021,** *64*, 2118-2124.

[24] Bootharaju, M. S.; Chang, H.; Deng, G. C.; Malola, S.; Baek, W.; Hakkinen, H.; Zheng, N. F.; Hyeon, T. *J. Am. Chem. Soc.* **2019,** *141*, 8422-8425.

[25] Soldan, G.; Aljuhani, M. A.; Bootharaju, M. S.; AbdulHalim, L. G.; Parida, M. R.; Emwas, A. H.; Mohammed, O. F.; Bakr, O. M. *Angew. Chem. Int. Ed.* **2016,** *55*, 5749-5753.

[26] Chang, W. T.; Lee, P. Y.; Liao, J. H.; Chakrahari, K. K.; Kahlal, S.; Liu, Y. C.; Chiang, M. H.; Saillard, J. Y.; Liu, C. W. *Angew. Chem. Int. Ed.* **2017,** *56*, 10178-10182.

[27] Liu, Y. Y.; Chai, X. Q.; Cai, X.; Chen, M. Y.; Jin, R. C.; Ding, W. P.; Zhu, Y. *Angew. Chem. Int. Ed.* **2018,** *57*, 9775-9779.

[28] Zhu, M.; Wang, P.; Yan, N.; Chai, X. Q.; He, L. Z.; Zhao, Y.; Xia, N.; Yao, C. H.; Li, J.; Deng, H. T.; Zhu, Y.; Pei, Y.; Wu, Z. K. *Angew. Chem. Int. Ed.* **2018,** *57*, 4500-4504.

[29] Li, S.; Du, X. S.; Li, B.; Wang, J. Y.; Li, G. P.; Gao, G. G.; Zang, S. Q. *J. Am. Chem. Soc.* **2018,** *140*, 594-597.

[30] Wan, X. K.; Wang, J. Q.; Nan, Z. A.; Wang, Q. M. *Sci. Adv.* **2017,** *3*.

[31] Hosier, C. A.; Ackerson, C. J. *J. Am. Chem. Soc.* **2019,** *141*, 309-314.

[32] Nguyen, T. A. D.; Jones, Z. R.; Leto, D. F.; Wu, G.; Scott, S. L.; Hayton, T. W. *Chem. Mater.* **2016,** *28*, 8385-8390.

[33] Huang, R. W.; Wei, Y. S.; Dong, X. Y.; Wu, X. H.; Du, C. X.; Zang, S. Q.; Mak, T. C. W. *Nat. Chem.* **2017,** *9*, 689-697.

[34] Lei, Z.; Pei, X. L.; Jiang, Z. G.; Wang, Q. M. *Angew. Chem. Int. Ed.* **2014,** *53*, 12771-12775.

[35] Luo, Z. T.; Yuan, X.; Yu, Y.; Zhang, Q. B.; Leong, D. T.; Lee, J. Y.; Xie, J. P. *J. Am. Chem. Soc.* **2012,** *134*, 16662-16670.

[36] De Nardi, M.; Antonello, S.; Jiang, D. E.; Pan, F. F.; Rissanen, K.; Ruzzi, M.; Venzo, A.; Zoleo, A.; Maran, F. *ACS Nano* **2014,** *8*, 8505-8512.

[37] Alhilaly, M. J.; Huang, R. W.; Naphade, R.; Alamer, B.; Hedhili, M. N.; Emwas, A. H.; Maity, P.; Yin, J.; Shkurenko, A.; Mohammed, O. F.; Eddaoudi, M.; Bakr, O. M. *J. Am. Chem. Soc.* **2019,** *141*, 9585-9592.

[38] Kang, X.; Zhu, M. Z. *Coord. Chem. Rev.* **2019,** *394*, 1-38.

[39] Zhao, Y.; Zhuang, S. L.; Liao, L. W.; Wang, C. M.; Xia, N.; Gan, Z. B.; Gu, W. M.; Li, J.; Deng, H. T.; Wu, Z. K. *J. Am. Chem. Soc.* **2020,** *142*, 973-977.

[40] Man, R. W. Y.; Yi, H.; Malola, S.; Takano, S.; Tsukuda, T.; Hakkinen, H.; Nambo, M.; Crudden, C. M. *J. Am. Chem. Soc.* **2022,** *144*, 2056-2061.

[41] Zhang, S. S.; Alkan, F.; Su, H. F.; Aikens, C. M.; Tung, C. H.; Sun, D. *J. Am. Chem. Soc.* **2019,** *141*, 4460-4467.

[42] Tian, F.; Chen, R. *J. Am. Chem. Soc.* **2019,** *141*, 7107-7114.

[43] Qu, M.; Li, H.; Xie, L. H.; Yan, S. T.; Li, J. R.; Wang, J. H.; Wei, C. Y.; Wu, Y. W.; Zhang, X. M. *J. Am. Chem. Soc.* **2017,** *139*, 12346-12349.

[44] Takano, S.; Ito, S.; Tsukuda, T. *J. Am. Chem. Soc.* **2019,** *141*, 15994-16002.

[45] Yao, Q. F.; Yu, Y.; Yuan, X.; Yu, Y.; Zhao, D.; Xie, J. P.; Lee, J. Y. *Angew. Chem. Int. Ed.* **2015,** *54*, 184-189.

[46] Chakraborty, P.; Baksi, A.; Mudedla, S. K.; Nag, A.; Paramasivam, G.; Subramanian, V.; Pradeep, T. *Phys. Chem. Chem. Phys.* **2018,** *20*, 7593-7603.

[47] Kang, X.; Wei, X.; Jin, S.; Wang, S. X.; Zhu, M. Z. *Inorg. Chem.* **2021,** *60*, 4198-4206.

[48] Chen, S.; Du, W. J.; Qin, C. W. L.; Liu, D. Y.; Tang, L.; Liu, Y.; Wang, S. X.; Zhu, M. Z. *Angew. Chem. Int. Ed.* **2020,** *59*, 7542-7547.

[49] Luong, L. M. C.; Malwitz, M. A.; Moshayedi, V.; Olmstead, M. M.; Balch, A. L. *J. Am. Chem. Soc.* **2020,** *142*, 5689-5701.

[50] Luong, L. M. C.; Lowe, C. D.; Adams, A. V.; Moshayedi, V.; Olmstead, M. M.; Balch, A. L. *Chem. Sci.* **2020,** *11*, 11705-11713.

[51] Nepomnyashchii, A. B.; Bröring, M.; Ahrens, J.; Bard, A. J. *J. Am. Chem. Soc.* **2011,** *133*, 8633-8645.

[52] Hesari, M.; Ding, Z. *Nat. Protoc.* **2021,** *16*, 2109-2130.

[53] Kang, X.; Zhou, M.; Wang, S. X.; Jin, S.; Sun, G. D.; Zhu, M. Z.; Jin, R. C. *Chem. Sci.* **2017,** *8*, 2581-2587.

[54] Kang, X.; Jin, S.; Xiong, L.; Wei, X.; Zhou, M. M.; Qin, C. W. L.; Pei, Y.; Wang, S. X.; Zhu, M. Z. *Chem. Sci.* **2020,** *11*, 1691-1697.

[55] Kang, X.; Wei, X.; Jin, S.; Yuan, Q. Q.; Luan, X. Q.; Pei, Y.; Wang, S. X.; Zhu, M. Z.; Jin, R. C. *PNAS* **2019,** *116*, 18834-18840.

[56] Kang, X.; Wei, X.; Wang, S. X.; Zhu, M. Z. *Inorg. Chem.* **2020,** *59*, 8736-8743.

[57] Kang, X.; Huang, L.; Liu, W.; Xiong, L.; Pei, Y.; Sun, Z. H.; Wang, S. X.; Wei, S. Q.; Zhu, M. Z. *Chem. Sci.* **2019,** *10*, 8685-8693.

[58] Kang, X.; Xu, F. Q.; Wei, X.; Wang, S. X.; Zhu, M. Z. *Sci. Adv.* **2019,** *5*.

[59] Walter, M.; Akola, J.; Lopez-Acevedo, O.; Jadzinsky, P. D.; Calero, G.; Ackerson, C. J.; Whetten, R. L.; Gronbeck, H.; Hakkinen, H. *PNAS* **2008,** *105*, 9157-9162.

[60] Yan, L.-L.; Yao, L.-Y.; Ng, M.; Yam, V. W.-W. *J. Am. Chem. Soc.* **2021,** *143*, 19008-19017.

[61] Wang, Z.; Zhu, Y.-J.; Li, Y.-Z.; Zhuang, G.-L.; Song, K.-P.; Gao, Z.-Y.; Dou, J.-M.; Kurmoo, M.; Tung, C.-H.; Sun, D. *Nat. Comm.* **2022,** *13*, 1802.

[62] Wang, Z.; Liu, J.-W.; Su, H.-F.; Zhao, Q.-Q.; Kurmoo, M.; Wang, X.-P.; Tung, C.-H.; Sun, D.; Zheng, L.-S. *J. Am. Chem. Soc.* **2019,** *141*, 17884-17890.

[63] Wang, Z.; Su, H.-F.; Tung, C.-H.; Sun, D.; Zheng, L.-S. *Nat. Comm.* **2018,** *9*, 4407.

[64] Zhen, Y. R.; Jin, S.; Kang, X.; Xu, C.; Fang, C.; Hu, D. Q.; Zhu, M. Z. *Inorg. Chem. Front.*

[65] Song, Y. B.; Li, Y. W.; Zhou, M.; Liu, X.; Li, H.; Wang, H.; Shen, Y. H.; Zhu, M. Z.; Jin, R. C. *Sci. Adv.* **2021,** *7*.

[66] Takano, S.; Hirai, H.; Nakashima, T.; Iwasa, T.; Taketsugu, T.; Tsukuda, T. *J. Am. Chem. Soc.* **2021,** *143*, 10560-10564.

[67] Li, J.; Wang, P.; Pei, Y. *J. Phys. Chem. Lett.* **2022,** *13*, 3718-3725.

[68] AbdulHalim, L. G.; Bootharaju, M. S.; Tang, Q.; Del Gobbo, S.; AbdulHalim, R. G.; Eddaoudi, M.; Jiang, D. E.; Bakr, O. M. *J. Am. Chem. Soc.* **2015,** *137*, 11970-11975.

[69] Döllefeld, H.; Weller, H.; Eychmüller, A. *J. Phys. Chem. B* **2002,** *106*, 5604-5608.

[70] Zhang, J.; Rowland, C.; Liu, Y. Z.; Xiong, H.; Kwon, S.; Sheychenko, E.; Schaller, R. D.; Prakapenka, V. B.; Tkachev, S.; Rajh, T. *J. Am. Chem. Soc.* **2015,** *137*, 742-749.

[71] Wei, X.; Kang, X.; Zuo, Z. W.; Song, F. Q.; Wang, S. X.; Zhu, M. Z. *Nat. Sci. Rev.* **2021,** *8*.

[72] Kang, X.; Li, Y.; Zhu, M.; Jin, R. *Chem. Soc. Rev.* **2020,** *49*, 6443-6514.

[73] Hesari, M.; Ding, Z. *J. Am. Chem. Soc.* **2021,** *143*, 19474-19485.

[74] He, L.; Yuan, J.; Xia, N.; Liao, L.; Liu, X.; Gan, Z.; Wang, C.; Yang, J.; Wu, Z. *J. Am. Chem. Soc.* **2018,** *140*, 3487-3490.

[75] Hesari, M.; Workentin, M. S.; Ding, Z. *ACS Nano* **2014,** *8*, 8543-8553.

[76] Hesari, M.; Workentin, M. S.; Ding, Z. *Chem. Sci.* **2014,** *5*, 3814.

[77] Zhai, Q.; Xing, H.; Zhang, X.; Li, J.; Wang, E. *Anal. Chem.* **2017,** *89*, 7788-7794.

[78] Guo, Y.; Tian, L.; Wu, J.; Wu, Y.; Liu, Y.; Du, J.; Lu, X. *Electroanalysis* **2021,** *33*, 2016-2024.

[79] Miao, W.; Choi, J.-P.; Bard, A. J. *J. Am. Chem. Soc.* **2002,** *124*, 14478-14485.

[80] Kahan, W. *Miscalculating Area and Angles of a Needle-like Triangle*; University of California, Berkeley: September 4, 1986. [Lecture Notes]

[81] Li, Y.; Li, S.; Nagarajan, A. V.; Liu, Z.; Nevins, S.; Song, Y.; Mpourmpakis, G.; Jin, R. *J. Am. Chem. Soc.* **2021,** *143*, 11102-11108.

[82] Li, G.; Jin, R. *Acc. Chem. Res.* **2013,** *46*, 1749-1758.

[83] Adsetts, J. R.; Chu, K.; Hesari, M.; Ma, J.; Ding, Z. *Anal. Chem.* **2021,** *93*, 11626-11633.

[84] Chu, K.; Adsetts, J. R.; Ma, J.; Zhang, C.; Hesari, M.; Yang, L.; Ding, Z. *J. Phys. Chem. C* **2021,** *125*, 22274-22282.

[85] Hong, Y.; Lam, J. W. Y.; Tang, B. Z. *Chem. Soc. Rev.* **2011,** *40*, 5361-5388.

[86] Peng, H.; Huang, Z.; Deng, H.; Wu, W.; Huang, K.; Li, Z.; Chen, W.; Liu, J. *Angew. Chem. Int. Ed.* **2020,** *59*, 9982-9985.

[87] Kim, J. M.; Jeong, S.; Song, J. K.; Kim, J. *Chem. Commun.* **2018,** *54*, 2838-2841.

Chapter 6

6 Elucidation of an Aggregate Excited State in the Electrochemiluminescence and Chemiluminescence of a Thermally Activated Delayed Fluorescence (TADF) Emitter†

The electrochemistry, electrochemiluminescence (ECL), and chemiluminescence (CL) properties of a thermally activated delayed fluorescence (TADF) emitter 4,4'-(1,2-dihydroacenaphthylene-5,6-diyl)bis(*N*,*N*-diphenylaniline) (TPA-ace-TRZ) and three of its analogues were investigated. TPA-ace-TRZ exhibits both a) delayed onset of ECL and, b) long-persistent luminescence, which we have attributed to the formation of an aggregate excited state in excimer or exciplex form. The evidence of this aggregate excited state was consistent across ECL annihilation and coreactant pathways as well as in CL. The absolute ECL efficiency of TPA-ace-TRZ using benzoyl peroxide (BPO) as coreactant was found to be 0.028%, which was 9-fold stronger than the $[Ru(bpy)_3]^{2+}$/BPO reference coereactant system. Furthermore, the absolute CL quantum efficiency of TPA-ace-TRZ was determined to be 0.92%. The performance and flexibility of the TADF emitter TPA-ace-TRZ under these various emissive pathways is highly desirable towards applications in sensing, imaging, and light-emitting devices.

6.1 Introduction

Electrochemiluminescence (ECL) involves the electro-generation of radical species that subsequently undergo electron-transfer reactions to form excited states, which release photons upon relaxation.[1, 2] ECL has many analytical applications including biological immunoassays,[3-5] analyte detection,[6, 7] single molecule detection,[5, 8-10] and various imaging application,[11, 12] along with various luminophors.[2, 13-20] Since ECL does not require an incident light source, detection can be achieved with excellent signal-to-noise

† This work has been published. Chu, K.[§]; Adsetts, J. [§]; Whitworth, Z.; Kumar, S.; Zysman-Colman, E.; Ding, Z. *Langmuir* (**2023**) 39, 2829-2837. [§] indicates equally contributed first author.

ratio and sensitivity.[18] There are two general pathways by which ECL can occur. The first is the annihilation pathway, where radical species generated by oxidation and reduction at an electrode interact to produce excited states. The second is the coreactant route, which introduces a secondary compound known as a coreactant, such as benzoyl peroxide (BPO). Upon reduction, BPO can form a benzoate radical through electrochemical and chemical reactions, which has significant oxidizing power, and is capable of oxidizing the luminophore radical anion to produce excited states. Due to the high redox power of coreactants, ECL in coreactant pathways often have greatly enhanced emission.[18]

Chemiluminescence (CL), on the other hand, is another type of luminescence where the excitation energy instead comes from chemical reactions.[21-24] In many ways, it is a more generalized version of ECL, and so CL-based detection techniques enjoy many of the same analytical benefits. One of the most studied CL reactions is the oxidation of an aryl oxalate ester with hydrogen peroxide; this reaction produces high-energy intermediates which are capable of chemically exciting luminophores[25-27]; radiative relaxation back to ground state releases the energy in the form of light. Excited-state species may also lose their energy by other mechanisms such as vibrational relaxation and collisions with other molecules; such non-radiative processes lead to decreased CL emission efficiency.[28, 29]

Numerous classes of ECL and CL luminophores have since been studied, including organic molecules[30, 31], phosphorescent metallic complexes[32, 33], nanomaterials,[15, 19, 20, 34, 35] and their emulsion droplets[36] like PL of luminophore aggregate at liquid/liquid interfaces.[37] Thermally activated delayed fluorescent (TADF) emitters are a new class of luminophores in ECL able to utilize thermally activated up-conversion of triplet to singlet states, thus enabling theoretical internal quantum efficiencies of up to 100%.[38] TADF relies on a small singlet-triplet energy gap, ΔE_{ST}. More recently, several reports have documented organic long-persistent luminescent compounds whose luminescence decays in the order of seconds.[39, 40] The long-lived luminescence in this class of emitters originates from charge separation, followed by a slow charge recombination route, often in a framework of electron-donating and electron-accepting molecules to facilitate the formation of charge separated states.[41] This phenomenon has been reported for photoluminescent materials (OLPL)[42], but also recently by us for

electrochemiluminescence (OLECL).[16, 43] In particular, there is evidence that the compounds that exhibit organic long-persistent luminescence often possess aggregate excited states.[44]

Recently, the synthesis and photophysical properties of a series of through-space charge-transfer thermally activated delayed fluorescence compounds 4,4'-(1,2-dihydroacenaphthylene-5,6-diyl)bis(*N*,*N*-diphenylaniline) (TPA-ace-TRZ) (**Figure 6.1A**), 4-(1,2-dihydroacenaphthylen-5-yl)-N,N-diphenylaniline (TPA-ace) (**Figure 6.1B**), 6-(4-(diphenylamino)phenyl)-1,2-dihydroacenaphthylene-5-carbonitrile (TPA-ace-CN) (**Figure 6.1C**), and 4,4'-(1,2-dihydroacenaphthylene-5,6-diyl)bis(N,N-diphenylaniline) (2TPA-ace) (**Figure 6.1D**) were first investigated by us.[45] Due to the intriguing electronic properties of TPA-ace-TRZ, we further explore in this study the electrochemistry, electrochemiluminescence, and chemiluminescence of TPA-ace-TRZ, **Figure 6.1A**. Using ECL-voltage curves and time-resolved ECL spectroscopy, we provide unique insights into the formation and emission characteristics into aggregate excited states. As well, the ECL and CL absolute quantum yields were determined for TPA-ace-TRZ, providing valuable electrochemical and spectroscopic insights.

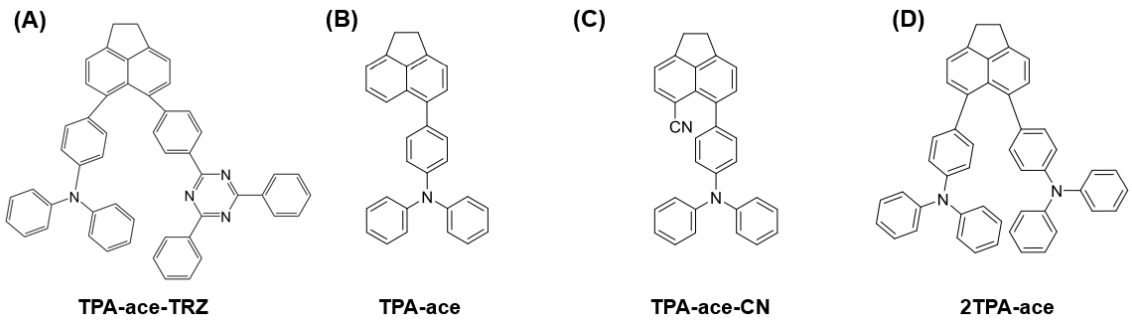

Figure 6.1. Structures of (A) TPA-ace-TRZ (B) TPA-ace, (C) TPA-ace-CN, and (D) 2TPA-ace.

6.2 Experimental

6.2.1 Materials and reagents

Tetrabutylammonium hexafluorophosphate ($TBAPF_6$, for electrochemical analysis, ≥99.0%), benzoyl peroxide (BPO, reagent grade, >98%) and ferrocene (>98%) were

purchased from Sigma-Aldrich Canada and used as received. SureSeal dichloromethane (DCM, ≥99.8%) was purchased from Sigma-Aldrich Canada and stored in a N_2-filled glovebox. The synthesis of the above compounds are reported elsewhere.[45]

6.2.2 Electrochemistry and electrochemiluminescence

A three-electrode system was used for all electrochemical measurements, where the working electrode was a 2 mm platinum disc inlaid in a glass tube, and the counter and quasi-reference electrodes were platinum wires. All potentials were reported relative to the Fc/Fc^+ redox couple where the formal potential was taken to be 0.342 V vs. SCE.[46] Electrochemiluminescence experiments were conducted inside a cylindrical glass tube with a flat quartz window at the bottom to allow for the detection of ECL light. The airtight ECL cell was assembled inside a nitrogen atmosphere glovebox (Model Nexus I, Vacuum Atmospheres Company, Hawthorne, CA) to minimize the effect of oxygen and moisture.

The potentiostat used for cyclic voltammetry and differential pulse voltammetry experiments was a CH Instruments Model 610a electrochemical workstation (CH Instruments Inc., Austin, TX). ECL emission was measured using a photomultiplier tube (Model R928, Hamamatsu, Japan) biased at −750 V, where the output signal as photocurrent was converted in a voltage for data acquisition using a picoammeter (Keithley 6487, Cleveland, OH). The electrochemical current and the ECL signal were recorded using a data acquisition board (DAQ Model 6036E, National Instruments, Austin, TX) and acquired using a custom LabVIEW program. For potential stepping experiments, a PAR263 potentiostat was utilized (Princeton Applied Research, Berwyn, PA), which also recorded the ECL signal by means of an external auxiliary input. ECL spectra were recorded using a spectrograph (Model SP2300i, Princeton Instruments, Trenton, NJ) with an attached CCD camera (Andor DU401-BR-DD-352, Oxford Instruments, UK) cooled to −65 °C. Wavelength calibration was accomplished using a mercury source (HG-1, Ocean Optics, Dunedin, FL) using a center wavelength of 546 nm. Accumulation ECL spectra were acquired by collecting all emission generated over the entire cyclic voltammogram program. Spooling ECL spectra were acquired each at a time interval of 1 s during a cyclic voltammogram; the obtained spectra were combined

in a three-dimensional plot using a custom MATLAB program. For all measurements, the spectrum recording was synchronized by means of a 5 V TTL pulse output from the potentiostat at the beginning of the potential scanning.

$$\Phi_{ECL} = \frac{Total\ photons}{Total\ electrons} \times 100$$

Equation 6.1

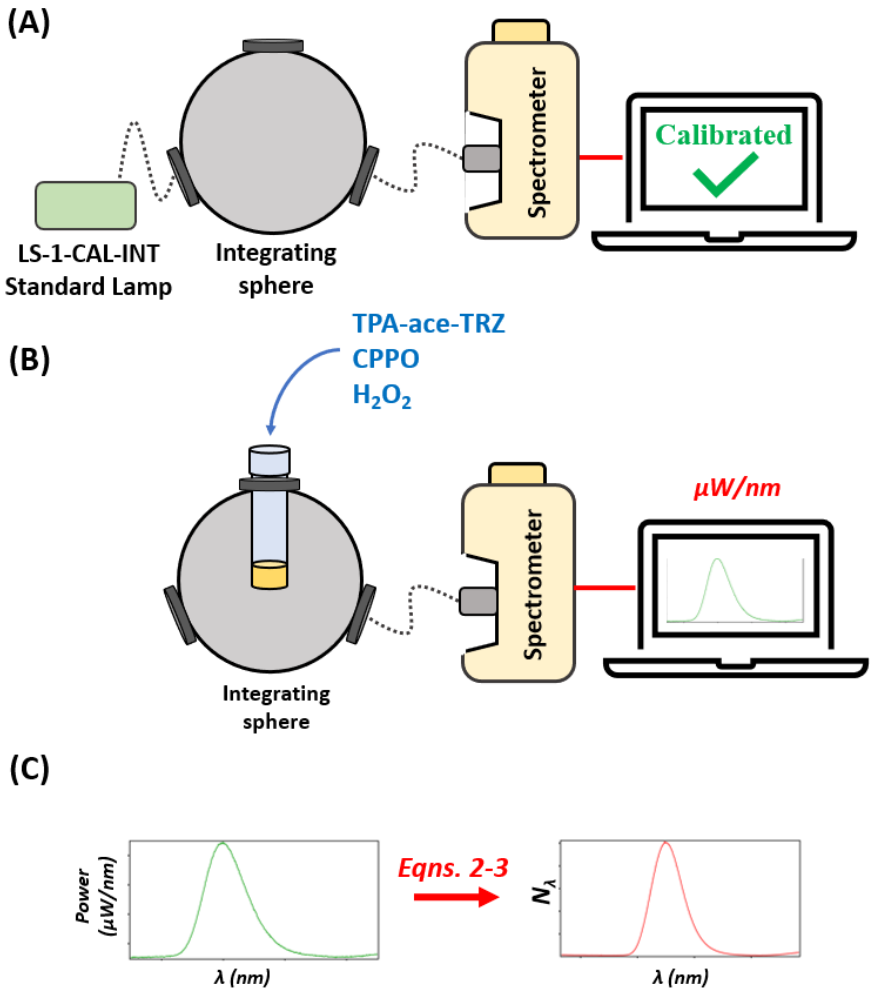

Figure 6.2. (A) Illustrative calibration procedure of the spectrometer and integrating sphere detection system. The LS-1-CAL-INT standard lamp was radiometrically calibrated by Ocean Insight Inc. to provide a known quantity of light. The lamp is automatically tracked by the OceanView software to provide the absolute irradiance power spectrum (power in unit of μ*W/nm* vs. wavelength in nm). (B) Measuring the

absolute chemiluminescence (CL) quantum efficiency. The CL reagents are added to the reaction vial, and the resulting emission is collected in absolute photon numbers by the calibrated spectrometer system. (C) Transformation from absolute power (μW/nm) to absolute number of photons (1/nm) at each individual wavelength, using Equations 2-3. The number of total photons can then be obtained by summing up the photons at each wavelength in the visible range between 400 and 700 nm. Dotted lines in the figure correspond to connections via an optical fiber.

6.2.3 Determination of the absolute ECL quantum efficiency

The spectrograph/CCD camera setup described above was standardized against a calibrated photodiode (S120VC, Thorlabs Optics, Newton, NJ) and power meter (PM100D, Thorlabs). Following this calibration procedure, the reading from the CCD camera, in *counts*, may be converted to an absolute quantity, in *photons*. In-depth experimental procedures and calibration formulas are described in detail elsewhere.[47, 48] Determination of the total number of electrons injected during an experiment was performed by integrating the electrochemical current (as measured by the electrochemical workstation) to obtain the total charge; transformation to number of electrons proceeds using the *elementary charge constant*. The absolute ECL quantum efficiency (Φ_{ECL}) is then determined using **Equation 6.1**.

6.2.4 Chemiluminescence

Chemiluminescence experiments were performed by adding the following reagents into the reaction vial: 10 mL ethyl acetate (reagent grade, >99.5%, Sigma Aldrich Canada) as the solvent, 50 mg bis(2,4,5-trichloro-6-(pentyloxycarbonyl)phenyl)oxalate (CPPO, >98%), 100 mg sodium acetate, and 3 mL of 30% hydrogen peroxide (H_2O_2). This recipe was adapted from a paper[49] with some modifications in consideration of the reagent solubility. The luminophore (TPA-ace-TRZ) was added at a concentration of 0.3 mg/mL. Spooling CL spectra were collected using a 6-inch integrating sphere (Labsphere Inc., North Sutton, NH). An optical fiber connected the integrating sphere to an optical spectrograph and sensor (USB2000+, Ocean Insights, Orlando, FL) which was controlled by OceanView software (Ocean Insight). Calibration of the Ocean Insight spectrometer

was performed using a radiometric standard lamp (Model LS-1-CAL-INT, Ocean Insights), as in **Figure 6.2A**. Determination of the chemiluminescence absolute efficiency (Φ_{CL}) was performed by converting an absolute irradiance power spectrum (W_λ in μW/nm vs. wavelength in nm) from the Ocean Insight spectrometer to an absolute photon spectrum (N_λ in photons/nm vs. wavelength in nm) using **Equation 6.2** and **Equation 6.3**, **Figure 6.2B**.

$$E_{photon,\lambda} = \frac{hc}{\lambda}$$

Equation 6.2

$$N_\lambda = \frac{W_\lambda}{E_{photon,\lambda}} \times t$$

Equation 6.3

where $E_{photon,\lambda}$ is energy of a photon at a specific wavelength, *h* Plank constant, *c* light speed, λ wavelength, *t* the accumulation time for acquiring the spectrum. Following **Equation 6.4** by summing up all the photons at each wavelength in the range between 400 and 700 nm, the absolute CL efficiency (Φ_{CL}) can be determined,

$$\Phi_{CL} = \frac{\sum_{\lambda=400}^{700} N_\lambda}{n_{CPPO} \times NA} \times 100\%$$

Equation 6.4

where n_{CPPO} is the number of CPPO molecules (the limiting reagent) in the reaction, and *NA* is Avogadro's constant (equal to 6.02×10^{23}).

6.3 Results and Discussion

6.3.1 Electrochemiluminescence via the annihilation pathway

The electrochemical and spectroscopic properties of the four complexes (TPA-ace-TRZ, TPA-ace, CN-TPA-ace, and 2TPA-ace) were studied. However, due to the very small singlet-triplet energy gap (ΔE_{ST}) of TPA-ace-TRZ (0.06 eV), we decided to investigate

this compound in more detail, as the small ΔE_{ST} could lead to enhanced electrochemiluminescence efficiencies through effective harvesting of triplet excitons.[50-52]

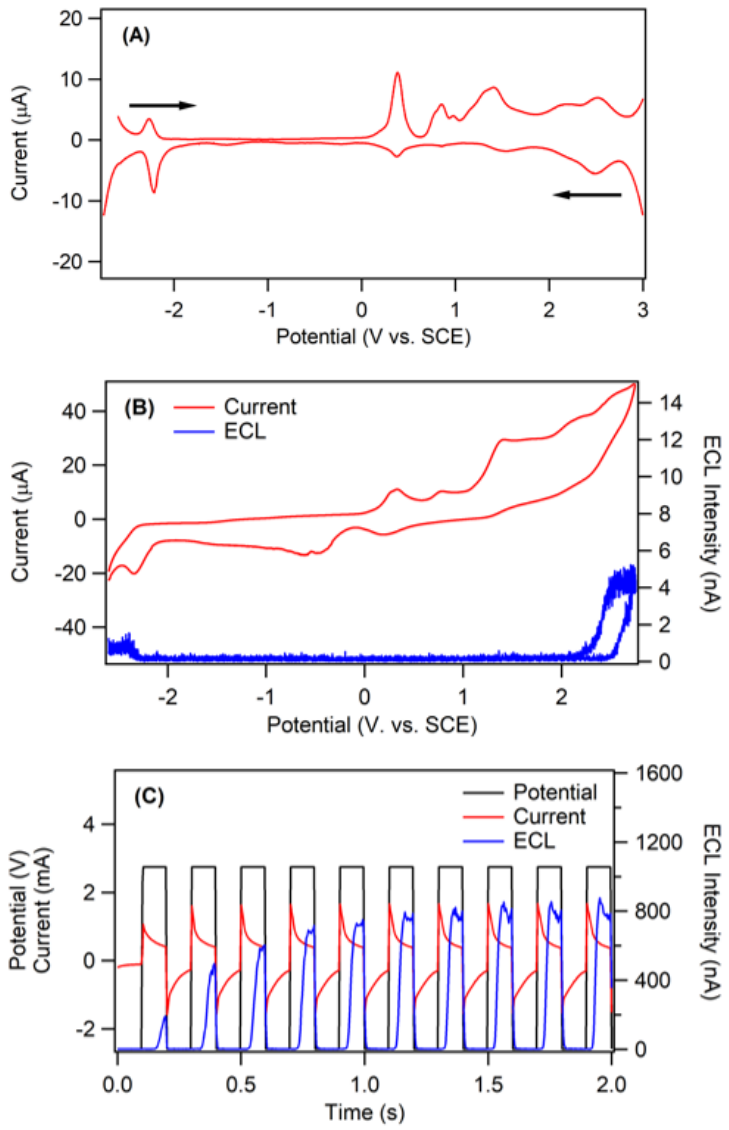

Figure 6.3. (A) Differential pulse voltammogram of 1.42 mM TPA-ace-TRZ in dichloromethane. Initial scan direction is indicated with arrows. (B) CV (red) and corresponding ECL voltage curve (blue) of 1.42 mM TPA-ace-TRZ in dichloromethane with 0.1 M $TBAPF_6$ as supporting electrolyte. Scan rate was 0.1 V/s. (C) Potential-time (black), current-time (red), and ECL-time (blue) profiles of TPA-ace-TRZ during potential stepping experiments at a pulsing frequency of 10 Hz.

The electrochemistry and the ECL behaviour of TPA-ace-TRZ in the annihilation pathway were first investigated. **Figure 6.3A** displays the differential pulse voltammograms (DPVs) of TPA-ace-TRZ in dichloromethane, while **Figure 6.3B** shows the cyclic voltammogram (red) and corresponding ECL voltage curve (blue). TPA-ace-TRZ undergoes multiple irreversible oxidation reactions and one quasi-reversible reduction reaction at −2.20 V as seen in the DPVs. One notable oxidation occurs at +0.50 V. However, ECL was only observed when the potential reached the oxidation peak at +2.30 V and the reduction peak at −2.20 V vs. SCE. This suggests that the generation of the radical anion, and at least a radical multi-cation of TPA-ace-TRZ is required for ECL. The intensity of ECL detected in the annihilation pathway was limited, with a maximum of 5 nA observed in the anodic scan. This is likely due to the low stability of the electrogenerated radical species; this issue is especially apparent in linear voltage sweep experiments, as there is a relatively long time gap between the generations of radical ion partners. It can also be seen that the ECL is more intense in the anodic region, which suggests that TPA-ace-TRZ$^{\bullet-}$ possesses greater stability compared to TPA-ace-TRZ$^{\bullet+}$, which agrees well with the reversibility of redox reactions.

The problem of large time delay between generations of radical anions and cations can be partially circumvented with potential stepping experiments, where the potential can be rapidly switched between anodic and cathodic voltages. **Figure 6.3C** shows the ECL-time curve for TPA-ace-TRZ in the annihilation pathway (ECL plotted in blue), where the potential was alternated between +2.75 V and −2.65 V at a rate of 10 Hz. The ECL intensity was greatly enhanced using this process, and a maximum of 800 nA could be observed during the anodic pulses. This intense ECL enabled us to acquire an accumulation spectrum of TPA-ace-TRZ in the annihilation pathway (**Figure 6.4**), where an emission peak centered at 630 nm was observed. The ECL efficiency of this system relative to $[Ru(bpy)_3]^{2+}$ was determined to be 3.4%. The electrochemistry and annihilation ECL behaviour in the same system was also studied for TPA-ace, TPA-ace-CN, and 2TPA-ace; **Figure 6.5 – Figure 6.16** provide the CV/ECL-voltage curves, DPVs, ECL pulsing profiles, and ECL annihilation accumulation spectra for these three compounds. The emission wavelengths were determined to be 595 nm, 509 nm, and 625 nm, respectively. The summary of the various emission pathways studied for these

compounds is provided in **Table 6.1**. The ECL emission is significantly red-shifted for 2TPA-ace and TPA-ace-TRZ compared to their PL emissions; this observation may be due to the formation of aggregate excited states, which form as a result of a reaction between two chromophores. These *excimers* – dimeric excited states – may be responsible for the red-shifted emission due to their greater degree of conjugation.[53-55]

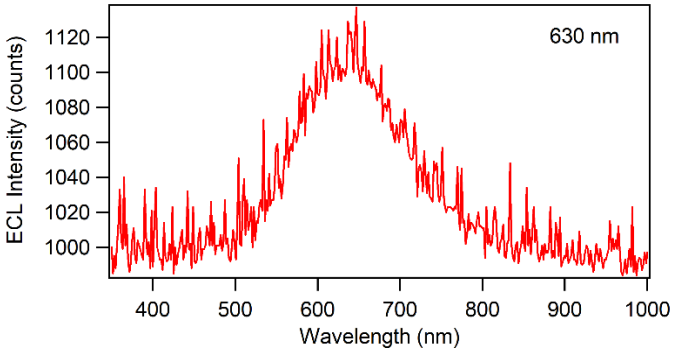

Figure 6.4. Accumulation spectrum of TPA-ace-TRZ ECL in the annihilation pathway.

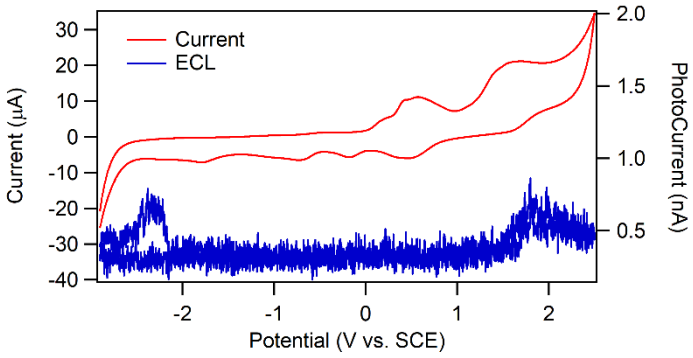

Figure 6.5. CV and ECL voltage curve of TPA-ace in dichloromethane with 0.1 M $TBAPF_6$ as the supporting electrolyte.

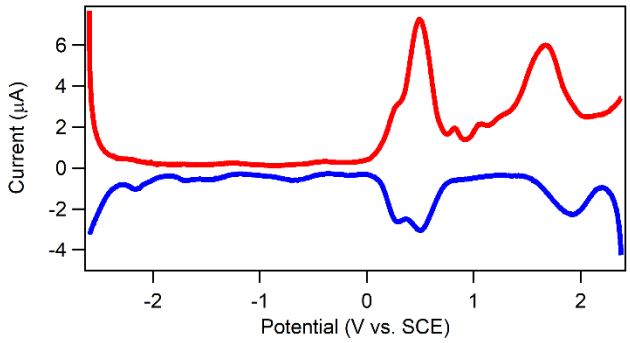

Figure 6.6. Differential pulse voltammograms of TPA-ace.

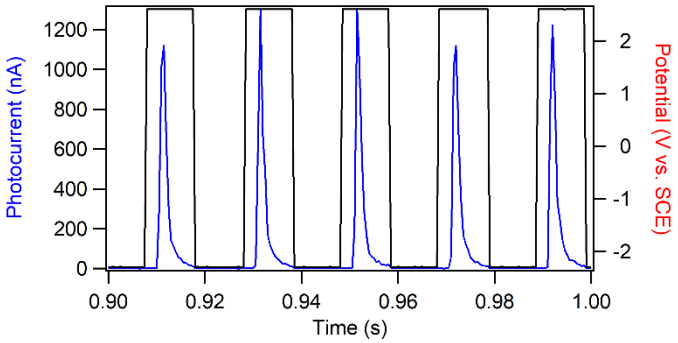

Figure 6.7. ECL-time curves during potential stepping experiments (10 Hz pulse frequency) of TPA-ace ECL in the annihilation pathway.

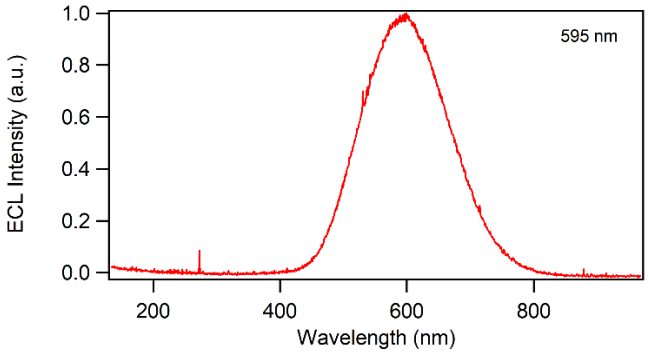

Figure 6.8. Accumulation ECL spectrum of TPA-ace in the annihilation pathway.

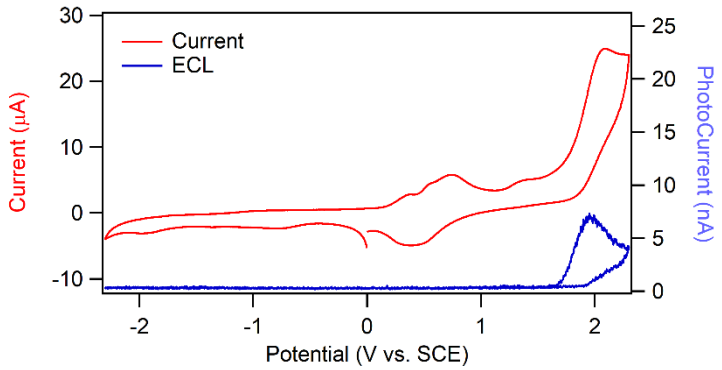

Figure 6.9. CV and ECL voltage curve of TPA-ace-CN in dichloromethane with 0.1 M $TBAPF_6$ as the supporting electrolyte.

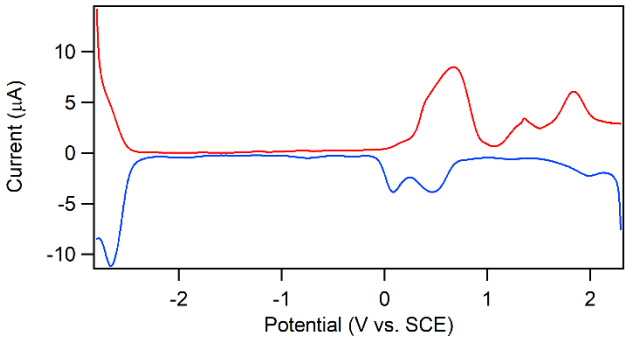

Figure 6.10. Differential pulse voltammograms of TPA-ace-CN.

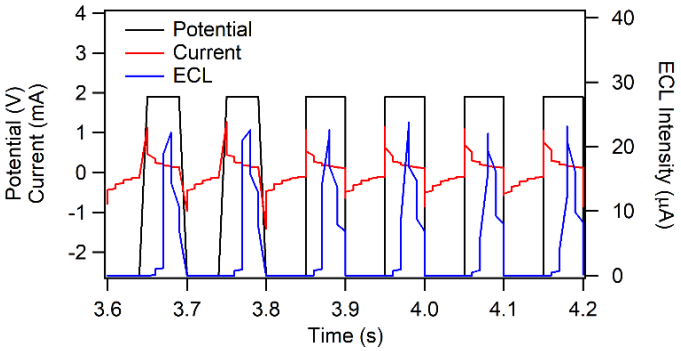

Figure 6.11. ECL-time curves for TPA-ace-CN ECL in the annihilation pathway.

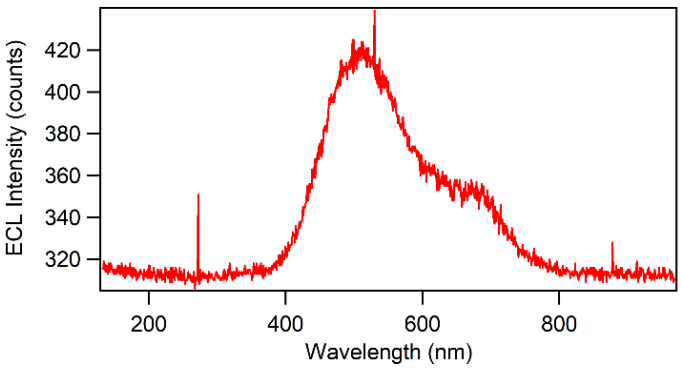

Figure 6.12. ECL accumulation spectrum for TPA-ace-CN in the annihilation pathway.

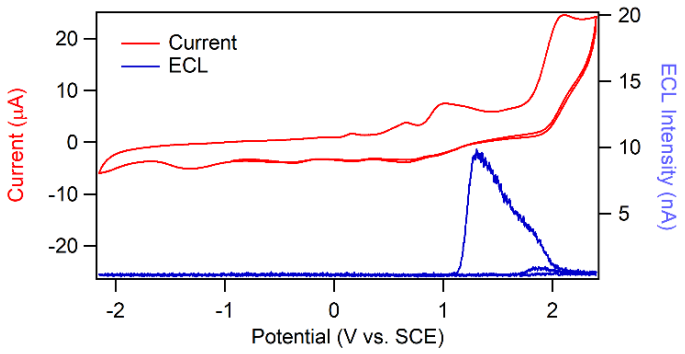

Figure 6.13. CV and corresponding ECL voltage curve of 2TPA-ace with 0.1 M $TBAPF_6$ as supporting electrolyte.

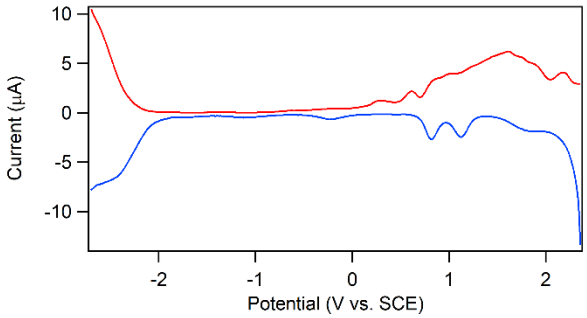

Figure 6.14. Differential pulse voltammograms of 2TPA-ace.

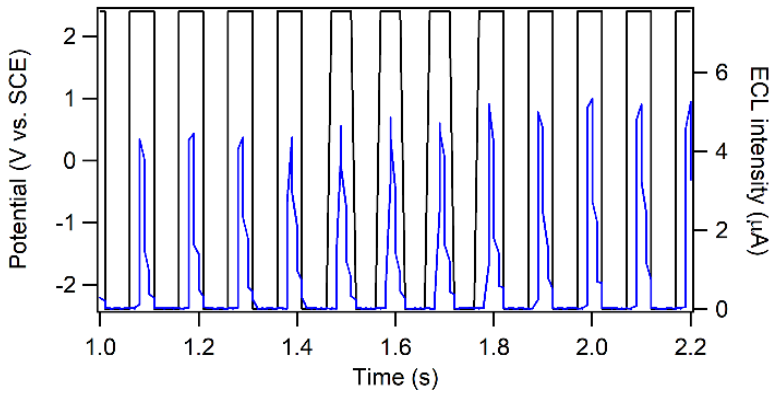

Figure 6.15. ECL-time curves during potential stepping experiment (10 Hz) for 2TPA-ace in the annihilation pathway.

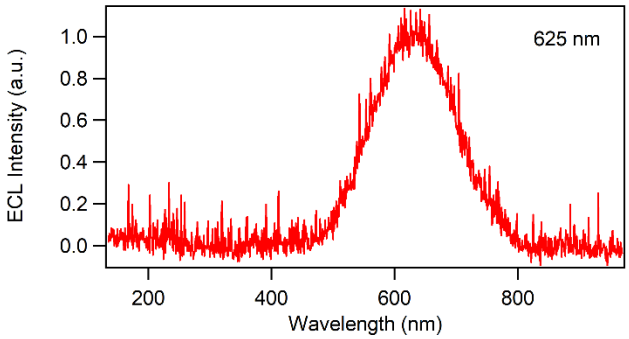

Figure 6.16. Accumulation ECL spectrum for 2TPA-ace in the annihilation pathway during potential pulsing experiments.

We also observed a noticeable delay in the onset of the ECL signal during potential stepping experiments; this can be seen as the ECL begins to increase approximately 25 milliseconds after each anodic step. The delay in the onset of ECL is therefore the time required to form the emissive excimer species. **Table 6.2** provides a summary of the ECL onset, ECL maximum, and the ECL decay profiles of TPA-ace-TRZ, TPA-ace, 2TPA-ace, and TPA-ace-CN in the ion-annihilation pathway. In all four compounds studied, there was a delay in both the onset of ECL and its decay back to baseline, i.e. ECL started to be detected after the beginning of the potential pulse, and ECL continued to persist after the potential pulse had ended. The former observation is, as stated, due to the required formation of emissive excimer species; the latter might be the phenomenon of *organic long-persistent ECL* (OLECL), which is characterized by long-lived emission

stemming from a charge-separation process followed by a slow charge-recombination route.[42, 56, 57] The formation of higher-order excited state species may be characterized by long-persistent luminescence.[44] Importantly, organic long-persistent emission is mechanically distinct from phosphorescence processes: organic long-persistent emission involves a slow charge recombination step, whereas phosphorescence requires a slow radiative transition between the triplet excited state and the ground state.[58-60] On average, we observed that this ECL onset delay and persistent ECL was longest for TPA-ace-TRZ, suggesting a slower excimer formation process for this compound than the others.

Table 6.1. Summary of photoluminescence (PL), electrochemiluminescence (ECL), and chemiluminescence (CL) emission in anhydrous dichloromethane. Numbers in parentheses in red color represent ECL efficiencies calculated relative to the $Ru(bpy)_3^{2+}$/BPO system.

	TPA-ace-TRZ	**TPA-ace-CN**	**2TPA-ace**	**TPA-ace**
Abs	340 nm	340 nm	340 nm	330 nm
PL	565 nm	495 nm	405 nm	410 nm
ECL Annihilation	630 nm (3%)	509 nm (7%)	625 nm (15%)	595 nm (3%)
ECL (10 mM BPO)	610 nm (2200%)	500 nm (2322%)	625 nm (1351%)	605 nm (86%)

Table 6.2. Summary of ECL onset, peak maxima, and end during ECL pulsing experiments.

	1. TPA-ace	**2. 2TPA-ace**	**3. TPA-ace-CN**	**4. TPA-ace-TRZ**
ΔE_{ST}[45]	0.88 eV	0.74 eV	0.22 eV	0.06 eV
ECL start delay	+23 ± 2.5 ms	+20 ± 1.8 ms	+18 ± 2.4 ms	+25 ± 3.7 ms
ECL max	+34 ± 3.5 ms	+31 ± 2.4 ms	+32 ± 3.9 ms	+57 ± 10 ms
ECL end	+111 ± 14 ms	+100 ± 1.8 ms	+100 ± 1.0 ms	+128 ± 14 ms

ECL Time offsets were determined from ECL-time profiles during potential pulsing experiments (as in **Figure 6.3C**, **Figure 6.7**, **Figure 6.11**, and **Figure 6.15** corresponding to TPA-ace-TRZ, TPA-ace, TPA-ace-CN, and 2TPA-ace, respectively. 'ECL start delay'

corresponds to the beginning of the increase from the ECL baseline. ‘ECL max’ corresponds to the point of maximum recorded ECL intensity. ‘ECL end’ corresponds to the point where the ECL returns to the baseline. All time offsets are reported with respect to the beginning of the potential pulse (t=0).

6.3.2 Electrochemiluminescence with benzoyl peroxide as coreactant

Next, we studied the ECL behaviour in the presence of a coreactant. Since **Figure 6.3B** indicates that the radical anion species is more stable, we selected benzoyl peroxide (BPO) as the oxidative-reduction coreactant. At a concentration of 10 mM BPO, a large enhancement in the ECL intensity was observed, which is due to the close potentials at which luminophore and coreactant can be reduced. In the above scenario, the two radical species react immediately upon generations so that the excited state concentration is elevated. **Figure 6.17A** demonstrates the CV and corresponding ECL voltage curve, where BPO is reduced at around −1.40 V vs. SCE to form the BPO radical anion ($BPO^{\bullet-}$). The benzoate radical ($PhCO_2^{\bullet}$) that is subsequently formed via a chemical reaction is a strong oxidizing agent which is capable of removing an electron from the TPA-ace-TRZ$^{\bullet-}$ radical anion to generate the excited state TPA-ace-TRZ* that relaxes to emit an ECL photon. The onset of the ECL peak is observed at −2.10 V vs. SCE, which corresponds closely with the reduction of TPA-ace-TRZ (seen from the DPVs in **Figure 6.3A**). This confirms that the TPA-ace-TRZ radical anion is key to the production of ECL. The ECL signal reached a maximum intensity of 24 μA at −2.20 V (approximately a 4800-fold enhancement when compared with that in the annihilation pathway), with the intensity decreasing at higher applied potentials due to the depletion of excited state concentration. **Figure 6.17B** illustrates the ECL emission spectrum of the TPA-ace-TRZ/BPO system, where a peak centered at 610 nm can be observed. This ECL emission wavelength under the coreactant pathway closely matches that of the annihilation pathway, indicating that a similar excited state could be present in both ECL pathways.

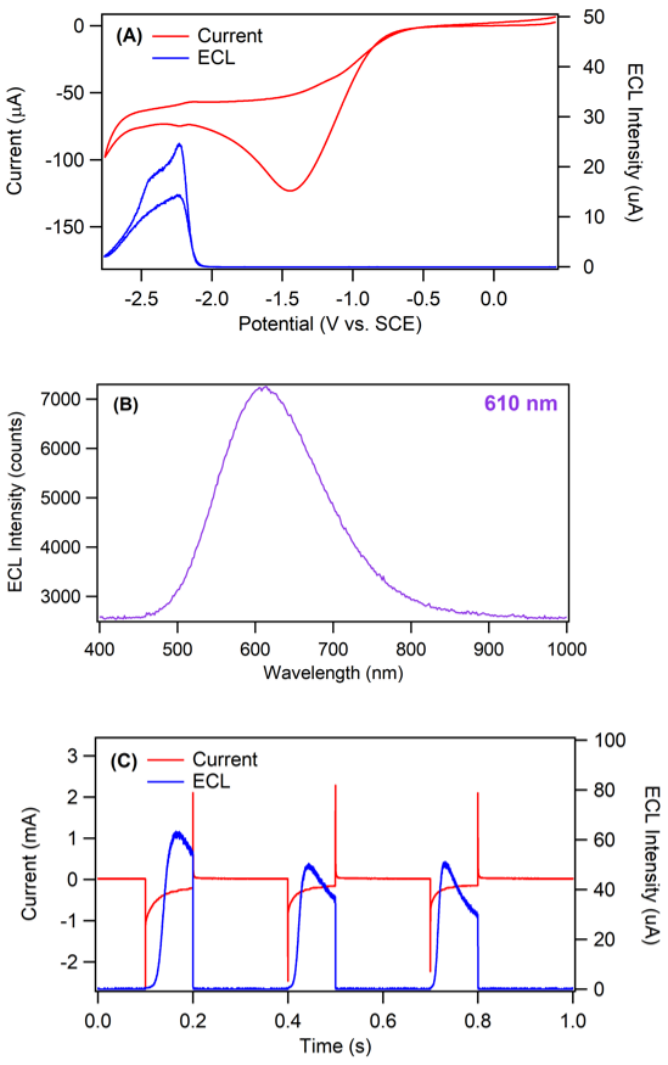

Figure 6.17. (A) Cyclic voltammogram (red) and ECL voltage curve (blue) of 1.42 mM TPA-ace-TRZ in dichloromethane and 0.1 M $TBAPF_6$ with 10 mM benzoyl peroxide as coreactant. Scan rate = 0.1 V/s. (B) ECL accumulation spectrum of TPA-ace-TRZ with 10 mM benzoyl peroxide (BPO). (C) Current-time (red) and ECL-time (blue) profile of TPA-ace-TRZ during potential pulsing (pulsing frequency was 10 Hz).

Figure 6.17C shows the ECL-time profile for TPA-ace-TRZ during potential stepping experiments in the BPO coreactant pathway. Similar to what was detected in the annihilation pathway, there was a delay in the onset of ECL emission compared to the beginning of the cathodic potential step. This observation strongly indicates the formation of a higher-order excited state. The production of an *exciplex* species (a heterogeneous

excited state[61, 62]) between TPA-ace-TRZ$^{-\bullet}$ and $PhCO_2^{\bullet}$ could be responsible for light emission in the coreactant pathway. This presence of exciplexes could also explain the small difference in emission wavelengths between the annihilation and coreactant pathways.

The ECL behaviour in the BPO coreactant system was also studied for TPA-ace, TPA-ace-CN, and 2TPA-ace; **Figure 6.18 – Figure 6.26** demonstrate the CV/ECL-voltage curves, accumulation, and spooling ECL spectra for these experiments. The emission wavelengths for TPA-ace, TPA-ace-CN, and 2TPA-ace were 500 nm, 625 nm, and 605 nm, respectively, which correspond very well to the annihilation ECL emission peak maxima. In general, the ECL emission was strongest for TPA-ace-TRZ and TPA-ace-CN, with an ECL maximum of 24 µA and 50 µA observed, respectively. In all four studied complexes, we observed a red-shift in their ECL emissions compared to their PL emissions; this can again be attributed to the formation of exciplexes.

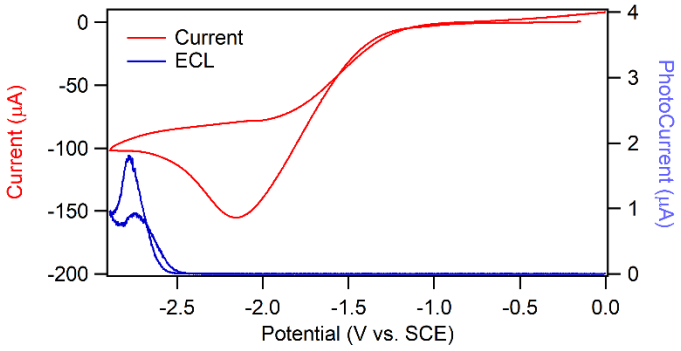

Figure 6.18. CV and ECL voltage curve of TPA-ace with 10 mM BPO as coreactant.

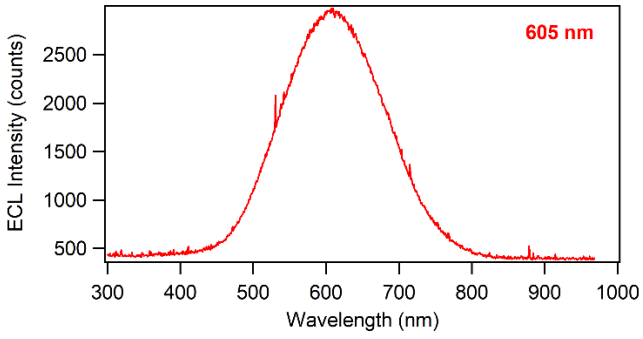

Figure 6.19. Accumulation ECL spectrum of TPA-ace with 10 mM BPO.

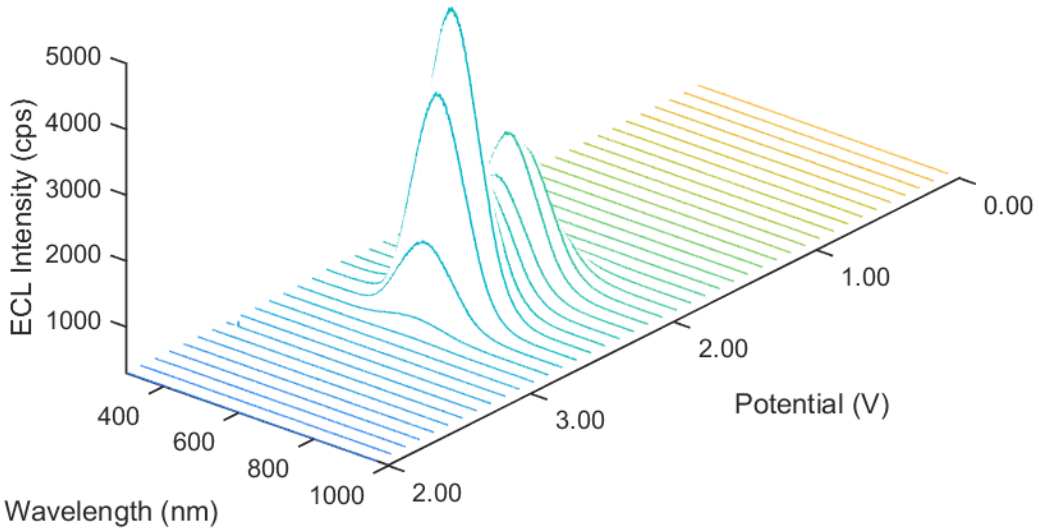

Figure 6.20. Spooling ECL spectrum of TPA-ace with 10 mM BPO as coreactant. Scan rate = 0.1 V/s, 1 spectrum/s.

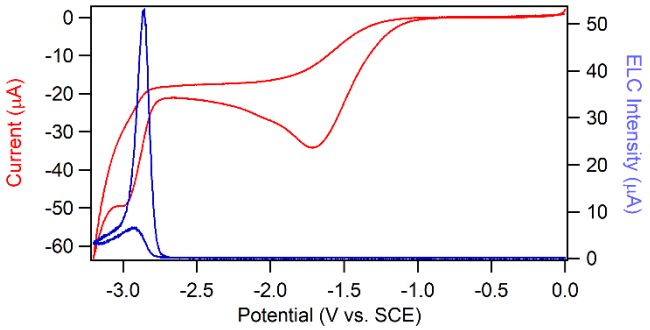

Figure 6.21. CV and ECL voltage curve for TPA-ace-CN with 5 mM BPO as coreactant.

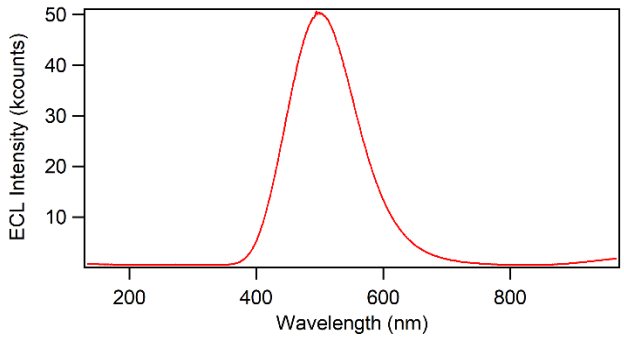

Figure 6.22. ECL accumulation spectrum for TPA-ace-CN with 5 mM BPO as coreactant.

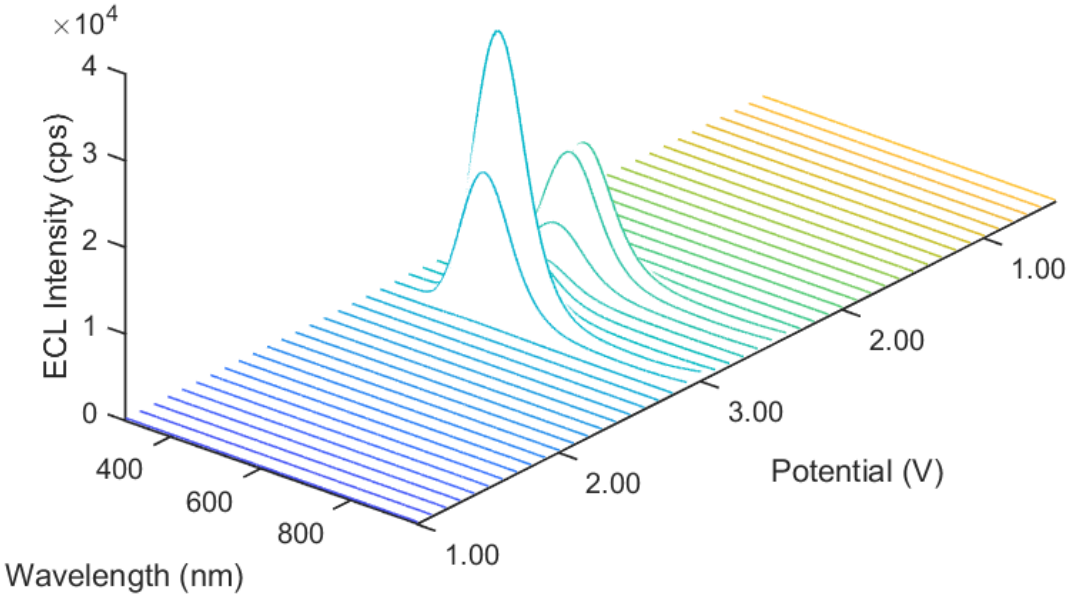

Figure 6.23. ECL spooling spectrum of TPA-ace-CN with 5 mM BPO as coreactant. Scan rate was 0.1 V/s, 1 spectrum/s.

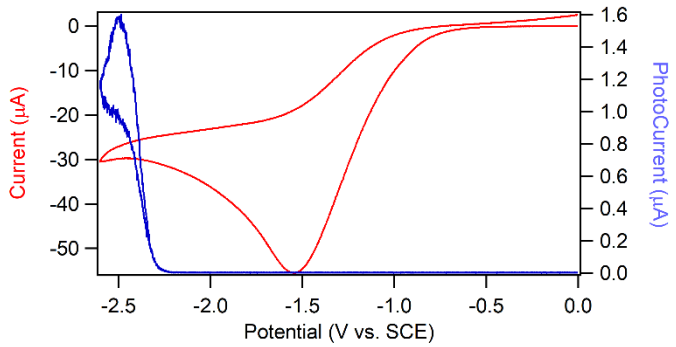

Figure 6.24. CV and ECL voltage curve for 2TPA-ace in the presence of 5 mM BPO as coreactant.

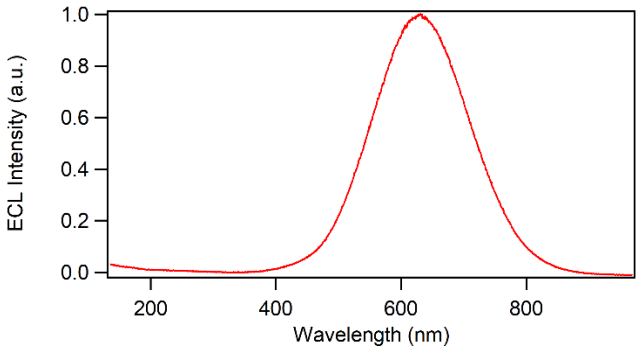

Figure 6.25. ECL accumulation spectrum of 2TPA-ace with 5 mM BPO.

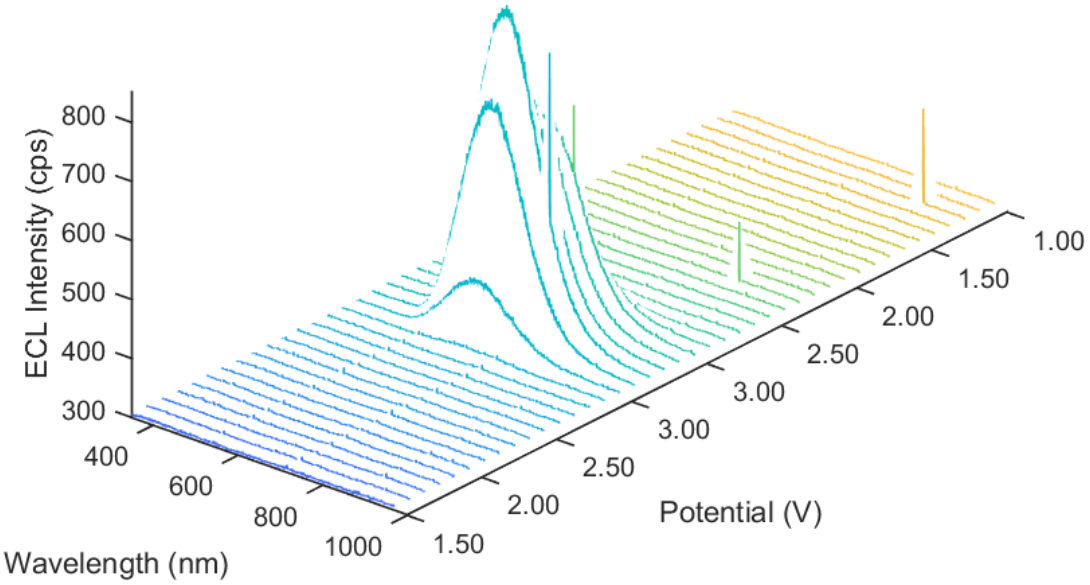

Figure 6.26. Spooling ECL spectra of 2TPA-ace with 5 mM BPO. Scan rate = 0.1 V/s, 1 spectrum/s.

We then employed spooling ECL spectroscopy to further study the emission during a potentiodynamic scan. In this technique, ECL spectra are continuously collected during a voltage scan to enable the correlation of light emission with specific applied potentials.[63] **Figure 6.27** shows the spooling spectra for TPA-ace-TRZ with 10 mM BPO. Like **Figure 6.17A**, ECL emission is detected when the potential reaches −2.10 V, with the maximum emission intensity achieved at a potential of −2.20 V. We can see a single peak throughout the scan with the wavelength remaining consistent, shown in the overlapped spectra in **Figure 6.28**. Using this information, the summary of the proposed mechanism is provided in **Figure 6.29**. TPA-ace-TRZ and BPO are both reduced at the electrode surface to produce TPA-ace-TRZ$^{\bullet-}$ and BPO$^{\bullet-}$, respectively. BPO$^{\bullet-}$ then loses a $PhCO_2^-$ group to produce the benzoate radical ($PhCO_2^{\bullet}$). The benzoate radical then removes an electron from the orbital of TPA-ace-TRZ$^{\bullet-}$ to generate the excited state TPA-ace-TRZ*, which subsequently forms an exciplex species with another $PhCO_2^{\bullet}$ molecule. The relaxation of this dimeric excited state back to ground state results in the emission of ECL.

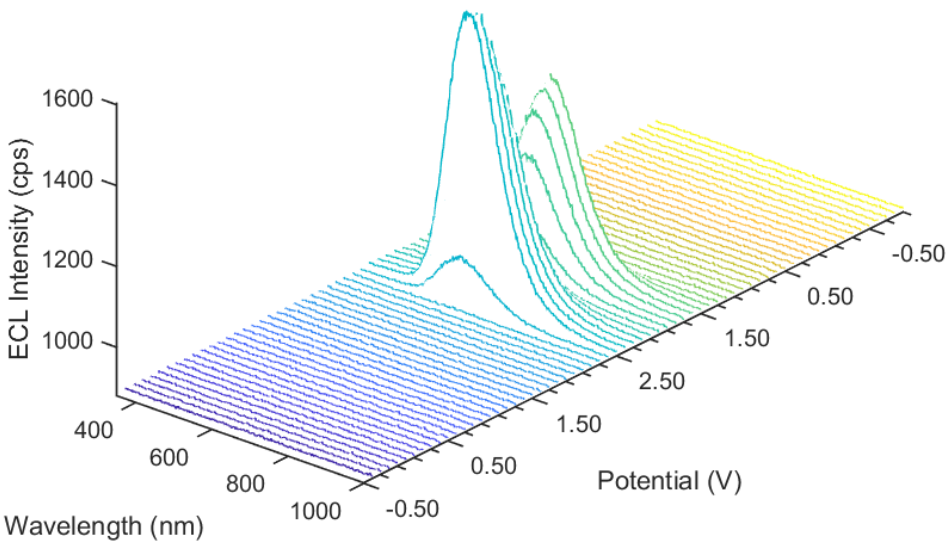

Figure 6.27. Spooling ECL spectra of TPA-ace-TRZ in the presence of 10 mM BPO as coreactant during a potentiodynamic experiment. The scan rate was 0.1 V/s and the exposure time of each spectrum was 1 s.

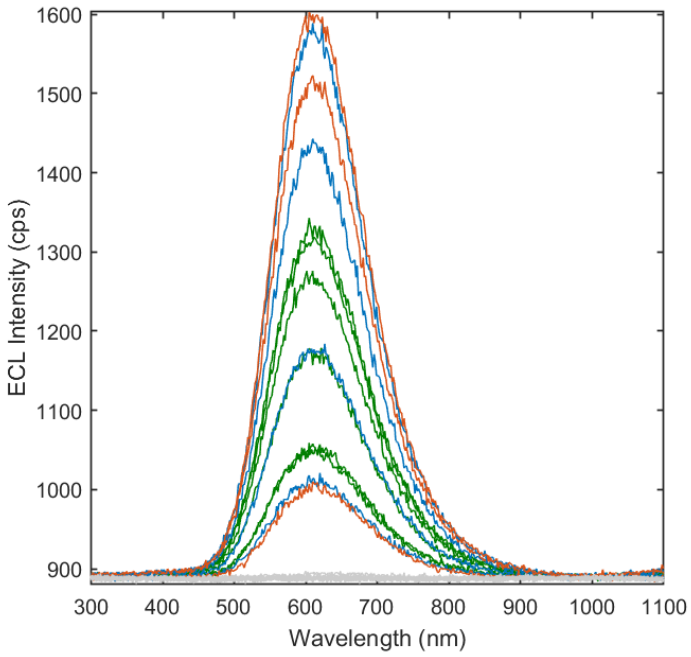

Figure 6.28. Overlaid ECL spooling spectra of TPA-ace-TRZ with 10 mM BPO as coreactant.

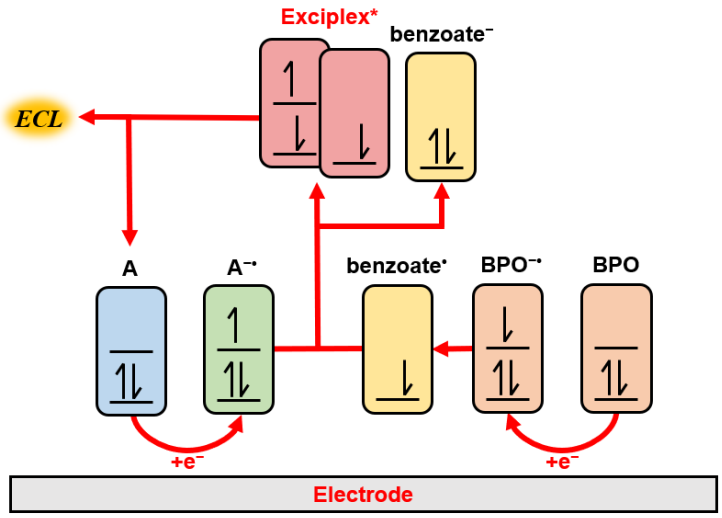

Figure 6.29. ECL reaction scheme for luminophore in the presence of BPO as coreactant. A = TPA-ace-TRZ, BPO = benzoyl peroxide.

6.3.3 Determination of the absolute ECL quantum efficiency

The absolute ECL quantum efficiency (Φ_{ECL}) of TPA-ace-TRZ was then determined to be 0.028% (**Table 6.3**), using our standardized spectrograph/CCD camera setup.[64] The Φ_{ECL} of TPA-ace-TRZ is approximately 9-fold stronger when compared to the reference system of $[Ru(bpy)_3]^{2+}$/BPO. It is evident that there a large discrepancy between the absolute and relative ECL efficiencies of this system. This is likely because the radical ion stabilities and reactivities of TPA-ace-TRZ and $[Ru(bpy)_3]^{2+}$ are quite different, and a direct comparison between these systems becomes problematic. In addition, there may be significant quenching of the excited states in the $[Ru(bpy)_3]^{2+}$/BPO system (particularly at the 10 mM concentrations we have employed in this study), leading to an artificial enhancement of the TPA-ace-TRZ relative efficiencies, wherein a reduction in the denominator of **Equation 6.5** increases the relative ECL yield. A key advantage of the absolute ECL determination is significant simplification of the physical/analytical procedure. Only a single measurement for the ECL emission on the spectrograph/CCD apparatus together with the corresponding electrochemical current is needed. In contrast, the relative ECL efficiency always requires a separate measurement of the $Ru(bpy)_3^{2+}$ standard. This increases the complexity of the test and introduces another potential area

of experimental bias. Traditional efficiencies measured relative to an external standard are consequently prone to misrepresentation of the true ECL efficiency. Therefore, reporting the absolute ECL efficiencies provides a highly representative measure of the ECL performance of a luminophore, and allows the meaningful comparison of the performance of various classes of luminophores. Although absolute ECL efficiencies have not been reported before for this class of compound, such measurements can provide valuable insight towards their electrochemical and electrochemiluminescence properties and behaviour.

Table 6.3. Absolute and relative ECL quantum efficiencies for TPA-ace-TRZ in the presence of 10 mM benzoyl peroxide as coreactant. The concentration was 1.5 mM for both luminophores and calculated during a cyclic voltammogram experiment (scan rate was 0.1 V/s).

	Photons	**Electrons**	**Φ_{ECL}**	**Rel. efficiency vs. $[Ru(bpy)_3]^{2+}$**
$[Ru(bpy)_3]^{2+}$	4.15×10^{11}	1.31×10^{16}	0.003%	
TPA-ace-TRZ	4.73×10^{12}	1.68×10^{16}	0.028%	9-fold

$$\text{rel. } \Phi_{ECL} = \frac{\left(\frac{\int ECL \times dt}{Current \times dt}\right)_x}{\left(\frac{\int ECL \times dt}{\int Current \times dt}\right)_{st}} \times 100$$

Equation 6.5

6.3.4 Chemiluminescence of TPA-ace-TRZ and its quantum efficiency

Finally, we explored the chemiluminescence (CL) properties of TPA-ace-TRZ via the *oxidation of a phenyl oxalate ester*. CL differs from ECL as the energy required to produce emissive excited state species comes from chemical reactions instead of an electrical current. With the addition of 10 mg/mL bis(2,4,5-trichloro-6-(pentyloxycarbonyl)phenyl)oxalate (CPPO) and hydrogen peroxide, bright yellow CL emission can be observed from the reaction vial (**Figure 6.30A and Figure 6.30B**). Briefly, CPPO reacts with H_2O_2 in the presence of a base catalyst (in these experiments, sodium salicylate was used) to produce oxalyl chloride, forming the high-energy 1,2-

dioxetanedione intermediate, which ultimately decomposes into CO_2. This reaction is exothermic, and the released energy can be subsequently absorbed by TPA-ace-TRZ to produce TPA-ace-TRZ*;[25, 26, 65] the relaxation of TPA-ace-TRZ* back to ground state releases a CL photon.

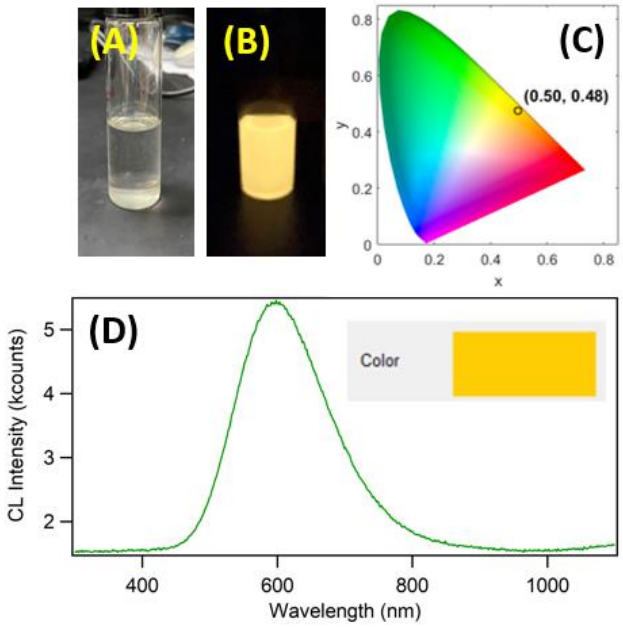

Figure 6.30. Colour photograph of TPA-ace-TRZ CL reaction vial (A) before adding H_2O_2 and (B) after addition of H_2O_2. (C) CIE colour coordinate diagram of the TPA-ace-TRZ CL reaction (0.3 mg/mL TPA-ace-TRZ, 10 mg/mL CPPO, 3 mL 30% H_2O_2). (D) Accumulation CL spectrum of 0.3 mg/mL TPA-ace-TRZ in dichloromethane; accumulation time was 10 s. The inset shows the calculated colour of the CL emission represented by coordinates x = 0.50 and y = 0.48.

The CL emission, when shown on the Commission International de l'Éclairage (CIE) colour diagrams, has coordinates of x=0.50 and y=0.48 (**Figure 6.30C**); this calculated colour matches very well with our photograph. The CL light was also measured by the spectrograph/CCD camera setup, where a broad emission peak could be observed centered at 610 nm (**Figure 6.30D**). This signal closely matches the emission observed in the ECL annihilation and coreactant pathways, suggesting that similar excited states – specifically higher-order conjugated excited states – could be present here. However, the

presence of excimers and/or exciplexes in the chemiluminescence process is highly intriguing, as the involvement of a secondary coreactant or molecule is not immediately obvious from the reaction mechanism.[26] We propose that the high-energy intermediate formed between the reaction of CPPO and H_2O_2 (pentyl 3,5,6-trichlorosalicylate) may be sufficiently long-lived and have sufficient reactivity to form an exciplex with TPA-ace-TRZ*. In this way, the formation of a dimeric excited state is achieved, analogous to the excited states previously observed in the ECL annihilation and coreactant pathways. Dimeric excited states in chemiluminescence are quite rare, with only a few select examples reported in literature[66-68]; this is in stark contrast with the increasingly widespread excimer and exciplex contribution in ECL pathways. It may be that the electro-generation of small, localized pockets of radical species in the vicinity of an electrode are ideal conditions for the formation of excimers and exciplexes. In contrast, CL involves the bulk mixing of reagents, and radical stability and reactivity may be limiting factors. In order for dimeric excited species to produce the dominant emission, as observed in our CL system, there should be a good balance – both chemically and stoichiometrically – between the luminophore and other reagents to generate the required radical species in sufficient quantities.

Nonetheless, the same excited state of TPA-ace-TRZ is shown to be easily accessible using very different modes of excitation: ultraviolet light in PL (**Figure 6.31**), electro-generation of radical species followed by electron transfer in ECL, and decomposition of high-energy chemical intermediates in CL. The overall flexibility and efficiency of TPA-ace-TRZ under these various emissive pathways suggests that it could be a promising luminophore in many light-emitting applications.

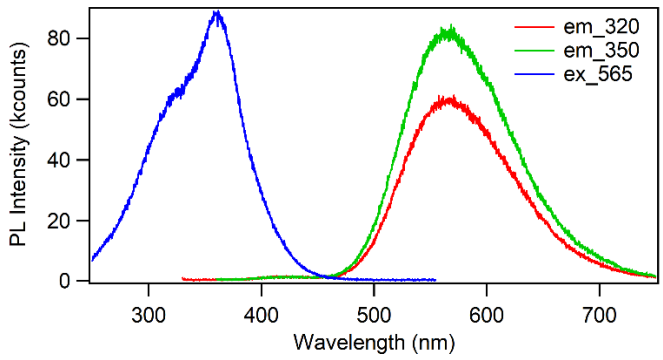

Figure 6.31. Photoluminescence excitation and emission spectra for TPA-ace-TRZ in dichloromethane.

This reaction was also monitored using spooling CL spectroscopy, a technique that examines the chemiluminescence emission of the system over time. **Figure 6.32** shows the spooling CL spectra, where each spectrum was collected for 10 s for a total of 150 s. Such an acquisition, measured using an externally calibrated spectrometer, enables the quantitative determination of the chemiluminescence quantum yield (Φ_{CL}), that is, the number of photons produced per molecule of CPPO (the limiting species in the CL reaction). After integration of each spectrum (with units of µW/nm) across the wavelength range of interest (400 to 800 nm), and a transformation using the photon energy (**Equation 6.1**), the number of photons per spectrum can be determined. Summing each spectrum over the entire experiment therefore yields the total number of photons collected.

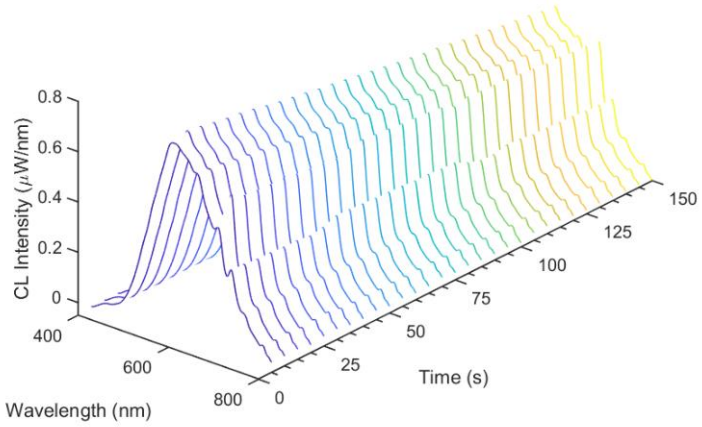

Figure 6.32. Spooling CL spectra of TPA-ace-TRZ with CPPO and H_2O_2 collected using a calibrated Ocean Insights optical spectrometer. Each spectrum is a 5 s exposure.

The Φ_{CL} of TPA-ace-TRZ was determined to be 0.11% over the duration of the 150 s experiment (**Figure 6.33**); the total efficiency was estimated to be 0.92% when assuming a linear extrapolation to the CL baseline (**Figure 6.34**). The compound TPA-ace-TRZ demonstrated remarkable stability during the CL test, with the emission wavelength remaining consistent throughout the 150 s experiment. This is further proof of the presence of a single excited state, which is the exciplex excited state. TPA-ace-TRZ also exhibited long lifetime in the CL pathway, providing visible emission to the naked eye during the entire experiment. The CL quantum efficiency of TPA-ace-TRZ is also very comparable to other luminophores such as luminol,[69] showcasing that this compound may have strong applications for clinical immunoassays,[70, 71] or analyte sensing.[72, 73]

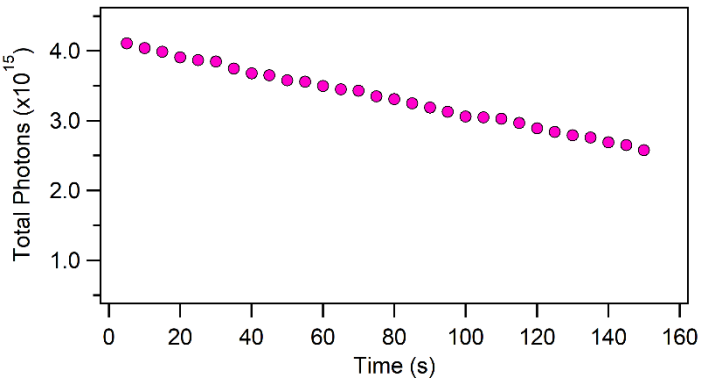

Figure 6.33. Total photons per spectrum calculated from the spooling CL experiment of TPA-ace-TRZ with CPPO and H_2O_2.

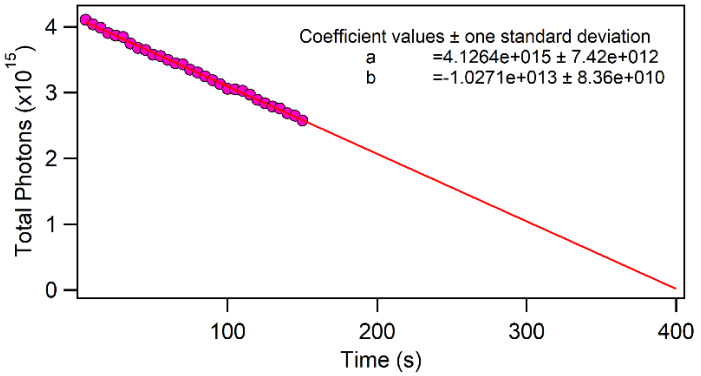

Figure 6.34. Linear extrapolation of the total CL photons to baseline. Linear fit performed using curve fitting function.

An estimation of the total CL photons curve was performed by extrapolating the linear fit to the x-intercept (when the total photons curve becomes zero). At this point, t = 400 s. The number of photons is therefore the area under the above plot. Calculating the area:

$$Area = \frac{base \times height}{2} = \frac{400\ s \times 4.11 \times 10^{15}}{2} = 8.22 \times 10^{17}\ photons$$

Equation 6.6

$$\Phi_{CL} = \frac{total\ photons}{n_{CPPO} \times NA} \times 100 = \frac{8.22 \times 10^{17}}{1.48 \times 10^{-4} \times 6.02 \times 10^{23}} \times 100 = 0.92\%$$

Equation 6.7

6.4 Conclusions

Here, we have studied the electrochemistry, electrochemiluminescence, and chemiluminescence of a through-space charge-transfer (TSCT) thermally activated delayed fluorescence (TADF) emitter. In particular, TPA-ace-TRZ was shown to possess excimer excited states in ECL annihilation pathways, and exciplex excited states in ECL coreactant and chemiluminescence pathways; these dimeric excited states caused significant red-shifted emissions compared to photoluminescence, and were the reason for the organic long-persistent ECL (OLECL) observed in these emitters. TPA-ace-TRZ exhibited an absolute ECL quantum efficiency and absolute CL quantum efficiency of 0.028% and 0.92%, respectively, determined using our standardized CCD camera and spectrometer.

6.5 References

[1] Richter, M. M. *Chem. Rev.* **2004,** *104*, 3003-36.

[2] Liu, Z.; Qi, W.; Xu, G. *Chem. Soc. Rev.* **2015,** *44*, 3117-42.

[3] Miao, W.; Bard, A. J. *Anal. Chem.* **2004,** *76*, 7109-7113.

[4] Zhan, W.; Bard, A. J. *Anal. Chem.* **2007,** *79*, 459-463.

[5] Dong, J.; Lu, Y.; Xu, Y.; Chen, F.; Yang, J.; Chen, Y.; Feng, J. *Nature* **2021,** *596*, 244-249.

[6] Parajuli, S.; Miao, W. *Anal. Chem.* **2009,** *81*, 5267-5272.

[7] Gorman, B. A.; Francis, P. S.; Dunstan, D. E.; Barnett, N. W. *Chem. Commun.* **2007**, 395-397.

[8] Collinson, M. M.; Wightman, R. M. *Science* **1995,** *268*, 1883-1885.

[9] Chang, Y.-L.; Palacios, R. E.; Fan, F.-R. F.; Bard, A. J.; Barbara, P. F. *J. Am. Chem. Soc.* **2008,** *130*, 8906-8907.

[10] Kanoufi, F.; Sojic, N. *Nature* **2021,** *596*, 194-195.

[11] Valenti, G.; Scarabino, S.; Goudeau, B.; Lesch, A.; Jović, M.; Villani, E.; Sentic, M.; Rapino, S.; Arbault, S.; Paolucci, F.; Sojic, N. *J. Am. Chem. Soc.* **2017,** *139*, 16830-16837.

[12] Anderson, T. J.; Defnet, P. A.; Zhang, B. *Anal. Chem.* **2020,** *92*, 6748-6755.

[13] Hesari, M.; Ding, Z. *J. Electrochem. Soc.* **2016,** *163*, H3116-H3131.

[14] Hesari, M.; Ding, Z. *Acc. Chem. Res.* **2017,** *50*, 218-230.

[15] Adsetts, J. R.; Hoesterey, S.; Gao, C.; Love, D. A.; Ding, Z. *Langmuir* **2020,** *36*, 14432.

[16] Yang, L.; Dong, L.; Hall, D.; Hesari, M.; Olivier, Y.; Zysman-Colman, E.; Ding, Z. *SmartMat* **2022,** *4*, e1149.

[17] Richter, M. M. *Chem. Rev.* **2004,** *104*, 3003-3036.

[18] Miao, W. *Chem. Rev.* **2008,** *108*, 2506-2553.

[19] Zhang, R.; Adsetts, J. R.; Nie, Y.; Sun, X.; Ding, Z. *Carbon* **2018,** *129*, 45-53.

[20] Wei, X.; Chu, K.; Adsetts, J. R.; Li, H.; Kang, X.; Ding, Z.; Zhu, M. *J. Am. Chem. Soc.* **2022,** *144*, 20421-20433.

[21] Liu, M.; Lin, Z.; Lin, J.-M. *Anal. Chim. Acta* **2010,** *670*, 1-10.

[22] Fan, Y.; Xing, H.; Zhai, Q.; Fan, D.; Li, J.; Wang, E. *Anal. Chem.* **2018,** *90*, 11651-11657.

[23] Liu, Y.; Shen, W.; Cui, H. *Anal. Chem.* **2019,** *91*, 10614-10621.

[24] Dong, S.; Wang, D.; Gao, X.; Fu, L.; Jia, J.; Xu, Y.; Zhang, B.; Zou, G. *Anal. Chem.* **2022,** *94*, 6902-6908.

[25] Kuntzleman, T. S.; Rohrer, K.; Schultz, E. *J. Chem. Educ.* **2012,** *89*, 910-916.

[26] Eghlimi, A.; Jubaer, H.; Surmiak, A.; Bach, U. *J. Chem. Educ.* **2019,** *96*, 522-527.

[27] Rauhut, M. M. *Acc. Chem. Res.* **1969,** *2*, 80-87.

[28] Dodeigne, C.; Thunus, L.; Lejeune, R. *Talanta* **2000,** *51*, 415-439.

[29] Tzani, M. A.; Gioftsidou, D. K.; Kallitsakis, M. G.; Pliatsios, N. V.; Kalogiouri, N. P.; Angaridis, P. A.; Lykakis, I. N.; Terzidis, M. A. *Molecules*, **2021**, *26*, 7664.

[30] Wong, J. M.; Zhang, R.; Xie, P.; Yang, L.; Zhang, M.; Zhou, R.; Wang, R.; Shen, Y.; Yang, B.; Wang, H.-B.; Ding, Z. *Angew. Chem. Int. Ed.* **2020,** *59*, 17461-17466.

[31] Dini, D. *Chem. Mater.* **2005,** *17*, 1933-1945.

[32] Xiong, C.-Y.; Wang, H.-J.; Liang, W.-B.; Yuan, Y.-L.; Yuan, R.; Chai, Y.-Q. *Chem. Eur. J.* **2015,** *21*, 9825-9832.

[33] Swanick, K. N.; Ladouceur, S.; Zysman-Colman, E.; Ding, Z. *Chem. Commun.* **2012,** *48*, 3179-3181.

[34] Chu, K.; Adsetts, J. R.; He, S.; Zhan, Z.; Yang, L.; Wong, J. M.; Love, D. A.; Ding, Z. *Chem. Eur. J.* **2020,** *26*, 15892-15900.

[35] Hesari, M.; Workentin, M. S.; Ding, Z. *ACS Nano* **2014,** *8*, 8543-8553.

[36] Bois, R.; Scarabino, S.; Ravaine, V.; Sojic, N. *Langmuir* **2017,** *33*, 7231-7238.

[37] Nabara, M.; Yamamoto, S.; Nishiyama, Y.; Nagatani, H. *Langmuir* **2020,** *36*, 10597-10605.

[38] Dias, F. B.; Bourdakos, K. N.; Jankus, V.; Moss, K. C.; Kamtekar, K. T.; Bhalla, V.; Santos, J.; Bryce, M. R.; Monkman, A. P. *Adv. Mater.* **2013,** *25*, 3707-3714.

[39] Alam, P.; Cheung, T. S.; Leung, N. L. C.; Zhang, J.; Guo, J.; Du, L.; Kwok, R. T. K.; Lam, J. W. Y.; Zeng, Z.; Phillips, D. L.; Sung, H. H. Y.; Williams, I. D.; Tang, B. Z. *J. Am. Chem. Soc.* **2022,** *144*, 3050-3062.

[40] Liang, X.; Zheng, Y.-X.; Zuo, J.-L. *Angew. Chem. Int. Ed.* **2021,** *60*, 16984-16988.

[41] Kabe, R.; Adachi, C. *Nature* **2017,** *550*, 384-387.

[42] Jinnai, K.; Nishimura, N.; Adachi, C.; Kabe, R. *Nanoscale* **2021,** *13*, 8412-8417.

[43] Kumar, S.; Tourneur, P.; Adsetts, J. R.; Wong, M. Y.; Rajamalli, P.; Chen, D.; Lazzaroni, R.; Viville, P.; Cordes, D. B.; Slawin, A.; Olivier, Y.; Cornil, J.; Ding, Z.; Zysman-Colman, E. *J. Mater. Chem. C* **2022,** *10*, 4646-4667.

[44] Nishimura, N.; Lin, Z.; Jinnai, K.; Kabe, R.; Adachi, C. *Adv. Funct. Mater.* **2020,** *30*, 2000795.

[45] Kumar, S.; Franca, L. G.; Stavrou, K.; Crovini, E.; Cordes, D. B.; Slawin, A. M. Z.; Monkman, A. P.; Zysman-Colman, E. *J. Phys. Chem. Lett.* **2021,** *12*, 2820-2830.

[46] Nepomnyashchii, A. B.; Bröring, M.; Ahrens, J.; Bard, A. J. *J. Am. Chem. Soc.* **2011,** *133*, 8633-8645.

[47] Chu, K.; Adsetts, J. R.; Ma, J.; Zhang, C.; Hesari, M.; Yang, L.; Ding, Z. *J. Phys. Chem. C* **2021,** *125*, 22274-22282.

[48] Adsetts, J. R.; Chu, K.; Hesari, M.; Ma, J.; Ding, Z. *Anal. Chem.* **2021,** *93*, 11626-11633.

[49] Hadd, A. G.; Lehmpuhl, D. W.; Kuck, L. R.; Birks, J. W.; Galen, P. M. *J. Chem. Educ.* **1999,** *76*, 1237.

[50] Rajamalli, P.; Senthilkumar, N.; Gandeepan, P.; Ren-Wu, C.-C.; Lin, H.-W.; Cheng, C.-H. *ACS Appl. Mater. Interfaces* **2016,** *8*, 27026-27034.

[51] Li, J.; Jiang, Y.; Cheng, J.; Zhang, Y.; Su, H.; Lam, J. W. Y.; Sung, H. H. Y.; Wong, K. S.; Kwok, H. S.; Tang, B. Z. *Phys. Chem. Chem. Phys.* **2015,** *17*, 1134-1141.

[52] Kim, M.; Choi, J. M.; Lee, J. Y. *Chem. Commun.* **2016,** *52*, 10032-10035.

[53] Suk, J.; Wu, Z.; Wang, L.; Bard, A. J. *J. Am. Chem. Soc.* **2011,** *133*, 14675-14685.

[54] Birks, J. B. *Rep. Prog. Phys.* **1975,** *38*, 903.

[55] Prieto, I.; Teetsov, J.; Fox, M. A.; Vanden Bout, D. A.; Bard, A. J. *J. Phys. Chem. A* **2001,** *105*, 520-523.

[56] Li, W.; Li, Z.; Si, C.; Wong, M. Y.; Jinnai, K.; Gupta, A. K.; Kabe, R.; Adachi, C.; Huang, W.; Zysman-Colman, E.; Samuel, I. D. W. *Adv. Mater.* **2020,** *32*, 2003911.

[57] Tan, S.; Jinnai, K.; Kabe, R.; Adachi, C. *Adv. Mater.* **2021,** *33*, 2008844.

[58] Jinnai, K.; Nishimura, N.; Kabe, R.; Adachi, C. *Chem. Lett.* **2019,** *48*, 270-273.

[59] Lin, Z.; Kabe, R.; Wang, K.; Adachi, C. *Nat. Comm.* **2020,** *11*, 191.

[60] Debye, P.; Edwards, J. O. *J. Chem. Phys,* **1952,** *20*, 236-239.

[61] Keszthelyi, C. P.; Bard, A. J. *Chem. Phys. Lett.* **1974,** *24*, 300-304.

[62] Ketter, J. B.; Wightman, R. M. *J. Am. Chem. Soc.* **2004,** *126*, 10183-10189.

[63] Hesari, M.; Ding, Z. *Nat. Protoc.* **2021,** *16*, 2109-2130.

[64] Adsetts, J. R.; Chu, K.; Hesari, M.; Whitworth, Z.; Qin, X.; Zhan, Z.; Ding, Z. *J. Phys. Chem. C* **2022,** *126*, 20155-20162.

[65] De Vico, L.; Liu, Y.-J.; Krogh, J. W.; Lindh, R. *J. Phys. Chem. A* **2007,** *111*, 8013-8019.

[66] Durán, N.; Zinner, K.; Baptista, R. C. d.; Vidigal, C. C. C.; Cilento, G. *Photochem. Photobiol.* **1976,** *24*, 383-388.

[67] Harris, D. G.; Chou, M. S.; Cool, T. A. *J. Chem. Phys,* **1985,** *82*, 3502-3515.

[68] Totsune, H.; Ohno, C.; Kambayashi, Y.; Nakano, M.; Ushijima, Y.; Tero-Kubota, S.; Ikegami, Y. *Arch. Biochem. Biophys.* **1999,** *369*, 233-242.

[69] White, E. H.; Bursey, M. M. *J. Am. Chem. Soc.* **1964,** *86*, 941-942.

[70] Weeks, I.; Beheshti, I.; McCapra, F.; Campbell, A. K.; Woodhead, J. S. *Clin. Chem.* **1983,** *29*, 1474-1479.

[71] Xiao, Q.; Xu, C. *TrAC, Trends Anal. Chem.* **2020,** *124*, 115780.

[72] Braman, R. S.; Hendrix, S. A. *Anal. Chem.* **1989,** *61*, 2715-2718.

[73] Yu, W.; Zhao, L. *TrAC, Trends Anal. Chem.* **2021,** *136*, 116197.

Chapter 7

7 Determining the Bimolecular Rate Constants for Annihilation Reactions of Electrogenerated $Ru(bpy)_3^{2+}$ Radical Ions by Means of Electrochemiluminescence at an Ultramicroelectrode†

The electrochemiluminescence and the associated bimolecular annihilation rate constant k_{ann} was modelled using finite element analysis. Experimentally, by using an ultramicroelectrode, we were able to capture the fast kinetic profile of electrochemiluminescence of $Ru(bpy)_3^{2+}$ in the annihilation pathway using high frequency potential stepping. The k_{ann} was estimated to be 10^7 $M^{-1}s^{-1}$ by fitting simulated ECL transients from COMSOL Multiphysics to experimental data at frequencies of 10 Hz, 100 Hz, and 1000 Hz. Our two-dimensional simulation model to simulate the hemispherical diffusion of electroactive species at an ultramicroelectrode is shown to be able to extract important chemical and kinetic information from electrochemiluminescence systems.

7.1 Introduction

Electrochemiluminescence (ECL) is the process where electrogenerated radicals at an electrode interact to produce excited states that can emit light when relaxing back to the ground state. The simplest ECL mechanism is the annihilation pathway, followed when a radical cation (generated at the anode) interacts with the radical anion (generated at the cathode) to produce the excited state. This phenomenon, since its discovery by Chandross, Hercules, and Bard[1-3] has developed into a powerful and sensitive analytical technique with many applications in bioanalysis, sensing, imaging, and light-emitting. Like with all light-emitting reactions, there has been a continuous effort towards improving and optimizing the quantum efficiency of the ECL process, such as by designing novel luminophores that can intrinsically harness the energy of triplet excitons

† Submitted to a journal.

by means of thermally activated delayed fluorescence (TADF), or by exploiting other emission enhancing effects of aggregation- or crystallization-induced electrochemiluminescence. An area that remains significantly underrepresented and seldom explored is that of numerical simulation of the ECL reaction. In a carefully designed ECL experiment, the mass transport via diffusion is the only method by which electroactive species can translocate within the medium, and therefore is the primary driving force for the ECL reaction. This means that simulating the ECL system using finite element analysis software is possible. Characterization and comparison of experiment ECL with simulated models can therefore be extremely useful when developing an understanding of ECL mechanisms and kinetics, and ultimately, can be an effective tool towards improving and optimizing ECL quantum efficiency.

This approach has been used in the past, for instance the Wightman group were very much pioneers in this field, using numerical simulation to model the high frequency ECL at microelectrodes.[4, 5] Their models were able to monitor individual chemical reactions in solution[6], demonstrating that it was possible to extract chemical information such as the bimolecular annihilation rate constant. However, the majority of such simulations have been developed in a single spatial dimension[7], that is, it can only accurately reproduce the linear diffusion characteristics of a macroelectrode. This is an unfortunate limitation, as it restricts the available electrode geometries for study. In the case for ultramicroelectrodes (commonly defined as electrodes with a critical dimension less than 25 μm[8, 9]) where diffusive flux at the electrode surface takes on a hemispherical geometry, a two-dimensional model is needed. With the growing popularity of micro- and nanoelectrode electrochemistry and electrochemiluminescence studies – for reasons of minimal ohmic drop, reduced interference from double layer capacitance, and very fast diffusion kinetics – to probe approaching to the single molecule reaction, it is vital to develop simulations that can reliably model these environments. In addition, were are able to show a domain transformation from medium frequency pulsing to high rate constant due to the high temporal resolution and high sensitivity of the photon counting instrumentation.

In this work, we simulate the electrochemiluminescence of the well-known luminophore $Ru(bpy)_3^{2+}$ in the annihilation mechanism at an ultramicroelectrode using COMSOL

Multiphysics. Using our newly developed two-dimensional COMSOL model, the fast electron transfer kinetics could be captured with high accuracy. We were able to estimate the biomolecular annihilation rate constant to be 10^7 $M^{-1}s^{-1}$. This approach to use numerical simulations in conjunction with ECL studies is shown to be a powerful tool to extract physical and chemical parameters of ECL systems, and could be important when finding the optimal conditions for these reactions to maximize efficiency.

7.2 Experimental

7.2.1 Materials and reagents

Tris(2,2'-bipyridine) ruthenium(II) hexafluorophosphate, $Ru(bpy)_3(PF_6)_2$ (97%, reagent grade), tetrabutylammonium hexafluorophosphate, $TBAPF_6$ (>99.0%, electrochemical grade), and ferrocene (98%) were purchased from Sigma-Aldrich Canada (Mississauga, ON) and used as received. Anhydrous acetonitrile (99.8%, SureSeal) was obtained from Sigma-Aldrich Canada and stored under an inert atmosphere.

7.2.2 Electrochemistry and electrochemiluminescence

A three-electrode system was used for all ECL experiments, where the working electrode was a platinum ultramicroelectrode (UME) with a diameter of 25 μm and RG>10 and the counter and reference electrodes were platinum coils. UMEs were fabricated in our lab following the procedure published elsewhere.[10] Before use, UMEs were hand-polished using FibrMet abrasive discs adhered with 0.3 μm alumina (Buehler Canada) and their electrochemical performance was tested using a solution of 0.9 mM ferrocenemethanol (FcMeOH) and 0.1 M KCl to verify the presence of characteristic steady state oxidation current.[9] All electrochemical analyses were performed in a glass cylindrical cell with a flat quartz window at the bottom to allow for the detection of ECL. The ECL cell with 0.5 mM $Ru(bpy)_3(PF_6)_2$ in acetonitrile solution with 0.1 M $TBAPF_6$ as supporting electrolyte was assembled in an oxygen- and moisture-free NEXUS I glovebox system (Vacuum Atmospheres Company, Hawthorne, CA). Cyclic voltammograms were obtained using a CHI 610a electrochemical analyzer (CH Instruments, Austin, TX). High-frequency potential stepping was achieved using a PAR Model 175 Universal Programmer (Princeton Applied Research, Princeton, NJ) in conjunction with a

bipotentiostat (Model AFCBP1, Pine Instrument Company, Grove City, PA) to sample the electrochemical current. All experimental voltages were reported relative to the ferrocene/ferrocenium (Fc/Fc^+) redox couple, with its oxidation potential taken as 0.342 V vs. SCE.[11]

The ECL signal was collected using a photon counting head (PCH), which is an all-in-one unit incorporating a photomultiplier and high-speed amplifier/discriminator/power supply circuits (Model H6240-02, Hamamatsu, Japan). The required 5 V input power was provided using the voltage delivery pins on a modified universal serial bus (USB) connector. The output signal from the PCH as pulse series was passed through an attenuator to reduce the outgoing voltage pulse magnitude to 200 mV, before arriving at an SR430 multichannel scaler/averager (Stanford Research Systems, Sunnyvale, CA) for data recording. The SR430 instrument collects the incoming voltage pulses from the PCH and sorts them into successive 'bins', allowing the acquisition of high resolution time-resolved ECL. The *bin width* (the time interval for each bin) and the *bins per record* setting define the total time for each experiment. The SR430 instrument receives an external trigger signal, provided by the PAR175 voltage programmer, and begins to acquire and accumulate the incoming data. The total acquisition time (*T*) is defined by the following **Equation 7.1**:

$$T = (N \times T_{bin}) + (N \times 250\ ns) + 150\ \mu s$$

Equation 7.1

where *N* is the number of bins per record, and T_{bin} is the bin width. The constant values of 250 ns and 150 µs correspond to the required accumulation time per bin, and the instrument processing overhead, respectively.[12] For example, N = 9216 and a bin width of 5.120 µs equals an acquisition time (*T*) of 47.19 ms, plus a processing time of 2.454 ms, for a total time of 49.64 ms. In general, a total of 1000 *records per scan* was used for all experiments, allowing the accumulation of multiple ECL events into a single file, dramatically improving the signal-to-noise and providing statistical capabilities. An external voltage trigger, provided by the PAR175 programmer, was used to begin each record enabling the synchronous acquisition of the ECL signal. The SR430 therefore

allows the acquisition and recording of data with extremely high frequency (down to a ns range) and with excellent signal-to-noise. These capabilities enable the accurate study of very fast reactions, such as those involved in the generation of ECL. A custom LabVIEW program was used to provide computer control and subsequent data acquisition of the SR430 instrument. **Figure 7.1** provides a schematic overview of the relevant equipment and instrumentation involved in the generation and acquisition of the ECL signal.

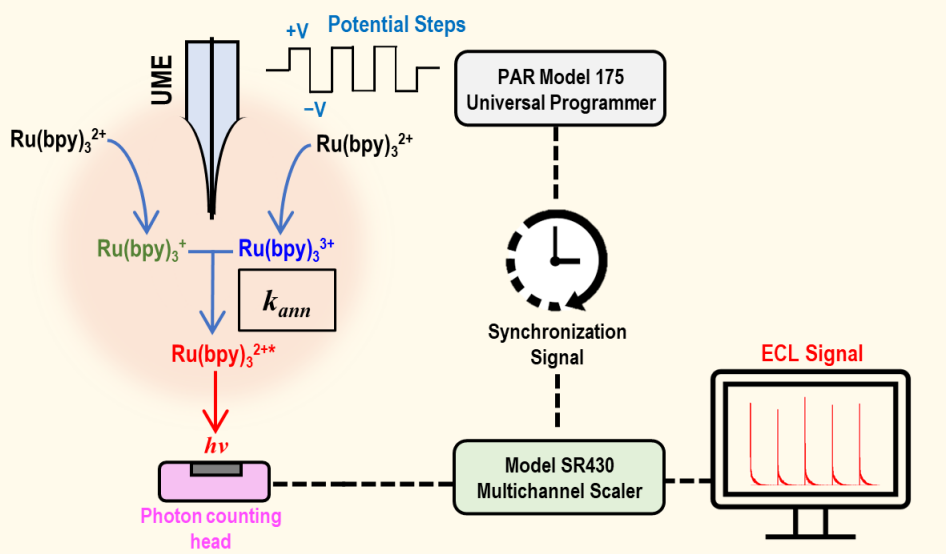

Figure 7.1. Instrument setup for generating high-frequency potential steps and measuring electrochemiluminescence.

7.2.3 Building the COMSOL simulation model: geometry and meshing

All theoretical simulations and calculations were performed using COMSOL Multiphysics software (version 5.3, COMSOL Inc., Burlington, MA), where the 'Transport of Diluted Species' (*tds*) module was used to treat diffusion and molecular reaction kinetics. A representative two-dimensional axisymmetric model of the ECL system under study was created, whereby the simulation plane rotated 360° around an axis vertically bisecting the working ultramicroelectrode reconstructs the experimental ECL space in three dimensions. This approach allows the accurate modelling of

hemispherical diffusion with respect to the electrode. The simulation plane is confined by five contiguous boundaries as labelled in **Figure 7.2A**: (1) a rotational axis of symmetry; (2) the electrode surface; (3) an insulating glass sheath assumed to be completely impermeable to species flux; and (4), (5) semi-infinite concentration boundaries representing the bulk of the ECL system. These five boundaries enclose within them a subdomain in which all diffusive flux and electron transfer reactions pertinent the ECL annihilation and the generation of ECL excited states are assumed to occur. Geometric discretization of the simulation space was performed with free triangular elements following the advancing front tessellation method, where the maximum element size and maximum element growth rate was 12.5 µm and 1.3, respectively, except at the electrode boundary, where the maximum element size was reduced to 0.125 µm to improve simulation accuracy in a region where significant fluctuation in concentration was expected. This results in a final mesh that is considerably finer as one approaches the electrode surface (**Figure 7.2B**).

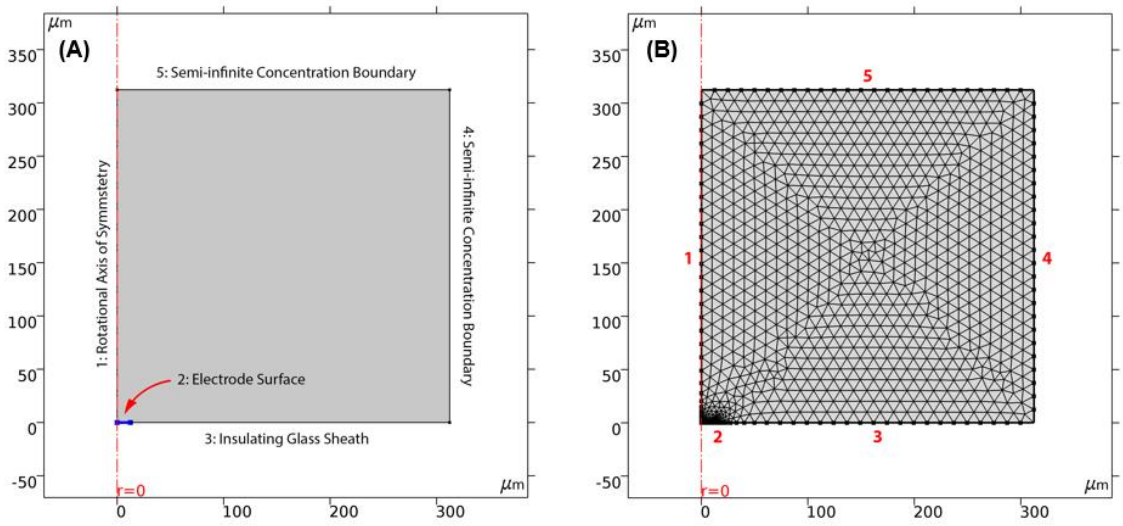

Figure 7.2. (A) Two-dimensional geometry of COMSOL simulation model with labelled boundaries. The electrode surface boundary was set to 12.5 µm, matching the radius of the experimental UME. (B) Triangular meshing pattern (advancing front algorithm) used in simulation model consisting of *2977* total elements. Geometry boundaries are labelled (as in the main text) for clarity.

7.2.4 Simulated Diffusion and Reaction kinetics

Fick's second law of diffusion was used to describe the concentration dependent movement of species within the simulation space. Its general form is given in **Equation 7.2**, where the Laplacian operator may be replaced with $\partial^2/\partial r^2 + (1/r)(\partial/\partial r) + \partial^2/\partial z^2$ as for the case of an inlaid disk ultramicroelectrode with axial symmetry coordination (**Equation 7.3**). In this form, r is the radial distance from the center of the electrode, z is the distance measured normal to the electrode surface, and c_0 is the concentration of the respective species. The diffusion coefficient D was set to 5.8×10^{-10} m^2/s for the $Ru(bpy)_3^{2+}$ complex and all of its electrogenerated derivatives, in accordance with previous studies.[4] This constant was assumed to be isotropic with respect to the simulated geometry. The initial concentration of the solution subdomain was set to 0.5 mol/m^3 to match the experimental $Ru(bpy)_3^{2+}$ concentration, along with the semi-infinite boundary conditions corresponding to bulk solution.

$$\frac{\partial C_O}{\partial t} = D_O \nabla^2 C_O$$

Equation 7.2

$$\frac{\partial C_0(r,z,t)}{\partial t} = D\left[\frac{d^2{}_0(r,z,t)}{dr^2} + \frac{1}{r}\frac{\partial c_0(r,z,t)}{\partial r} + \frac{\partial^2 c_0(r,z,t)}{\partial z^2}\right]$$

Equation 7.3

Table 7.1. COMSOL model definitions.

Name	Definition	Value
D	Diffusion coefficient	5.8×10^{-10} m^2/s
C	Initial concentration of parent species	0.5 mol/m^3
F	Faraday's constant	96485 C/mol
k^0	Std. rate constant for heterogeneous electron transfer	0.01 m/s
T	Temperature	298 K
E_p	Positive potential step	1.65 V
E_n	Negative potential step	−1.35 V

The Butler-Volmer (B-V) kinetic equation[13] was used to relate the applied potential at the electrode with the resultant flux of electroactive species at the electrode boundary (given in **Equation 7.4**), where F is the Faraday constant, A is the surface area of the electrode, k^0 is the standard rate constant for heterogeneous electron transfer, α is the charge transfer coefficient, f is a scalar quantity equal to F/RT (with R being the gas constant, and T the temperature), $E-E^0$ is the overpotential, defined as the difference between the applied potential (E) and the standard redox potential (E^0), and C_O and C_R are the concentrations of the respective oxidized or reduced species.

$$i = FAk^0\left[C_O(0,t)e^{-\alpha f\left(E-E^{0\prime}\right)} - C_R(0,t)e^{(1-\alpha)f\left(E-E^{0\prime}\right)}\right]$$

Equation 7.4

Reduction and oxidation of the $Ru(bpy)_3^{2+}$ parent species, and their subsequent electron transfer reactions to generate the $Ru(bpy)_3^{2+*}$ excited state were modelled using chemical reactions in COMSOL's chemical species transport module. Each of these reactions, shown below in **Figure 7.3**, is controlled by individual rate constants. A summary of these reactions, and their respective rate constants is given in **Table 7.2**. The emission rate constant (k_{em}) was obtained from previously reported literature,[14] along with estimations of the bimolecular annihilation rate constant and the radical decay constants.[15, 16]

$$Ru(bpy)_3^{2+} + e^- \underset{kb_{red}}{\overset{kf_{red}}{\rightleftharpoons}} Ru(bpy)_3^{+}$$

$$Ru(bpy)_3^{3+} + e^- \underset{kb_{ox}}{\overset{kf_{ox}}{\rightleftharpoons}} Ru(bpy)_3^{2+}$$

$$Ru(bpy)_3^{3+} + Ru(bpy)_3^{+} \xrightarrow{k_{ann}} {}^*Ru(bpy)_3^{2+} + Ru(bpy)_3^{2+}$$

$${}^*Ru(bpy)_3^{2+} \xrightarrow{k_{em}} Ru(bpy)_3^{2+} + \boldsymbol{hv}$$

Figure 7.3. ECL reactions. (A) Reduction of $Ru(bpy)_3^{2+}$ to form $Ru(bpy)_3^{+}$. (B) Oxidation of $Ru(bpy)_3^{2+}$ to form $Ru(bpy)_3^{+}$. (C) Annihilation reaction between

$Ru(bpy)_3^{2+}$ and $Ru(bpy)_3^{+}$ to form the excited state $*Ru(bpy)_3^{2+}$. (D) Relaxation of $*Ru(bpy)_3^{2+}$ excited state to release an ECL photon.

Table 7.2. COMSOL reactions and their rate constants.

Inward flux at electrode surface		
m	-(kfox*mox+kbox*m)+(-kfred*m+kbred*mred)	
mox	(-kfox*mox*kbox*m)	
mred	-(-kfred*m+kbred*mred)	
ECL annihilation reactions		
R_m	(kem*me)+(kann*mox*mred)+(kq*mred*me)+(kq*mox*me)	
R_{mox}	-(kann*mox*mred)-(ko1*mox)	
R_{mred}	-(kann*mox*mred)-(kr1*mred)	
R_{me}	-(kem*me)+[kann*(mox*mred)-(kq*me*(mred+mox)]	
Electrochemistry and ECL rate constants		
k_{ann}	Annihilation rate constant	$8.89\times10^6\ M^{-1}s^{-1}$
k_{em}	Emission rate constant[14]	$1.47\times10^7\ M^{-1}s^{-1}$
k_q	Quenching rate constant	$8.89\times10^6\ M^{-1}s^{-1}$
k_{o1}	Radical cation decay constant	$2.98\times10^3\ M^{-1}s^{-1}$
k_{r1}	Radical anion decay constant	$1.48\times10^2\ M^{-1}s^{-1}$

After a time-dependent computation of concentration profiles, the normal diffusive fluxes of $Ru(bpy)_3^{3+}$ and $Ru(bpy)_3^{+}$ were integrated along the electrode boundary (Boundary 2 in **Figure 7.2**), allowing the derivation of electrode current following the relationship given in **Equation 7.5** and **Equation 7.6.**[13] The concentration of the ECL excited state $*Ru(bpy)_3^{2+}$ was obtained by a surface integration across the entire solution subdomain with respect to time. The excited state concentration versus time profile was then normalized against the experimental ECL signal for comparison.

Table 7.3. COMSOL integration parameters.

Description	**Integrated as…**
curr1 [*mox*]	−2*pi*r*F_const*tds.ndflux_mox
curr2 [*mred*]	−2*pi*r*F_const*tds.ndflux_mred
$*Ru(bpy)_3^{2+}$ [*me*]	kem*me

$$J_0(0,t) = -D_0\left[\frac{\partial C_0(x,t)}{\partial x}\right]_{x=0}$$

Equation 7.5

$$i = nFAD_0\left[\frac{\partial C_0(x,t)}{\partial x}\right]_{x=0}$$

Equation 7.6

Calculations were performed using the PARDISO solver, with both relative and absolute tolerances under automatic physics control. The average solving time for these simulations (starting from t = 0 and including four anodic steps and four cathodic steps) was between two to three minutes, which demonstrates the computational efficiency of our model even on conventional processors. Unless explicitly mentioned here, all other programming parameters are assumed to be their default values. A preliminary comparison between the one-dimensional ECL simulation reported by Shen *et al.*[15] and the two-dimensional simulation developed for this work was performed to verify the validity of our theoretical model. The result from this evaluation is presented in **Figure 7.4**, where an excellent overlap between the two ECL vs. time profiles was observed. This agreement greatly increases our confidence in reporting our results below.

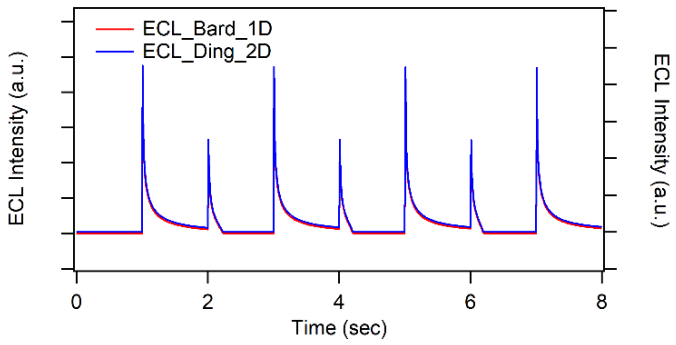

Figure 7.4. Comparison between reference 1-D simulation ECL (Shen *et al.* 2010)[15] and the 2-D simulations presented in this work.

7.2.5 Parametric simulation of the bimolecular ECL annihilation rate constant (k_{ann})

Figure 7.5A shows an example of theoretical ECL transients simulated at a frequency of 10 Hz using different values for the bimolecular annihilation rate constant, k_{ann}. The profile of the ECL curve is shown to be highly dependent on the value of k_{ann}. As this rate constant is increased, the ECL maximum occurs closer to the onset of the potential step. This is because $Ru(bpy)_3^+$ and $Ru(bpy)_3^{3+}$ can interact more readily when k_{ann} is large, thereby generating the necessary ECL excited states quicker. As follows, the decay in the ECL signal also occurs faster; this is because the value for the emission rate constant (k_{em}) is typically much higher as it is a unimolecular reaction. Therefore the profile of the ECL curve is almost entirely determined by the annihilation rate constant and the diffusion coefficient. In the scenario of the lowest k_{ann} value, an onset and decay in the ECL signal can be observed, showing that a slower annihilation reaction results in a more gradual ECL profile. By overlapping these theoretical curves over the experimental ECL curves, the bimolecular rate constant for ECL annihilation can be determined. When this parametric study of k_{ann} was repeated at a frequency of 1 Hz (**Figure 7.6**), we observed a very similar trend, where the faster the ECL annihilation reaction, the quicker the ECL signal reaches a peak before it decays. This demonstrates that the simulation can still accurately model very fast reactions even at lower frequencies. In addition, by using an ultramicroelectrode (where the rate of diffusion is fast relative to the rate of consumption of electroactive species), we are able to study ECL kinetic phenomena with high accuracy and correctly interpret fast rate constants. In addition, the effects of k_{ann} were studied at higher pulsing frequencies (100 Hz, **Figure 7.7**, and 1000 Hz, **Figure 7.8**). We observe the aforementioned analytical trend even at these frequencies, which indicates that these rate-controlled reactions are actually much faster than the pulsing frequency (even when using an ultramicroelectrode). This finding suggests that, experimentally, it may be advantageous to use slower pulsing frequencies (10 Hz or lower) to monitor and study ECL reactions; this significantly reduces instrumental complexity and synchronization issues while still providing accurate results.

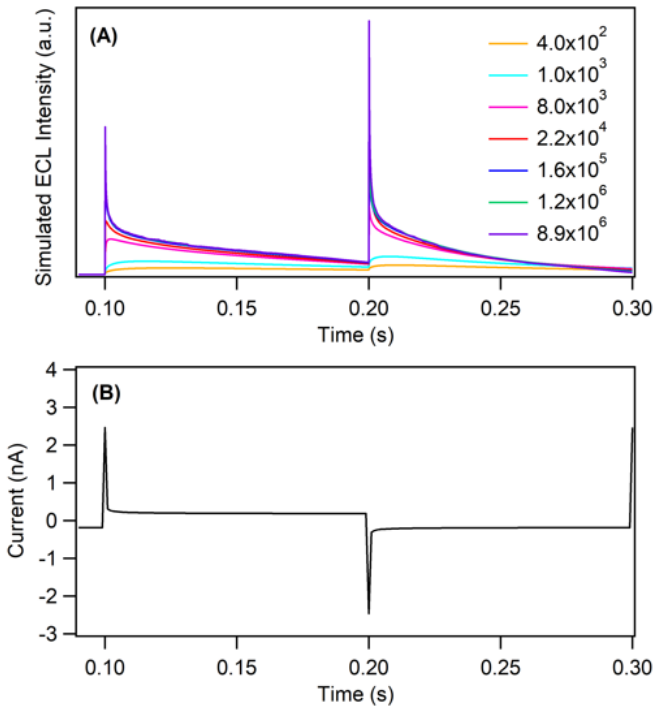

Figure 7.5. (A) Simulated ECL transients for different values of k_{ann} (the annihilation rate constant), where the diffusion coefficient was 5.8×10^{-10} m^2/s and the concentration was 0.5 mol/m^3. Pulsing frequency was 10 Hz. (B) Current-time profile (10 Hz) for simulated ECL experiment.

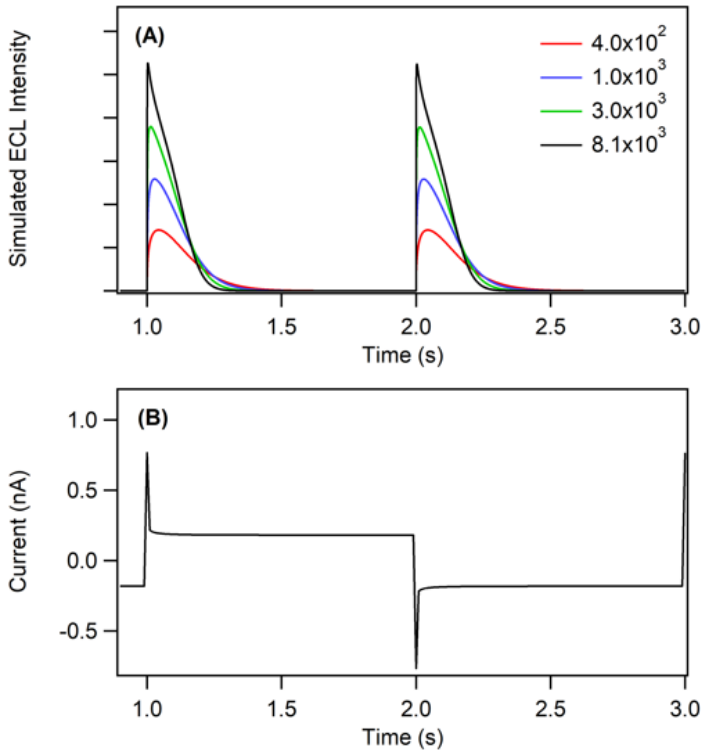

Figure 7.6. Simulated ECL transients for different values of k_{ann} (the annihilation rate constant), where the diffusion coefficient was 5.8×10^{-10} m^2/s and the concentration was 0.5 mol/m^3. Pulsing frequency was 1 Hz.

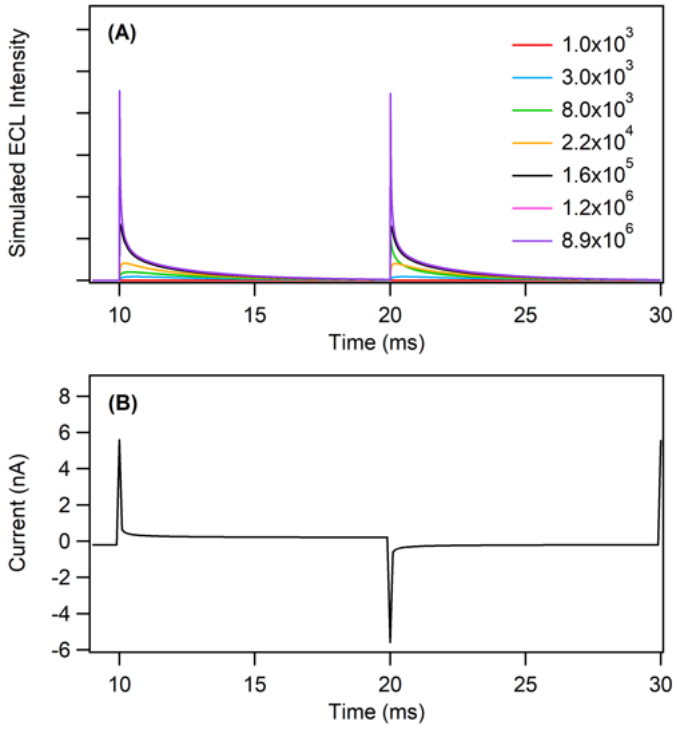

Figure 7.7. Simulated ECL transients for different values of k_{ann} (the annihilation rate constant), where the diffusion coefficient was 5.8×10^{-10} m^2/s and the concentration was 0.5 mol/m^3. Pulsing frequency was 100 Hz.

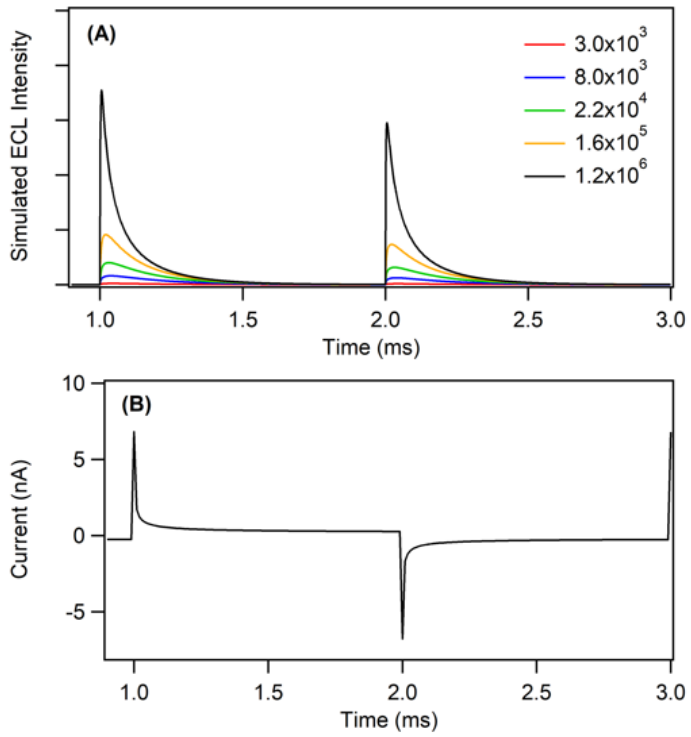

Figure 7.8. Simulated ECL transients for different values of k_{ann} (the annihilation rate constant), where the diffusion coefficient was 5.8×10^{-10} m^2/s and the concentration was 0.5 mol/m^3. Pulsing frequency was 1000 Hz.

7.3 Results and Discussion

7.3.1 Electrochemistry of $Ru(bpy)_3^{2+}$

Figure 7.9A shows the cyclic voltammogram of 0.5 mM $Ru(bpy)_3^{2+}$ in anhydrous acetonitrile using a 25 µm diameter platinum ultramicroelectrode at a scan rate of 20 mV/s. The cathodic scan shows three successive reductions of $Ru(bpy)_3^{2+}$ at formal potentials of −1.25 V, −1.45 V, and −1.65 V, while the anodic scan shows a single oxidation at a formal potential of +1.40 V. This matches up well with previously reported electrochemical studies for this ruthenium complex[16, 17]. In all these redox cases, a well-defined steady-state current can be observed, confirming diffusion-limited redox behaviour that is characteristic of electrochemistry with ultramicroelectrodes. Only the first reduction and oxidation of $Ru(bpy)_3^{2+}$ was selected for this study, thereby limiting the production of ECL to the simplest energy sufficient annihilation route involving the

interaction of $Ru(bpy)_3^{+\bullet}$ and $Ru(bpy)_3^{3+\bullet}$ to generate the excited state $Ru(bpy)_3^{2+*}$.[18] Potential steps of −1.35 V and +1.65 V (corresponding to the steady state current region) were used to generate the anionic and cationic radical species of $Ru(bpy)_3^{2+}$, respectively. The potential stepping program at the electrode surface was recreated using a unit step function (*flc1hs*, smoothed Heaviside function)[19], of which the input argument was a time-dependent sine wave. This resulted in a square wave whose minimum and maximum values could be controlled to desired potentials while simultaneously allowing the modulation of the periodic frequency (**Figure 7.9B**). We define here, at least in the context of this work, the pulsing frequency as the number of cathodic or anodic pulses over time; that is, a pulse frequency of 10 Hz corresponds to a pulse width of 100 msec. The corresponding simulated ECL profile, shown in the dotted trace, was then generated by integrating the excited state concentration (*me*) across the solution subdomain. Individual cathodic and anodic pulses were then extracted, and compared against the experimental ECL signals.

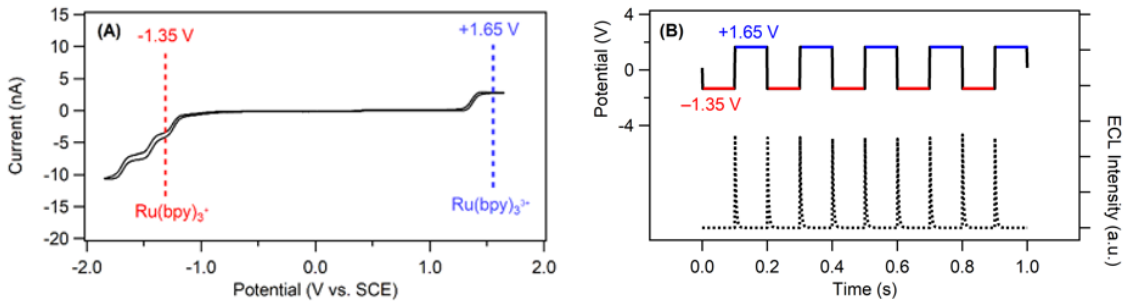

Figure 7.9. (A) Cyclic voltammogram of 0.5 mM $Ru(bpy)_3(PF_6)_2$ in acetonitrile with 0.1 M $TBAPF_6$ as supporting electrolyte at a platinum ultramicroelectrode with a diameter of 25 µm at a scan rate of 0.02 V/s. Indicated potentials represent reducing and oxidizing potentials for $Ru(bpy)_3^{2+}$ to generate the anodic and cathodic radical species. (B) Potential stepping vs. time program (solid) and corresponding simulated ECL profile (dotted).

Figure 7.10 shows a summary of the simulated $Ru(bpy)_3^{2+}$ annihilation ECL vs. time profiles; (A) and (B) displays the first cathodic and first anodic ECL transients when the electrode potential stepping frequency was 10 Hz, and (C) and (D) shows these ECL

transients at 100 Hz. The experimental data is plotted as coloured traces and the simulated data is plotted as dotted lines. In all four scenarios, there is a very good agreement between the two sets of data, which demonstrates that our simulation is capable of recreating all important features of the experimental signal, especially the sharp onset of the ECL peak, and the decay pattern as the excited states are consumed. The intensity of the ECL signal (both in terms of peak height and total counts) is significantly greater at lower frequencies, which may be due to the greater relative concentrations of radical species present in the vicinity of the electrode surface when the potential is switched. While the electrode is biased, the continuous generation of electrogenerated radicals causes the accumulation of these species in the area surrounding the electrode. Since the total injected charge is greater for lower frequency experiments, the enhancement in the local concentration of excited states results in the increased ECL intensity. These electrochemical insights are crucial when assessing the absolute quantum efficiency of ECL luminophores, which we have previously demonstrated in our work.[20, 21] It is evident that $Ru(bpy)_3^{2+}$, like most ECL luminophores, has an "ideal" potentiodynamic driving program which is highly dependent on radical diffusivity, stability, and reactivity.

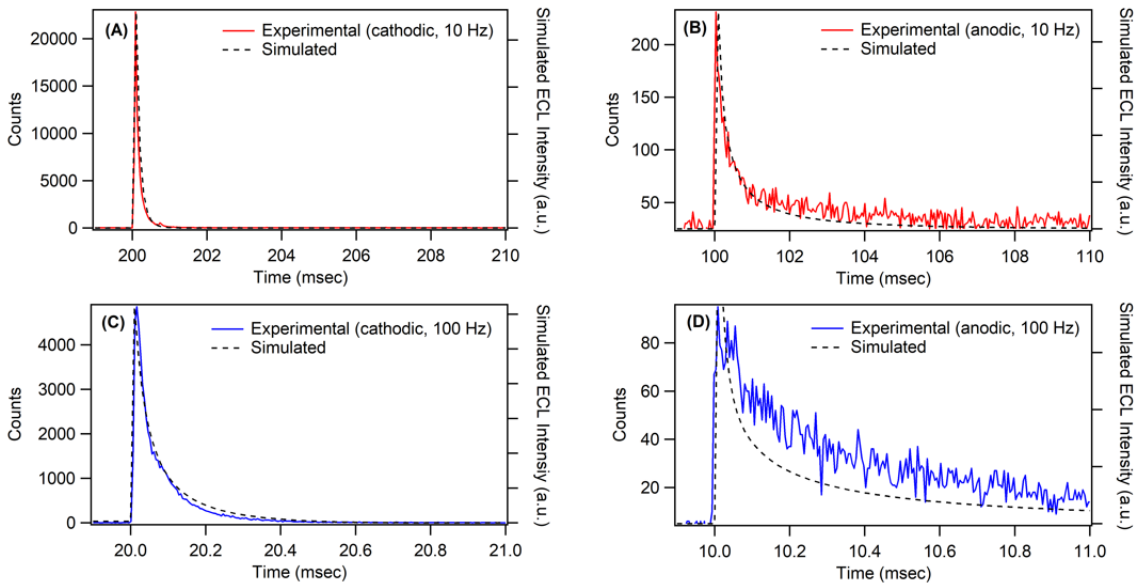

Figure 7.10. Comparison of experimental (coloured traces) and simulated (dotted traces) ECL transients of 0.5 mM $Ru(bpy)_3^{2+}$ via the annihilation pathway. (A) 10 Hz, cathodic

ECL peak, (B) 10 Hz, anodic ECL peak, (C) 100 Hz, cathodic ECL peak, (D) 100 Hz, anodic ECL peak. For 10 Hz experiments, the bin width was 40.96 µs and the bins per record was 10240. For 100 Hz experiments, the bin width was 5.120 µs and the bins per record was 9216. For all experiments, a total of 1000 records were collected.

It can also be observed that the intensity of the ECL signal is greater for the cathodic step for both 10 Hz and 100 Hz, which suggests a difference in the overall stability of radical cations and anions. This behaviour is not uncommon among ECL luminophores, where the donation and withdrawal of electron density may be localized on specific areas of the molecule, and are therefore subject to steric or electrostatic interference from adjacent ligands or groups.[15, 22, 23] While chemical structures are not explicitly defined in our simulation model, their nonetheless tangible effects on electrochemical oxidation and reduction can be indirectly described by two additional reactions which model the decay of the electrogenerated radicals of $Ru(bpy)_3^{2+}$; the rate constants for k_{o1} and k_{r1} are provided in **Table 7.2**. These reactions serve to modulate the concentrations of $Ru(bpy)_3^{+\bullet}$ and $Ru(bpy)_3^{3+\bullet}$ after they have been generated by a potential bias at the electrode, thereby defining the quantity of electroactive species available for reaction at any potential step $t > 0$. In our experiments, the greater relative intensity of the cathodic potential step suggests that the stability of the radical anion of $Ru(bpy)_3^{+}$ is greater than that of the radical cation $Ru(bpy)_3^{3+}$. This is reflected in the experimental data, as $Ru(bpy)_3^{+}$ is able to survive longer in solution to meet and with its electrochemical counterpart $Ru(bpy)_3^{3+}$ to generate excited states. This phenomenon of asymmetrical ECL transients has been observed for various ECL luminophores, including BODIPY and BODIPY-derivatives,[24, 25] iridium complexes,[26] and helicene compounds.[27]

The ECL transients were also simulated at pulsing frequencies of 1000 Hz and 10 kHz, shown in **Figure 7.11.** It can be observed that the simulated results have difficulty in accurately representing the experimental ECL data, particularly for the anodic ECL pulses. This is likely because the electron-transfer reactions to generate ECL excited states is highly diffusion-controlled, and the high frequency potential steps do not allow sufficient time for the concentration of electrogenerated radicals to equilibrate. Therefore,

this is a limitation of the computational model when simulating very high frequency potential pulsing.

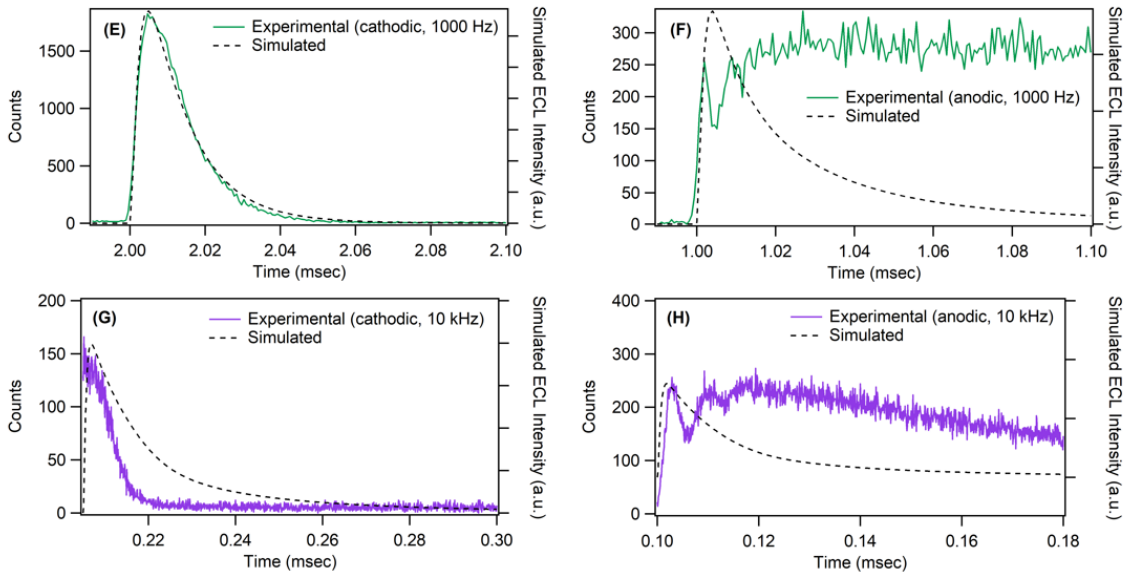

Figure 7.11. Comparison of experimental and simulated ECL transients. (E) 1000 Hz, cathodic ECL peak, (F) 1000 Hz, anodic ECL peak, (G) 10 kHz, cathodic, and (H) 10 kHz, anodic. For 1000 Hz experiments, the bin width = 640 ns, bins per record = 7168. For 10 kHz experiments, bin width = 40 ns, bins per record = 6144. For all experiments, a total of 1000 records were collected.

7.4 Conclusions

In conclusion, we have successfully simulated the $Ru(bpy)_3^{2+}$ ECL mechanism via the annihilation pathway using potential stepping at 10 Hz and 100 Hz in COMSOL Multiphysics software. Our simulation was effective in recreating all features of the ECL intensity vs. time profile. We envision that computer simulations such as the one described in this work will play an ever-increasing role in ECL characterization and studies, as many experimental factors (including the annihilation rate constant, emission rate constant, and the radical decay constants) can be easily found using software parameterization. These factors may be extremely significant in the characterization and research of newer, increasingly efficient ECL luminophores. We plan to investigate other

electrochemiluminescence systems, including the $Ru(bpy)_3^{2+}$/TPrA system, using our new computational model.

7.5 References

[1] Chandross, E. A.; Sonntag, F. I. *J. Am. Chem. Soc.* **1964,** *86*, 3179.

[2] Hercules, D. M. *Science* **1964,** *145*, 808-809.

[3] Santhanam, K. S. V.; Bard, A. J. *J. Am. Chem. Soc.* **1965,** *87*, 139-140.

[4] Collinson, M. M.; Wightman, R. M. *Anal. Chem.* **1993,** *65*, 2576-2582.

[5] Collinson, M. M.; Pastore, P.; Maness, K. M.; Wightman, R. M. *J. Am. Chem. Soc.* **1994,** *116*, 4095-6.

[6] Collinson, M. M.; Wightman, R. M. *Science* **1995,** *268*, 1883-5.

[7] Pastore, P.; Magno, F.; Collinson, M. M.; Wightman, R. M. *J. Electroanal. Chem.* **1995,** *397*, 19-26.

[8] Heinze, J. *Angew. Chem. Int. Ed.* **1993,** *32*, 1268-1288.

[9] Ying, Y.-L.; Ding, Z.; Zhan, D.; Long, Y.-T. *Chem. Sci.* **2017,** *8*, 3338-3348.

[10] Zhu, R.; Ding, Z. *Can. J. Chem.* **2005,** *83*, 1779-1791.

[11] Sahami, S.; Weaver, M. J. *J. Electroanal. Chem. Interfacial Electrochem.* **1981,** *122*, 155.

[12] SR430 Multichannel Scaler/Averager. https://www.thinksrs.com/downloads/pdfs/manuals/SR430m.pdf (accessed 2022-11-14).

[13] Bard, A. J.; Faulkner, L. R.; White, H. S., *Electrochemical Methods: Fundamentals and Applications*. 3rd ed.; Wiley: 2022; p 1104.

[14] Wightman, R. M.; Forry, S. P.; Maus, R.; Badocco, D.; Pastore, P. *J. Phys. Chem. B* **2004,** *108*, 19119-19125.

[15] Shen, M.; Rodríguez-López, J.; Huang, J.; Liu, Q.; Zhu, X.-H.; Bard, A. J. *J. Am. Chem. Soc.* **2010,** *132*, 13453-13461.

[16] Rodríguez-López, J.; Shen, M.; Nepomnyashchii, A. B.; Bard, A. J. *J. Am. Chem. Soc.* **2012,** *134*, 9240-9250.

[17] Tokel-Takvoryan, N. E.; Hemingway, R. E.; Bard, A. J. *J. Am. Chem. Soc.* **1973,** *95*, 6582.

[18] Richter, M. M. *Chem. Rev.* **2004,** *104*, 3003-36.

[19] Davies, B., *Integral Transforms and Their Applications*. 3 ed.; Springer: New York, 2002.

[20] Chu, K.; Adsetts, J. R.; Ma, J.; Zhang, C.; Hesari, M.; Yang, L.; Ding, Z. *J. Phys. Chem. C* **2021,** *125*, 22274-22282.

[21] Adsetts, J. R.; Chu, K.; Hesari, M.; Ma, J.; Ding, Z. *Anal. Chem.* **2021,** *93*, 11626-11633.

[22] Hesari, M.; Ding, Z. *J. Am. Chem. Soc.* **2021,** *143*, 19474-19485.

[23] Hesari, M.; Ding, Z. *Chem. Eur. J.* **2021,** *27*, 14821-14825.

[24] Sartin, M. M.; Camerel, F.; Ziessel, R.; Bard, A. J. *J. Phys. Chem. C* **2008,** *112*, 10833-10841.

[25] Suk, J.; Omer, K. M.; Bura, T.; Ziessel, R.; Bard, A. J. *J. Phys. Chem. C* **2011,** *115*, 15361-15368.

[26] Yang, L.; Adsetts, J. R.; Zhang, R.; Balónová, B.; Piqueras, M. T.; Chu, K.; Zhang, C.; Zysman-Colman, E.; Blight, B. A.; Ding, Z. *J. Electroanal. Chem.* **2022,** *906*, 115891.

[27] Li, H.; Voci, S.; Wallabregue, A.; Adam, C.; Labrador, G. M.; Duwald, R.; Hernández Delgado, I.; Pascal, S.; Bosson, J.; Lacour, J.; Bouffier, L.; Sojic, N. *ChemElectroChem* **2017,** *4*, 1750-1756.

Chapter 8

In this chapter, we explore light emitting electrochemical cells (LECs) constructed using graphene quantum dots. We discuss the characterization and testing towards the electroluminescence performance of these luminophores.

8 Electrogenerated chemiluminescence and Electroluminescence of N-Doped Graphene Quantum Dots Fabricated from an Electrochemical Exfoliation Process in Nitrogen-Containing Electrolytes[†]

Artificial lighting sources are one of the most important technological developments for our modern lives; the search for cost-effective and efficient luminophores is therefore crucial to a sustainable future. Graphene quantum dots (GQDs) are carbon-based nanomaterials that exhibit exceptional optical and electronic properties, making them a prime candidate for a luminophore in a light-emitting device. GQDs made from a facile top-down electrochemical exfoliation process in this report showed strong photoluminescent emission at 450 nm, and electrogenerated chemiluminescence at 660 nm in the presence of BPO as a coreactant. When introduced into solid-state light-emitting electrochemical cells, for the first time, the GQDs displayed a broad white emission centered at 610 nm, corresponding to *Commision Internationale de l'eclairage* (CIE) colour coordinates of 0.38 and 0.36.

8.1 Introduction

Graphene quantum dots (GQDs) are a class of zero-dimensional carbon-based nanomaterials, characterized by a lateral size of typically 10 nm or less, with a well-defined crystal lattice.[1-5] Due to their tunable photoluminescence, high stability, and low toxicity, GQDs have numerous applications in a wide variety of research areas ranging

---

[†] This work has been published. Chu, K.; Adsetts, J.; He, S.; Zhan, Z.; Yang, L.; Wong, J.; Love, D.; Ding, Z. Electrogenerated Chemiluminescence and Electroluminescence of N-doped Graphene Quantum Dots Fabricated from an Electrochemical Exfoliation Process in Nitrogen-Containing Electrolytes. *Chem. Eur. J.* (**2020**) 26, 15892-15900.

from bioimaging, sensors, energy storage, photovoltaics, to catalysis.[2, 6-12] GQDs have a very high surface area to volume ratio, which allows their surfaces to be readily functionalized with various organic or biological species, further increasing their versatility.[13] Heteroatom doping involves the addition of one or more novel elements into the GQD lattice, permitting the tuning of many physical and structural properties.[14, 15] In general, synthesis of GQDs can be classified in one of two categories: top-down, where the nano-sized particles are fragmented off of a larger bulk structure; and bottom-up, where the GQDs are built up from smaller molecular precursors.[16] Top-down methods often utilize readily available and low-cost carbon sources as starting materials, significantly reducing the production cost of GQDs. In summary, GQDs represent an extremely versatile nanomaterial that continues to expand in applications and scope every year.

Electrogenerated chemiluminescence or electrochemiluminescence (ECL) is a process where radical species generated at electrode surfaces undergo electron transfer reactions to form excited states, that can subsequently emit light.[17, 18] There are two general pathways by which ECL can occur.[18] The first is ion annihilation, where the anionic and cationic radical luminophore species generated by reduction and oxidation at the electrode, respectively, interact to produce excited states. The second is the coreactant pathway, which involves the use of a secondary compound known as a coreactant. Upon reduction or oxidation, coreactants produce radical species that can interact with the luminophore of interest to produce excited states. Due to the high redox power of these radicals, ECL generated via the coreactant pathway is often enhanced compared to the annihilation route.[19] ECL has been widely used in many applications including immunoassays and analyte detection due to its high sensitivity and wide dynamic range.[20-26] ECL has also been reported in several light-emitting applications, where solid-state devices utilizing traditional ECL luminophores exhibited highly efficient, low-voltage operation.[27-30]

The first example of a polymer light-emitting electrochemical cell (LEC) was introduced in 1995.[31] Unlike traditional LEDs that often require many electron and hole transport layers, LECs typically consist of a single light-emitting layer containing both the

luminophore (normally a polymer) and electrolyte sandwiched between an anode and a cathode.[32-34] In addition, LECs are relatively insensitive to electrode work functions, enabling the use of air-stable materials.[32, 35] These attributes greatly reduce the cost and complexity of LECs, making them a very attractive candidate for complimenting or replacing existing light-emitting technology. In particular, white light-emitting sources are among the most sought after in the lighting industry: homes and offices, automobiles and the transportation sector, and commercial electronic devices using LCD screens are all examples from modern society that would benefit from cost-effective, efficient white light-emitting luminophores.

Herein, the synthesis and characterization of top-down GQDs are described, and the photoluminescent properties of the GQDs are reported. ECL of the GQDs from the annihilation and coreactant pathways is revealed, and spooling ECL spectroscopy is used to analyze the excited states responsible for the observed emissions. Finally, the properties and performance of novel GQD-based white-emitting LECs is discussed.

8.2 Experimental

8.2.1 Chemicals and reagents

Electrochemical grade acetonitrile (ACN, 99.8%, SureSeal) was purchased from Sigma-Aldrich Canada, Mississauga, Ontario and stored in an N_2-filled glovebox. ECL coreactants used were tri-*n*-propylamine (TPrA, >98%, Sigma-Aldrich Canada) and benzoyl peroxide (BPO, reagent grade, >98%, Sigma-Aldrich). The supporting electrolyte was tetrabutylammonium perchlorate (TBAP, electrochemical grade, >99.0%, Sigma-Aldrich). Ferrocene (Fc, 98%, Sigma-Aldrich) was used as an internal standard for potential calibrations. All chemicals were used and stored at room temperature except TPrA which was stored at 4°C.

8.2.2 Top-down electrochemical exfoliation

Graphene quantum dots were produced via a top-down electrochemical exfoliation process, where a constant current was passed through a graphite rod working electrode (Sigma-Aldrich) and a platinum plate counter electrode (Tianjin Aida, China). 0.1 M of

tetrabutylammonium perchlorate was used as the supporting electrolyte dissolved in the anhydrous acetonitrile. The current was provided by a Keithley 2400 SMU from Tektronix (Oregon, United Sates), which simultaneously recorded the corresponding potential. The resulting suspension was filtered through a 0.2 μm polytetrafluoroethylene (PTFE) filter before being dialyzed for 24 hours in ultrapure water using a cellulose ester dialysis bag with a molecular weight cut-off of 1000 Da (Spectra/Por Biotech, China). The final product was dried in a freeze-drier and redispersed in solvent for characterization.

8.2.3 Absorption and photoluminescence spectroscopy

Photoluminescence (PL) measurements were taken using a luminescence spectrometer (PTI Fluorolog, QM7/2005, London, ON) with excitation and emission slit widths set to 0.25 mm, integration time set to 0.1 s, and step size set to 0.25 nm. Absorbance measurements were measured using a UV-visible spectrometer (Varian Cary UV Bio-50). The quartz cuvette used had a path length of 1 cm. The PL quantum yield was calculated by comparing integrated PL intensities (λ_{ex} = 370 nm) and absorbance (λ_{abs} = 370 nm) of a GQD sample with a quinine sulfate reference, whose $\Phi = 0.54$.[36] PL signals were integrated using the cumulative trapezoidal method in MATLAB. Quantum yields were calculated using the following equation, where *m* is the slope, η is the refractive index of the solvent used, *x* is the sample, and *st* is the standard.

$$\Phi_x = \Phi_{St}\left(\frac{m_x}{m_{St}}\right)\left(\frac{\eta^2{}_x}{\eta^2{}_{St}}\right)$$

Equation 8.1

8.2.4 X-ray photoelectron spectroscopy (XPS)

The XPS analyses were carried out with a Kratos AXIS Supra spectrometer using a monochromatic Al K(alpha) source (15mA, 15kV). The instrument work function was calibrated to give a binding energy (BE) of 83.96 eV for the Au 4f7/2 line for metallic gold and the spectrometer dispersion was adjusted to give a BE of 932.62 eV for the Cu 2p3/2 line of metallic copper. The Kratos charge neutralizer system was used on all

specimens. Survey scan analyses were carried out with an analysis area of 300 x 700 microns and a pass energy of 160 eV. High resolution analyses were carried out with an analysis area of 300 x 700 microns and a pass energy of 20 eV. Spectra have been charge corrected to the main line of the carbon 1s spectrum (adventitious carbon) set to 285.0 eV. Spectra were analyzed using CasaXPS software.

8.2.5 Electrochemistry and electrochemiluminescence

A three-electrode system was used for all electrochemical measurements, where a 2 mm platinum disc inlaid in a soft glass tube served as the working electrode (WE), and two coiled platinum wires were the counter and quasi-reference electrodes. All electrochemical analyses were performed in a glass cylinder with a flat quartz window at the bottom to allow for the detection of ECL. The experimental potentials were calibrated using ferrocene as the internal standard, with the redox potential of the Fc/Fc^{+} couple taken as 0.400 V vs. SCE.[37]

Electrochemical experiments were carried out using a CHI610a electrochemical workstation (CH Instruments, Austin, TX). Voltammetric ECL curves were obtained by correlating the applied potential to the ECL intensity from a photomultiplier tube (PMT, Hamamatsu, Model R928, Japan) biased at −750 V. The photocurrent as the ECL intensity from the PMT was transmitted to a Keithley 6487 picoammeter/voltage source (Keithley, Cleveland, OH) where it was converted to a voltage signal for data acquisition. All ECL, current and applied potential signals were sent to a computer through a data acquisition board (DAQ 6036E, National Instruments, NI, Austin TX) and recorded using a custom NI LabVIEW program. ECL efficiencies were obtained by calculating the ratio of integrated ECL intensity to charge, relative to $Ru(bpy)_3^{2+}$ systems.

ECL spectra were collected using a spectrometer (Acton 2300i, Princeton Instruments, Trenton, NJ) and an attached CCD camera (Model DV420-BV, Andor Technology, Belfast, UK) cooled to −65°C. Wavelength calibration was performed using a mercury-argon lamp (Ocean Optics, HG-1). Spooling ECL spectra were acquired each at a time interval of 1 or 2 s during a potential scanning process. The obtained spectra were spooled together in a plot using a custom MATLAB program.

8.2.6 LEC fabrication and testing

ITO-banded glass was purchased from Jinghui Electronic Technologies Ltd, China. Prior to use, they were sonicated in solutions of 2% Hellmanex, ultrapure Milli-Q water, isopropyl alcohol, and 10% NaOH successively for 15 minutes each, before being dried at 85°C. Poly(3,4-ethylenedioxythiophene) polystyrene sulfonate (2.8% PEDOT:PSS, Sigma-Aldrich) was filtered using a 0.1 μm PVDF (polyvinylidene fluoride) syringe filter and diluted in a 1:1 ratio using isopropyl alcohol. The emitter solution was prepared by mixing solutions of GQDs, TMPE (trimethylolpropane ethoxylate), and LiTf (lithium trifluoromethanesulfonate) to a final mass ratio of 1:0.5:0.03 mg/mL in tetrahydrofuran (THF). The PEDOT:PSS and emitter solutions were sequentially deposited onto the ITO-banded glass using a Laurell Technologies spin-coater (Model WS-400B-6NPP/LITE), with 50 μL loading volume, at 6000 rpm for 60 seconds. The Al-doped ZnO layer was deposited using a Savannah Thermal atomic layer deposition system (ALD, Cambridge Technologies, Cambridge, MA). Aluminum electrodes with a thickness of approximately 130 nm were deposited using a Plasmionique thermal evaporator (Montreal, QC).

LEC testing was performed using a Keithley 2400 as the power source, with the ITO electrode connected as the cathode and the aluminum electrode connected as the anode. Photocurrent as the electroluminescence (EL) intensity from the LEC was measured using a Hamamatsu R928 photomultiplier tube biased at −750 V. The EL, current and applied potential signals of the LEC devices were recorded using a NI myDAQ acquisition device, connected to a computer running a custom LabVIEW program.

8.3 Results and discussion

8.3.1 Characterization of top-down graphene quantum dots

Graphene quantum dots (GQDs) were synthesized using a top-down electrochemical exfoliation process, where the nano-sized particles were electromechanically fragmented from a graphite rod working electrode. A constant current was applied to the working electrode, causing the intercalation of electrolyte ions into the graphite lattice, similar to our previous report on preparation of GQDs by means of multiwalled carbon nanotube electro-exfoliation with the potentiodynamic method.[1] In total, four different current

densities were tested: 4, 20, 40, and 80 mA/cm^2 (hereafter GQD-4, GQD-20, GQD-40, and GQD-80 assigned to the corresponding dots, respectively), and the resulting GQDs were purified and characterized. The current densities were calculated from the current applied and the total surface area of the graphite electrode that was immersed in the electrolyte solution.

Low-magnification TEM images of the GQDs prepared from a water dispersion (**Figure 8.1A**) reveal that the quantum dots are roughly disk shaped with an average diameter of 8.6 ± 1.0 nm (**Figure 8.1B**). High-resolution (HR-TEM) images show the GQDs have a clearly defined graphitic structure with an interplanar spacing of 0.21 nm, which corresponds well to the (11$\bar{2}$0) lattice planes of graphene.[38, 39]

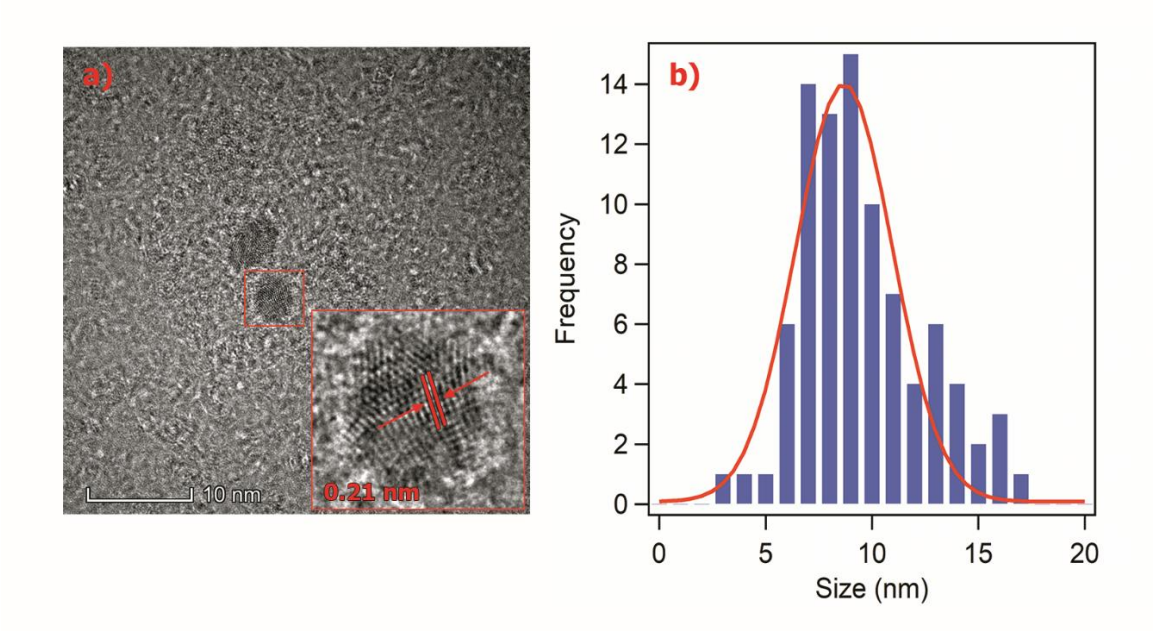

Figure 8.1. (A) Low-magnification TEM image of electrochemically prepared GQDs. Inset is an expanded high-resolution TEM image, showing the lattice structure. (B) Particle size distribution histogram with the data fitted using a Gaussian distribution function. Particle size was determined by FIJI image processing software, by comparison of the attached scale bar with at least 50 individual dots.

Next, the surface composition of the GQDs was analyzed using X-ray photoelectron spectroscopy (XPS). The XPS survey scan (**Figure 8.2A**) has three significant peaks at

281.00, 395.00, and 527.00 eV, showing the presence of carbon (79.7 at%), nitrogen (9.9 at%), and oxygen (9.3 at%), respectively. The high-resolution C_{1s} spectrum (**Figure 8.2B**) depicts the presence of primarily C-C/C-H bonds (285.00 eV), along with C-OH/C-O-C (286.50 eV) and C=O bonds (287.80 eV), indicating that the surface of the GQDs has a variety of oxygen-containing functional groups, which are likely formed from the oxidation of graphite during the exfoliation process.[40] The assignment is confirmed by the high-resolution O_{1s} spectrum in **Figure 8.2C**. The high-resolution N_{1s} XPS spectrum (**Figure 8.2D**) shows the presence of C-N, O=C-N, and aromatic N, indicating the successful incorporation of nitrogen into the graphene quantum dot structure. These functional groups allow the GQDs to be dispersible in aqueous medium.[41, 42]

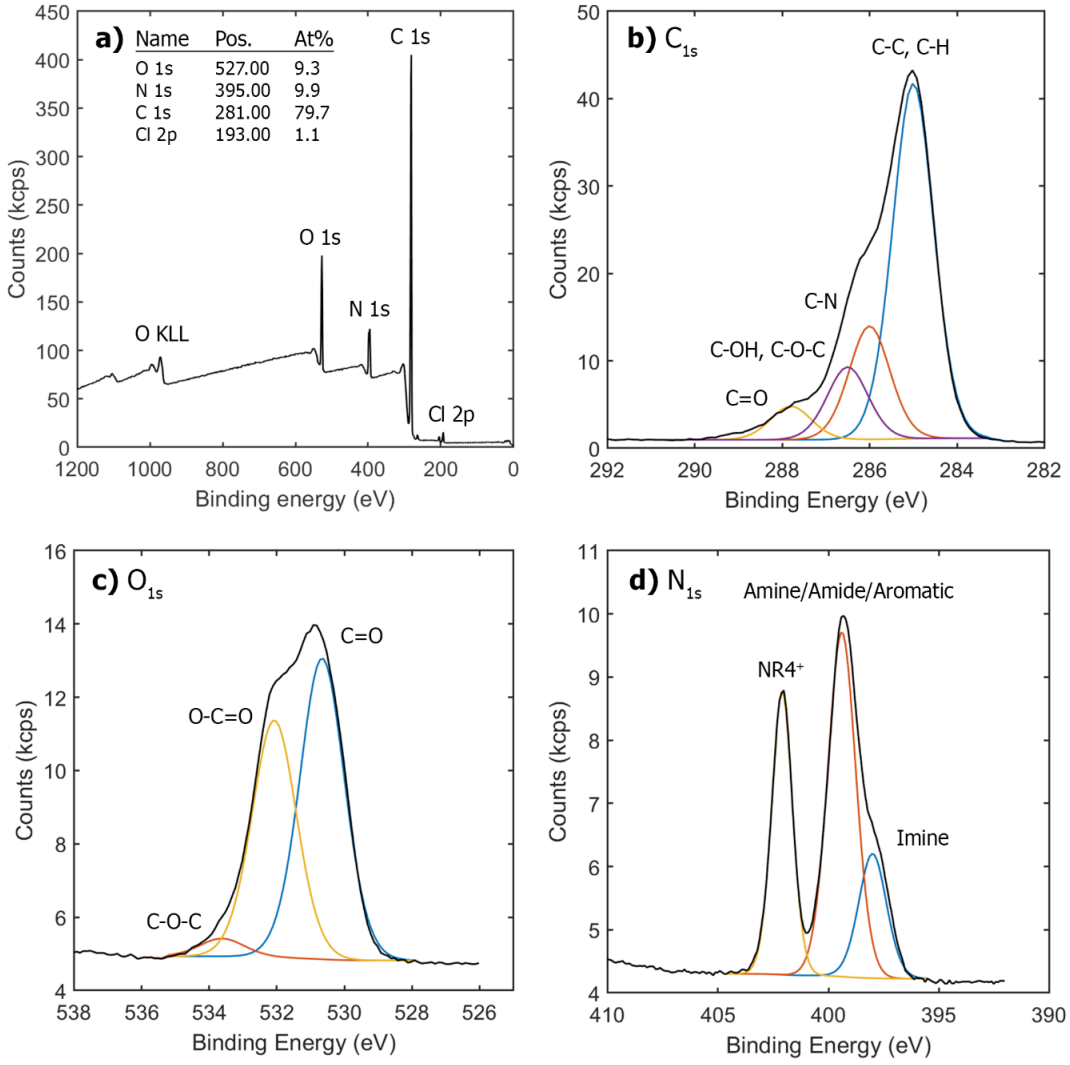

Figure 8.2. (A) XPS survey scan and high-resolution XPS spectra of (B) C1s, (C) O1s, and (D) N1s for GQD-40.

The photoluminescence properties of the GQDs were tested in water. All samples showed good dispersibility, with concentrations of approximately 0.1 mg/mL appearing faint yellow under daylight and light blue under ultraviolet (UV) illumination (inset in **Figure 8.3A**). The absorbance spectrum of the GQDs showed no obvious absorption peaks, while the PL excitation and emission maxima were 370 and 450 nm, respectively (**Figure 8.3A**). The GQDs also exhibited excitation-dependent emission (**Figure 8.3B**), which is commonly observed in luminescent carbon nanomaterials.[43-45] This behaviour is very

interesting, likely due to the variability in the sizes of the GQDs, as quantum confinement causes the bandgap energy of nanostructures to change as a function of their sizes.[46] Except for GQD-4, the photoluminescence quantum yields (PLQY) for the GQD samples ranged from 4-5% relative to a quinine sulfate standard (**Table 8.1** and **Figure 8.4**). The similarity of the quantum yields suggests that the overall structure of the GQDs is very similar regardless of the applied current density. Of these samples, GQD-40 showed the highest PLQY at 5.1%, and all further characterization will be specific to this sample.

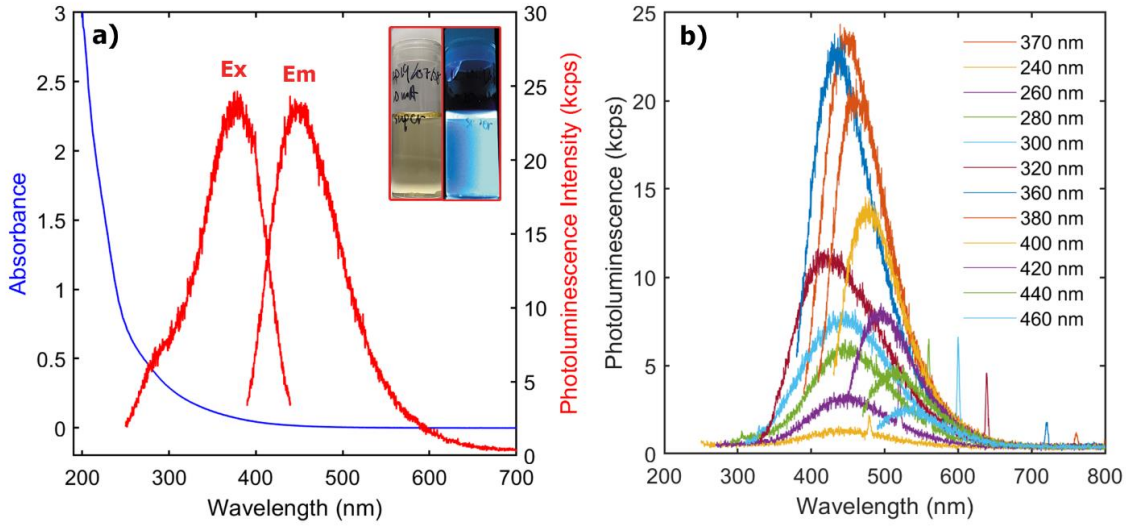

Figure 8.3. (A) UV-visible absorption (blue trace) and photoluminescence excitation and emission spectra (red trace) of top-down GQDs. Left and right insets show GQDs dispersed in water viewed under daylight and UV light, respectively. (B) Photoluminescence spectra of GQDs at different excitation wavelengths.

Table 8.1. Photoluminescence quantum yields (PLQY) for GQDs prepared at various current densities.

	Quinine sulfate	GQD-4 (4 mA/cm^2)	GQD-20 (20 mA/cm^2)	GQD-40 (40 mA/cm^2)	GQD-80 (80 mA/cm^2)
Quantum yield	54.0	1.9	4.6	5.1	4.2

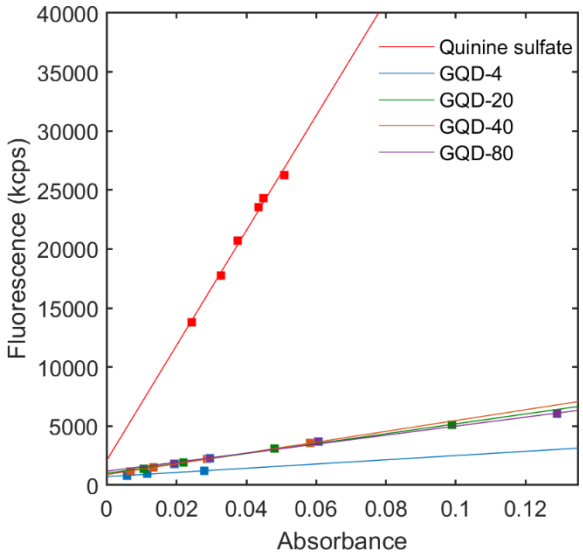

Figure 8.4. Correlation of photoluminescence intensity to absorbance of GQD samples and a 0.1 mM quinine sulfate solution.

The electrochemical exfoliation procedure described here has advantages for the production of GQDs as it is highly scalable, low-cost, and allows a high degree of control over the properties of the final product. By controlling the amount of current, the rate of the exfoliation process may be tuned, and the most efficient experimental conditions selected.

8.3.2 Electrochemistry and electrochemiluminescence of top-down graphene quantum dots

The electrochemistry of the GQDs was investigated next. **Figure 8.5A** demonstrates the differential pulse voltammograms (DPVs) of 0.3 mg/mL of GQDs dispersed in anhydrous acetonitrile. When the potential was cathodically scanned, there was a reduction peak at −0.80 V, which may be due to the reduction of oxygen-containing functional groups on the GQDs.

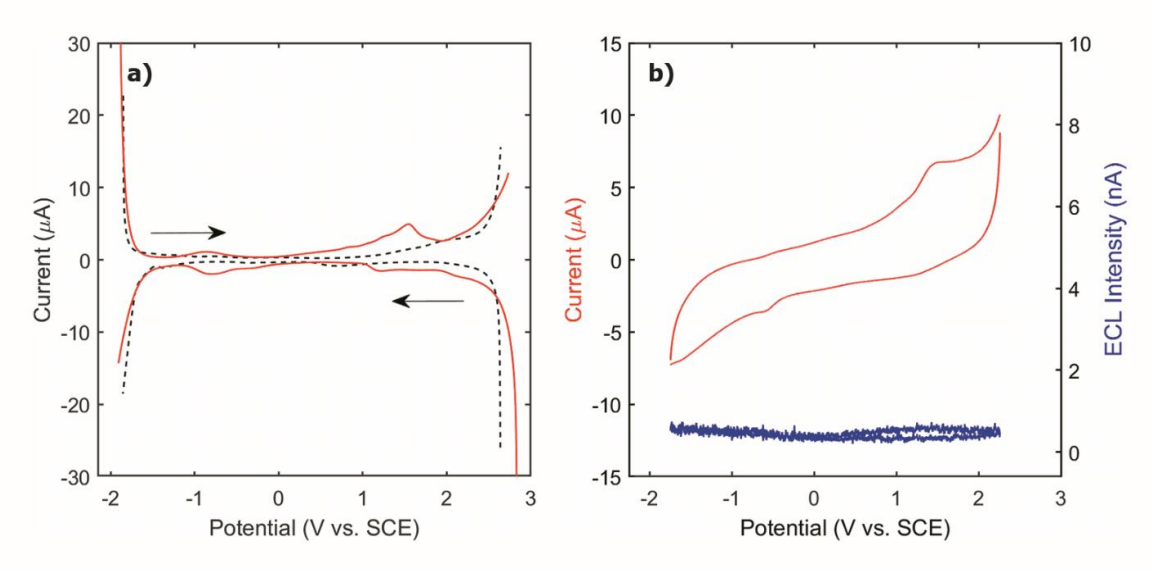

Figure 8.5. (A) Differential pulse voltammograms (DPVs) of GQDs in acetonitrile (red trace). Blank experiment is shown in the dotted black trace. The arrows indicate the initial scan direction. (B) Cyclic voltammogram (CV) and the corresponding ECL voltage curve for GQDs in the annihilation pathway.

When the potential was anodically scanned, there were two oxidation peaks observed at 1.2 V and 1.6 V, which is attributed to the oxidation of these same groups. **Figure 8.5B** shows the cyclic voltammogram (CV) and corresponding ECL voltage curve for the GQDs in the annihilation pathway. No appreciable ECL was recorded, which suggests that the GQD radical anionic and cationic species may be unstable or very short-lived, and unable to undergo efficient electron transfer in the vicinity of the working electrode to produce excited states.

Two coreactant-GQD systems were then explored to see if the ECL could be enhanced. **Figure 8.6A** shows the ECL of the GQDs with the addition of 5 mM benzoyl peroxide (BPO). We observe first the reduction of BPO to $BPO^{\bullet-}$, a species that subsequently decomposes to form the benzoate radical, a strong oxidizing agent. This species is capable of oxidizing GQDs to form GQD radical cations. $BPO^{\bullet-}$ itself may act as a reducing agent, injecting an electron into the LUMO of GQD radical cations, forming the excited state; relaxation of GQD* results in the emission of a photon (**Figure 8.7**). The

ECL onset potential is approximately −1.5 V, which is slightly more negative than the reduction potential of BPO; this suggests that the reduction of $GQD^{\bullet+}$ by the benzoate radical is the rate-controlling step in the ECL production. This may be due to the fact that the benzoate radical is a very strong oxidizing agent ($E°_{benzoate}$ = 1.5 V vs. SCE)[47], and can readily accept an electron from the GQD species. However, $BPO^{\bullet-}$ is a transient species, and requires time to accumulate in sufficient concentrations for reduction of $GQD^{\bullet+}$ to occur. A maximum of approximately 700 nA of photocurrent was recorded with the GQD-BPO pathway. In contrast, the direct electron transfer between $GQD^{\bullet-}$ and $GQD^{\bullet+}$ to produce ECL is unlikely, probably due to the relative instability of the $GQD^{\bullet+}$ radical species. The overall ECL efficiency of the GQD-BPO coreactant system was determined to be 1.2% relative to $Ru(bpy)_3^{2+}$.

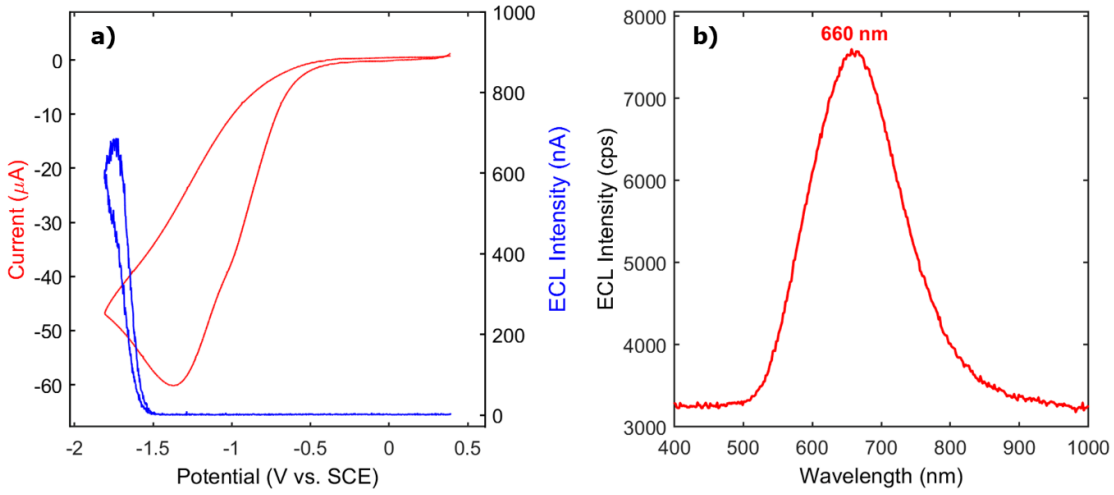

Figure 8.6. (A) Cyclic voltammograms and ECL voltage curves of 1 mg/mL GQDs in acetonitrile with 0.1 M TBAP in the presence of 5 mM BPO. (B) Accumulation ECL spectrum of the GQD-BPO coreactant system.

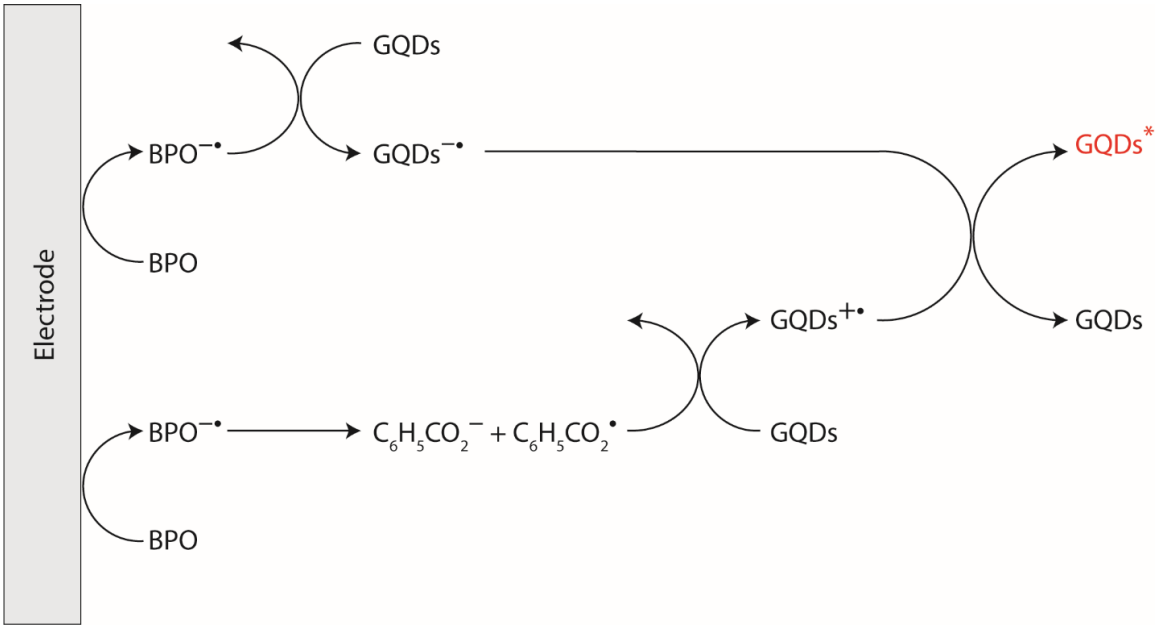

Figure 8.7. The proposed GQD-BPO ECL coreactant mechanism.

Figure 8.8 presents the spooling ECL spectra of the GQD-BPO coreactant system, which illustrates how the ECL signal changes during a potential scan. As the applied potential is moved to more negative values, we see the evolution (red) and devolution (blue) of the ECL signal. The figure inset shows the overlapped traces; there is one peak located at 660 nm, suggesting that a single excited state is responsible for the ECL emission.

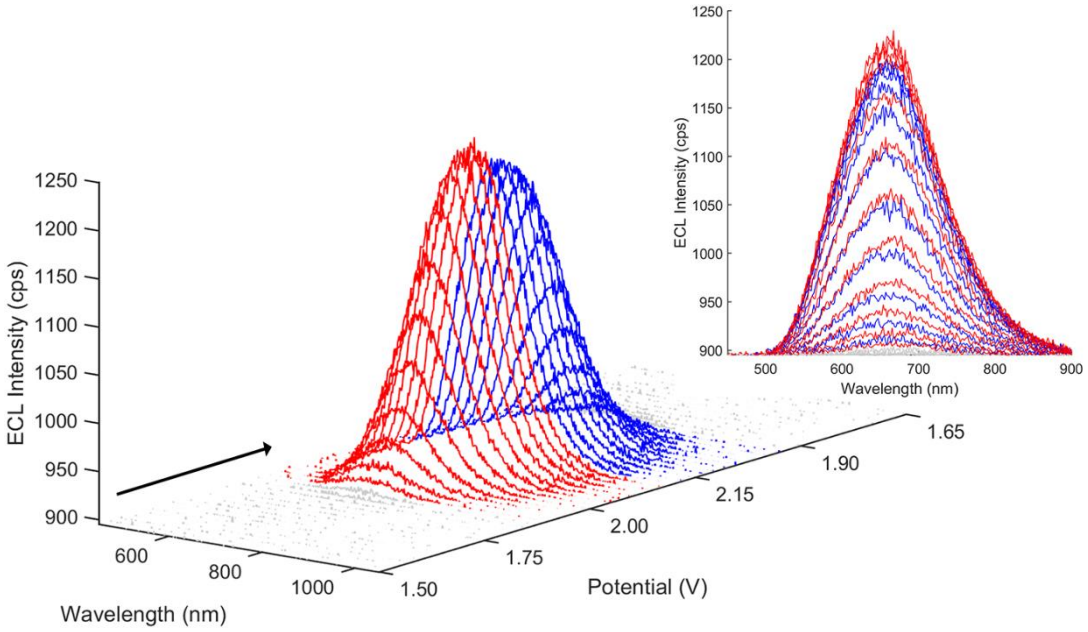

Figure 8.8. ECL spooling spectra of GQDs with 5 mM BPO. Scan rate was 0.1 V/sec. Red traces show spectra before emission maximum. Blue traces are spectra after emission maximum. Inset shows overlapped spectra.

The ECL of the GQDs with 5 mM TPrA was also tested (**Figure 8.9**). A maximum of approximately 5 nA of photocurrent was observed, which is significantly weaker than the ECL from the BPO coreactant system, **Figure 8.9A**. This is likely because of the instability of the $GQD^{\bullet+}$ radical species, as it cannot undergo efficient electron transfer with $TPrA^{\bullet}$ to produce excited states for ECL. The relative ECL efficiency of the GQD-TPrA system was determined to be 0.01%. An accumulation ECL spectrum was collected, where an emission peak at 650 nm was observed, **Figure 8.9B**. This is very similar to the emission seen in the BPO coreactant system, suggesting that the same GQD excited state is present here.

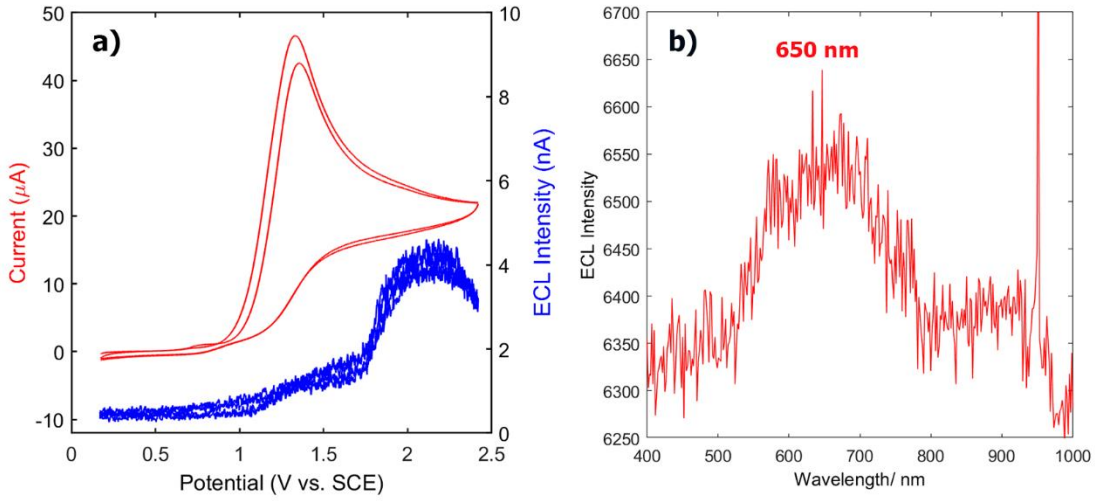

Figure 8.9. (A) Cyclic voltammograms and voltammetric ECL curves of 1 mg/mL GQDs in acetonitrile with 5 mM TPrA. (B) Accumulation ECL spectrum of the GQD-TPrA coreactant system.

8.3.3 GQD-based light-emitting electrochemical cells

The GQDs were then incorporated into the light-emitting layer of sandwich-type LECs (the schematic of the LECs is shown as an inset in **Figure 8.10A**). When the applied potential between the ITO and aluminum electrodes was slowly increased (**Figure 8.10A**), significant current began to flow at approximately 3 V, although no electroluminescence was observed until the potential had increased to 7 V. This delay between the onset of current flow and the onset of photocurrent is consistent with the electrochemical doping model (ECD) of LECs, where the formation of the luminescent p-i-n junction is preceded by the injection of electrons and holes at the anode and cathode, respectively.[48] Once the p-n junction is formed, subsequent injected charges recombine radiatively in the insulating region, leading to the emission of light via electroluminescence. The EL intensity increased steadily from the onset potential, reaching a maximum of 800 nA at 12.5 V. The luminous efficiency of the GQD-LEC was calculated to be 0.14% relative to a $Ru(bpy)_3^{2+}$ standard in the annihilation pathway. When a constant current of 1 mA was used to drive the LEC (**Figure 8.10B**) a gradual increase in both the potential and electroluminescence intensity was observed, indicating

that the resistance between the electrodes is decreasing as device operation continues, and the luminescent junction may not be particularly stable. After approximately 20 minutes of continuous operation, a large increase in the operating voltage was observed, suggesting that a short-circuit occurred. **Figure 8.10C** shows a 120 second accumulation spectrum of the GQD-LECs during a constant current experiment, where a broad peak centered at approximately 610 nm can be seen. This signal is attributed to the emission of light from the radiative recombination of excitons between oxidized and reduced GQD species in the luminescent junction of the LECs. This emission is quite similar to that observed during ECL, which suggests some similarity between these two mechanisms. This indicates that ECL may be a valuable analytical technique for predicting the emissive behaviour of novel luminophores in solid-state light emitting devices. The figure inset shows a colour photograph of the LEC during operation. The *Commision Internationale de l'eclairage* (CIE) coordinate diagram of the spectrum is displayed in **Figure 8.10D**, where a balanced, white emission is observed (colour coordinates of x=0.38, and y=0.36).

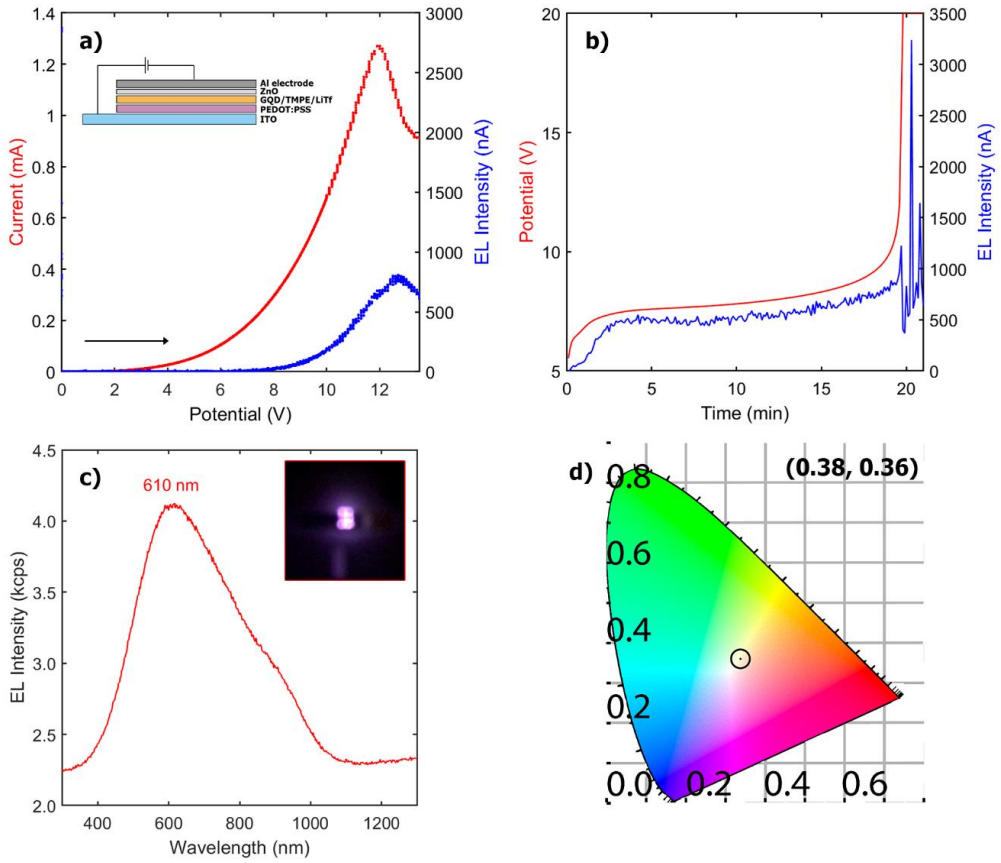

Figure 8.10. (A) A linear voltage sweep of the GQD-based LECs. Inset is a schematic of the LEC device showing the individual layers (not to scale). (B) 1 mA constant current experiment. (C) 120 second accumulation spectrum. Original spectrum is shown as a dotted black line, which was curve fitted using a Gaussian distribution function. The inset shows a colour photograph of the LEC during operation. (D) CIE (*Commision Internationale de l'eclairage)* 1931 coordinate colour diagram of GQD-LEC emission.

GQD-based luminophores can be a very promising alternative for existing light-emitting technology. As shown here, they can be easily incorporated into few-layer solid-state light emitting devices by solution-based processing, which decreases device manufacturing complexity and cost. In particular, the GQD's ability to natively emit white light provides them many advantages. Currently, most white LEDs mix two or more monochromatic sources, which decreases their overall luminous efficiency because of the additional light sources required.[49, 50] Having a single source capable of supplying white light should result in significantly enhanced device efficiencies.

8.4 Conclusions

Graphene quantum dots were synthesized using an electrochemical exfoliation process, a top-down method for their preparation from graphite rods. The presence of N-containing functional groups was confirmed using XPS analysis. The GQDs were found to have PL emission at 450 nm, with a photoluminescent quantum yield of 5%. No ECL was observed from the GQDs in the annihilation pathway. With the addition of 5 mM BPO as coreactant the ECL was enhanced to 700 nA with a relative efficiency of 1.2%. Spooling ECL spectroscopy was used to confirm the existence of a single excited state responsible for emission at 660 nm in the whole ECL process. When the GQDs were utilized in the light-emitting layer of LECs, balanced white electroluminescence at centered at 600 nm was observed for the first time upon the application of electricity. The first batch of the LECs work well, although the relative EL efficiency of 0.14% is to be improved.

8.5 References

[1] Zhou, J.; Booker, C.; Li, R.; Zhou, X.; Sham, T.-K.; Sun, X.; Ding, Z. *J. Am. Chem. Soc.* **2007,** *129*, 744-745.

[2] Gao, F.; Liu, F.; Bai, X.; Xu, X.; Kong, W.; Liu, J.; Lv, F.; Long, L.; Yang, Y.; Li, M. *Carbon* **2019,** *141*, 331-338.

[3] Tajik, S.; Dourandish, Z.; Zhang, K.; Beitollahi, H.; Le, Q. V.; Jang, H. W.; Shokouhimehr, M. *RSC Adv* **2020,** *10*, 15406-15429.

[4] Li, M.; Chen, T.; Gooding, J. J.; Liu, J. *ACS Sens.* **2019,** *4*, 1732-1748.

[5] Yuan, F.; Ding, L.; Li, Y.; Li, X.; Fan, L.; Zhou, S.; Fang, D.; Yang, S. *Nanoscale* **2015,** *7*, 11727-33.

[6] Zhang, R. Z.; Ding, Z. F. *J. Anal. Test.* **2018,** *2*, 45-60.

[7] Yuan, F.; Li, S.; Fan, Z.; Meng, X.; Fan, L.; Yang, S. *Nano Today* **2016,** *11*, 565-586.

[8] Chung, S.; Revia, R. A.; Zhang, M. *Adv Mater* **2021,** *33*, e1904362.

[9] Liu, Q. W.; Sun, J. H.; Gao, K.; Chen, N.; Sun, X. T.; Ti, D.; Bai, C. C.; Cui, R. R.; Qu, L. T. *Mater. Chem. Front.* **2020,** *4*, 421-436.

[10] Wang, S. C.; Li, Z. J.; Xu, X. P.; Zhang, G. J.; Li, Y.; Peng, Q. *Adv. Mater. Inter.* **2019,** *6*, 1801480.

[11] Chen, Y.; Cao, Y.; Ma, C.; Zhu, J. J. *Mater. Chem. Front.* **2020,** *4*, 369-385.

[12] Chen, A.; Liang, W.; Wang, H.; Zhuo, Y.; Chai, Y.; Yuan, R. *Anal. Chem.* **2020,** *92*, 1379-1385.

[13] Hasan, M. T.; Gonzalez-Rodriguez, R.; Ryan, C.; Pota, K.; Green, K.; Coffer, J. L.; Naumov, A. V. *Nano Res.* **2019,** *12*, 1041-1047.

[14] Li, X.; Lau, S. P.; Tang, L.; Ji, R.; Yang, P. *Nanoscale* **2014,** *6*, 5323-8.

[15] Niu, F. S.; Xu, Y. H.; Liu, J. X.; Song, Z. Q.; Liu, M. L.; Liu, J. Q. *Electrochim. Acta* **2017,** *236*, 239-251.

[16] Lim, S. Y.; Shen, W.; Gao, Z. *Chem. Soc. Rev.* **2015,** *44*, 362-81.

[17] Richter, M. M. *Chem. Rev.* **2004,** *104*, 3003-3036.

[18] Hesari, M.; Ding, Z. *J. Electrochem. Soc.* **2016,** *163*, H3116-H3131.

[19] Miao, W. *Chem. Rev.* **2008,** *108*, 2506-2553.

[20] Juzgado, A.; Solda, A.; Ostric, A.; Criado, A.; Valenti, G.; Rapino, S.; Conti, G.; Fracasso, G.; Paolucci, F.; Prato, M. *J. Mater. Chem. B* **2017,** *5*, 6681-6687.

[21] Xu, J.; Li, J.; Wang, C.; Zhao, W. *Luminescence* **2020,** *35*, 34-42.

[22] Qin, X.; Dong, Y.; Wang, M.; Zhu, Z.; Li, M.; Yang, D.; Shao, Y. *ACS Sens* **2019,** *4*, 2351-2357.

[23] Luo, J. H.; Li, Q.; Chen, S. H.; Yuan, R. *ACS Appl Mater Interfaces* **2019,** *11*, 27363-27370.

[24] Zhu, H.; Jin, R.; Jiang, D.; Zhu, J. J. *ACS Appl Mater Interfaces* **2019,** *11*, 46666-46670.

[25] Hu, L.; Xu, G. *Chem Soc Rev* **2010,** *39*, 3275-304.

[26] Liu, Z.; Qi, W.; Xu, G. *Chem. Soc. Rev.* **2015,** *44*, 3117-42.

[27] Gao, F. G.; Bard, A. J. *J. Am. Chem. Soc.* **2000,** *122*, 7426-7427.

[28] Moon, H. C.; Lodge, T. P.; Frisbie, C. D. *J. Am. Chem. Soc.* **2014,** *136*, 3705-12.

[29] Xu, G. F.; Niu, Y. S.; Yang, X. C.; Jin, Z. Y.; Wang, Y.; Xu, Y. H.; Niu, H. T. *Adv. Opt. Mater.* **2018,** *6*, 1800951.

[30] Xu, Y.; Gao, Y.; Li, T.; Du, Y.; Li, J.; Wang, E. *Adv. Funct. Mater.* **2007,** *17*, 1003-1009.

[31] Pei, Q.; Yu, G.; Zhang, C.; Yang, Y.; Heeger, A. J. *Science* **1995,** *269*, 1086-8.

[32] Hu, S.; Gao, J. In *Materials and physics of light-emitting electrochemical cells (LECs)*, Elsevier Ltd.: 2019; pp 727-757.

[33] Hu, S.; Gao, J. *ACS Appl Mater Interfaces* **2019,** *11*, 1117-1124.

[34] AlTal, F.; Gao, J. *J. Am. Chem. Soc.* **2018,** *140*, 9737-9742.

[35] Gozzi, G.; Cagnani, L. D.; Faria, R. M.; Santos, L. F. *J. Solid State Electrochem.* **2016,** *20*, 2127-2133.

[36] Wang, L.; Zhou, H. S. *Anal. Chem.* **2014,** *86*, 8902-5.

[37] Elgrishi, N.; Rountree, K. J.; McCarthy, B. D.; Rountree, E. S.; Eisenhart, T. T.; Dempsey, J. L. *J. Chem. Educ.* **2018,** *95*, 197-206.

[38] Shen, C.; Ge, S.; Pang, Y.; Xi, F.; Liu, J.; Dong, X.; Chen, P. *J. Mater. Chem. B* **2017,** *5*, 6593-6600.

[39] Chen, H.; Wang, Q.; Shen, Q.; Liu, X.; Li, W.; Nie, Z.; Yao, S. *Biosens. Bioelectron.* **2017,** *91*, 878-884.

[40] Ming, H.; Ma, Z.; Liu, Y.; Pan, K.; Yu, H.; Wang, F.; Kang, Z. *Dalton Trans* **2012,** *41*, 9526-31.

[41] Yang, Y.; Xiao, X. C.; Xing, X. X.; Wang, Z. Z.; Zou, T.; Wang, Z. D.; Zhao, R. J.; Wang, Y. D. *MRX* **2019,** *6*, 095615.

[42] Zheng, B. J.; Chen, Y. F.; Li, P. J.; Wang, Z. G.; Cao, B. Q.; Qi, F.; Liu, J. B.; Qiu, Z. W.; Zhang, W. L. *Nanophotonics* **2017,** *6*, 259-267.

[43] Khan, W. U.; Wang, D.; Zhang, W.; Tang, Z.; Ma, X.; Ding, X.; Du, S.; Wang, Y. *Sci. Rep.* **2017,** *7*, 14866.

[44] Yu, J.; Xu, C. X.; Tian, Z. S.; Lin, Y.; Shi, Z. L. *New J. Chem.* **2016,** *40*, 2083-2088.

[45] Yuan, Y. H.; Liu, Z. X.; Li, R. S.; Zou, H. Y.; Lin, M.; Liu, H.; Huang, C. Z. *Nanoscale* **2016,** *8*, 6770-6.

[46] Li, H.; He, X.; Kang, Z.; Huang, H.; Liu, Y.; Liu, J.; Lian, S.; Tsang, C. H. A.; Yang, X.; Lee, S.-T. *Angew. Chem. Int. Ed.* **2010,** *49*, 4430-4434.

[47] Hesari, M.; Workentin, M. S.; Ding, Z. *Chem. Sci.* **2014,** *5*, 3814-3822.

[48] Gao, J. *Curr. Opin. Electrochem.* **2018,** *7*, 87-94.

[49] Schubert, E. F.; Kim, J. K. *Science* **2005,** *308*, 1274-8.

[50] Su, H. C.; Chen, Y. R.; Wong, K. T. *Adv. Funct. Mater.* **2020,** *30*, 1906898.

Chapter 9

In this chapter, we explore light emitting electrochemical cells (LECs) constructed using $Ru(bpy)_3^{2+}$. We discuss the optimization of these LECs using a ZnO interlayer, and its effects on the stability, performance, and efficiency.

9 Spooling Electroluminescence Spectroscopy of $Ru(bpy)_3^{2+}$ Light-Emitting Electrochemical Cells with an Atomic Layer Deposited Zinc Oxide Electron-Transporting/Hole-Blocking Interlayer†

Light-emitting electrochemical cells (LECs) are being developed as an alternative to traditional OLEDs for lighting applications. In this study, a 10 nm conformal ZnO electron-transport/hole-blocking interlayer was applied via atomic layer deposition to $Ru(bpy)_3^{2+}$ model LECs, resulting in a four-fold luminance enhancement from 7.1 to 28 cd/m^2, along with a significant improvement in device sustainability and lifetimes. Device electroluminescent efficiency was increased by 175%. Spooling electroluminescence spectroscopy was used here for the first time showcasing the in-situ monitoring of LECs. ZnO-RuBPY-LECs showed extremely stable red-orange emission at 645 nm, while reference RuBPY-LECs demonstrated a 20-nm blue-shift, attributed to device degradation.

9.1 Introduction

Light-emitting electrochemical cells (LECs) in their simplest form contain a layer of luminescent material combined with an ionic salt sandwiched between two electrodes. These devices were first constructed by Pei, Heeger et al., who prepared light-emitting conducting polymer LECs.[1] Quantum dots, small organic and inorganic molecules have emerged as new light-emitting materials to produce a wide array of devices offering efficient, long-lasting performance in the subsequent decades.[2, 3] In fact, LECs are solid-

---

† This work has been published. Chu, K.; Adsetts, J.; Moore, C.; Ding, Z. Spooling Electrochemiluminescence Spectroscopy of $Ru(bpy)_3^{2+}$ Light-Emitting Electrochemical Cells with an Atomic Layer Deposited Zinc Oxide Electron-Transporting/Hole-Blocking Interlayer. *ACS Appl. Electron. Mater.* (**2020**) 2, 3825-3830.

state electroluminescence (EL) devices distinguished from liquid electrochemical cells where the light generation is via electrochemiluminescence (ECL).[4, 5] Under the influence of an applied electric field, the accumulation of anions at the anode and cations at the cathode induce p- and n-type electrochemical doping of the light-emitting layer. Radiative recombination of injected charge carriers in the intrinsic or non-doped region between these doped regions releases energy in the form of electroluminescence (EL).[5, 6] LECs have many advantages when compared to other light-emitting devices: their inherently fewer-layer design allows for the use of solution-processed techniques, greatly reducing fabrication complexity and cost. LECs also exhibit great flexibility as a wide range of materials have been successfully incorporated as the light-active substances, such as ionic transition metal complexes (iTMCs),[6, 7] host-guest systems, conjugated polymers,[5] and quantum dots (QDs).[8-10] These characteristic allow the fine-tuning and manipulation of LEC emissive properties simply by changing the electroluminescent layer.[10, 11] Development of light-emitting technology has been at the forefront of scientific research for many years. Advancements such as the organic light-emitting diode (OLED) have become nearly ubiquitous in our daily lives, as seen in various display technologies, portable hand-held devices, and general lighting.[12-14] LECs are anticipated to be complementary to OLEDs.

However, some of the drawbacks of LECs are their lower efficiency and operational lifetimes when compared to existing lighting technologies. These disadvantages are typically due to an imbalance in injected charge carriers, and electrochemical degradation localized at the cathode/light-emitting layer interface, respectively.[15] A common design strategy to improve luminous efficiency in multi-layered OLEDs is the use of charge extraction and transport interlayers, where the incorporation of materials with intermediate electronic structures facilitates the injection and migration of charge carriers through the device architecture. ZnO is a popular material for an electron transport layer (ETL) due to its high electron mobility, high stability, and visible-range transmittance.[16] This material has been previously utilized for LECs, where nanoparticle ZnO films were shown to improve the brightness and efficacy of Ir-based iTMC-LECs.[17] The low-temperature preparation and fabrication of ZnO films also allows techniques such as atomic layer deposition (ALD) to be used. ALD provides very precise thickness control,

producing thin films with excellent homogeneity and uniformity when compared to nanoparticle films. ALD-deposited ZnO films were recently shown to extend device lifetimes in QD- and perovskite-LEDs, particularly by improving the interface between the cathode and light-emitting layer. [18, 19] In this work, we present the advantages of a 10 nm ALD-deposited ZnO layer as an electron transport/hole blocking layer in $Ru(bpy)_3^{2+}$ (RuBPY) model LECs in an effort to enhance device efficiency and operational lifetimes.

Overall luminance and device efficiency were remarkably improved after the addition of this supporting layer. In addition, long-term device sustainability was also significantly improved. In-situ spooling EL spectroscopy showcasing the emissive changes of the LECs during their operation is presented here for the first time, where ZnO-RuBPY-LECs demonstrated a highly stable emission centered at 645 nm.

9.2 Experimental

9.2.1 Materials and reagents

Electrochemical grade acetonitrile (CH_3CN, 99.8%, SureSeal) was purchased from Sigma-Aldrich Canada, Mississauga, ON. Tris(2,2'-bipyridine)ruthenium(II) hexafluorophosphate ($Ru(bpy)_3(PF_6)_2$, RuBPY, 97%) and lithium trifluoromethanesulfonate (LiTf, 99%) were obtained from Sigma-Aldrich Canada, and stored in a vacuum-sealed desiccator. Polyethylene oxide (PEO, avg. M_v = 100,000) was bought from Sigma-Aldrich Canada, and used as received.

9.2.2 LEC fabrication and testing

Pre-patterned 15x15 mm^2 glass substrates with a 3 mm width horizontal indium tin oxide (ITO) band electrode (blue in **Figure 9.5**) in the middle were purchased from Jinghui Electronic Technologies Ltd., China. The ITO thickness is 150 nm with a sheet resistance of 8 Ω/□. Prior to use, they were sonicated in solutions of 2% Hellmanex, ultra-pure Milli-Q water, isopropyl alcohol, and 10% NaOH successively for 15 minutes, before being dried at 85°C overnight in an oven. Poly(3,4-ethylenedioxythiophene) polystyrene sulfonate (PEDOT:PSS, 2.8%, Sigma-Aldrich) was filtered using a 0.2 μm PTFE syringe filter and diluted in a 1:1 ratio using isopropyl alcohol. The light-emitting layer was

prepared by mixing solutions of lithium trifluoromethanesulfonate (LiTf), polyethylene oxide (PEO), and RuBPY to a final mass ratio of 1:10:15 mg/mL in anhydrous CH_3CN. The PEDOT:PSS and RuBPY light-emitting layers were sequentially deposited onto the cleaned ITO-banded glass using a Laurell Technologies spin-coater (Model WS-400B-6NPP/LITE). The PEDOT:PSS layer was spin-coated at 6000 rpm for 60 s, and annealed at 120°C for 1 hour. The RuBPY/PEO/LiTf layer was spin-coated at 2500 rpm for 60 s, and annealed at 70°C for 1 h. The 10 nm ZnO layer was deposited using a Savannah thermal atomic layer deposition system at a controlled temperature of 150°C. (Cambridge Technologies, Cambridge, MA). Diethyl zinc (DEZ) and H_2O were used as the ZnO ALD precursors. Aluminum electrodes with a thickness of approximately 130 nm were deposited using a thermal evaporator system (Plasmionique, Montreal, QC) at a vacuum pressure of at least $5x10^{-6}$ torr. A patterned shadow-mask resulted in the deposition of five separate aluminum electrodes (with 2 mm width and 1 mm gap between Al bands shown in **Figure 9.5**) perpendicular to the ITO band; hereafter, a 'device' is defined as the plane intersection of a vertical aluminum band and the ITO electrode, with an active area of 6 mm^2 per device. Five devices were obtained for each ITO substrate and up to twelve substrates can be fabricated for each batch.

Luminance-current-voltage tests were performed using a Keithley 2400 source-measure unit as the power source, with the ITO-PEDOT:PSS electrode connected as the anode, and the aluminum electrode connected as the cathode. Photocurrent, as the electroluminescence (EL) intensity from the LECs, was measured using a Hamamatsu R928 photomultiplier tube (PMT) biased at −750 V. The EL, current, and applied potential signals of the LEC devices were recorded using a NI myDAQ data acquisition device connected to a computer, and a custom LabVIEW program that simultaneously controlled and recorded the experiment. The relative efficiency of a RuBPY-LEC with the ZnO interlayer — defined here as the ratio of the integrated photocurrent (photons) to integrated current (charge) — relative to that of a device without the ZnO was determined using equation 1 and was found to be 168%. This value was further corrected with spectrum sensitivity curve in **Figure 9.1**. Approximately, PMT responsivity at the peak wavelength in an EL spectrum was taken as the correction factor. For instance, the emission wavelengths for the ZnO-RuBPY-LECs and the RuBPY-LECs were measured

to be 645 nm and 635 nm, respectively, taken from Figure 7 of the manuscript. Using the responsivity values of the PMT at these wavelengths (39.15 mA/W @ 645 nm, and 40.65 mA/W @ 635 nm) in **Figure 9.1**, the luminous efficiencies of the ZnO-RuBPY-LECs vs. RuBPY-LECs were corrected, resulting in an average enhancement of 175%.

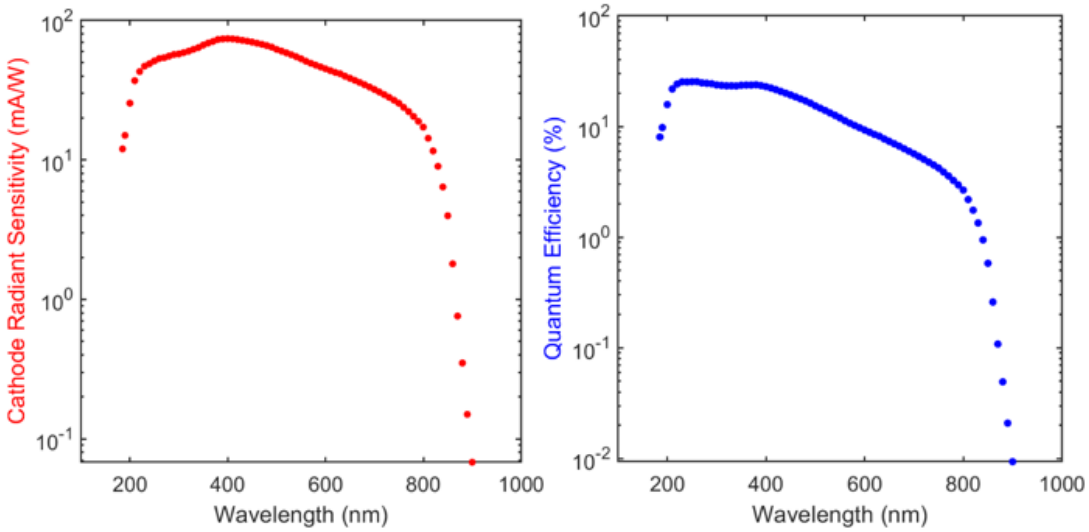

Figure 9.1. Cathode Radiant Sensitivity versus wavelength (left) and Quantum Efficiency versus wavelength (right) of the used photomultiplier tube, R928 (Hamamatsu, Japan). Digital curves revealed in PDF format online at https://www.hamamatsu.com/resources/pdf/etd/R928_R928P_R955_R955P_TPMS1091E.pdf were requested from Hamamatsu, Japan.

Pulsed potential tests were performed using an Autolab electrochemical system (PGSTAT30, Metrohm, Switzerland), with the aforementioned Hamamatsu PMT used to measure the device electroluminescence. All LEC testing was performed in a NEXUS I glovebox system (Vacuum Atmospheres Company, Hawthorne, CA). Spectra were collected using a spectrometer (Acton 2300i, Princeton Instruments, Trenton, NJ) and an attached CCD camera (Model DV420-BV, Andor Technology, Belfast, UK) cooled to −65°C. Wavelength calibration was performed using a mercury-argon lamp (HG-1, Ocean Optics, Orlando, FL). *Commision Internationale de l'eclairage* (CIE) colour coordinate diagrams were calculated and plotted using a custom MATLAB script.

A Minolta LS-110 luminance meter (Konica Minolta, Japan) with a No. 135 close-up lens (average focal length = 536 mm) was used to measure luminance (cd/m^2), and the Hamamatsu R928 PMT was used to measure the photocurrent of a red reference light-emitting diode (TLHK4600, Vishay Intertechnology, Malvern, PA), establishing a linear correlation between the two detectors that could be used to determine the corresponding luminance values of the RuBPY LECs. An optical power meter (Thorlabs PM100D, Newton, NJ) with a calibrated silicon photodiode (Thorlabs S120VC) was used to measure the optical power, in Watts, of the RuBPY LECs.

The photon flux Φ_{phd}, the number of photons per second hitting a surface defined by the distance between the emitting source and the detector with units of photons$\cdot s^{-1}sr^{-1}$, and the total detector area, of the RuBPY LECs were calculated using the following equation, where H is the Keithley ammeter sensitivity in electrons$\cdot s^{-1}V^{-1}$, V_{phd} is the PMT measured response through the ammeter in volts, and Ω_{phd} is the effective solid angle of the detector in steradians (sr).[1] phd = photodetector.

$$\Phi_{phd} = \frac{H}{C \times \Omega_{phd}} \times V_{phd}$$

Equation 9.1

The spectral dependence, C, is a measure of the average response of the photodetector to specific incident light of a known spectrum, with units of electrons per photon. It is calculated using the following equation, where $Q(\lambda)$ is the quantum efficiency of the photodetector (**Figure 9.1B**) and $S(\lambda)$ is the intensity normalized, background corrected RuBPY emission spectrum (Supplementary Figure S7).

$$C = \frac{\int Q(\lambda)S(\lambda)d\lambda}{\int S(\lambda)d\lambda}$$

Equation 9.2

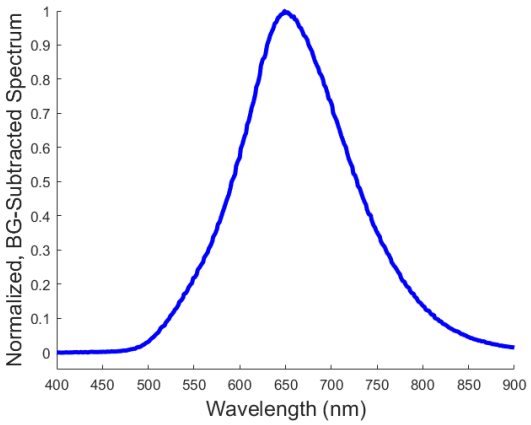

Figure 9.2. Intensity normalized background-corrected emission spectrum of RuBPY LECs.

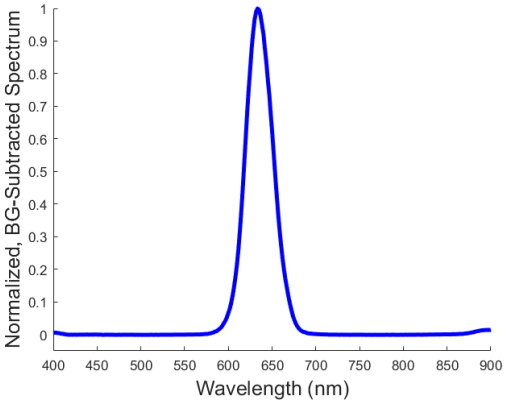

Figure 9.3. Intensity normalized background-corrected emission spectrum of red reference LED.

Before calculating photon flux, the PMT's photon flux was calibrated using the red reference LED with a measured spectrum shown in **Figure 9.3** and the calibrated photodiode. A 0-2 V scan at 0.01 V/s of the LED on both instruments at known distances allowed for the comparison of photon flux in photons·$s^{-1}sr^{-1}$ between the two instruments. Average calibration values were extracted from the comparison of the linear detection ranges of both instruments and applied to all future measurements to ensure accuracy in the photon flux measurements.

The luminous efficiency (η_{lum}) of the RuBPY LECs was calculated using the following equation, where the photopic function *P(λ)* in lumens/watt (**Figure 9.4**) corrects for the response of the human eye during daylight (defined by the correction factor *K*), π accounts for the emitted photons in the forward hemisphere, and V_{LEC} and I_{LEC} are the driving voltages and corresponding current values of the RuBPY-LECs, sourced and measured simultaneously using a Keithley 2400 unit.

$$\eta_{lum} = \frac{\pi HK}{C\Omega_{phd}} \frac{V_{phd}}{V_{LEC} I_{LEC}}$$

Equation 9.3

$$K = \frac{\int P(\lambda) S(\lambda) \frac{hc}{\lambda} d\lambda}{\int S(\lambda) d\lambda}$$

Equation 9.4

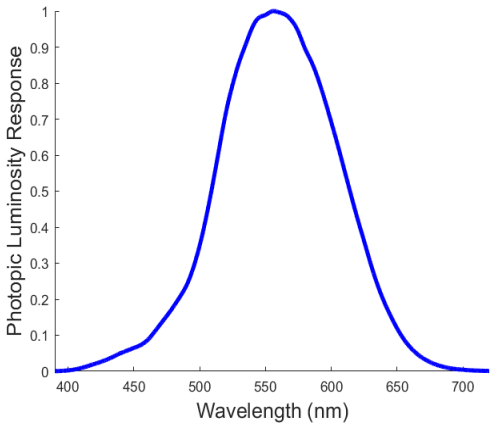

Figure 9.4. The photopic luminosity function, which describes the average spectral sensitivity of the human eye. This spectrum was multiplied by a correction factor of 683.002 lm/W before being used in any calculations.

9.3 Results and Discussion

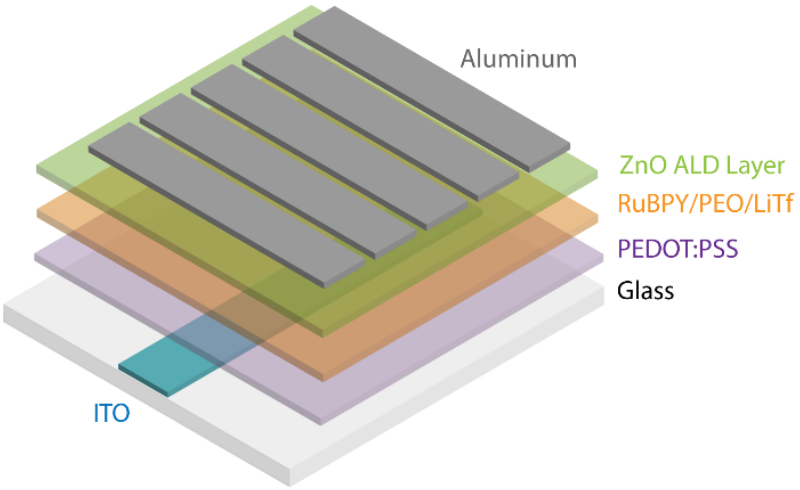

Figure 9.5. Expanded device structure of RuBPY-LEC with a 10 nm ZnO ETL/HBL.

The design of the RuBPY-LECs is illustrated in **Figure 9.5**. The transparent anode is 100 nm poly(3,4-ethylenedioxythiophene) polystyrene sulfonate (PEDOT:PSS) coated indium-tin-oxide (ITO). The 100 nm light-emitting layer is RuBPY mixed with an ion conductive polymer polyethylene oxide (PEO) and an ionic salt lithium trifluoromethanesulfonate (LiTf). Herein, we add a 10 nm ZnO coating, applied via atomic layer deposition (ALD), to act as an electron transport/hole blocking layer (ETL/HBL). A 130 nm thick layer of aluminum is thermally evaporated as the top contact to act as the electron-injecting cathode. The reference RuBPY-LEC has the same configuration structure as the above except with the absence of the 10 nm ZnO interlayer.

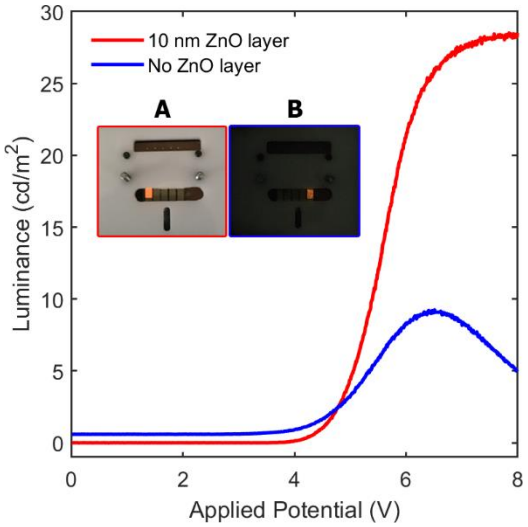

Figure 9.6. EL intensity vs. applied potential plots for RuBPY-LECs with a 10 nm ZnO-ETL/HBL (red trace) and without the ZnO layer (blue trace). The scan rate used was at 0.05 V/s. Insets (A) and (B), respectively, show colour photographs of the two RuBPY LECs during operation.

The performance of the two types of LECs was first tested using a linear voltage sweep while simultaneously measuring the device electroluminescence (**Figure 9.6**). When the applied potential was increased from 0 to 8 V at a rate of 50 mV/sec, the reference RuBPY-LECs exhibited a turn-on voltage of 3.6 ± 0.2 V, with the electroluminescence (EL) intensity reaching a maximum luminance of 7.1 ± 1.0 cd/m^2. When a 10 nm ZnO layer was deposited on top of the emissive layer, the device performance of the RuBPY-LECs was enhanced by approximately four times, showing maximum luminance values of 28 ± 1.5 cd/m^2. This improvement clearly demonstrates the benefits of the ZnO layer, as electron injection and transport at the cathode is increased, leading to an enhancement of the luminous performance.

We can see that the current flow between the electrodes of the LEC is significantly increased when the ZnO interlayer is added, again hinting at its strong electron injecting and transporting capabilities (**Figure 9.7** and **Figure 9.8**). Despite the large increase in the operating current, the relative electroluminescent efficiency of a RuBPY-LEC with the ZnO interlayer, defined here as the ratio of the integrated photocurrent (photons) to

integrated current (charge) relative to that of a device without the ZnO layer, was still greatly improved (**Figure 9.9**):

$$\Phi_{\mathrm{EL}} = \frac{\left(\frac{\int \mathrm{EL}\,\mathrm{dt}}{\int \mathrm{Current}\,\mathrm{dt}}\right)_{x}}{\left(\frac{\int \mathrm{EL}\,\mathrm{dt}}{\int \mathrm{Current}\,\mathrm{dt}}\right)_{ref}}$$

Equation 9.5

where *ref* and *x* refer to the reference RuBPY-LEC in the absence of ZnO interlayer and sample RuBPY-LEC in the presence the ZnO, respectively. Note that the relative efficiency was further corrected using the PMT responsivity values of the peak wavelengths in EL spectra (**Figure 9.1**) shown in Experimental section in Supporting Information.

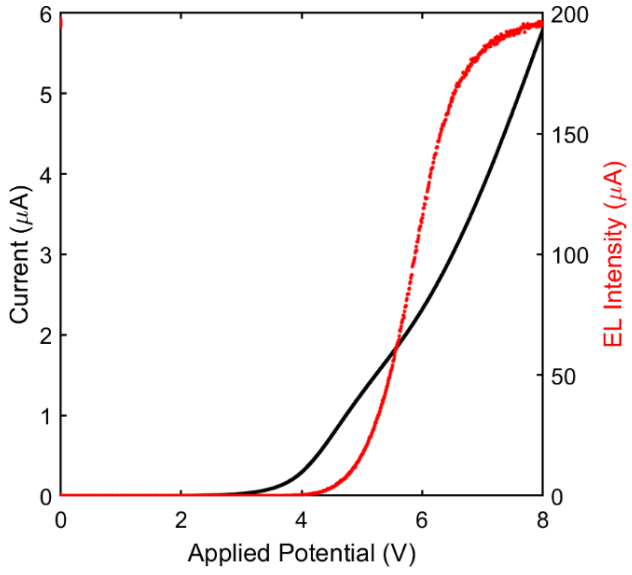

Figure 9.7. Current and EL intensity vs. applied potential for RuBPY-LECs in the presence of the 10 nm ZnO layer.

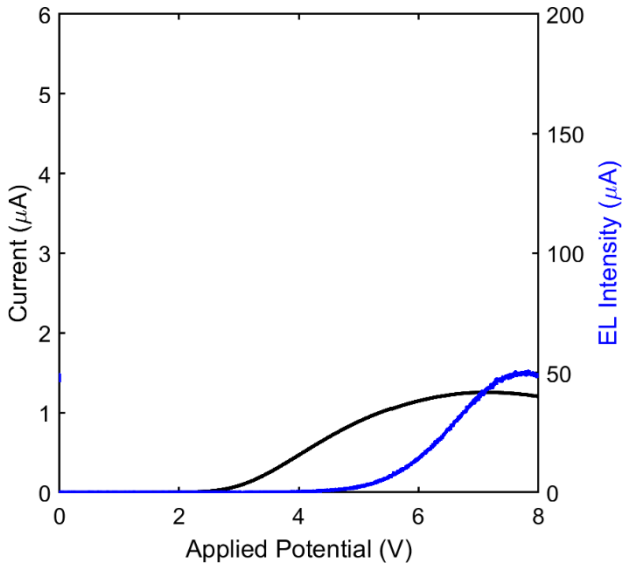

Figure 9.8. Current and EL intensity vs. applied potential for reference RuBPY-LECs with no ZnO layer.

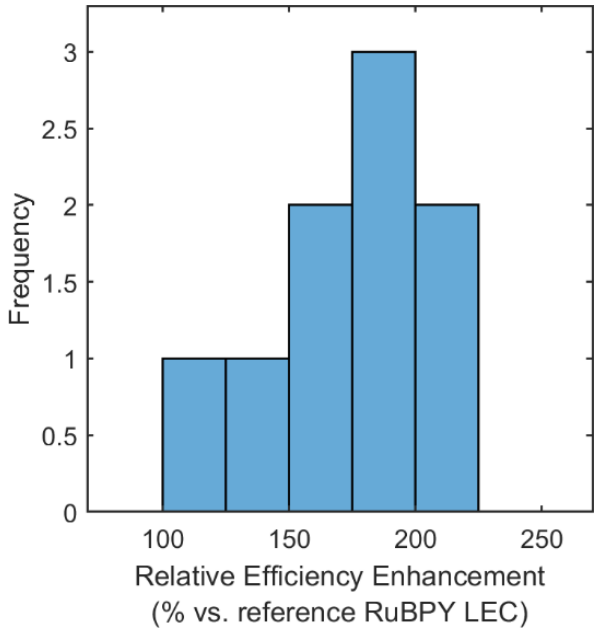

Figure 9.9. Relative PMT efficiency histogram of ZnO-RuBPY-LECs vs. reference RuBPY-LECs in the initial test of linear voltage sweep experiments as in **Figure 9.7** and **Figure 9.8.**

The relative efficiency histogram from the initial test of linear voltage sweep experiments as in **Figure 9.7** and **Figure 9.8** indicates the ZnO-RuBPY-LECs display an average of

175% electroluminescent efficiency relative to reference RuBPY-LECs, up to a maximum of 200%.

This enhancement in the efficiency indicates a superior charge carrier balance resulting in efficient recombination in the light-emitting layer as reported for an Ir-based iTMC-LEC with a ZnO nanoparticle layer up to 50 nm.[17] The above result suggests that the hole blocking functionality of the ZnO layer is also a very important factor when considering device performance, as the deep valence band of the ZnO layer should significantly lower the parasitic current by suppressing excess hole leakage into the aluminium cathodes. In this way, charge carrier flow that does not contribute to radiative recombination is minimized (**Figure 9.10**), enabling the design of brighter and more efficient LECs. Also of note is that the voltage at which the maximum EL intensity is observed is lowered (6.3 V vs. 7.8 V for the ZnO-RuBPY-LECs and RuBPY-LECs, respectively). This decreased optimal operating voltage should lead to LECs with a better power efficiency.

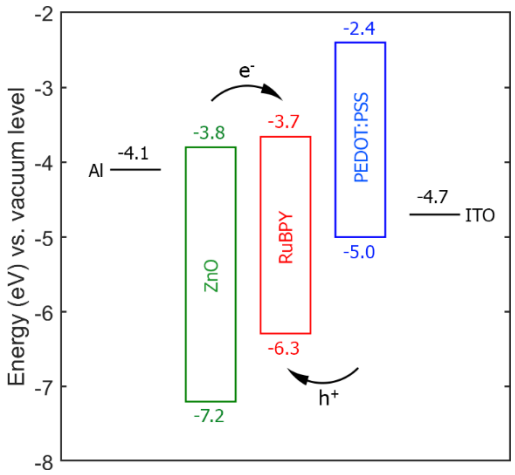

Figure 9.10. Energy level diagram of RuBPY-LECs showing the constituting layers in the LEC architecture. The values for energy levels of Al, ZnO, PEDOT:PSS, and ITO were taken from literature.[20-23] HOMO and LUMO energy levels for RuBPY were estimated from the oxidation and reduction potentials , of $Ru(bpy)_3^{2+}$, respectively.

The ZnO-LECs have improved stability at higher applied potentials, which is evidenced by the maintenance of a ‘steady-state emission’ when maximum luminance is achieved. In contrast, RuBPY-LECs without this ZnO layer show a defined luminance maximum

that decreases as the potential scan continues. Repeated voltage cycling of the LECs establishes an apparent trend where devices with the added ZnO layer are much more resistant to degradation over time. **Figure 9.11** shows the maximum recorded luminance over a series of five identical voltage sweeps. RuBPY-LECs with a ZnO layer retain over 95% of maximum luminance after multiple repeated cycles, while reference RuBPY-LECs drop to just 20% after similar tests. This is further demonstrated by the relative EL efficiency histogram from the test 5 of linear voltage sweep experiments, where an average efficiency of 220% with a maximum of 310% is observed (**Figure 9.12**). **Figure 9.13** and **Figure 9.14** show the luminous efficiencies of ZnO-RuBPY-LECs and reference RuBPY-LECs, respectively. In LECs with a ZnO layer, a maximum luminous efficiency of 20 lm/W at a current density of 0.38 A/m^2 was observed, while reference LECs had a maximum of 12 lm/W at a current density of 0.24 A/m^2. This enhancement can be attributed to improved electron-hole balance in the recombination zone of these devices, which is likely the result of both the electron-injecting and hole-blocking functionality of the added ZnO layer.

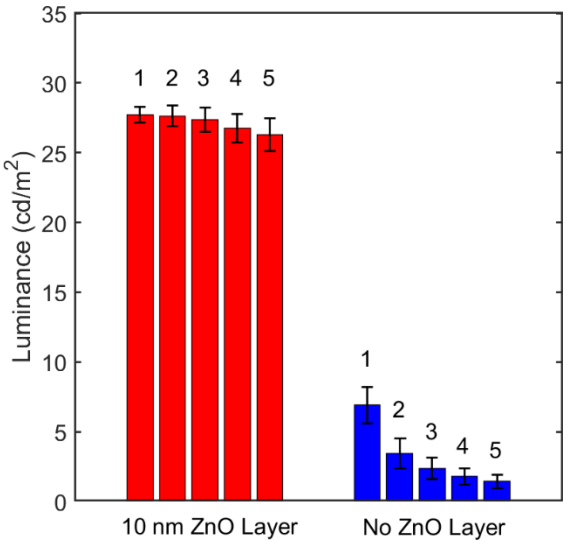

Figure 9.11. Repeated voltage cycling of the RuBPY-LECs with and without a ZnO layer. The numbers above the bars indicate the number of times each device was tested. Error bars heights represent one standard deviation measured across at least eight different devices.

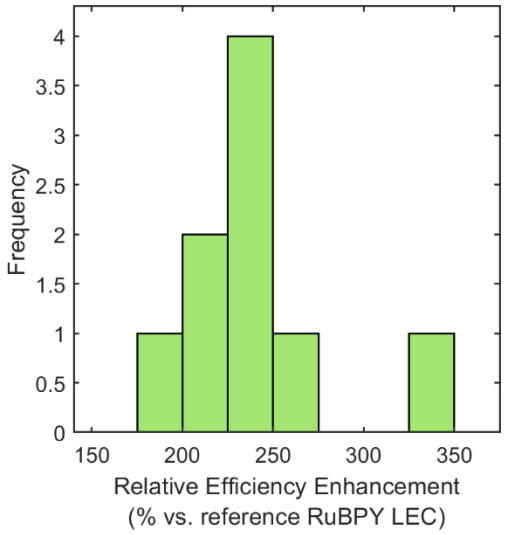

Figure 9.12. Relative electroluminescent efficiency histogram of ZnO-RuBPY-LECs vs. RuBPY-LECs from test 5 as in **Figure 9.11**.

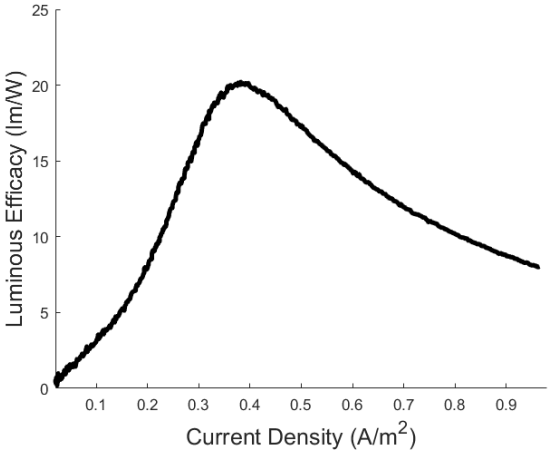

Figure 9.13. Luminous efficiency (lm/W) of ZnO-RuBPY-LECs vs. current density.

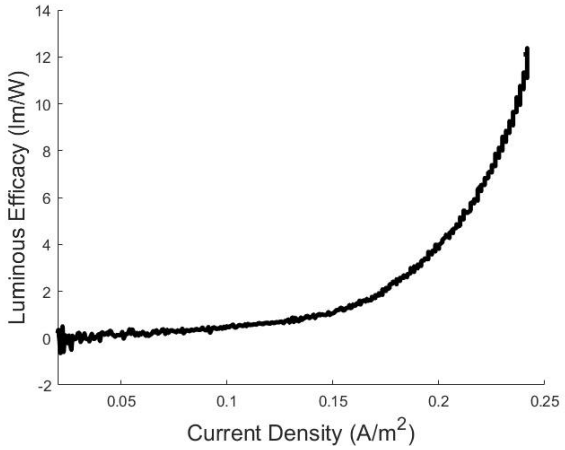

Figure 9.14. Luminous efficiency (lm/W) of reference RuBPY-LECs vs. current density.

To examine the RuBPY-LEC behaviour more closely during operation, spooling EL spectroscopy (adapted from spooling ECL spectroscopy, which has been used extensively by our group in recent years to comprehensively study ECL luminophore excited states and their light emission mechanisms[24]) was utilized for the first time. Here, EL spectra of the LECs were recorded at predefined intervals during a potentiodynamic scan, enabling the time-dependent study of LECs during their operation. **Figure 9.15A** shows the spooling EL spectra for a RuBPY-LEC with the ZnO-ETL/HBL during a forward potential scan. The data can be divided into three sections corresponding to the turn-on voltage region (yellow), an intermediate voltage region as the luminance approaches its maximum intensity (green), and the high voltage region where the luminance begins to decay (blue). The figure insets are individual emission spectra extracted from the overall plot, where a 645 nm emission peak is observed throughout the entire potential scan. However, in RuBPY-LECs without this ZnO layer (**Figure 9.15B**) a blue-shift of approximately 20 nm in peak wavelength was observed from 640 nm at the onset of light emission, to 620 nm as the RuBPY-LECs advance towards higher applied potentials. This shift in the emission wavelength, seen in conjunction with a decline in the emission intensity, likely signifies an irreversible change in the morphology and functionality of the light-emitting RuBPY film. The overall EL intensity was also approximately four times greater when the ZnO-ETL/HBL was added, which agrees well with the previous luminance-voltage results in **Figure 9.6**.

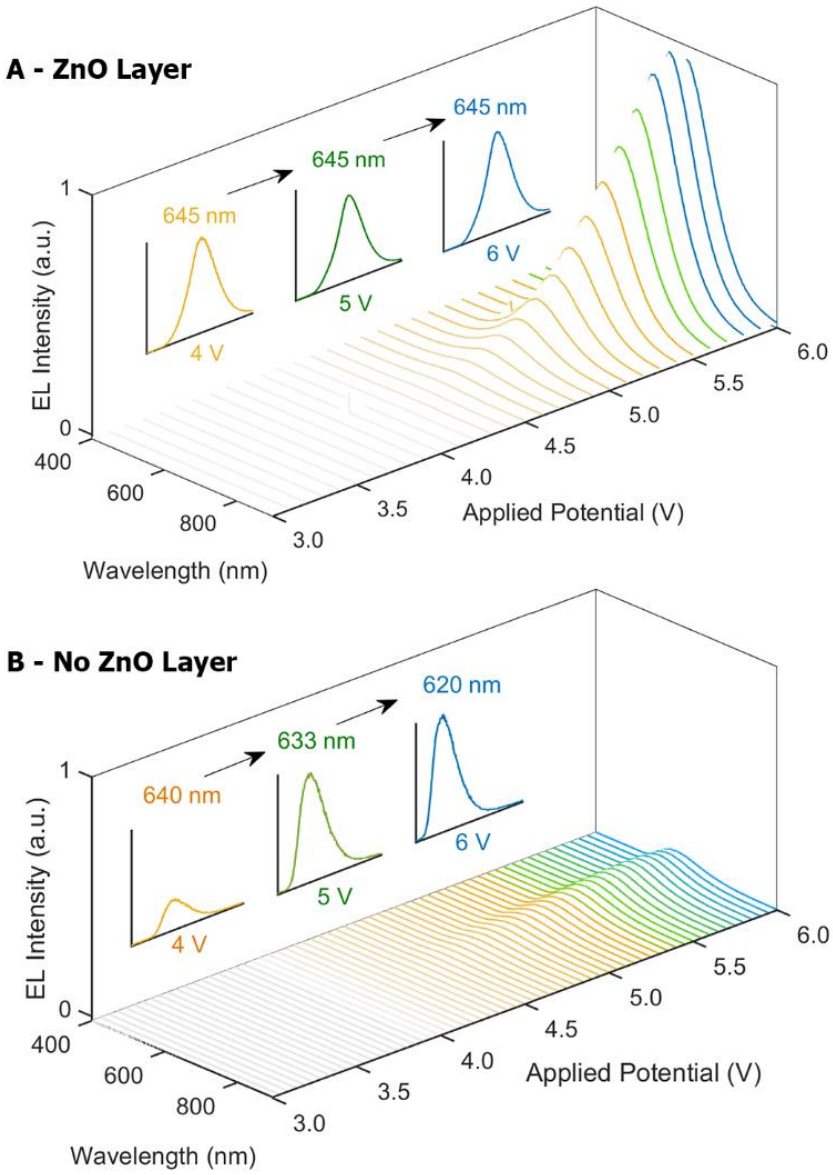

Figure 9.15. Spooling EL spectra of RuBPY-LECs with the added ZnO-ETL/HBL (A) and without the ZnO-ETL/HBL (B) during a forward potential scan. Insets for each figure correspond to selected spectrum collected at three specific voltages.

This behaviour indicates the ZnO layer can provide some degree of protection against degradation in these LECs. Among the most catastrophic of failure modes, electrical short circuits occur when surface and layer imperfections cause a bridging of the two electrodes in an LEC, leading to localized ‘dark spots’ and material decomposition.[25, 26] The formation of these electrical shorts are strongly suspected in the unprotected RuBPY-

LECs, where several dark spots with decreased luminescence were evident after a few seconds of operation (**Figure 9.6** inset B). A non-luminescent dark spot may simply be viewed as a 'less orange' than neighbouring fully emitting sections; therefore, the overall perceived emission wavelength will appear slightly blue-shifted. ZnO-RuBPY-LECs, in contrast, showed no sign of these dark spots, instead displaying bright and uniform emission across the entire active area. In this sense, spooling EL spectroscopy as described here can be a useful technique to evaluate the stability and lifetime of electroluminescent devices, if deviations from the expected emission wavelength are taken as performance-lowering defects.

These observations suggest that ZnO, while fulfilling its primary role as an electron transport/hole blocking layer and significantly enhancing device performance, may also act as a protective 'buffer layer' between the light-emitting RuBPY layer and the aluminum electrodes. The suppression of destructive oxidation reactions between the RuBPY layer and the aluminum cathodes can prevent the shifting of the location of the recombination zone in these devices, which may play a part in the improved spectral stability of ZnO-RuBPY-LECs. This added semiconducting layer can potentially shield the LEC from various external elements that might cause premature failure, including moisture and oxygen from atmosphere, which is known to precipitate a variety of destructive reactions upon penetrating the device structure. This apparent quenching of the device luminescence may be due to the formation of oxo-bridged dimeric species of $Ru(bpy)_3^{2+}$, a reaction that can be exacerbated by the presence of oxygen and moisture.[27, 28] The advantages of atomic layer deposition are also realized here, as the technique can apply highly homogeneous and conformal layers onto a substrate regardless of the roughness and irregularities of underlying layers.[29] Precise thickness control is achievable through controlling the number of growth cycles, which allows for easy and quick deposition of the ZnO layer as reported for the active layer of organic solar cells[30] and ETL of quantum dot LEDs.[18, 19] The efficiency enhancement of our LEC devices is higher than that of Ir-based iTMC LEC with a ZnO nanoparticle layer.[17]

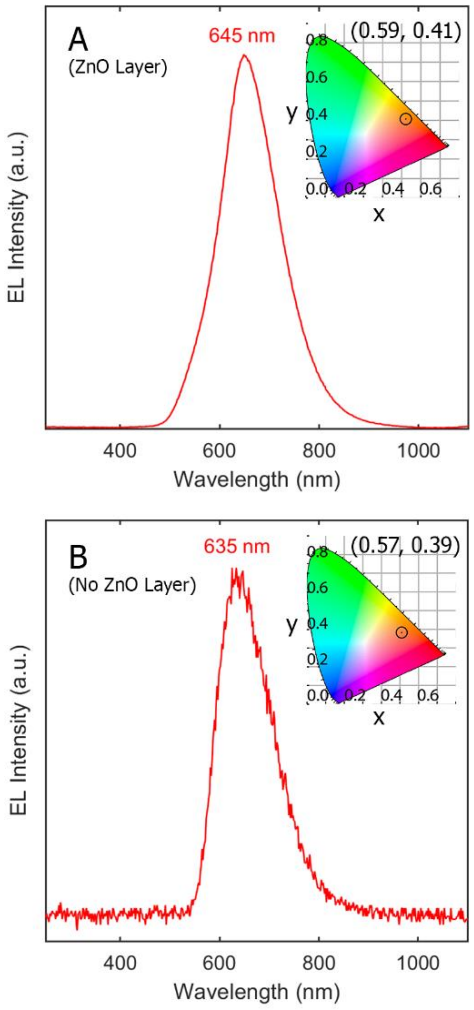

Figure 9.16. Accumulation spectra and their CIE chromaticity diagrams (insets) for a ZnO-RuBPY-LEC (A) and RuBPY-LEC (B).

Figure 9.16A and **Figure 9.16B** shows accumulated spectra for a ZnO-RuBPY-LEC (645 nm emission peak) and RuBPY-LECs (635 nm emission peak), respectively. These emissions correspond to CIE (*Commission Internationale de l'eclairage*) 1931 colour coordinates of (0.58, 041) and (0.57, 0.39), respectively. These results match well with previously reported OLEDs utilizing $Ru(bpy)_3^{2+}$ as a luminophore,[31] which is very encouraging since the added ZnO layer positively impacts the performance of the LECs.

9.4 Conclusions

In conclusion, we have shown that the addition of a conformal ZnO electron transport/hole blocking layer to simple RuBPY-LECs can significantly improve their luminous performance, sustainability, and efficiencies. Furthermore, this ZnO layer could have valuable applications for the protection of LECs from external degradation factors, possibly reducing the need for complex encapsulation procedures for future light-emitting devices. Based on the discussed advantages of this multi-purpose, highly practical, non-intrusive ZnO layer, it is anticipated to fabricate future enhanced luminance and long lifetime LECs.

9.5 References

[1] Pei, Q.; Yu, G.; Zhang, C.; Yang, Y.; Heeger, A. J. *Science* **1995,** *269*, 1086-8.

[2] Chu, K.; Adsetts, J. R.; He, S.; Zhan, Z.; Yang, L.; Wong, J. M.; Love, D. A.; Ding, Z. *Chem. Eur. J.* **2020,** *26*, 15892-15900.

[3] Bowler, M. H.; Mishra, A.; Adams, A. C.; Blangy, C. L. D.; Slinker, J. D. *Adv. Funct. Mater.* **2020,** *30*, 1906715.

[4] Hesari, M.; Ding, Z. *J. Electrochem. Soc.* **2016,** *163*, H3116-H3131.

[5] Gao, J. *Curr. Opin. Electrochem.* **2018,** *7*, 87-94.

[6] Housecroft, C. E.; Constable, E. C. *Coord. Chem. Rev.* **2017,** *350*, 155-177.

[7] Henwood, A. F.; Pal, A. K.; Cordes, D. B.; Slawin, A. M. Z.; Rees, T. W.; Momblona, C.; Babaei, A.; Pertegás, A.; Ortí, E.; Bolink, H. J.; Baranoff, E.; Zysman-Colman, E. *J. Mater. Chem. C* **2017,** *5*, 9638-9650.

[8] Alahbakhshi, M.; Mishra, A.; Haroldson, R.; Ishteev, A.; Moon, J.; Gu, Q.; Slinker, J. D.; Zakhidov, A. A. *ACS Energy Lett.* **2019,** *4*, 2922-2928.

[9] Mishra, A.; Alahbakhshi, M.; Haroldson, R.; Bastatas, L. D.; Gu, Q.; Zakhidov, A. A.; Slinker, J. D. *Adv. Opt. Mater.* **2020,** *8*, 2000226.

[10] Fresta, E.; Costa, R. D. *J. Mater. Chem. C* **2017,** *5*, 5643-5675.

[11] Tang, S.; Edman, L., Light-Emitting Electrochemical Cells: A Review on Recent Progress. In *Photoluminescent Materials and Electroluminescent Devices*, Armaroli, N.; Bolink, H. J., Eds. Springer International Publishing: Cham, 2017; pp 375-395.

[12] Wei, Y.-C.; Wang, S. F.; Hu, Y.; Liao, L.-S.; Chen, D.-G.; Chang, K.-H.; Wang, C.-W.; Liu, S.-H.; Chan, W.-H.; Liao, J.-L.; Hung, W.-Y.; Wang, T.-H.; Chen, P.-T.; Hsu, H.-F.; Chi, Y.; Chou, P.-T. *Nat. Photon.* **2020,** *14*, 570-577.

[13] Zhang, Y.-L.; Ran, Q.; Wang, Q.; Liu, Y.; Hänisch, C.; Reineke, S.; Fan, J.; Liao, L.-S. *Adv. Mater.* **2019,** *31*, 1902368.

[14] Yuan, M.; Quan, L. N.; Comin, R.; Walters, G.; Sabatini, R.; Voznyy, O.; Hoogland, S.; Zhao, Y.; Beauregard, E. M.; Kanjanaboos, P.; Lu, Z.; Kim, D. H.; Sargent, E. H. *Nat. Nanotechnol.* **2016,** *11*, 872-877.

[15] Gao, J. *Chempluschem* **2018,** *83*, 183-196.

[16] Xiong, L. B.; Guo, Y. X.; Wen, J.; Liu, H. R.; Yang, G.; Qin, P. L.; Fang, G. J. *Adv. Funct. Mater.* **2018,** *28*, 1802757.

[17] Marcantonio, M. D.; Gellner, S.; Namanga, J. E.; Frohleiks, J.; Gerlitzki, N.; Vollkommer, F.; Bacher, G.; Nannen, E. *Adv. Mater. Technol.* **2017,** *2*, 1600215.

[18] Kim, G. H.; Noh, K.; Han, J. S.; Kim, M.; Oh, N.; Lee, W.; Na, H. B.; Shin, C. S.; Yoon, T. S.; Lim, J.; Cho, S. Y. *Adv. Mater. Inter.* **2020,** *7*, 2000343.

[19] Yun, H. S.; Noh, K.; Kim, J.; Noh, S. H.; Kim, G. H.; Lee, W.; Na, H. B.; Yoon, T. S.; Jang, J.; Kim, Y.; Cho, S. Y. *Physica Status Solidi-Rapid Research Letters* **2020,** *14*, 1900573.

[20] Frohleiks, J.; Wefers, F.; Wepfer, S.; Hong, A. R.; Jang, H. S.; Nannen, E. *Adv. Mater. Technol.* **2017,** *2*, 1700154.

[21] Dehghan, M.; Behjat, A. *RSC Adv* **2019,** *9*, 20917-20924.

[22] Tang, H. Y.; Shang, Y. Q.; Zhou, W. J.; Peng, Z. J.; Ning, Z. J. *Solar RRL* **2019,** *3*, 1800256.

[23] Spalla, M.; Planes, E.; Perrin, L.; Matheron, M.; Berson, S.; Flandin, L. *ACS Appl. Energy Mater.* **2019,** *2*, 7183-7195.

[24] Hesari, M.; Ding, Z. *Acc. Chem. Res.* **2017,** *50*, 218-230.

[25] Wang, W.; Lim, S. F.; Chua, S. J. *J. Appl. Phys.* **2002,** *91*, 5712-5715.

[26] Kim, Y.; Choi, D.; Lim, H.; Ha, C. S. *Appl. Phys. Lett.* **2003,** *82*, 2200-2202.

[27] Soltzberg, L. J.; Slinker, J. D.; Flores-Torres, S.; Bernards, D. A.; Malliaras, G. G.; Abruna, H. D.; Kim, J. S.; Friend, R. H.; Kaplan, M. D.; Goldberg, V. *J. Am. Chem. Soc.* **2006,** *128*, 7761-4.

[28] Slinker, J. D.; Kim, J. S.; Flores-Torres, S.; Delcamp, J. H.; Abruna, H. D.; Friend, R. H.; Malliaras, G. G. *J. Mater. Chem.* **2007,** *17*, 76-81.

[29] George, S. M. *Chem. Rev.* **2010,** *110*, 111-131.

[30] Frankenstein, H.; Leng, C. Z.; Losego, M. D.; Frey, G. L. *Org. Electron.* **2019,** *64*, 37-46.

[31] Gao, F. G.; Bard, A. J. *J. Am. Chem. Soc.* **2000,** *122*, 7426-7427.

Chapter 10

10 Conclusions and Future Work

10.1 Conclusions

In this thesis, various luminescent materials were characterized for their performance in electrochemiluminescence (ECL) toward light-emitting applications, with a particular emphasis on electroluminescence (EL) pathways for operation in light-emitting electrochemical cells. Chemiluminescence of some TADF compounds was also investigated – as alternative mechanisms to produce emissive excited states could yield valuable insight towards optimization of these luminophores across different luminescent systems.

Chapter 1 serves as the introductory text to this thesis. In this chapter, insight into the light emitting pathway of electrochemiluminescence (ECL) was provided, together with the different enhancement mechanisms that lead to enhanced ECL including thermally activated delayed fluorescence (TADF), hydrogen-bonding ECL, and aggregation- and crystallization-induced ECL.

In Chapter 2, the top-down and bottom-up synthesis, unique photophysical properties and applications of carbon quantum dots (CQDs) were summarized.

In Chapter 3, novel developments of methodology, instrumentation, and calculation of the absolute ECL quantum efficiency (QE) was carried out, using a photon counting head as the photodetector. In Chapter 4, this methodology was expanded to use a spectrograph/CCD camera. This groundwork to accurately and reproducibly determine the QE of new luminophores will be very important in the future ECL research. For these works, we were able to develop a method to determine the QE of ECL co-reactant systems. The QE of a reference compound $Ru(bpy)_3^{2+}$ was calculated to be 3.2% and 10.0% under the annihilation and TPrA coreactant pathways, respectively.

In Chapter 5, we studied the electrochemical and luminescent properties of Pt-Ag noble metal nanoclusters. Through the use of electrochemistry, photoluminescence, and in-situ

time-resolved spectroscopy, we discovered a number of different excited states that were responsible for ECL emission for these nanoclusters. Furthermore, we learned that the effective surface area (which is the geometric surface are exposed for external reaction) was directly correlated with the quantum efficiency of the nanoclusters. This finding is anticipated to be useful for future design of ECL luminophores. In Chapter 6, the electrochemistry, electrochemiluminescence, and chemiluminescence of a TADF emitter (TPA-ace-TRZ) was investigated. We discovered that this compound exhibited delayed onset ECL and long-persistent luminescence, which was attributed to the formation of an aggregated excited state known as an excimer. This aggregate excited state was also present in both electrochemiluminescence and chemiluminescence pathways, which demonstrates the flexibility and potential applications for TPA-ace-TRZ.

In Chapter 7, the development of a computer model to simulate ECL electron transfer and light emission reactions was performed. The simulations were carried out using COMSOL Multiphysics software. In this work, we were able to estimate the bimolecular rate constant of $Ru(bpy)_3^{2+}$ annihilation ECL to be in the range of 10^7 $M^{-1}s^{-1}$ by using an ultramicroelectrode and high frequency potential pulsing at 10 Hz, 100 Hz, and 1000 Hz. This model to simulate the hemispherical diffusion of electroactive species is shown to be able to extract important chemical and kinetic information from ECL systems.

Chapter 8 summarizes the two types of LECs we fabricated in the lab. Our top-down CQDs synthesized from a top-down electrochemical exfoliation process showed strong photoluminescence and electrochemiluminescence. The CQD-LEC demonstrated bright white emission at a wavelength of 610 nm with an efficiency of 0.14%. To improve upon this efficiency, we experimented by adding a zinc oxide layer to the LECs to enhance the electron transporting capabilities of the deposited films, in Chapter 9. The ZnO-LECs exhibited improved stability and up to 4-fold enhancement of the brightness.

10.2 Future Work

The research field of thin-film optoelectronic devices has been expanding rapidly, and so there is a continual need for highly efficient and cheap luminescent materials to be investigated. These advancements will also benefit the various applications discussed in this thesis, such as for bioanalysis, chemical sensing, and imaging.

There are many different novel materials that exhibit the properties that show promise for applications in LECs. One of these is black phosphorous (BP), an allotrope of elemental phosphorous. Single-layered BP, also known as phosphorene, displays many similarities to graphene: it has a tunable bandgap, excellent charge transport and optical characteristics. We propose to study in detail the photoluminescence and electrochemical properties of this nanomaterial. BP could be an important candidate for a luminophore in LECs, and investigating the light emitting reactions of this new material could help confirm the contribution of core and surface states in luminescence, since their involvement may be similar to that of CQDs.

We also plan to expand on the computer simulation project to model ECL reactions in COMSOL. Currently, we have only simulated ECL annihilation reactions, which is a small subset of ECL reactions. We propose to further progress the simulations to model the various coreactant systems such as the oxidative-reduction type (with tri-propylamine) and the reductive-oxidation (with benzoyl peroxide). Successful development and implementation of these ECL models will significantly improve our understanding of how ECL reactions work, and will be an important step in optimizing these reactions.

Finally, this thesis only briefly explored the extensive possibilities for organic and carbon nanomaterial LECs. As a future project, we would like to investigate a wider range of luminescent materials for their feasibility as LEC luminophores, such as the Pt-Ag nanocluster system, or the TADF compounds discussed herein. In particular, we imagine that the aggregation- and crystallization-induced enhanced emission observed for those compounds will be even more pronounced in the solid state (when deposited as a thin-film for LECs). However, the primary challenge for incorporating these materials would

be their compatibility with solvent systems for spin-coating, or their thermal stability during ALD and PVD layer deposition. A careful and methodical study will be required to fine-tune the parameters required for bright and efficient LECs.

Appendices

Appendix A: Reproduction Permission for paper "Nanocluster Transformation Induced by SbF_6^- Anions toward Boosting Photochemical Activities."

Nanocluster Transformation Induced by SbF6– Anions toward Boosting Photochemical Activities

Author: Xiao Wei, Kenneth Chu, Jonathan Ralph Adsetts, et al
Publication: Journal of the American Chemical Society
Publisher: American Chemical Society
Date: Nov 1, 2022

Copyright © 2022, American Chemical Society

PERMISSION/LICENSE IS GRANTED FOR YOUR ORDER AT NO CHARGE

This type of permission/license, instead of the standard Terms and Conditions, is sent to you because no fee is being charged for your order. Please note the following:

- Permission is granted for your request in both print and electronic formats, and translations.
- If figures and/or tables were requested, they may be adapted or used in part.
- Please print this page for your records and send a copy of it to your publisher/graduate school.
- Appropriate credit for the requested material should be given as follows: "Reprinted (adapted) with permission from {COMPLETE REFERENCE CITATION}. Copyright {YEAR} American Chemical Society." Insert appropriate information in place of the capitalized words.
- One-time permission is granted only for the use specified in your RightsLink request. No additional uses are granted (such as derivative works or other editions). For any uses, please submit a new request.

If credit is given to another source for the material you requested from RightsLink, permission must be obtained from that source.

Appendix B: Reproduction Permission for paper "Physical Strategy to Determine Absolute Electrochemiluminescence Quantum Efficiencies of Coreactant Systems Using a Photon-Counting Photomultiplier Device."

Physical Strategy to Determine Absolute Electrochemiluminescence Quantum Efficiencies of Coreactant Systems Using a Photon-Counting Photomultiplier Device

Author: Kenneth Chu, Jonathan R. Adsetts, Jing Ma, et al
Publication: The Journal of Physical Chemistry C
Publisher: American Chemical Society
Date: Oct 1, 2021

Copyright © 2021, American Chemical Society

PERMISSION/LICENSE IS GRANTED FOR YOUR ORDER AT NO CHARGE

This type of permission/license, instead of the standard Terms and Conditions, is sent to you because no fee is being charged for your order. Please note the following:

- Permission is granted for your request in both print and electronic formats, and translations.
- If figures and/or tables were requested, they may be adapted or used in part.
- Please print this page for your records and send a copy of it to your publisher/graduate school.
- Appropriate credit for the requested material should be given as follows: "Reprinted (adapted) with permission from {COMPLETE REFERENCE CITATION}. Copyright {YEAR} American Chemical Society." Insert appropriate information in place of the capitalized words.
- One-time permission is granted only for the use specified in your RightsLink request. No additional uses are granted (such as derivative works or other editions). For any uses, please submit a new request.

If credit is given to another source for the material you requested from RightsLink, permission must be obtained from that source.

Appendix C: Reproduction permission for paper "Absolute Electrochemiluminescence Quantum Efficiency of Au Nanoclusters by Means of a Spectroscopy Charge-Coupled Device Camera."

Absolute Electrochemiluminescence Quantum Efficiency of Au Nanoclusters by Means of a Spectroscopy Charge-Coupled Device Camera

Author: Jonathan R. Adsetts, Kenneth Chu, Mahdi Hesari, et al
Publication: The Journal of Physical Chemistry C
Publisher: American Chemical Society
Date: Dec 1, 2022

Copyright © 2022, American Chemical Society

PERMISSION/LICENSE IS GRANTED FOR YOUR ORDER AT NO CHARGE

This type of permission/license, instead of the standard Terms and Conditions, is sent to you because no fee is being charged for your order. Please note the following:

- Permission is granted for your request in both print and electronic formats, and translations.
- If figures and/or tables were requested, they may be adapted or used in part.
- Please print this page for your records and send a copy of it to your publisher/graduate school.
- Appropriate credit for the requested material should be given as follows: "Reprinted (adapted) with permission from {COMPLETE REFERENCE CITATION}. Copyright {YEAR} American Chemical Society." Insert appropriate information in place of the capitalized words.
- One-time permission is granted only for the use specified in your RightsLink request. No additional uses are granted (such as derivative works or other editions). For any uses, please submit a new request.

If credit is given to another source for the material you requested from RightsLink, permission must be obtained from that source.

Appendix D: Reproduction permission for paper “Electrogenerated Chemiluminescence and Electroluminescence of N-Doped Graphene Quantum Dots Fabricated from an Electrochemical Exfoliation Process in Nitrogen-Containing Electrolytes.”

JOHN WILEY AND SONS LICENSE
TERMS AND CONDITIONS

Jun 28, 2023

This Agreement between University of Western Ontario -- Kenneth Chu ("You") and John Wiley and Sons ("John Wiley and Sons") consists of your license details and the terms and conditions provided by John Wiley and Sons and Copyright Clearance Center.

License Number	5577811448616
License date	Jun 28, 2023
Licensed Content Publisher	John Wiley and Sons
Licensed Content Publication	Chemistry - A European Journal
Licensed Content Title	Electrogenerated Chemiluminescence and Electroluminescence of N-Doped Graphene Quantum Dots Fabricated from an Electrochemical Exfoliation Process in Nitrogen-Containing Electrolytes

Licensed Content Author	Zhifeng Ding, David A. Love, Jonathan M. Wong, et al
Licensed Content Date	Oct 6, 2020
Licensed Content Volume	26
Licensed Content Issue	68
Licensed Content Pages	9
Type of use	Dissertation/Thesis
Requestor type	Author of this Wiley article
Format	Print and electronic
Portion	Full article
Will you be translating?	No
Title	Investigating luminescent materials and optimization strategies for next-generation light emitting electrochemical cells
Institution name	University of Western Ontario
Expected presentation date	Aug 2023
Requestor Location	Canada Attn: University of Western Ontario
Publisher Tax ID	EU826007151

Total 0.00 CAD

Terms and Conditions

TERMS AND CONDITIONS

This copyrighted material is owned by or exclusively licensed to John Wiley & Sons, Inc. or one of its group companies (each a"Wiley Company") or handled on behalf of a society with which a Wiley Company has exclusive publishing rights in relation to a particular work (collectively "WILEY"). By clicking "accept" in connection with completing this licensing transaction, you agree that the following terms and conditions apply to this transaction (along with the billing and payment terms and conditions established by the Copyright Clearance Center Inc., ("CCC's Billing and Payment terms and conditions"), at the time that you opened your RightsLink account (these are available at any time at http://myaccount.copyright.com).

Terms and Conditions

The materials you have requested permission to reproduce or reuse (the "Wiley Materials") are protected by copyright.

You are hereby granted a personal, non-exclusive, non-sub licensable (on a stand-alone basis), non-transferable, worldwide, limited license to reproduce the Wiley Materials for the purpose specified in the licensing process. This license, **and any CONTENT (PDF or image file) purchased as part of your order,** is for a one-time use only and limited to any maximum distribution number specified in the license. The first instance of republication or reuse granted by this license must be completed within two years of the date of the grant of this license (although copies prepared before the end date may be distributed thereafter). The Wiley Materials shall not be used in any other manner or for any other purpose, beyond what is granted in the license. Permission is granted subject to an appropriate acknowledgement given to the author, title of the material/book/journal and the publisher. You shall also duplicate the copyright notice that appears in the Wiley publication in your

use of the Wiley Material. Permission is also granted on the understanding that nowhere in the text is a previously published source acknowledged for all or part of this Wiley Material. Any third party content is expressly excluded from this permission.

With respect to the Wiley Materials, all rights are reserved. Except as expressly granted by the terms of the license, no part of the Wiley Materials may be copied, modified, adapted (except for minor reformatting required by the new Publication), translated, reproduced, transferred or distributed, in any form or by any means, and no derivative works may be made based on the Wiley Materials without the prior permission of the respective copyright owner. **For STM Signatory Publishers clearing permission under the terms of the STM Permissions Guidelines only, the terms of the license are extended to include subsequent editions and for editions in other languages, provided such editions are for the work as a whole in situ and does not involve the separate exploitation of the permitted figures or extracts,** You may not alter, remove or suppress in any manner any copyright, trademark or other notices displayed by the Wiley Materials. You may not license, rent, sell, loan, lease, pledge, offer as security, transfer or assign the Wiley Materials on a stand-alone basis, or any of the rights granted to you hereunder to any other person.

The Wiley Materials and all of the intellectual property rights therein shall at all times remain the exclusive property of John Wiley & Sons Inc, the Wiley Companies, or their respective licensors, and your interest therein is only that of having possession of and the right to reproduce the Wiley Materials pursuant to Section 2 herein during the continuance of this Agreement. You agree that you own no right, title or interest in or to the Wiley Materials or any of the intellectual property rights therein. You shall have no rights hereunder other than the license as provided for above in Section 2. No right, license or interest to any trademark, trade name, service mark or other branding ("Marks") of WILEY or its licensors is granted hereunder, and you agree that you shall not assert any such right, license or interest with respect thereto.

NEITHER WILEY NOR ITS LICENSORS MAKES ANY WARRANTY OR REPRESENTATION OF ANY KIND TO YOU OR ANY THIRD PARTY, EXPRESS,

IMPLIED OR STATUTORY, WITH RESPECT TO THE MATERIALS OR THE ACCURACY OF ANY INFORMATION CONTAINED IN THE MATERIALS, INCLUDING, WITHOUT LIMITATION, ANY IMPLIED WARRANTY OF MERCHANTABILITY, ACCURACY, SATISFACTORY QUALITY, FITNESS FOR A PARTICULAR PURPOSE, USABILITY, INTEGRATION OR NON-INFRINGEMENT AND ALL SUCH WARRANTIES ARE HEREBY EXCLUDED BY WILEY AND ITS LICENSORS AND WAIVED BY YOU.

WILEY shall have the right to terminate this Agreement immediately upon breach of this Agreement by you.

You shall indemnify, defend and hold harmless WILEY, its Licensors and their respective directors, officers, agents and employees, from and against any actual or threatened claims, demands, causes of action or proceedings arising from any breach of this Agreement by you.

IN NO EVENT SHALL WILEY OR ITS LICENSORS BE LIABLE TO YOU OR ANY OTHER PARTY OR ANY OTHER PERSON OR ENTITY FOR ANY SPECIAL, CONSEQUENTIAL, INCIDENTAL, INDIRECT, EXEMPLARY OR PUNITIVE DAMAGES, HOWEVER CAUSED, ARISING OUT OF OR IN CONNECTION WITH THE DOWNLOADING, PROVISIONING, VIEWING OR USE OF THE MATERIALS REGARDLESS OF THE FORM OF ACTION, WHETHER FOR BREACH OF CONTRACT, BREACH OF WARRANTY, TORT, NEGLIGENCE, INFRINGEMENT OR OTHERWISE (INCLUDING, WITHOUT LIMITATION, DAMAGES BASED ON LOSS OF PROFITS, DATA, FILES, USE, BUSINESS OPPORTUNITY OR CLAIMS OF THIRD PARTIES), AND WHETHER OR NOT THE PARTY HAS BEEN ADVISED OF THE POSSIBILITY OF SUCH DAMAGES. THIS LIMITATION SHALL APPLY NOTWITHSTANDING ANY FAILURE OF ESSENTIAL PURPOSE OF ANY LIMITED REMEDY PROVIDED HEREIN.

Should any provision of this Agreement be held by a court of competent jurisdiction to be illegal, invalid, or unenforceable, that provision shall be deemed amended to achieve as

nearly as possible the same economic effect as the original provision, and the legality, validity and enforceability of the remaining provisions of this Agreement shall not be affected or impaired thereby.

The failure of either party to enforce any term or condition of this Agreement shall not constitute a waiver of either party's right to enforce each and every term and condition of this Agreement. No breach under this agreement shall be deemed waived or excused by either party unless such waiver or consent is in writing signed by the party granting such waiver or consent. The waiver by or consent of a party to a breach of any provision of this Agreement shall not operate or be construed as a waiver of or consent to any other or subsequent breach by such other party.

This Agreement may not be assigned (including by operation of law or otherwise) by you without WILEY's prior written consent.

Any fee required for this permission shall be non-refundable after thirty (30) days from receipt by the CCC.

These terms and conditions together with CCC's Billing and Payment terms and conditions (which are incorporated herein) form the entire agreement between you and WILEY concerning this licensing transaction and (in the absence of fraud) supersedes all prior agreements and representations of the parties, oral or written. This Agreement may not be amended except in writing signed by both parties. This Agreement shall be binding upon and inure to the benefit of the parties' successors, legal representatives, and authorized assigns.

In the event of any conflict between your obligations established by these terms and conditions and those established by CCC's Billing and Payment terms and conditions, these terms and conditions shall prevail.

WILEY expressly reserves all rights not specifically granted in the combination of (i) the license details provided by you and accepted in the course of this licensing transaction, (ii) these terms and conditions and (iii) CCC's Billing and Payment terms and conditions.

This Agreement will be void if the Type of Use, Format, Circulation, or Requestor Type was misrepresented during the licensing process.

This Agreement shall be governed by and construed in accordance with the laws of the State of New York, USA, without regards to such state's conflict of law rules. Any legal action, suit or proceeding arising out of or relating to these Terms and Conditions or the breach thereof shall be instituted in a court of competent jurisdiction in New York County in the State of New York in the United States of America and each party hereby consents and submits to the personal jurisdiction of such court, waives any objection to venue in such court and consents to service of process by registered or certified mail, return receipt requested, at the last known address of such party.

WILEY OPEN ACCESS TERMS AND CONDITIONS

Wiley Publishes Open Access Articles in fully Open Access Journals and in Subscription journals offering Online Open. Although most of the fully Open Access journals publish open access articles under the terms of the Creative Commons Attribution (CC BY) License only, the subscription journals and a few of the Open Access Journals offer a choice of Creative Commons Licenses. The license type is clearly identified on the article.

The Creative Commons Attribution License

The Creative Commons Attribution License (CC-BY) allows users to copy, distribute and transmit an article, adapt the article and make commercial use of the article. The CC-BY license permits commercial and non-

Creative Commons Attribution Non-Commercial License

The Creative Commons Attribution Non-Commercial (CC-BY-NC)License permits use, distribution and reproduction in any medium, provided the original work is properly cited and is not used for commercial purposes.(see below)

Creative Commons Attribution-Non-Commercial-NoDerivs License

The Creative Commons Attribution Non-Commercial-NoDerivs License (CC-BY-NC-ND) permits use, distribution and reproduction in any medium, provided the original work is properly cited, is not used for commercial purposes and no modifications or adaptations are made. (see below)

Use by commercial "for-profit" organizations

Use of Wiley Open Access articles for commercial, promotional, or marketing purposes requires further explicit permission from Wiley and will be subject to a fee.

Further details can be found on Wiley Online Library http://olabout.wiley.com/WileyCDA/Section/id-410895.html

Other Terms and Conditions:

v1.10 Last updated September 2015

Appendix E: Reproduction permission for paper "Spooling Electroluminescence Spectroscopy of $Ru(bpy)_3^{2+}$ Light-Emitting Electrochemical Cells with an Atomic Layer Deposited Zinc Oxide Electron-Transporting/Hole-Blocking Interlayer."

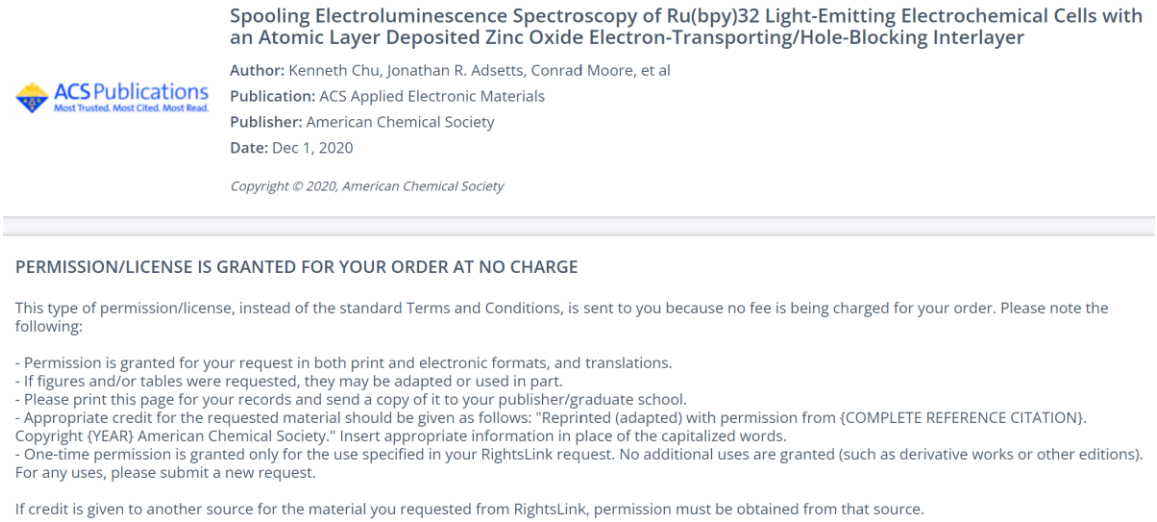

Spooling Electroluminescence Spectroscopy of Ru(bpy)32 Light-Emitting Electrochemical Cells with an Atomic Layer Deposited Zinc Oxide Electron-Transporting/Hole-Blocking Interlayer

ACS Publications
Most Trusted. Most Cited. Most Read.

Author: Kenneth Chu, Jonathan R. Adsetts, Conrad Moore, et al
Publication: ACS Applied Electronic Materials
Publisher: American Chemical Society
Date: Dec 1, 2020

Copyright © 2020, American Chemical Society

PERMISSION/LICENSE IS GRANTED FOR YOUR ORDER AT NO CHARGE

This type of permission/license, instead of the standard Terms and Conditions, is sent to you because no fee is being charged for your order. Please note the following:

- Permission is granted for your request in both print and electronic formats, and translations.
- If figures and/or tables were requested, they may be adapted or used in part.
- Please print this page for your records and send a copy of it to your publisher/graduate school.
- Appropriate credit for the requested material should be given as follows: "Reprinted (adapted) with permission from {COMPLETE REFERENCE CITATION}. Copyright {YEAR} American Chemical Society." Insert appropriate information in place of the capitalized words.
- One-time permission is granted only for the use specified in your RightsLink request. No additional uses are granted (such as derivative works or other editions). For any uses, please submit a new request.

If credit is given to another source for the material you requested from RightsLink, permission must be obtained from that source.

Curriculum Vitae

Name: Kenneth Chu

Education:
Doctor of Philosophy 2018 – 2023
Physical and Analytical Chemistry
The University of Western Ontario, London, ON

Bachelor of Science 2011 – 2016
Honour Specialization in Chemistry and Biochemistry
Science Internship Program
The University of Western Ontario, London, ON

Awards:
Ontario Graduate Scholarship 2021, 2022
Analytical Chemistry Division Ryan-Harris Graduate Travel Award 2023
Roy Young Chemistry Graduate Scholarship 2023
CSC 2004 Conference Travel Award 2022
G. Michael and Joanne Bancroft Research Award 2021

Teaching Experience:
Laboratory Teaching Assistant 2018 – 2023
The University of Western Ontario, London, ON

Publications:

First Author/First Co-author equally contributed

Chu, K.; Ding, Z.; Zysman-Colman, E. Materials for Electrochemiluminescence: TADF, Hydrogen-bonding, and Aggregation-and Crystallization-Induced Emission Luminophores. *Chem. Eur. J.* (2023) e202301504.

Chu, K.; **Adsetts, J.** (equally contributed first author); Whitworth, Z.; Kumar, S.; Zysman-Colman, E.; Ding, Z. Elucidation of an Aggregate Excited State in the Electrochemiluminescence and Chemiluminescence of a Thermally Activated Delayed Fluorescence (TADF) Emitter. *Langmuir* 2023, 39, 2829-2837.

Adsetts, J.; **Chu, K**. (equally contributed first author); Hesari, M.; Whitworth, Z.; Qin, X.; Zhan, Z.; Ding, Z. Absolute Electrochemiluminescence Quantum Efficiency of Au Nanoclusters by Means of a Spectroscopy Charge-coupled Device Camera. *J. Phys. Chem. C* 2022, 126, 20155-20162.

Wei, X.; **Chu, K**. (equally contributed first author); Adsetts, J.; Li, H.; Kang, X.; Ding, Z.; Zhu, M. Nanocluster Transformation Induced by SbF_6^- Anions Toward Boosting Photochemical Activities. *J. Am. Chem. Soc.* 2022, 144, 20421-20433.

Chu, K.; Adsetts, J.; Ma, J.; Zhang, C.; Hesari, M.; Yang, L.; Ding, Z. Physical Strategy to Determine Absolute Electrochemiluminescence Quantum Efficiencies of Coreactant Systems Using a Photo-counting Photomultiplier Device. *J. Phys. Chem. C* 2021, 125, 22274-22282.

Chu, K.; Adsetts, J.; Moore, C.; Ding, Z. Spooling Electroluminescence Spectroscopy of $Ru(bpy)_3^{2+}$ Light-Emitting Electrochemical Cells with an Atomic Layer Deposited Zinc Oxide Electron-Transporting/Hole-Blocking Interlayer. *ACS Appl. Electron. Mater.* 2020, 2, 3825-3830.

Chu, K.; Adsetts, J.; He, S.; Zhan, Z.; Yang, L.; Wong, J.; Love, D.; Ding, Z. Electrogenerated Chemiluminescence and Electroluminescence of N-Doped Graphene Quantum Dots Fabricated from an Electrochemical Exfoliation Process in Nitrogen-Containing Electrolytes. *Chem. Eur. J.* 2020, 26, 15892-15900.

Co-authored papers

Qin, X.; Zhang, C.; Whitworth, Z.; Zhan, Z.; **Chu, K.**; Hu, P.; Jahanghiri, S.; Zhou, J.; Chen, J.; Zhang, Q.; Ding, Z. Highly efficient electrochemiluminescence of nitrogen-doped carbon quantum dots. *ASEM*, 2023, 2, 100062.

Qin, X.; Yang, L.; Zhan, Z.; Cieplechowicz, E.; **Chu, K.**; Zhang, C.; Jahanghiri, S.; Welch, G.; Ding, Z. A Graphene-Like N-annulated perylene diimide dimer compound for highly efficient electrochemiluminescence. *Electrochim. Acta* 2023, 450, 142226.

Zhan, Z.; Qin, X.; **Chu, K.**; Sun, X.; Ding, Z. Absolute Quantum Efficiencies for Electrochemiluminescence and Chemiluminescence of Protoporyphrin IX Dimethyl Ester. *J. Electroanal. Chem.* 2023, 932, 117220.

Qin, X.; Zhan, Z.; Zhang, R.; **Chu, K.**; Whitworth, Z.; Ding, Z. Nitrogen- and sulfur-doped graphene quantum dots for chemiluminescence. *Nanoscale* 2023, 15, 3864-3871.

Qin, X.; Zhan, Z.; Jahanghiri, S.; **Chu, K.**; Zhang, C.; Ding, Z. Metal-organic frameworks for Electrochemical and Electrochemiluminescence Immunoassays. *J. Electrochem.* 2023, DOI: 10.13208/j.electrochem.2218003.

Yang, L.; Zhang, R.; Balónová, B.; True, A.; **Chu, K.**; Adsetts, J.; Zhang, C.; Qin, X.; Zysman-Colman, E.; Blight, B.; Ding, Z. Insights into the electrochemiluminescence process of a hydrogen-bonding iridium (III) complex. *J. Electroanal. Chem.* 2022, 920, 116594.

Qin, X.; Yang, L.; Xin, W.; Patel, D.; **Chu, K.**; Kelland, L.; Adsetts, J.; Zhang, C.; Workentin, M.; Pagenkopf, B.; Ding, Z. Correlating structures to electrochemiluminescence efficiencies of silole compounds in coreactant systems. *ChemElectroChem* 2022, 9, e20220605.

Adsetts, J.; Whitworth, Z.; **Chu, K.**; Yang, L.; Zhang, C.; Ding, Z. Closely following equivalent circuit changes during operation of graphene dot light-emitting electrochemical cells. *ChemElectroChem* 2022, 9, e202101512.

Yang, L.; Adsetts, J.; Zhang, R.; Balónová, B.; Piqueras, M.; **Chu, K.**; Zhang, C.; Zysman-Colman, E.; Blight, B.; Ding, Z. Determining absolute electrochemiluminescence quantum efficiencies of two iridium complexes. *J. Electroanal. Chem.* 2022, 906, 115891.

Yang, L.; De-Jager, C.; Adsetts, J.; **Chu, K.**; Liu, K.; Zhang, C.; Ding, Z. Analyzing near-infrared electrochemiluminescence of graphene quantum dots in aqueous media. *Anal. Chem.* 2021, 93, 12409-12416.

Adsetts, J.; **Chu, K.**; Hesari, M.; Ma, J.; Ding, Z. Absolute electrochemiluminescence efficiency quantification strategy exemplified with $Ru(bpy)_3^{2+}$ in the annihilation pathway. *Anal. Chem.* 93, 11626-11633.

Wong, J.; Xu, J.; Zhang, R.; **Chu, K.**; Ding, Z.; Liu, L. Discovering the link between electrochemiluminescence and energy transfer pathways for Mn-doped $CsPbCl_3$ quantum dot films. *J. Phys. Chem. C* 2021, 125, 13696-13705.

He, S.; **Chu, K.**; Wong, J.; Yang, L.; Adsetts, J.; Zhang, R.; Chen, Y.; Ding, Z. Electrochemiluminescence of bare glassy carbon with benzoyl peroxide as the coreactant in N,N-dimethylformamide. *J. Anal. Test.* 2020, 4, 257-263.

Adsetts, J.; Zhang, R.; Yang, L.; **Chu, K.**; Wong, J.; Love, D.; Ding, Z. Efficient white electrochemiluminescent emission from carbon quantum dot films. *Front. Chem.*, 2020, 580822.

Oral Presentations:

"Spectroscopic and electrochemiluminescence insights into metallic nanoclusters." Kenneth Chu, Zhifeng Ding. 106th Canadian Chemistry Conference and Exhibition, Vancouver, BC. June 2023.

"Electrochemiluminescence and the absolute quantum yield of Pt-Ag nanoclusters." Kenneth Chu, Zhifeng Ding. 8th Canadian Conference on Bioinorganic Chemistry, Parry Sound, ON. May 2023.

"Electrochemiluminescence and spectroscopic insights into metallic nanoclusters." Kenneth Chu, Zhifeng Ding. 64th International Conference on Analytical Sciences and Spectroscopy, Kingston, ON. August 2022.

"Fabrication and Optimization Strategies for Light-Emitting Electrochemical Cells." Kenneth Chu, Zhifeng Ding. 105th Canadian Chemistry Conference and Exhibition, Calgary, AB, June 2022.

"Fabrication and characterization of light-emitting electrochemical cells with different emission wavelengths." Kenneth Chu, Zhifeng Ding. 3rd Annual Research Symposium (Western University ECS Student Chapter), London, ON, December 2019.

"Optimization strategies for incorporation of graphene quantum dots into light emitting electrochemical cells." Kenneth Chu, Zhifeng Ding. 102nd Canadian Chemistry Conference and Exhibition, Quebec City, QC, June 2019.

"Graphene quantum dots for next-generation light emitting devices." Kenneth Chu, Zhifeng Ding. 7th International Conference on Bioinorganic Chemistry, Parry Sound, ON, May 2019.